OPTOELECTRONIC APPLICATIONS OF LEAD HALIDE PEROVSKITES

Jonathon R. Harwell

A Thesis Submitted for the Degree of PhD
at the
University of St Andrews

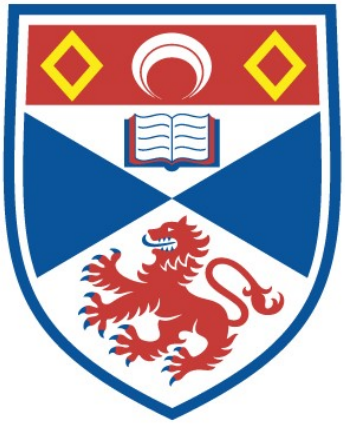

2018

Optoelectronic Applications of Lead Halide Perovskites

Jonathon R Harwell

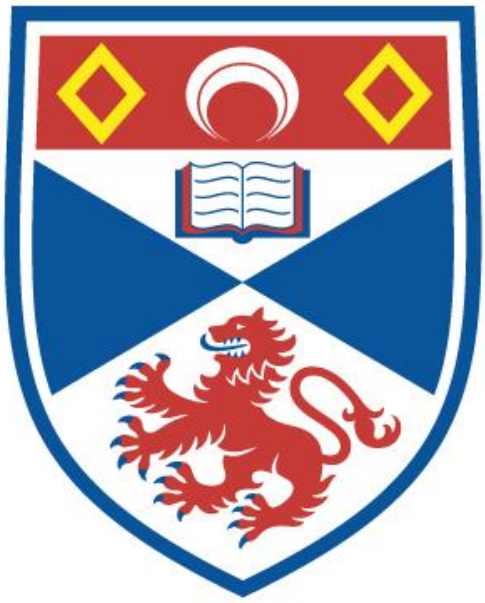

University of
St Andrews

This thesis is submitted in partial fulfilment for the degree of PhD

At the University of St Andrews

April 2018

Candidate's declaration

I, Jonathon Robert Harwell, do hereby certify that this thesis, submitted for the degree of PhD, which is approximately 76,000 words in length, has been written by me, and that it is the record of work carried out by me, or principally by myself in collaboration with others as acknowledged, and that it has not been submitted in any previous application for any degree.

I was admitted as a research student at the University of St Andrews in September 2014.

I received funding from an organisation or institution and have acknowledged the funder(s) in the full text of my thesis.

Date Signature of candidate

Supervisor's declaration

I hereby certify that the candidate has fulfilled the conditions of the Resolution and Regulations appropriate for the degree of PhD in the University of St Andrews and that the candidate is qualified to submit this thesis in application for that degree.

Date Signature of supervisor

Permission for publication

In submitting this thesis to the University of St Andrews we understand that we are giving permission for it to be made available for use in accordance with the regulations of the University Library for the time being in force, subject to any copyright vested in the work not being affected thereby. We also understand, unless exempt by an award of an embargo as requested below, that the title and the abstract will be published, and that a copy of the work may be made and supplied to any bona fide library or research worker, that this thesis will be electronically accessible for personal or research use and that the library has the right to migrate this thesis into new electronic forms as required to ensure continued access to the thesis.

I, Jonathon Robert Harwell, confirm that my thesis does not contain any third-party material that requires copyright clearance.

The following is an agreed request by candidate and supervisor regarding the publication of this thesis:

Printed copy

Embargo on all of print copy for a period of 1 year on the following ground(s):

- Publication would preclude future publication

Supporting statement for printed embargo request

Some of the work in the thesis is yet to be published

Electronic copy

Embargo on all of electronic copy for a period of 1 year on the following ground(s):

- Publication would preclude future publication

Supporting statement for electronic embargo request

Some parts of the Thesis have yet to be published

Title and Abstract

- I agree to the title and abstract being published.

Date Signature of candidate

Date Signature of supervisor

Underpinning Research Data or Digital Outputs

Candidate's declaration

I, Jonathon Robert Harwell, understand that by declaring that I have original research data or digital outputs, I should make every effort in meeting the University's and research funders' requirements on the deposit and sharing of research data or research digital outputs.

Date Signature of candidate

Permission for publication of underpinning research data or digital outputs

We understand that for any original research data or digital outputs which are deposited, we are giving permission for them to be made available for use in accordance with the requirements of the University and research funders, for the time being in force.

We also understand that the title and the description will be published, and that the underpinning research data or digital outputs will be electronically accessible for use in accordance with the license specified at the point of deposit, unless exempt by award of an embargo as requested below.

The following is an agreed request by candidate and supervisor regarding the publication of underpinning research data or digital outputs:

Embargo on all of electronic files for a period of 1 year on the following ground(s):

- Publication would preclude future publication

Supporting statement for embargo request

Some of the work in the thesis has yet to be published in a scientific journal

Date Signature of candidate

Date Signature of supervisor

Acknowledgements

The work in this thesis was made possible by the efforts of so many incredible people, and I certainly would not have made it through with my sanity intact were it not for all your help. I would first like to thank Prof. Ifor Samuel for the opportunity to work on this project, and for his guidance and expertise in this field. Without your help correcting my many writing mistakes, and the help of Prof. Michael Carpenter and Prof. Graham Turnbull, I wouldn't have gotten any of this work published.

I would also like to thank all of my co-workers at the organic semiconductor centre for all their help and insight in innumerable areas. But in particular I would like to thank Dr Stuart Thompson for teaching me the cheerful field of solar cell fabrication, and Dr Lethy Jagadamma and Natalie Mica for their advice when it was all going wrong! Some special thanks goes out to Dr Guy Whitworth and Dr Gordon Hedley for introducing me to lasers and making a huge portion of this thesis possible. I am also grateful for Dr Julia Payne for her microscopically detailed knowledge of solid state chemistry, and her work producing samples for our measurements.

Research at St Andrews would have ground to a halt without the tireless efforts of Callum Smith and all the other cleanroom technicians. Everyone in the department agrees that you guys do an amazing job, and I'd like to thank you specially for keeping the gloveboxes up and running and stopping the CABIE from leaking chlorine everywhere! St Andrews is lucky to have you.

I wouldn't have been able to make it through this PhD without the love and support of my parents, Tricia Harwell and Gordon Harwell. Thank you for always being there for me, especially in the difficult times surrounding the completion of this thesis. My twin sister, Claire Durrant, also deserves credit for the competitive edge she has provided over the years. I didn't know it was even possible to pass one's viva with zero corrections until you managed it!

Finally, I owe my sanity and my lack of an existential catastrophe to James Burch, for taking me climbing and keeping me entertained with misremembered historical quotes, and all my friends who go kayaking with me. Particularly Kirsten Rendle, Alison Galloway, Paul Brear, Jen Hartnett, and many others. My grand designs may have led us into some tree infested ditches in the past, but you have all stuck with me even when we are breaking icicles out of our hair or digging our tents out of the snow, and your friendship has kept me cheerful even at my lowest points. A five-hour drive with you to run some lubricated rocks in low water is better than any weekend spent indoors! You give me something to look forward to at the end of every week and I can't thank you enough.

Collaborations

Much of the work in this thesis was performed in collaboration with other research groups. The collaborations of significance are listed as follows. The work on Kelvin Probe and Air Photoemission in Chapter 4 was performed in collaboration with Prof. Iain Baikie at KP Technology Ltd, Wick. The experiments on A site vacancies also presented in chapter 4 was performed in collaboration with Prof. John Irvine's group in the department of chemistry, University of St Andrews. The work on perovskite nanocrystals in chapter 7 was performed in collaboration with Dr Dan Credgington based in the Cavendish Laboratory at the University of Cambridge. Finally, the resonant ultrasound study shown in chapter 8 was performed in collaboration with Prof. Michael Carpenter at the department of Earth Sciences, University of Cambridge, and Prof. John Irvine's group at the university of St Andrews.

Publications

Publications Directly associated with this PhD are as follows.

Published

- Guy L. Whitworth, J.R.Harwell., David N. Miller, Gordon J. Hedley, Wei Zhang, Henry J. Snaith, Graham A. Turnbull, and Ifor D. W. Samuel ***Nanoimprinted distributed feedback lasers of solution processed hybrid perovskites*** Optics Express, 2016. **24**(21): p. 23677-23684.
- J. R. Harwell, T.K.Baikie., I. D. Baikie, J. L. Payne, C. Ni, J. T. S. Irvine, G. A. Turnbull, I. D. W. Samuel ***Probing the energy levels of perovskite solar cells via Kelvin probe and UV ambient pressure photoemission spectroscopy*** Physical Chemistry Chemical Physics, 2016. **18**: p. 19738-19745
- J. R. Harwell, G.L.Whitworth., G. A. Turnbull, I. D. W. Samuel, ***Green Perovskite Distributed Feedback Lasers***. Sci. Rep., 2017. **7**: p. 11727.

Accepted, Awaiting Publication

- Jonathon R. Harwell, Julia L. Payne, Muhammad T. Sajjad, Frank J. L. Heutz, Daniel M. Dawson, Pamela S. Whitfield, John T. S. Irvine, Ifor D. W. Samuel, Michael A. Carpenter ***The Role of Lattice Distortion and A Site Cation in the Phase Transitions of Methylammonium Lead Halide Perovskites*** Physical Review Materials

Funding

This work was supported by the Engineering and Physical Sciences Research Council (grant number EP/M506631/1)

Abstract

Hybrid perovskites are a new class of semiconductor which have proven to be an ideal material for making thin film solar cells. They have the advantages of flexibility, low cost, and easy processing, whilst achieving efficiencies competitive with monocrystalline silicon. Many of the properties which make them ideal for solar cells are also applicable to light emitting devices, and there is now increasing interest in their application for light emitting diodes (LEDs) and lasers. This thesis aims to use a range of novel spectroscopy techniques to investigate the origin of these favourable properties, and to exploit these properties to produce high performance distributed feedback lasers.

A detailed understanding of the origins of the excellent properties of hybrid perovskites is of crucial importance in the search for new variations with improved performance or lowered toxicity. This thesis uses Kelvin probe, air photoemission, and resonant ultrasound spectroscopy to probe deeply into the underlying physics of hybrid perovskite single crystals and devices. Using these techniques, we are able to produce detailed maps of the energy levels in a common perovskite solar cell, and we also gain strong insight into the underlying strains and instabilities in the perovskite structure that give rise to their elastic properties.

The strong light emission of hybrid perovskites is then exploited to produce high quality distributed feedback lasers emitting in the green and infrared part of the spectrum. These lasers are observed to have superior stability, good thresholds, and many interesting beam parameters owing to their high refractive index. We explore a wide range of processing methods in order to achieve the lowest lasing threshold and the best stability. Finally, we investigate the properties of low dimensional perovskites and investigate their potential in optoelectronic applications.

Chapter 1 – Introduction

The field of organic optoelectronics has made huge progress in recent years, and now commercial devices incorporating organic semiconductors are becoming commonplace in our day to day lives in areas ranging from vibrant displays to flexible sensors, circuit boards, and solar cells. Organic semiconductors (OSCs) are extremely attractive for commercial applications because they can provide a range of advantages over more conventional inorganic semiconductors such as silicon. Firstly, most OSCs are soluble in common solvents such as toluene or chlorobenzene, meaning that high quality thin films of them can be easily fabricated via spin-coating or blade-coating, as opposed to more complicated processes such as the growth of single crystals or evaporation deposition. OSCs can also be printed directly onto a flexible substrate which, combined with their solution processability, opens the possibility of low cost roll-to-roll mass production of flexible devices – a similar method to how newspapers are printed. Finally, OSCs are carbon based molecules where the number of possible structures is essentially infinite. This means that there is a wealth of possible structures to choose from with a diverse range of properties that can be tailored to any specific application. This combination of advantages means that OSCs are seeing increased use in multiple areas including light assisted medicine, chemical sensing, displays, and flexible electronics. Improving the properties of these materials even further could be all that is needed to start another revolution in electronic applications.

Despite their wide and extensive advantages, the commercialisation of OSC devices has been limited by a few key factors. The most significant of which being that, despite their tuneability and simple processing, the outright device performance of OSCs is generally outclassed by the current market dominator in optoelectronics - inorganic semiconductors. The reasons for this shall be discussed further in the second chapter, but the underlying theme is that inorganic semiconductors tend to be superior in terms of stability and performance, whilst OSCs have superior processability, flexibility and tuneability. While the performance of OSCs is constantly improving, the aim of achieving the best of both worlds has led to the development of hybrid perovskites - a new class of semiconductor which aims to combine the advantages of both classes with the disadvantages of neither.

Hybrid perovskites are a very recently discovered material which only first saw use in semiconductor devices in 2009 [1]. But in the time since then they have quickly risen to dominate research in optoelectronics because they are extremely cheap, tuneable, solution processable, and are even coming close to competing with inorganic semiconductors in terms of outright performance. Solar cells made from lead halide perovskites have now reached efficiencies as high as 22.7% [2], making

them competitive even with monocrystalline silicon solar cells, which have a record efficiency of 25.8% [2]. However perovskite solar cells have the potential for much lower payback times as they are more lightweight (potentially reducing installation costs), use cheap and earth abundant starting materials, and have much simpler fabrication routes. Two major reasons for this high performance are that perovskites have higher charge mobilities than most OSCs approaching 1 $cm^2V^{-1}s^{-1}$ [3] (allowing for low series resistance), and their excellent ability to emit light (which contributes to a high output voltage). These two factors have also sparked research into perovskites for light emission, and the early results are extremely promising, with perovskite light emitting diodes reaching external quantum efficiencies as high as 11% whilst also maintaining high stability and brightness [4, 5]. Lasers exploiting perovskites as a laser medium have also become a subject of intense interest, with perovskite lasers able to operate at reasonably low thresholds with good stability in the green and infrared parts of the spectrum [6].

This thesis provides an in-depth study into using perovskites in optoelectronic devices, with a particular focus on their use in thin film distributed feedback lasers. This work first performs detailed studies on the properties of perovskites as a solar cell material, while using some of this insight to study potential new materials which could replace the lead component of the material, thus eliminating a key barrier to commercialisation. The thesis then attempts to gain an insight into the cause of the excellent properties of perovskites by studying them with advanced techniques including time resolved photoluminescence (PL) and resonant ultrasound spectroscopy (RUS). The work then applies the experience and insight gained in these experiments to a practical use by exploiting perovskites as a gain medium in distributed feedback lasers, thus providing all-solution processed lasers with superior stability and light emission. Finally, the impact of forcing low dimensional operation in perovskites is explored through the study of layered perovskites (2D systems) and perovskite nanocrystals (0D systems), with the aim of creating light emitting materials with lower thresholds, higher stability, and better colour tuneability.

Chapter 2 Introduces the underlying physical principles of how both organic and inorganic semiconductors work, and the resulting differences between the two classes. The implications for this are then discussed on how solar cells and light emitting diodes will operate using the two materials, as well as why a good solar cell material should also be good at emitting light. It shall then explain the underlying mechanics behind photoluminescence and stimulated emission in thin film semiconductors, leading to a discussion of how this can be exploited to achieve high quality lasing in extremely thin films. Finally, hybrid perovskites are introduced. Their physics, properties, and low

dimensional analogues, and the way these features can impact their performance optoelectronic devices are discussed in detail.

Chapter 3 Starts by explaining the various processing steps that are needed make a thin film LED, solar cell or laser, before describing in detail the set-ups used to measure the performance of the resulting devices. It then goes on to describe the details of the advanced techniques used to study the properties of the perovskites in depth. This includes intensity dependent photoluminescence quantum yield, time resolved photoluminescence, and Kelvin probe/air photoemission studies.

Chapter 4 Presents the author's work on fabricating perovskite solar cells and in-depth studies of them using Kelvin probe and surface photovoltage techniques. This chapter first reports the various techniques which were employed to achieve high efficiency, followed by a Kelvin probe study of the best structure in an attempt to identify avenues for improvement. Finally, it discusses several attempts to alter the properties of the perovskite by introducing vacancies into the crystal lattice via doping with diamine cations or with bismuth. The last of these was intended to provide a route to achieving high efficiency in a lead-free material.

Chapter 5 Consists of our early work studying the photoluminescence properties of methylammonium lead halides. We explore how the photoluminescence quantum yield of a perovskite film can vary with the pump intensity and how altering the processing conditions can affect that. Under sufficient intensity, amplified spontaneous emission is observed from the perovskite film, and we discuss what processes must be optimised in order to create an infrared emitting distributed feedback laser.

Chapter 6 Follows work attempting to optimise the performance of the perovskite in order to achieve the best stability and the lowest lasing threshold. The focus of the study switches from methylammonium lead iodide to methylammonium lead bromide because the latter emits in the green rather than the infrared, making it easier to optimise and also allowing it to fill the green gap in current commercial lasers. The trade-off between photoluminescence quantum yield (PLQY) and film quality is examined, and an optimal deposition method is developed in order to make a high performance laser with low threshold and excellent stability. We then perform further study into the properties of the lasing modes in this laser and find that the polarisation can be easily tuned by simple switching of the grating period.

Chapter 7 Attempts to overcome some of the limitations in the tuneability of 3 dimensional perovskites by studying perovskite nanocrystals (PNCs) as an alternative lasing material. PNCs proved to have remarkably high PLQY even at low excitation densities, and can be easily tuned to

emit at any wavelength in the visible spectrum. We are able to fabricate lasers from these materials but find that the lasing threshold is fairly high despite their excellent light emission. We discuss methods for overcoming this issue and compare and contrast the properties of lasers from nanocrystals with those from 3D perovskites. It also explores the properties of 2 dimensional layered perovskites by introducing much larger cations into the bulk structure in order to separate it into layers. We observe that this slightly blue shifts the bandgap and greatly enhances the light emission from the thin film. Film PLQY values as high as 73% are achieved, along with excellent film quality and stability. The layered nature of this system introduces some very interesting photophysics, and also makes them ideal for the study of polaritons at room temperature. Unfortunately despite the excellent light emission we found that the lasing threshold was extremely high, making this material unsuitable for real world applications. However the superior light emission and absence of triplet excitons gives them the potential to be an excellent LED material.

Chapter 8 Discusses a highly advanced and detailed study on single crystals of methylammonium lead halides using resonant ultrasound and time resolved photoluminescence. The impact of strain, hydrogen bonding, and underlying instabilities in the crystal lattice are studied, and we attempt to draw conclusions on how these mechanisms could affect the device performance.

References

1. Kojima, A., et al., *Organometal Halide Perovskites as Visible-Light Sensitizers for Photovoltaic Cells.* Journal of the American Chemical Society, 2009. **131**: p. 6050-6051.
2. Laboratory, N.R.E. *Best Solar Cell Efficiencies*. 2017 [cited 2017; Available from: https://www.nrel.gov/pv/assets/images/efficiency-chart.png.
3. Motta, C., F. El-Mellouhi, and S. Sanvito, *Charge carrier mobility in hybrid halide perovskites.* Scientific Reports, 2015. **5**.
4. Mingjian Yuan, L.N.Q., Riccardo Comin, Grant Walters, Randy Sabatini, Oleksandr Voznyy, Sjoerd Hoogland, Yongbiao Zhao, Eric M. Beauregard, Pongsakorn Kanjanaboos, Zhenghong Lu, Dong Ha Kim, Edward H. Sargent, *Perovskite energy funnels for efficient light-emitting diodes.* Nature Nanotechnology, 2016. **11**: p. 872-877.
5. Nana Wang, L.C., Rui Ge, Shuting Zhang, Yanfeng Miao, Wei Zou, Chang Yi, Yan Sun, Yu Cao, Rong Yang, Yingqiang Wei, Qiang Guo, You Ke, Maotao Yu, Yizheng Jin, Yang Liu, Qingqing Ding, Dawei Di, Le Yang, Guichuan Xing, He Tian, Chuanhong Jin, Feng Gao, Richard H. Friend, Jianpu Wang, Wei Huang, *Perovskite light-emitting diodes based on solution-processed self-organized multiple quantum wells.* Nature Photonics, 2016. **10**: p. 699-704.
6. Zhang, Q., et al., *Advances in Small Perovskite-Based Lasers.* Small Methods, 2017. **1**(9).

Chapter 2 – Solar Cells, OLEDs and Perovskites

Semiconductor theory

Basics of Semiconductors

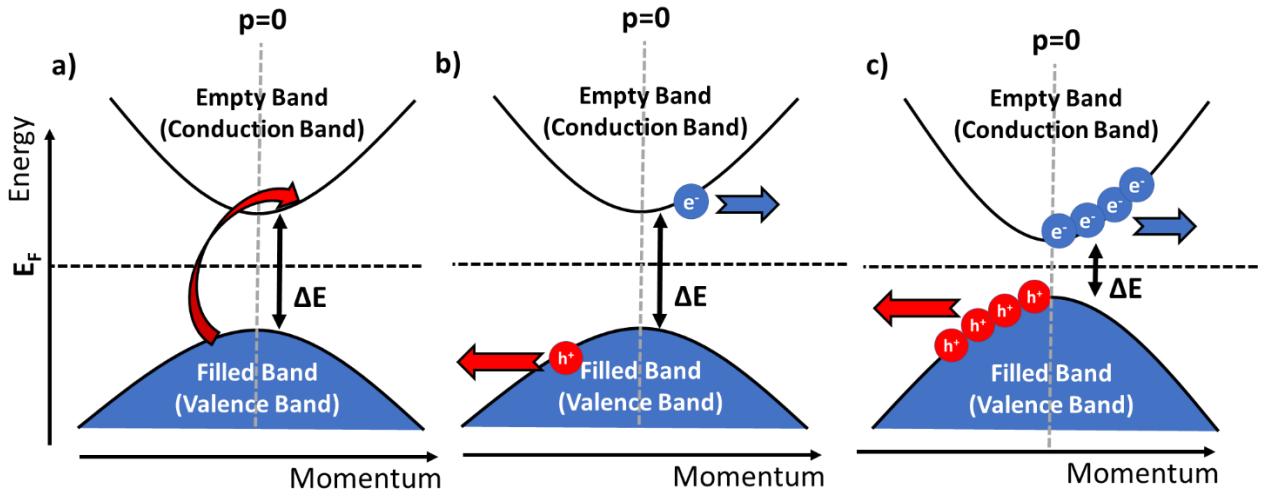

Figure 1 – a) A semiconductor at 0 kelvin. b) Conduction in a wide bandgap semiconductor where the bandgap is so wide that few electrons exist in the conduction band, c) A semiconductor where the bandgap is narrow enough to allow many charge carriers to exist above bandgap for the conduction of electricity.

In order to understand what makes perovskites special, we must first come up with a rigorous understanding of how a semiconductor works in the first place. In any solid, electrons occupy quantum states which are defined by their energy, momentum, and spin. The available states for electrons to occupy tend to congregate into bands, with forbidden regions in between the bands where there are no available states. No electrons can exist within the forbidden region, and the minimum width of the forbidden region is known as the band gap. A semiconductor is a material where, at zero temperature, electrons fill all the available states up to the edge of a band, while all the states in the next band are fully unoccupied. The lower energy, filled band is known as the valence band while the unoccupied band is known as the conduction band (see figure 1a). We can also define a quantity known as the Fermi level (E_F), which is the energy of the highest occupied state at zero temperature, and in a normal semiconductor this sits exactly in the middle of the band gap [1].

In order to conduct electricity, an electron needs to move to a new state so that the net momentum of the system is no longer zero (i.e. it is no longer symmetrical about the p=0 line on figure 1). At zero temperature, this is not possible because all the electrons are in the valence band where there are no available states to move to (because it is completely filled). Therefore no conduction will

occur at zero temperature, but when heat is added to the system some electrons are promoted into the conduction band where there are plenty of available states to move to for the conduction of electricity. The more electrons which occupy the conduction band, the better the conduction of electricity, and the number of electrons which get promoted to the valence band is related to the ratio of the thermal energy (k_BT) compared to the bandgap (ΔE). Hence semiconductors will tend to get more conductive as the temperature is increased or the bandgap is narrowed [1].

In a semiconductor, both the electrons in the conduction band, and the gaps they leave behind in the valence band are able to carry a current. The gaps they leave behind are known as holes, and they act as quasiparticles with positive charge. Thus a semiconductor carries charge through both electrons and holes, as opposed to just electrons which are the dominant carrier in metals.

Doping

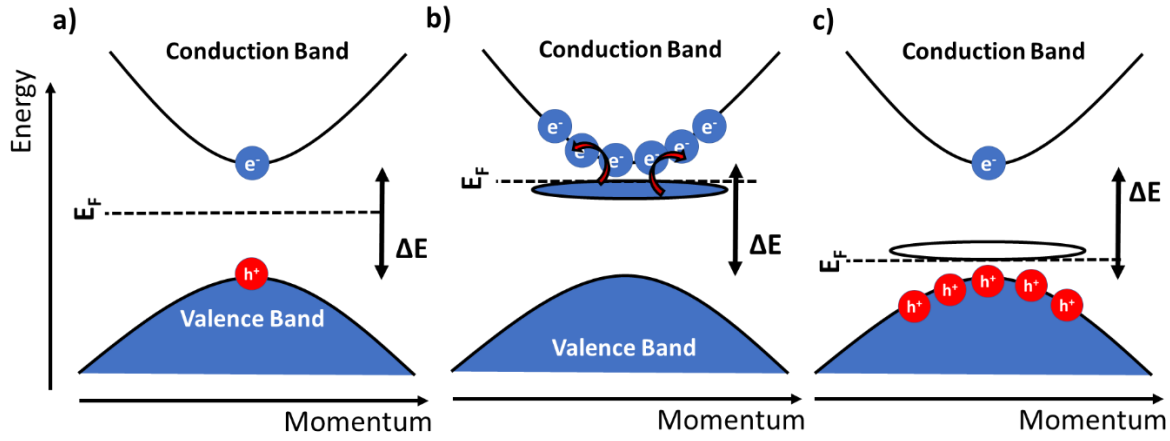

Figure 2- a) An undoped semiconductor, b) An n-type material with a donor level near the conduction band, while c) A p type material with an acceptor level near the valence band. The Fermi level is shifted by the doping.

In a normal semiconductor the Fermi level lies in the middle of the band gap and, because there are a relatively small number of electrons in the conduction band, will always be several orders of magnitude less conductive than a metal. One way we can improve this property is by doping. Doping is a process where one adds a small number of impurities to a semiconductor in order to add a new energy level inside the bandgap to aid conduction. For instance, one could add a small energy level just below the conduction band which is designed to be full of electrons as shown in figure 2 (b). This level can easily donate electrons into the conduction band and hence we are much more able to produce a current of electron charge carriers. This is known as n doping, and it shifts the Fermi level of the material towards the conduction band while making it so the dominant charge carrier in the material is electrons. The opposite process is called p doping, where an empty energy level is placed near the valence band to give the valence electrons somewhere to be promoted to, thus creating an

excess of holes and lowering the Fermi level as shown in figure 2(c). A mixture of both p and n doping will move the fermi level back to the middle of the bandgap, creating ambipolar conduction in the same way as in the undoped case, but with a much higher density of free charge carriers. The limiting case of extremely high doping is that a semiconductor will become metallic in nature, but even very low levels of doping can have a very strong effect on a material's properties, creating effects which can be exploited in a wide variety of different electronic devices.

Semiconductor Interactions with Light

One of the more interesting features of semiconductors is the way they interact with light. The fact that they have a wide region where electrons are forbidden to enter means that a low energy photon will never be absorbed, as it cannot provide enough energy to get the electron across the bandgap. Hence semiconductors are transparent to all photons until the photon energy becomes equal to the energy of the material's bandgap. Once the photon energy is greater than or equal to the bandgap, the material will become strongly absorbing as there are suddenly a lot of states available for the electron to be excited into, with absorbed photon creating a free electron and a hole as shown in figure 3. Thus, in a semiconductor with flat bands the absorption spectrum would follow a step function, with zero absorption below the bandgap and strong absorption above the bandgap. In a real semiconductor the bands are curved, meaning that the number of available states for absorption does not follow an exact step function. Hence the absorption onset is not perfectly vertical, but the basic idea is the same nonetheless.

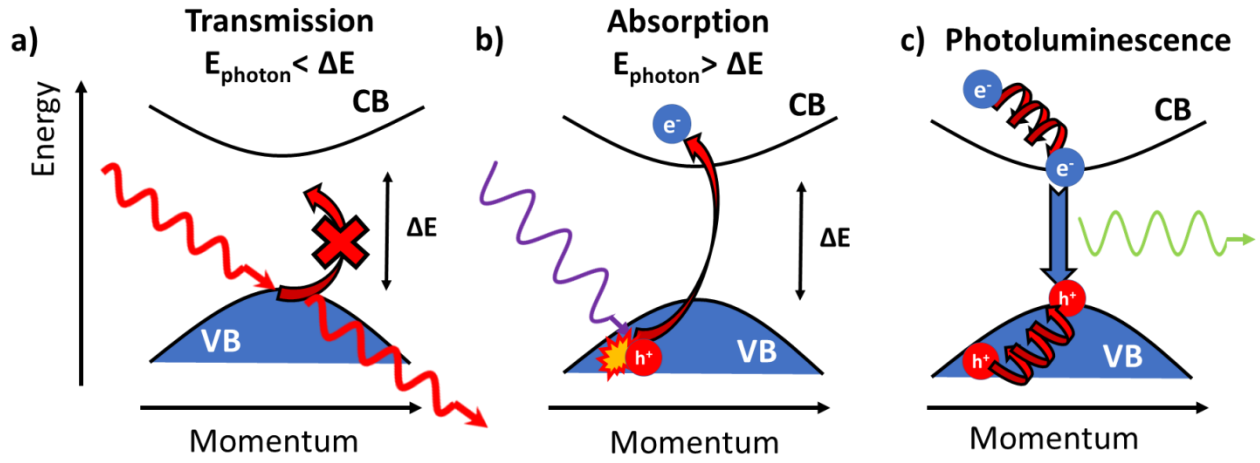

Figure 3-a) A low energy photon being transmitted because it cannot promote electrons across the bandgap from the valence band (VB) to the conduction band (CB), b) A high energy photon being absorbed by promoting an electron, c) An electron and hole thermalizing before recombining to release a photon by photoluminescence.

Once an electron has been excited to well above the bandgap, it decays down to the lowest possible energy state. The first step for this is thermalisation, where the electron will quickly move down through the available states in the conduction band, dissipating its energy as heat in the process. This is a very fast process, and the electron will usually reach the band edge in under a picosecond (ps). The same process occurs for the hole which is created in the valence band, with the exception that holes "bubble up" to the valence band maximum (VBM) rather than "falling down" to the conduction band minimum (CBM). Once at the band edge, the electron cannot cross the bandgap by thermalisation, so it has to decay via photoluminescence (PL). PL is a slower process where the electron hops across the bandgap and recombines with a hole on the other side, releasing its energy as a photon in the process. Thus, when a semiconductor is excited with more energy than the bandgap, the semiconductor will always emit a photon of the same energy as the bandgap and release any excess energy as waste heat. In an ideal semiconductor one would expect the emission spectrum to look like a delta function centred around the bandgap energy. But in a real material several factors such as defect states, interactions with phonons, and the shape of the energy bands will combine to broaden the spectrum.

A notable exception to these rules is indirect bandgap semiconductors. Semiconductors with an indirect bandgap have a band diagram like that shown in figure 4 (b), where the minimum of the conduction band is not at the same momentum as the maximum of the valence band. This means that an electron needs to simultaneously absorb a photon and a phonon in order to cross the bandgap. A phonon is a quasiparticle formed by a lattice vibration, and these carry a lot of momentum but little energy (while a photon carries a lot of energy but little momentum). Hence the photon provides the required energy and the phonon provides the momentum. This is clearly far less likely than simply just absorbing a single photon and therefore the absorption and emission from an indirect bandgap semiconductor is far weaker than that from a direct bandgap material. Silicon is by far the most widely used semiconducting material, and it is a classic example of an indirect bandgap material, with a direct bandgap of 3.3 eV and an indirect bandgap of 1.14 eV. Because of this it is unsuitable for most light emitting applications, and its absorption is comparatively weak compared to other semiconductors. Solar cells made from silicon need to be hundreds of microns thick as opposed to hundreds of nanometres thick when using direct bandgap materials. This effect can be clearly seen in the absorption spectrum of silicon when compared to a direct bandgap material such as gallium arsenide (GaAs), as shown on figure 4 (c). GaAs has a very clear step in absorption around its bandgap at 900 nm [2], corresponding to direct bandgap absorption. The absorption of silicon at its bandgap of 1100 nm turns on more gradually due to the bandgap being indirect with a second, much clearer edge seen at ~400 nm which corresponds to the direct bandgap absorption [2].

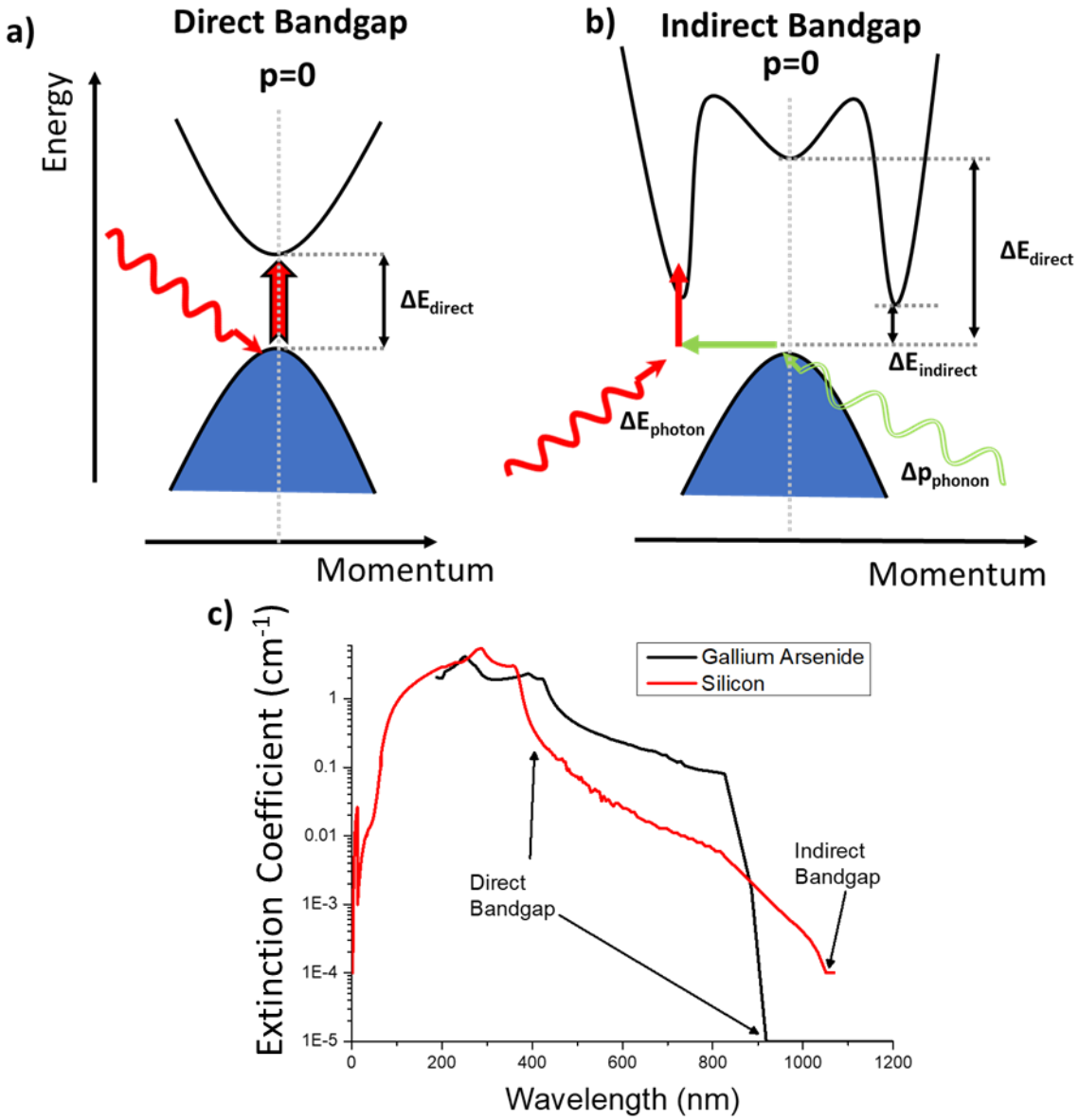

Figure 4 – What the band diagrams tend to look like in a real semiconductor. a) A direct bandgap semiconductor, where a photon can easily make an electron cross the bandgap. b) An indirect bandgap, where promoting an electron requires the simultaneous absorption of a photon to provide energy and a phonon to provide the momentum to get it from the VBM to CBM. Only photons with energy greater than ΔE_{direct} can be absorbed without the help of a phonon. c) A comparisson between the absorption constant of Silicon (indirect) and GaAs (direct). The direct gap absorption can be clearly seen while the indirect absorption is much weaker. Data taken from Palik et al [2].

Organic Semiconductors – An introduction

The most commonly used class of semiconductor is inorganic semiconductors. These are usually crystalline solids such as silicon or gallium arsenide, and their bandgap originates from the overlap of the electron wavefunction with the crystal lattice. An alternative form of semiconductor which is gaining increased popularity is organic semiconductors (OSCs). OSCs are carbon-based molecules, often based on conjugated polymers, which possess many of the properties of inorganic

semiconductors whilst having the easy processing advantages of most plastics [3]. OSCs have a direct bandgap, and they obey all of the rules of semiconductors we have discussed thus far. Like inorganics, their energy bands arise from a linear combination of atomic orbitals. But a key difference is that the bands in inorganics are formed from the overlap of a free electron wavefunction with a crystal lattice, while the bands in OSCs arise from the overlap of p orbitals from π bonds in carbon-carbon double bonds. The bandgap is caused by the difference in energy between the highest occupied molecular orbital (HOMO) and the lowest unoccupied molecular orbital (LUMO).

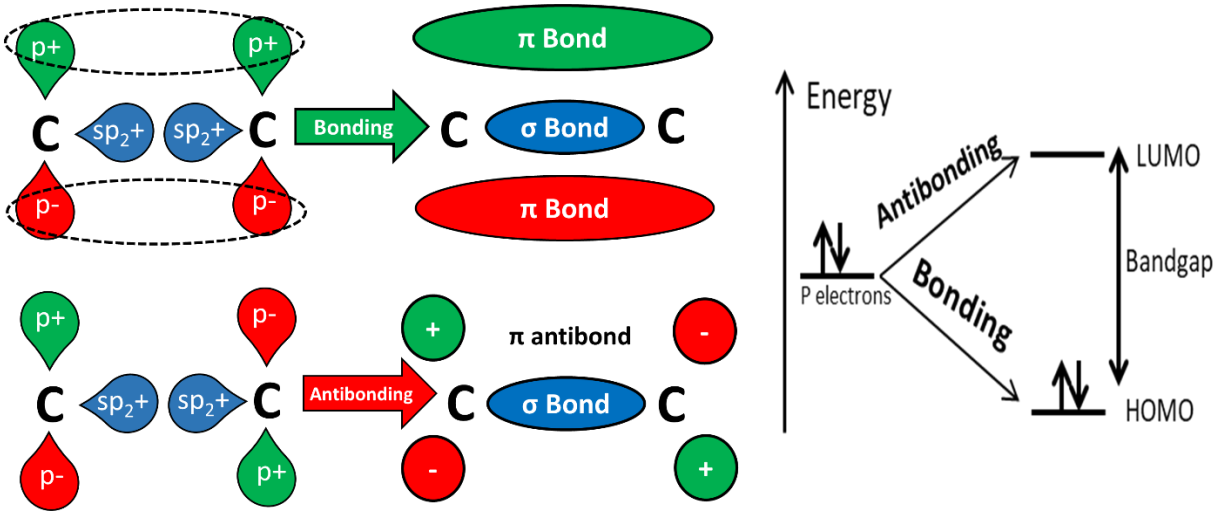

Figure 5 - a) How a π bond and antibond form in a C=C double bond. The bonding orbital is lower in energy than the antibond because the electrons are on average closer to the carbon atoms. b)How the bonding splits the energy levels to create an upper and lower band – or a HOMO and a LUMO

A double bond between two carbon atoms consists of a sigma bond and a pi bond. The sigma bond is formed by the overlap between two sp^2 hybridised orbitals lying in the plane of the bond, while the pi bond is formed by two p orbitals perpendicular to the bond having a small overlap. This weaker bond creates a cloud of electron density above and below the bond as shown in figure 5 (a). These configurations have both bonding (constructive interference of wavefunctions) and antibonding (destructive interference) configurations which split the energy levels of carbon into two. The bonding orbitals are lower in energy than electrons in isolated carbon, and hence they fill up completely with electrons and form the HOMO – the OSC equivalent of a valence band. The antibonding orbitals are higher in energy than the original carbon, and hence they remain unoccupied, thus forming the LUMO (equivalent to conduction band). The bandgap is determined by the difference in energy between the HOMO and LUMO, which can be varied by controlling how well the orbitals in the bond can overlap [3].

The picture above is simplified by the fact that it only has two atoms, and it does not explain how an OSC can conduct electricity – we may have a semiconducting region but it is useless if the electron cannot escape the local bond. However, in an OSC molecule there are not just one but a long line of carbon atoms alternating between single and double bonds. This is called a conjugated chain, and in this situation the isolated double bonds will merge to form one long delocalised cloud where the electrons are free to move up and down the chain. There are two available electrons per repeat unit in this chain, meaning that the HOMO level is completely filled and the chain gains semiconducting properties. A good example of how this occurs is to look at the simplest conjugated polymer - polyacetylene (shown in figure 6). It can be drawn as a line of alternating single bonds, with a π bond over each double bond, but closer study shows that the overlap between the p orbitals can just as easily happen over the single bonds as the double bonds. Therefore, a better picture is that the p orbitals all overlap in a chain to form one a single cloud of delocalised charge which the electrons can freely move through [3]. Thus allowing the polymer to conduct electricity along the conjugated chain. There are many other kinds of conjugated polymer, such as polythiophene, polyfluorene, and polyphenylene vinylene. These all possess different properties which can be further tuned by adding different functional groups to the main backbone.

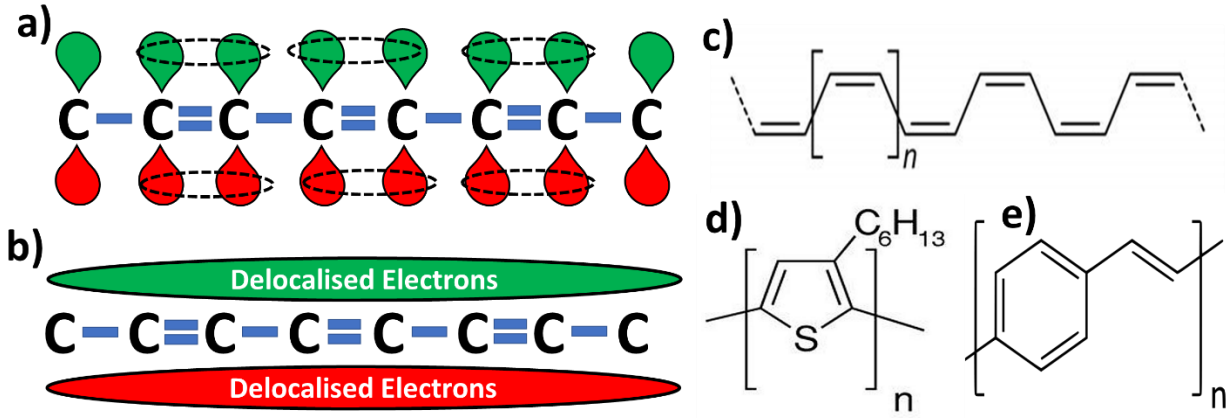

Figure 6 - a) The alternating double and single bonds in a conjugated polymer, while b) How this forms a conducting cloud of electrons. Examples of conjugated polymers are c)polyacetylene, d)poly-3-hexyl thiophene, and e) polyphenylene vinylene. Note the chains of alternating bonds in each of them.

The key advantage of making a semiconductor this way is that one can add functional groups to the OSC to make it readily soluble in a simple solvent such as toluene. This greatly simplifies the manufacture of devices because one can print a device from a solution at low temperatures rather than having to carefully grow a single crystal of the material. OSCs can be printed on flexible substrates, and can get high performance even in very thin films thanks to their direct bandgap. Thus OSC devices have the potential to be extremely cheap and more widely useable than devices from

inorganics. Finally, the versatility of the carbon structure provides a high degree of freedom when designing a molecule – meaning a material can be tuned to exactly meet the requirements in a device.

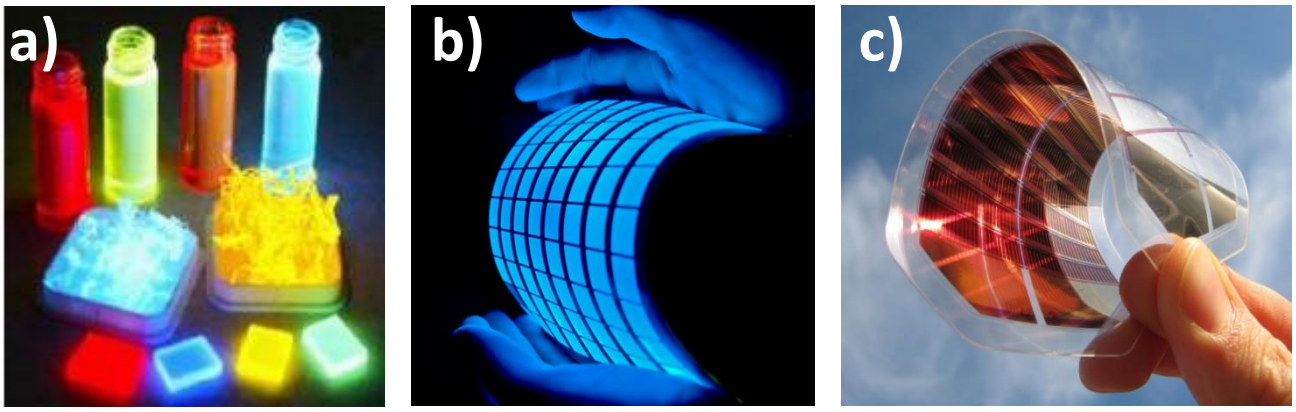

Figure 7 - OSCs in various applications - a) light emitting polymers in solution, powder, and thin film. b) A flexible lighting panel made from OSCs. c) A flexible organic solar cell. (Image sources: [4-6])

Organic Semiconductors – Excitons

Another major difference between inorganic and organic semiconductors is the presence of excitons. As mentioned earlier, when a semiconductor absorbs a photon it creates an electron and hole. The electron and hole are attracted to each other due to their opposite charge and hence will try to orbit each other in a way similar to how a hydrogen atom works. This orbiting pair then acts as a single quasi particle known as an exciton, which has neutral charge and will eventually decay when the electron finally falls back into the hole, releasing a photon in the process. Excitons do not exist at room temperature in most inorganic semiconductors because the binding energy of the exciton is usually in the order of only 15 milielectronvolts (meV) [7]. This means that thermal collisions at room temperature, which have an energy of roughly 25 meV, are more than sufficient to break up the exciton and separate it into a free electron and hole. In OSCs the exciton binding energy can be as high as 500 – 1000 meV [8], so the excitons are strongly bound and will not be separated into free charges unless we provide conditions that force them to split.

Whether the presence of excitons is a good or bad thing depends entirely on what device you are trying to make. If you are trying to make solar cells then excitons are highly detrimental because you will not be able to extract any of the charges you create when you absorb a photon – they will simply exist briefly as an exciton and then decay back to the ground state. Therefore solar cells made from OSCs must have a donor and an acceptor to separate the charges so they can be used to make a current[9]. This will be discussed in more detail later. On the other hand, having your charges in an exciton is generally very good in a light emitting application, as it gives the material a very high

radiative rate. Thus any charges that are created will quickly create photons before any non-radiative pathways can destroy them, giving your device a high brightness and efficiency.

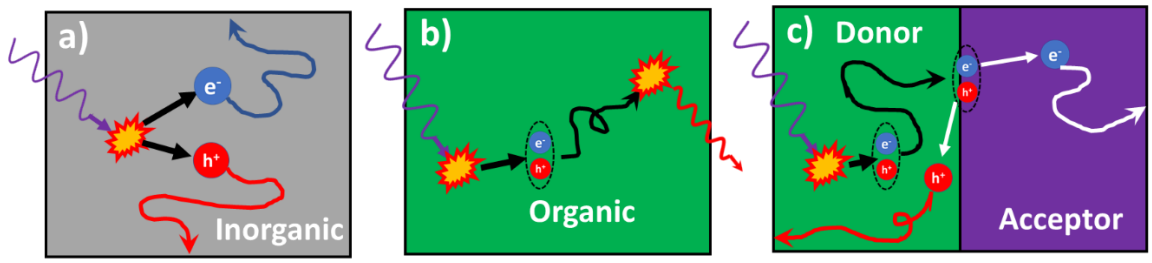

Figure 8 – Photon absorption in a) inorganic and b) organic semiconductors. Charges in inorganic semiconductors are quickly separated into electrons and holes which are free to move independently, while in OSCs the charges are bound together as a pair called an exciton. This exciton will eventually recombine to emit a photon unless it can diffuse to a material which can separate it, as is shown in part c).

The presence of excitons is also essential for the study of another intriguing quasiparticle known as a polariton. Polaritons are essentially the quantum mechanical solution to a coupled oscillator, where a photon is forced to interact strongly with an oscillating dipole [10]. An exciton is a very strong oscillator with a large cross section to interact with light, making it perfect for creating this quantum phenomena. Studying polaritons with most inorganic semiconductors often requires cryogenic temperatures in order to prevent the excitons from dissociating [11]. Polaritons in OSCs on the other hand can easily be studied at room temperature, and coupling effects are much stronger due to the high oscillator strength of the exciton in organics [12]. Hence OSCs are expected to play a pivotal role in this young and promising research field.

Devices from Organic Semiconductors

Organic Light Emitting Diodes (OLEDs)

The most successful application of OSCs thus far has been their use in light emitting diodes (LEDs). Since their inception several decades ago [13], inorganic LEDs have become increasingly popular due to their ability to create intense light sources extremely efficiently and cheaply. However OLEDs are receiving great commercial interest because their unique features can overcome many of the design constraints imposed by inorganic LEDs, allowing them to open up a wealth of new applications. OLEDs are not as bright or efficient as the best inorganic LEDs, but they are extremely thin, lightweight and flexible whilst also being easy to print on a large scale. In addition, the size of an OLED can be varied enormously to either work as a room panel for a large area lighting source or as a pixel on a mobile phone display. A particular advantage of OLEDs in displays is that they are not epitaxially grown, meaning that red, green, and blue pixels can all be printed on the same substrate

as opposed to being limited to an array of identical pixels which must have colour converters to achieve full colour display [14]. Because of this, high-end devices with OLED screens are becoming commonplace, and the prevalence of OLEDs is expected to dramatically increase as the technology improves.

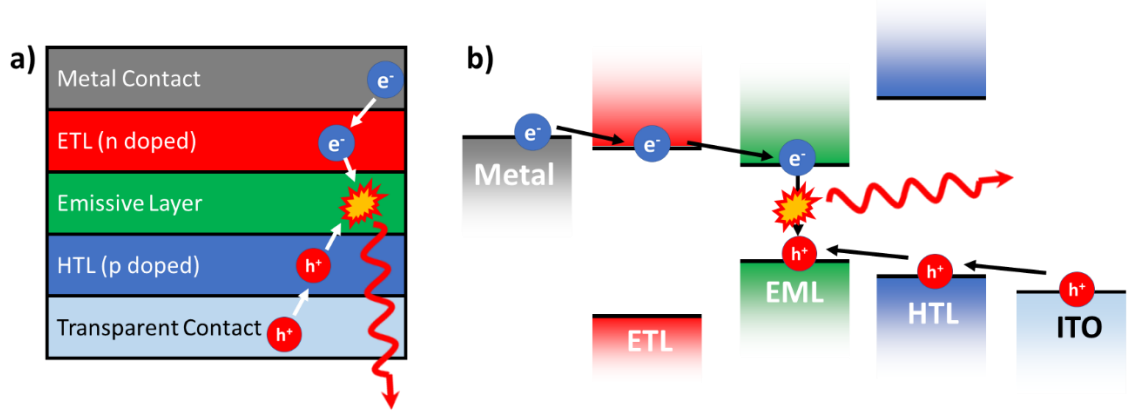

Figure 9 - a) The structure of a basic OLED b) The band diagram for the same OLED. Note the bands have to be precisely aligned to force the charge carriers to flow in the desired direction.

The three main components of a basic OLED are an emissive layer (EML), a hole transporting layer (HTL), and an electron transporting layer (ETL), and they are placed in the structure shown on figure 9. The objective is to put electrons in the LUMO and holes in the HOMO of the emissive layer, which will then form excitons and recombine to create light emission. This is accomplished with a monolithic structure, where an anode is deposited on a substrate and the HTL, EML, ETL, and finally the cathode are deposited sequentially on top of each other to form the device. Note that one or both contacts must be transparent for the generated light to escape. The cathode will inject electrons into the ETL, which has its LUMO aligned with the LUMO of the EML to remove any barriers for the electrons, while the HTL carries holes from the anode into the HOMO of the EML. The alignment of the energy levels in this device is crucial to the performance of the device, as any misalignment will create barriers to the current flow and possibly create an excess of one type of charge, thus spoiling the operation of the device [14]. The external quantum efficiency (EQE) of this device – that is the number of photons released from the device per charge passing through the device - can be approximated by the following equation:

$$EQE \approx \phi_{Ext} = \phi_{Capture} * \phi_{Rad} * \phi_{Spin} * \phi_{Outcouple},$$

where $\phi_{capture}$ is the fraction of charges that successfully become excitons, ϕ_{Rad} is the efficiency of radiative recombination of the exciton, ϕ_{spin} is the fraction of excitons that become singlets, and $\phi_{Outcouple}$ is the fraction of photons that can escape the device. ϕ_{Rad} is usually approximated by

the photoluminescence quantum yield (PLQY) of the EML – that is the number of photons the EML emits per exciton created. In a good OLED, ϕ_{rad} and $\phi_{capture}$ are close to 1, and the efficiency is limited by ϕ_{spin} and $\phi_{Outcouple}$.

ϕ_{Spin} comes about because of the spin statistics of creating an exciton. ϕ_{spin} is important because most OSCs are fluorescent emitters, where the only excitons which emit light are singlet states (i.e. the electron and hole have opposite spin). Almost 100 % of the excitons created via optical excitation will be singlet states, meaning fluorescent OSCs can emit PL with up to 100 % efficiency. However, when the excitons are generated via electrical injection only 25 % of the excitons generated will be singlet states, and the remaining 75 % will be triplets (electron and hole are same spin) [14, 15]. Triplet states do not decay radiatively in most materials because decaying via the emission of a photon will leave two electrons in the same state with the same spin, which is forbidden by the Pauli exclusion principle. Therefore, the only way for a triplet exciton is to decay is through an alternative route that can flip the spin, but if this occurs in a fluorescent material then the energy of exciton is wasted as heat instead of being released as light. Note that this is not a problem for inorganic semiconductors as the charges are not bound as excitons, so a charge can easily move around to find a counterpart with the right spin. But it is a big problem for OLEDs because charges in a triplet exciton cannot leave to find another charge with the correct spin, and so the efficiency of a fluorescent OLED is limited to a maximum of 25% before any other effects are taken into consideration.

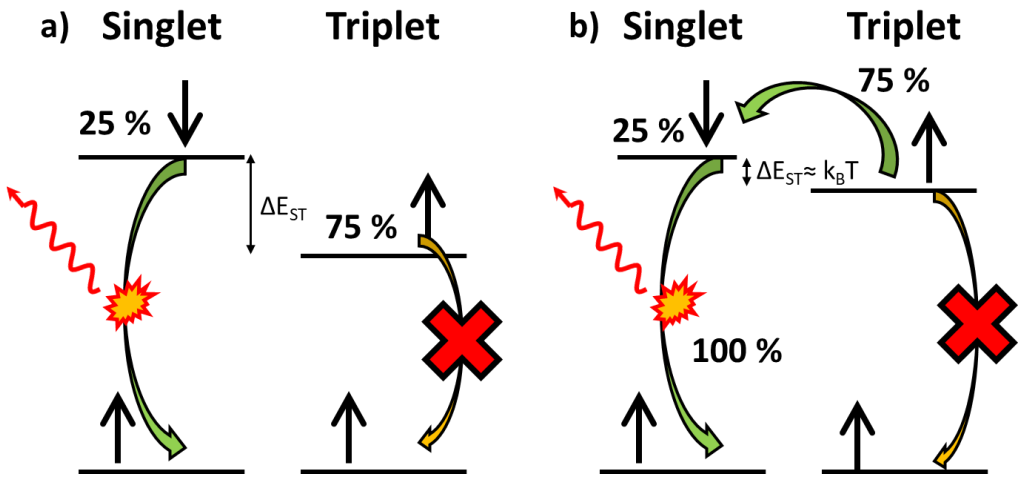

Figure 10 - Spin statistics of organic semiconductors. Part a) A fluorescent emitter, where 75% of excitons are triplet states on electrical injection. These are lower energy than singlets and cannot emit light unless the material is phosphorescent. b) A TADF emitter which gets round this issue by having the triplet sufficiently high energy that it can thermally hop to the singlet to emit light.

Work to combat this effect has mainly revolved around using heavy metal complexes to induce phosphorescence, where spin-orbit coupling with the heavy metal ion provides a mechanism for the triplet states to decay radiatively, or by tuning the energy levels of the molecule to allow thermally activated delayed fluorescence (TADF). TADF is a process where the singlet and triplet states are close enough in energy that thermal excitations can convert triplets into singlets before they decay non-radiatively, thus allowing all generated excitons to decay via the singlet state in the way shown in figure 10. Both phosphorescence [16] and TADF [17] can increase ϕ_{Spin} to 100%, but maintaining this introduces a major design constraint on molecules which can be used in an OLED, and an efficient emitter in the deep blue part of the spectrum has yet to be discovered.

The very best OLEDs to date can achieve near 100% efficiency in ϕ_{Spin}, ϕ_{Inject}, and ϕ_{rad}, [18]but the record EQE values are still limited to around 35% [19](or ~6% in the case of a fluorescent emitter) due to the final parameter – outcoupling. If outcoupling was not a problem then OLEDs could easily match or even exceed the ~70% EQE values seen in inorganic LEDs [20], but unfortunately the design of an OLED results in a large fraction of the light being waveguided inside the device. When an exciton decays in any LED, the photon is emitted in a random direction. If the photon is perpendicular to the device plane then it will easily escape. But if it is emitted beyond a critical angle then total internal reflection will prevent the light from escaping the sample, as seen in figure 11, and it will eventually be lost to the sample edge or through coupling to surface plasmons in the metal contacts [21]. The cone of light which can escape ends up being quite narrow due to the relatively high refractive index of OLED materials, and so the EQE of the device is fundamentally limited. Because of this, there is now a major focus on overcoming this issue by many routes, such as microlens arrays [22], adding scatterers to the devices [23] or by designing molecules which preferentially emit photons perpendicular to the substrate [24].

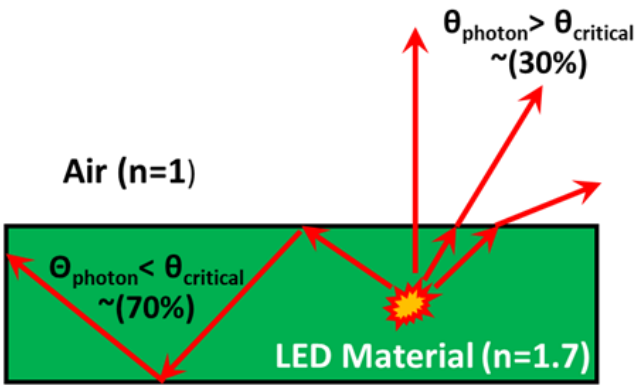

Figure 11- Outcoupling in LEDs – In an OLED the light emission is emitted randomly inside a high index slab, meaning that ~70% can't escape the film due to total internal reflection and is waveguided.

Despite these issues to overcome, OLEDs are still commercially viable and are seeing increased use despite their slightly limited efficiency. Indeed, the biggest barrier to commercialisation was not efficiency but stability. Most OSCs are known to degrade on contact with water or oxygen, and the degradation is accelerated when they have a current running through them [25]. The magnitude of this problem depends on the OSC being used, but the best performing material would not necessarily be the most stable, resulting in optimisation problems. It was only after considerable investment into encapsulation and processing techniques that companies were able to create OLED devices which were stable for long enough to be useful. But now encapsulation technologies are good enough that a consumer OLED display can last for years without visible degradation.

Solar Cells – Basics of solar cell design

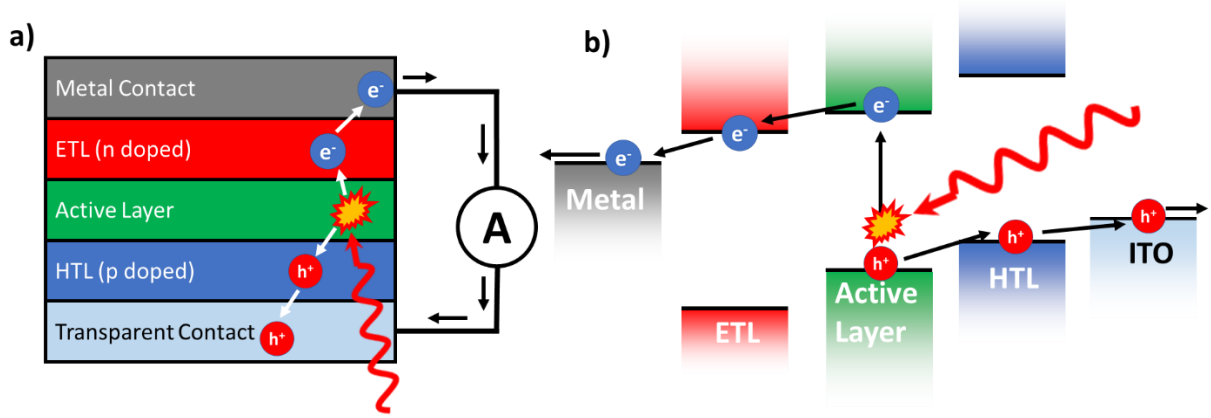

Figure 12 - a) Design of a basic solar cell operating in short circuit. b) Energy level diagram of a solar cell, note that the levels are aligned to force the charges to drift to different contacts

In many ways a solar cell can be viewed as an LED operating in reverse – in an LED we want to inject electrons from one side and holes from the other side and have them recombine to form photons. However in a solar cell the aim is to absorb incoming photons, turn them into electrons and holes, and then extract them at the contacts. As such, the basic design of a solar cell looks very similar to an OLED, with an absorber sandwiched between an HTL and an ETL and at least one transparent contact. A key difference is that the absorber layer must now be 100-200 nm thick in order to absorb enough light to be useful [26], as opposed to in OLEDs where the emissive layer only needs to be ~10 nm thick, but as long as the absorber is a good conductor this has little impact on the electrical properties of the device. Hence the current density to voltage graph (J-V curve) of a solar cell in the dark looks exactly like an OLED. Very little current is passed below a set turn-on voltage, and beyond this the current exponentially increases before tending to a constant gradient determined by the resistance of the diode. When the solar cell is put in sunlight, the entire curve is shifted downwards as the solar cell produces current in the opposing direction. The J-V curve is divided into 4 quadrants

as shown in figure 13 (a), and the most important quadrant is the fourth quadrant, which has positive voltage but negative current. Any points appearing in the fourth quadrant correspond to the generation of power because the solar cell is doing work against the voltage source by producing a current in the opposite direction. The points where the curve crosses the y and x axes are called the short circuit current density (Jsc) and open circuit voltage (Voc) respectively. Jsc corresponds to the current density the solar cell will provide if receives no resistance and is just connected to a loop of wire – producing pure current but no voltage. Voc corresponds to the equilibrium potential difference we will observe across the solar cell if it is left connected to floating terminals – i.e. creating max voltage but no current. Since power is equal to current times voltage, the total power we get at either of these points will be zero, and the point where we get maximum power will be somewhere near the apex of the curve. In an ideal world the curve would be completely square-shaped, meaning that the maximum power would just be Voc times Jsc, but in any device we have to add a final term called the fill factor (FF). FF is the ratio between the area of rectangle formed from the maximum power point of the curve and a rectangle formed just from the Jsc and Voc. A straight line gives a FF of 25% while a perfect rectangle has a FF of 100%, leading to the following equation[26].

$$Power\ output = J_{sc} \times V_{oc} \times FF$$

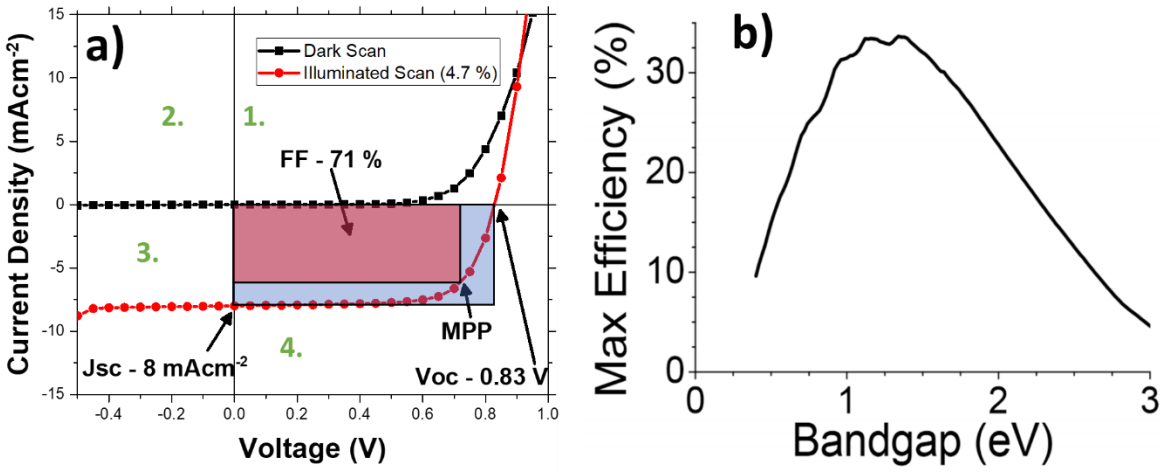

Figure 13- a) The Current density - voltage (J-V) curve of a solar cell created in St Andrews. The FF is defined as the area ratio between the red box (from the origin to the max power point) and the blue box (between the Jsc and Voc). b) A graph of maximum efficiency vs bandgap derived by Shockley and Queisser [27].

Attempting to maximise the power output of a solar cell presents an interesting optimisation problem. The Jsc of a solar cell is defined by how much light the solar cell absorbs while the maximum Voc it can achieve is related to the bandgap – the bigger the bandgap, the higher the Voc.

However, the sun emits light in a broad spectrum from UV to the far infrared, and so we can only improve one parameter at the expense of the other. We can increase the bandgap to increase the Voc, but this will always decrease the Jsc because only photons with higher energy than the bandgap will be absorbed. The optimal bandgap for a solar cell working on earth can be calculated to be 900 nm (1.4 eV), which gives a theoretical maximum efficiency of 33%. This is known as the Schockley-Queisser limit [27], and sets a maximum on best efficiency a solar cell with a given bandgap can achieve. Silicon's bandgap is slightly redder than optimal with a value of 1100 nm. This gives it a theoretical maximum efficiency of ~30%, and the record efficiency of 25.3% comes very close to this. The Schockley-Queisser limit can be overcome by making a cell from two materials – a high bandgap material to absorb the high energy photons and a low bandgap cell to absorb the photons the top cell misses. There is great potential to achieve very high efficiency solar cells with this method, but it greatly complicates the design of the solar cell, and unless the top cell is of exceptional quality and transparency then you often lose more than you gain.

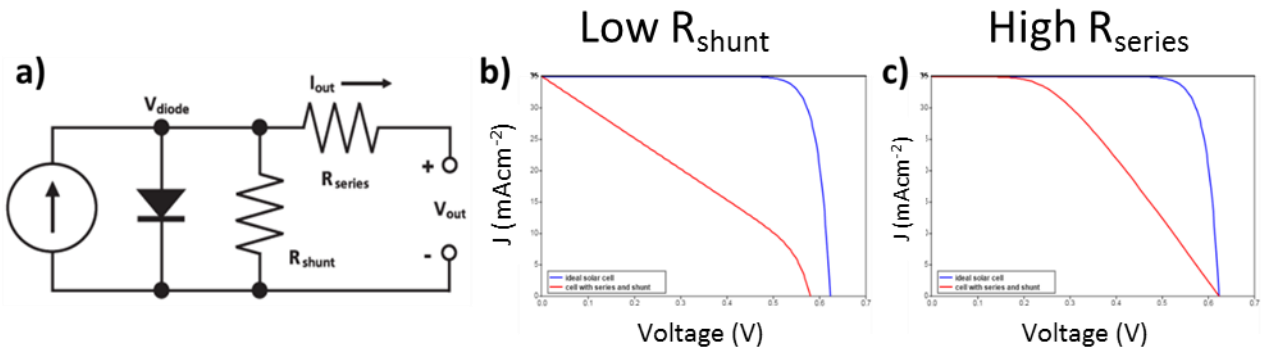

Figure 14 – a)The equivalent circuit for a general solar cell. R_{shunt} is controlled by the quality of the film, R_{series} by the conductivity of the materials, and V_{diode} by the bandgap of the solar cell. b) the J-V curve of a device with a low shunt resistance and c) a device with high series resistance (image reference [28])

Other Factors controlling Solar Parameters

The above calculations have assumed that the solar cell in question is perfect in every way, but most materials will not achieve the theoretical maximum in each parameter. The Jsc can be less than predicted if the device is not perfectly efficient at separating and extracting charges from absorbed photons, or if the above-bandgap absorption is not 100% - as is the case in most materials. The fill factor of the solar cell is also strongly dependent on the quality of the material being used. A large number of pinholes in the film will allow shunting pathways for the current to recombine without creating energy. This can be seen with the J-V curve having a slope (as opposed to being completely flat) in the low voltage region of the curve. The will also be reduced if the solar cell material is a weak electrical conductor, as if the solar cell has a high resistance then the steepness of the curve in

the high voltage region will be reduced, to the detriment of the FF and overall efficiency. Thus in order to maximise FF and Jsc a solar cell material must be a strong absorber whilst also being an excellent conductor and forming a high quality film with zero pinholes. These conditions seem to be fairly intuitive, but getting the maximum Voc possible from a given bandgap is somewhat more complicated.

Understanding what limits the open circuit voltage in a solar cell requires knowledge of how the Voc comes about in the first place. When in short circuit, an ideal solar cell will extract 100% of the charges generated to the contacts and none of them will recombine. But in open circuit the charges have nowhere to go, and so they simply build up on the edges of the device and create a potential difference across the device – i.e the open circuit voltage. If there was no recombination then these charges would continue building up to infinite voltage, which is clearly not physical. However this is not the case because there are always ways a charge can recombine in a solar cell, and so eventually a dynamic equilibrium is reached at a potential difference where the rate of recombination equals the rate of charge generation. The lower the recombination rate, the higher this equilibrium voltage will be, and so our aim should be to minimise recombination. There are two ways charge can recombine in a device – radiative and non-radiative pathways. In order to prevent a breaking of the second law of thermodynamics, anything which has an absorbing transition must have an equally strong emitting transition in the opposite direction. That is a strong absorber must also have strong emission and hence fast radiative recombination. However most materials which strongly absorb do not emit light – most paints do not glow under UV for example. The reason for this is that most materials have a large number of non-radiative pathways which remove the created charges before they have a chance to emit a photon. The important point to note is that, while it is thermodynamically impossible to remove the radiative recombination pathways, it is theoretically possible (although quite difficult) to remove all the non-radiative pathways in a material. Therefore an ideal solar cell in theory would have 100% PLQY, giving it the lowest recombination rate possible and hence the maximum Voc [29]. In reality it is rare to find a material which optimises all the other solar cell parameters whilst also having high PLQY, but even so the best solar cells can also function as LEDs with a remarkably high efficiency [30].

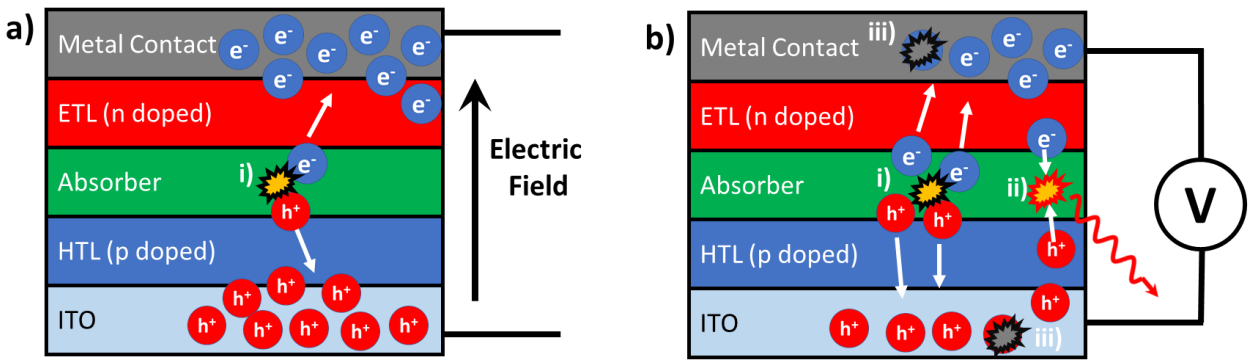

Figure 15 – a) How charges build up in a solar cell in open circuit. If there was no recombination the electric field due to the charge separation would build up to infinity. b) in reality a dynamic equilibrium is reached with charge generation (i) competing with radiative (ii) and non-radiative (iii) recombination.

Organic Solar cells

The current commercial photovoltaic market is dominated by monocrystalline silicon, but there is constant research to find alternative materials which can overcome the limitations of silicon – particularly its costly manufacture and bulky design. Organic solar cells are one such avenue which has the potential to revolutionise solar power by creating cheap, portable, and lightweight solar cells that can be used in any situation. They are of particular use in wilderness or small device situations where maximum performance for minimum weight and bulk is required. Organic solar cells can be cheaply printed using roll-to-roll processing methods, and can even be made to be semi-transparent for use in solar windows or other high-end architecture. Several commercial organic photovoltaic (OPV) companies have started in recent years, such as Konarka and InfinityPV, but they remain confined to niche applications because their efficiency cannot compete with commercial silicon solar cells. The key reason for this is that the absorption of most OSCs does not overlap well with the solar spectrum. OSCs absorb most strongly in the visible spectrum while much of the energy in the solar spectrum is in the near infrared, meaning the maximum current they can achieve is fundamentally limited. However this feature makes them ideal for charging devices for indoor applications where most of the light is in the visible region. In this situation OPVs can match or even exceed the efficiency of silicon solar cells [31], meaning that there is still room for OPVs to contribute to a major market.

When making an OSC, the first problem one runs into is excitons. As mentioned earlier, light absorbed in an organic solar cell will create a neutral exciton instead of free charges, and these excitons need to be broken apart in order to get any current. The most effective way to break apart an exciton is to have it diffuse to a boundary between a donor and an acceptor. The donor molecule will have a shallow HOMO, meaning the hole part of the exciton will be attracted to the donor, while

the acceptor will have a deep LUMO which the electron is attracted to. Thus when an exciton diffuses to the boundary it splits, with the electron moving away in the acceptor and the hole carried away in the donor as seen in figure 17. Note that some voltage is lost during this process, which is why OPVs have modest Voc values despite having fairly wide bandgaps. The simplest structure of organic solar cell which aims to do this looks very similar to an OLED – a monolithic structure with an HTL, an absorbing layer (donor), and an ETL(acceptor) [26]. The bottom contact is made from a transparent conductor such as indium tin oxide (ITO) in order to let the light in, and the absorber layer must be sufficiently thick to absorb most of the incoming light.

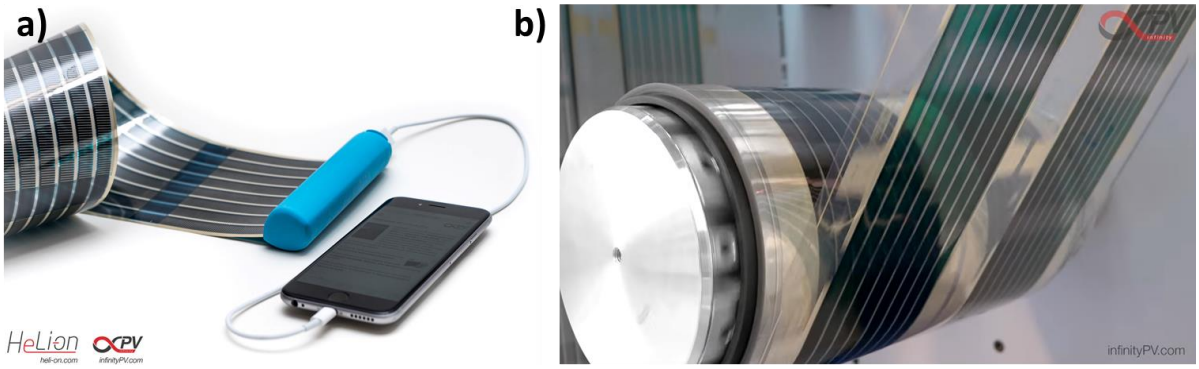

Figure 16 - Commercial Organic solar cells - a) a compact reel as a portable phone charger. b) Roll-to-roll production of large area organic solar cells. (Image sources: infinityPV.com).

This architecture is known as a planar heterojunction (shown in figure 8c and 12a), and when using organic semiconductors it will get a very poor efficiency because in most materials an exciton will only diffuse about 5-10 nm in its lifetime before recombining to waste its energy as heat [32]. An absorber layer which can absorb enough of the incoming light to be useful has to be at least 100 nm thick, and so most of the created excitons will never reach the boundary before they decay, resulting in a poor efficiency. To overcome this issue, all organic solar cells must employ a bulk heterojunction (BHJ) architecture [9, 26]. In this system the donor and the acceptor are blended together in such a way that no part of the donor is ever more than 10 nm away from the acceptor. This is extremely effective at separating the excitons into charges but comes with the caveat that the exact morphology of the blend must be exactly right. If the donor and the acceptor are too well blended then the charges will not have a clear route to the contacts, lowering the efficiency, but if they are not blended enough then some of the excitons will not reach a boundary before they decay [33].

This morphology is also liable to change over time, meaning that the device efficiency may drop if the device is used for long periods. It is also difficult to achieve the ideal morphology consistently over large areas, meaning that commercial OPVs often struggle to reproduce the high efficiencies

observed in the laboratory. All of these issues are continually being improved upon. But it is for these reasons that commercial OPV is likely to focus on indoor applications in the medium term, where their low cost, light weight, and flexibility can be maximally utilised in an environment where they can achieve high efficiency.

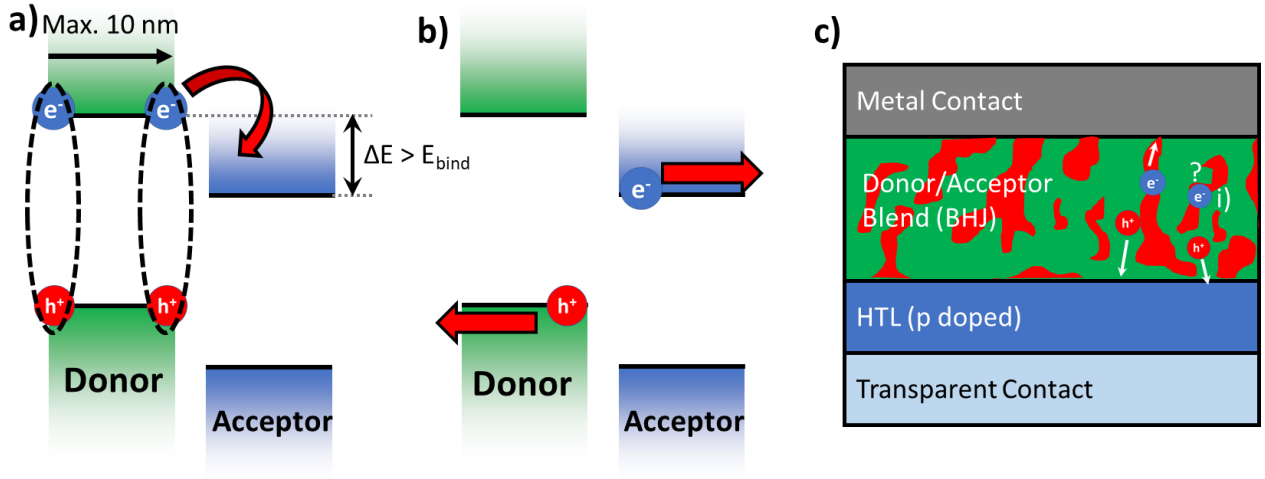

Figure 17 – Separating excitons in organic solar cells – a) A donor and an acceptor, which must have their LUMO levels offset by an energy greater then the exciton binding energy. If the exciton diffuses to this boundary then the charges will be separated as shown in b). c) A solar cell with a BHJ – note that the electron at i) is trapped because there is no clear path to diffuse to the contacts

Thin Film Lasers

The final major application of OSCs we shall discuss in this work is in thin film distributed feedback (DFB) lasers. Organic DFB lasers aim to produce high quality laser output from a very compact source whilst also incorporating all the advantages of organics such as tuneable properties, solution processing, and large area flexible substrates [34]. If they reached commercial viability they could be applied in a range of areas where inorganic diode lasers are currently unsuitable such as sensing, light-assisted medicine, and security tagging. DFB lasing from thin films exploits the same waveguiding effect that causes problems in OLEDs to create a lasing cavity without using conventional mirrors. In this section we will first discuss the physics of how DFB lasers work, before discussing the advantages and challenges of using OSCs in this role.

The three essential components of a laser are gain, mode confinement, and resonant feedback. Most direct bandgap semiconductors that are good at emitting light are able to provide strong gain because they act as quasi 4 level lasing systems as shown in figure 18 [35]. The requirements for a 4 level system are: 1) a ground state which is almost fully occupied, 2) a high energy state with a very short lifetime, 3) an upper emission state with a long lifetime and a strong stimulated emission cross section into the final state 4) which should have a very short lifetime in order to ensure that it is as empty as possible, thereby achieving population inversion. At first glance, a simple semiconductor

looks like a 2 level system, with just a conduction band and a valence band, but if it is excited with energy greater than the bandgap then a quasi-4 level system emerges, with the VBM acting as position 4) and the CBM acting as position 3). When a photon is absorbed, a hole is created deep within the valence band and an electron is created high in the conduction band. The electron now effectively occupies position 2) and the hole occupies position 1). These will both decay extremely quickly to the CBM and VBM, meaning that position 3) will be quickly filled with electrons and position 4) will be quickly filled with holes, making it effectively empty. The exact energies of positions 1) and 2) will not be well defined in this system, but this is irrelevant so long as they can still decay quickly to the lasing states.

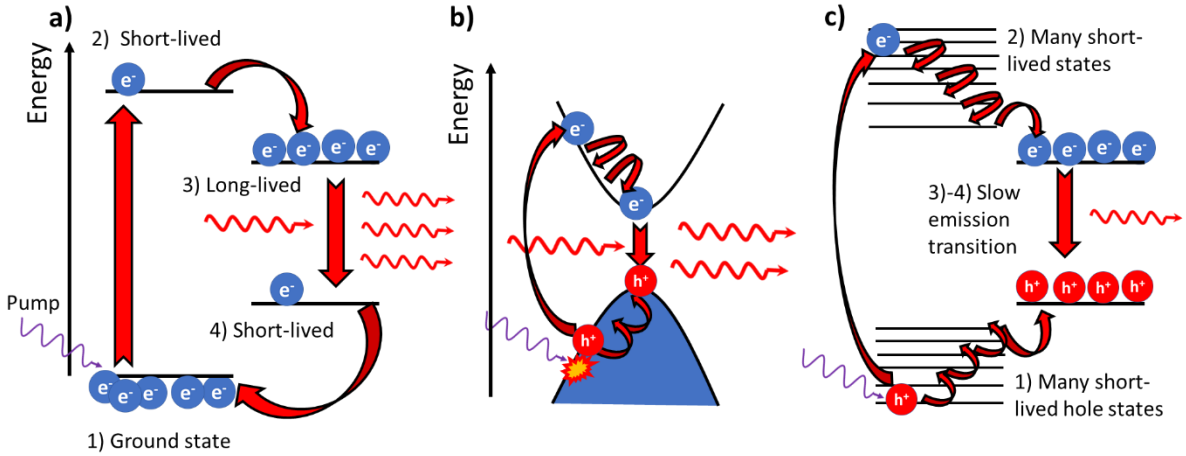

Figure 18 - a) Energy level diagram for a 4 level laser, b) Stimulated emission in a direct bandgap semiconductor. c) Equivalent energy level diagram for part b). Note how b) achieves a large population inversion in the same way as a).

Most OSCs have a refractive index (RI) of around 1.7, while glass (a common substrate for DFB lasers) has a RI of ~1.5. Because the polymer has higher RI, a photon emitted in the plane of the film will be waveguided inside the OSC film. The resulting photon mode will propagate through the film, but a portion of its electric field will penetrate into the glass and capping layer above the sample. Thus the effective refractive index which the mode experiences will be a combination of all three layers rather than simply the RI of the pure OSC. In a thick film there will be very little leakage of the mode into the surrounding layers, and so the effective RI will tend towards that of the OSC, but in a thin film the modes leak out significantly, and the effective RI will be more affected by the surroundings. If the effective RI of the film becomes equal to the RI of one of the cladding layers then the waveguiding will stop and the photon will escape the film. The thickness at which this occurs is known as the cut off thickness, and a film must be thicker than the cut-off thickness in order to allow waveguiding. Note that the higher the film's refractive index is, the thinner the cut-off thickness will be.

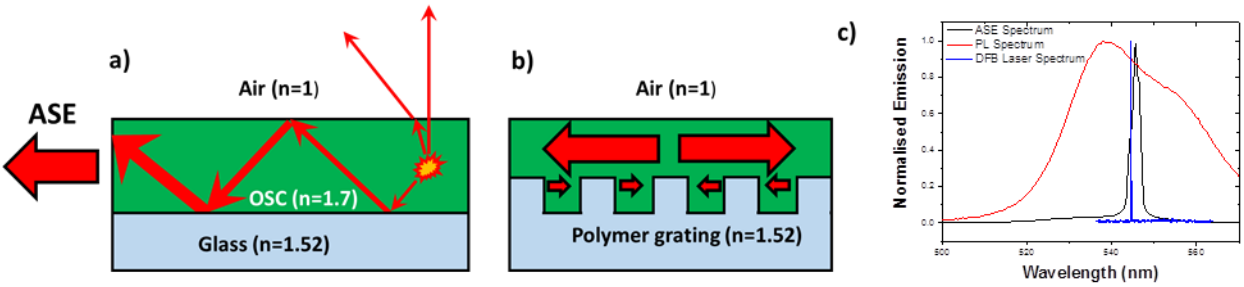

Figure 19 - Lasing in organic semiconductor films. a) How waveguided light in an OSC film with population inversion will be amplified as it propagates. b) How first order diffraction from a grating can serve to provide resonant feedback for lasing. c) Normalised spectra for photoluminescence, ASE, and DFB lasing in a lasing material made and measured in St Andrews.

Assuming that an OSC film is above the cut-off thickness, many photons which are emitted via photoluminescence (PL) will be waveguided through the film to the edge of the sample. If a detector were to be placed at the edge of the sample, we would see light which followed a spectrum very similar to the material's normal PL spectrum. If the sample is excited so that it has population inversion along a straight path to the detector, the PL will see gain and be amplified on its way to the detector. Photons with different wavelengths will all be competing for the same gain, and the result is that the photons with the highest gain/loss ratio will be amplified. This causes the broad PL spectrum to collapse into a narrow spike centred around the wavelength with the maximum net gain as shown on figure 19. This is usually on the red end of the PL spectrum because the bluer photons will experience higher loss due to reabsorption and scattering within the film. This process is a precursor to lasing called amplified spontaneous emission. It has the mode confinement and population inversion sufficient to amplify an incoming pulse, but it does not have the feedback component required to achieve coherent emission.

Feedback in a thin film is achieved through the use of scattering off a grating [35, 36]. Instead of being deposited on a flat film of glass, the OSC is deposited on a grating of specific shape and period. First order diffraction off of each line in this grating will have a cross section to reflect any waveguided photons back in the direction they came. If the effective wavelength of the photon in the mode is equal to the period of the grating, then every scattering event adds up in phase and resonance is achieved. However if the wavelength is slightly different from the grating period then the scattering will be out of phase and the mode will quickly become very lossy. Thus a diffraction grating is able to create a resonant photon mode with an extremely high Q factor without using any metallic mirrors [32]. This means DFB lasers have exceptionally narrow linewidths of significantly less than 1 nm, which makes them excellent for communications and sensing applications.

A small side note is that one can't use a simple first order grating to make an effective laser as it does not provide any means for the laser light to escape the film. An analogy of this is a normal

mirror cavity laser made with two perfectly reflecting mirrors. This gives very low threshold as there is no loss in the cavity, but it is not of any use unless we let some of the light out by making one of the mirrors partially reflecting. The way this is accomplished in DFB lasers is to use a second order grating instead of a first order grating. A second order grating has twice the period of a first order grating so resonance is still achieved for the same wavelength, but now the first order scattering mode will scatter the light directly out of the film, and only the weaker second order scattering will provide in-plane feedback (see figure 20). The effective result is like a cavity laser with a very leaky second mirror. Lots of light is outcoupled, but the lasing threshold is significantly increased because the cavity is much lossier. A compromise between these two extremes is sometimes reached by using a mixed order grating, where the grating is mostly 1st order except for a narrow strip in the middle which is 2nd order. In theory this gives the best of both worlds by providing a low loss cavity with a small point to outcouple light from, and it does provide lasing at a substantially lower threshold than a 2nd order grating [37]. However, the beam quality from this design tends to be poor because the light is escaping from a very narrow slit, which makes it strongly divergent due to diffraction.

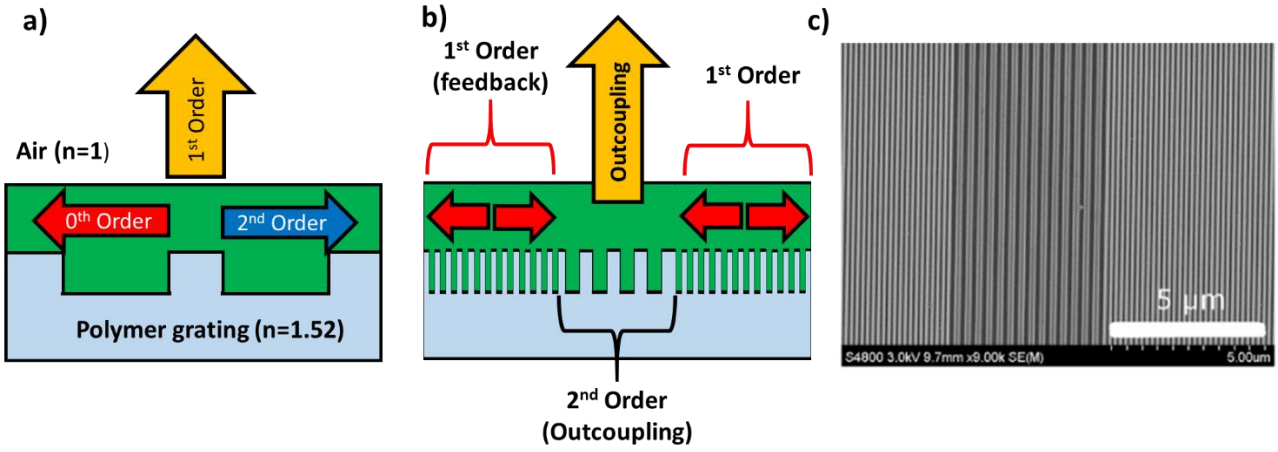

Figure 20 - a) A 2nd order grating b) A mixed order grating c) Scanning electron microscopy image of a mixed order grating(Image source [37]).

The emission beam profile from a distributed feedback laser is controlled by the shape of the grating structure, and usually goes in line with modes along the grating vectors. A 1D grid grating has only a single vector, and so the emission beam shows strong divergence in one axis, with strong confinement in the other axis, resulting in a profile shown on figure 21 a. A 2D micropillar grating has two orthogonal vectors, which creates possibilities for several different modes. Two independent modes are possible by exciting just the x or the y mode, creating a (1,0) or a (0,1) mode. These

modes are identical to ones coming out of a 1D grating, but together they create a cross-like emission beam as seen in figure 21b. A third mode is possible by making a superposition of both modes to create a (1,1) mode. This mode creates a donut shaped beam with either azimuthal or radial polarisation, but it is not usually observed in lasers made from OSCs. Emission from a mixed order grating should in theory be similar to a normal 1D grating, but it is much more divergent because the emission comes from a very narrow point.

OSCs are an excellent material for making DFB lasers because they are strongly customisable, solution processable, and most importantly have very strong transition dipole moments, which gives them a very large stimulated emission cross section and hence a low lasing threshold. However they are not without their problems. The first and most notable issue is that OSCs are vulnerable to photooxidation. Most OSCs have vital bonds in them which can be broken down by oxygen, and this process is greatly accelerated by the intense electric fields the material experiences when in lasing operation. This means that polymer lasers must be operated at low powers and encapsulated in order to operate for long periods.

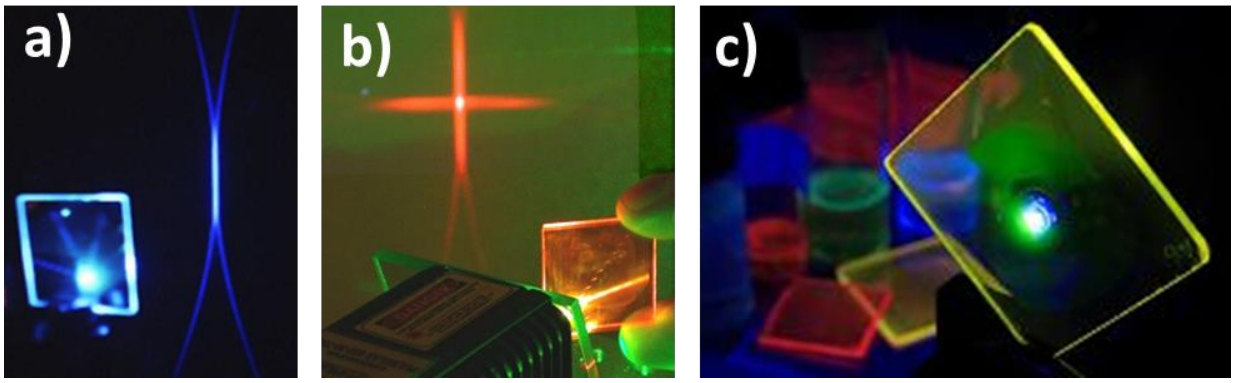

Figure 21 - Optically pumped polymer lasers printed on glass.. a) Emission from a 1D grating, creating a stripe-shaped output, b) Emission from a 2D grating, hence it has a cross-like beam. c) An organic laser pumped with an LED rather than another laser [38]

Secondly, OSC lasers are limited to short (nanosecond) pulses by the accumulation of triplet excitons. An OSC laser will gradually turn off in a pulse longer than 100 ns because triplet excitons quench the emission [39]. When an OSC is excited by optical pumping, all the generated excitons will be singlets. Singlet states are good because they can recombine radiatively to produce gain. However a small fraction of the singlet states will convert to triplet states via intersystem crossing. Although only a small fraction of the excitons will do this, the triplet states rapidly accumulate because a triplet exciton exists for several microseconds while a singlet state will be removed in the order of picoseconds by stimulated emission. Triplet states are bad because if a singlet and a triplet exciton meet, the triplet can steal the energy of the singlet by forcing it to the ground state and

promoting itself to an excited state. The triplet then thermalizes back down to its ground state and is not used up in the process, so one triplet exciton can quench many singlets in its lifetime. The result of this is that losses will rapidly accumulate in an OSC laser over long pulses, and the laser will turn off if it operates continuously for more than a few 10s of nanoseconds. Hence all OSC lasers are pulsed in order to give the triplets time to decay before the laser starts again.

The holy grail of OSC lasers is to find a way to pump them electrically rather than optically, because a polymer laser is of very limited use commercially if it requires a second laser to make it operate. Unfortunately achieving this presents some major difficulties. First and foremost, injecting electrons electrically into an OSC means the 75% of the excitons will be triplets instead of just a small fraction, making the long pulse issue many times worse to the point of killing the laser operation completely [39]. Secondly, reaching lasing threshold through electrical pumping will require current densities in the order of kA/cm^2. Most OSC laser materials have fairly poor electron and hole mobilities, meaning that it is unlikely this could be achieved without overheating the material. Finally, pumping a laser using a standard OLED device structure will also run into issues with plasmon losses from the metal contacts – mode leakage from the OSC into the metal contacts causes the electric field to dissipate its energy as surface plasmons in the metal, introducing losses to the mode which will increase the threshold beyond the point of feasibility

In conclusion, organic semiconductors are an extremely promising class of material with an enormous number of potential uses. They have many unique properties which make them favourable for commercial applications, with OPVs and OLEDs in particular being ideally suited for use in high technology compact devices. This rapid rate of progress has now inspired the search for a new generation of semiconductor which can maintain the many favourable properties of organics whilst aiming to circumvent their difficulties. The most successful material to be discovered in this search is lead halide perovskites.

Hybrid Perovskites

The term “perovskite” refers to a commonly studied of crystal structure with the formula ABX_3. The crystal has a primitive cubic unit cell with an A cation on each corner of the cube, a B cation in the centre of the cube, and an X anion in the centre of each face, as shown on figure 22. Various kinds of perovskites appear in a vast range of fields including superconductors, piezoelectrics, and earth sciences, but the class of material of interest to us in this thesis is methylammonium lead iodide ($CH_3NH_3PbI_3$, also known as $MAPbI_3$) and its variants. This class of material is usually referred to as hybrid perovskites because they often incorporate an organic component, and they possess many of

the advantages of both organic and inorganic materials. Hybrid perovskites are also unusual in that they are halide perovskites, using a halogen such as I^- or Br^- in the X site, while most perovskites studied in the literature are oxides. This gives them many interesting and unique properties which have proved to make them an ideal semiconducting material for optoelectronic applications.

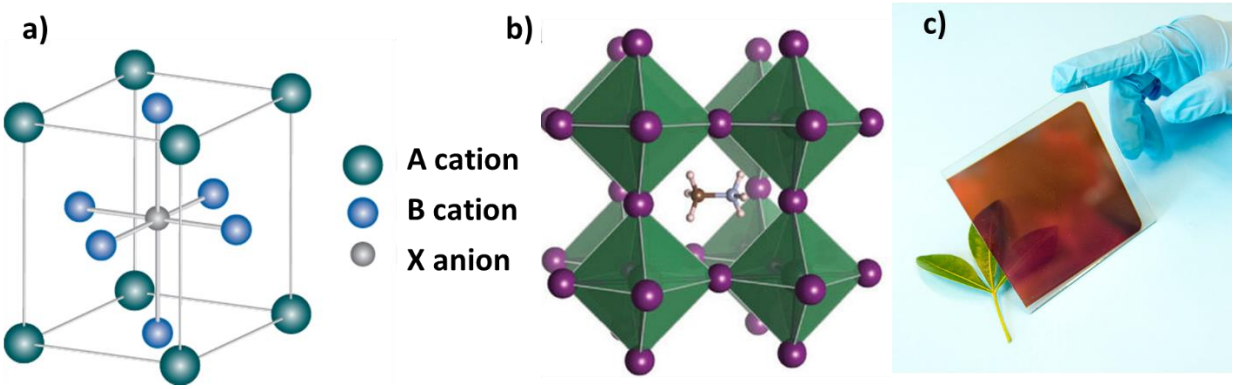

Figure 22 - a) The unit cell of a perovskite crystal, b) $MAPbI_3$ shown in the more common depiction of a perovskite crystal, where the octahedra formed by the Iodide cations can be clearly seen. A lead ion occupies the centre of each octahedron, and the MA cation can be clearly seen in the centre. (Image source Barnes et al.[40]) c) A thin film of $MAPbI_3$ deposited on glass (Image source Oxford Photovoltaics).

Halide perovskites began to receive interest in 2009 when Miyasaka et al attempted to use methylammonium lead iodide as sensitisers in a solid state dye sensitised solar cell, where they achieved a modest efficiency of 4%[41]. This sparked interest from several other research groups, and it was quickly realised that the perovskite was performing many more functions than a normal dye. In a dye sensitised solar cell (DSSC) the current is carried by an electron transporting layer of titanium dioxide (TiO_2) and a hole transporting material called 2,2',7,7'-Tetrakis[N,N-di(4-methoxyphenyl)amino]-9,9'-spirobifluorene (Spiro-Ometad). To absorb light, a portion of the TiO_2 is made to be mesoporous to give it a very high surface area, which a non-conducting dye is then adhered to, as shown on figure 23. The dye (or perovskite in this case) is never designed to conduct electricity and instead is always in contact with both the TiO_2 and Spiro-Ometad, allowing electrons and holes to be instantly extracted from the dye. However in perovskite solar cells it was quickly realised that the mesoporous TiO_2 could be removed and the efficiency would be unchanged or even increased[42]. This meant that the perovskite was not only separating the excitons into electrons and holes of its own accord, but it was also conducting them several hundred nanometres to their desired contacts. This discovery proved that perovskites had truly remarkable properties, and a large amount of research groups started studying the material in detail.

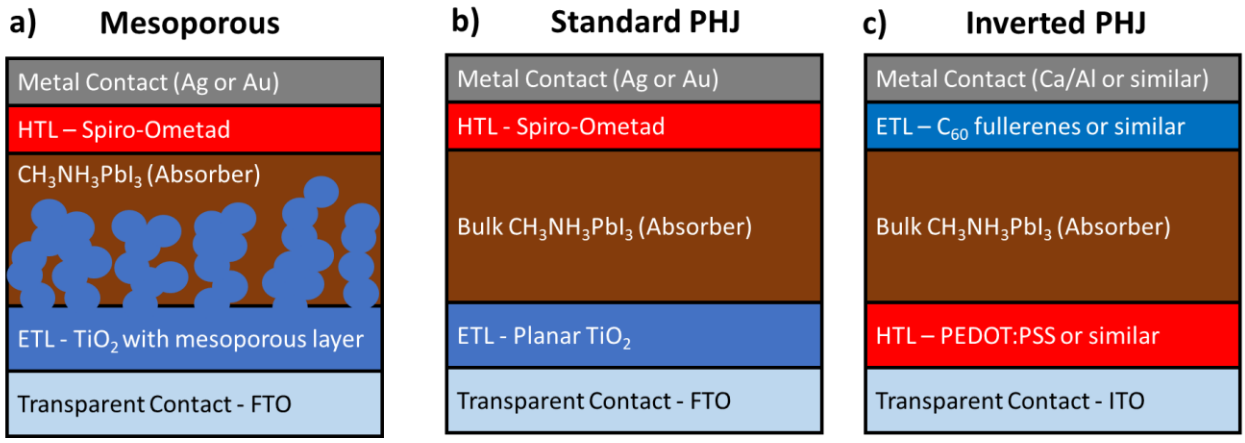

Figure 23 - Different designs of perovskite solar cell - a) A mesoporous structure based on solid state dye sensitised solar cells, b) a standard planar heterojunction with the ETL on the bottom, c)An inverted PHJ with the HTL on the bottom - note that the definitions for inverted and non-inverted are reversed between organic and perovskite solar cells.

It was found that $CH_3NH_3PbI_3$ had a very low exciton binding energy of only a few meV at room temperature [43, 44], meaning that almost all absorbed photons were instantly separated into electrons and holes without the need for a bulk heterojunction. It was also extremely conductive to both charge carriers, exhibiting mobilities of up to 100 $cm^2V^{-1}s^{-1}$ [45] and charge diffusion lengths of ~1 micron [46]– many orders of magnitude larger than in the materials used in organic solar cells. This meant that a planar heterojunction architecture would be able to achieve near 100% charge extraction even with very thick absorber layers. $CH_3NH_3PbI_3$ also proved to be a strong light emitter, which allowed perovskite solar cells to achieve a high open circuit voltage [47, 48]. Finally and most importantly, $CH_3NH_3PbI_3$ is very soluble in solvents such as dimethylformamide (DMF) and dimethyl sulphoxide (DMSO), meaning it can be easily deposited by solution processing. All these properties made lead halide perovskites seem to be the ideal solar cell material, and solar cells based on perovskites have now reached efficiencies of 22.7% as of 2017 [49], making them competitive with the best silicon solar cells whilst also retaining all the easy processing properties of organics.

Making Perovskite solar cells

Another major advantage of $CH_3NH_3PbI_3$ is that it uses cheap and earth abundant starting materials in its composition, and to make a film of perovskite one can simply dissolve two precursor salts together and then spin coat them. The basic chemical reaction is:

$$CH_3NH_3I + PbI_2 \rightarrow CH_3NH_3PbI_3.$$

Methylammonium Iodide (MAI) and lead iodide (PbI_2) are dissolved in equal molar ratio in a solvent such as DMSO. These precursors are very soluble, and total concentrations of over 1000 $mgml^{-1}$ can be achieved fairly easily. Once dissolved, the solution is deposited on a substrate via spin coating,

and the chemical reaction occurs as the solvent evaporates, thus making a thin film of the perovskite. The ideal result is a smooth film made of large, densely packed crystals with no pinholes in the film. The crystals will ideally be as large as possible in order to minimise the number of crystal boundaries a charge must cross on its way to the contacts. Conduction is much slower across the crystal boundaries, and they are also known to contain a much higher density of trap states due to the presence of dangling bonds [50, 51], which can induce recombination and thus lower the efficiency of the device. Achieving the best possible film requires a large amount of optimisation, and as such the exact recipe for preparing and spin coating a solution varies wildly from group to group. An overview of these various recipes shall be provided in the next chapter.

Most perovskite solar cells are a planar heterojunction structure similar to the simplest kind of organic solar cell, although some groups still use the mesoporous TiO_2 in their devices. A subtle difference is that most perovskite solar cells are "inverted" relative to the standard organic structure – that is they have their ETL at the bottom of the cell instead of the top. To prevent confusion, I shall refer to devices with an HTL on the bottom contact as "inverted", and devices with an ETL on the bottom as "non inverted" (see figure 23).

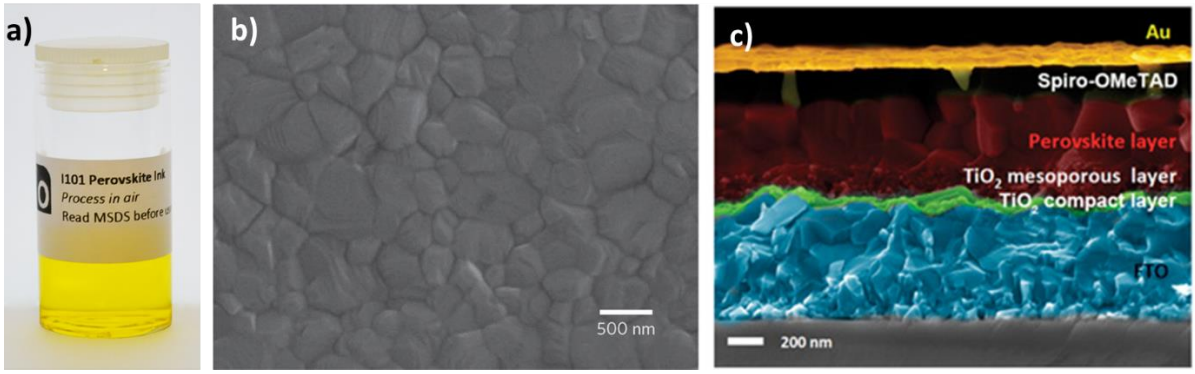

Figure 24 - a) a solution of perovskite precursor (image reference [52]), b) an SEM image of a good perovskite thin film(reference [53]). Note the large crystals and lack of pinholes, c) A transverse image of a good perovskite solar cell (reference [48]). The layers have been artificially coloured for clarity

In spite of their excellent performance and properties, perovskite solar cells are not without their problems. Firstly, good results from perovskite solar cells are often difficult to reproduce. As shall be discussed in the next chapter, this is due to the nature of the spin coating involving an optimised chemical reaction, meaning that even small changes to the local environment cause huge differences in the experimental outcome. Secondly, $CH_3NH_3PbI_3$ and its variants all contain a significant lead component, which raises questions as to whether they will be considered to be acceptable for consumer use. Counter arguments say that this might not be a problem because the solar cells will be well encapsulated, and even if there was a leak then the overall amount of lead would be very

small because the films involved are less than a micron thick. In any case, a lead-free alternative would obviously be preferable, and a huge amount of work has gone into finding lead-free alternative materials with equivalent properties. But unfortunately nothing has yet come close to competing with $CH_3NH_3PbI_3$. The only material to come close in performance is $CH_3NH_3SnI_3$, with a solar cell efficiency of 6% [54], but solar cells from this material are extremely unstable due to Sn^{2+} being easily oxidised to Sn^{4+}, and the tin perovskite appears to have more defect states than its lead counterpart [54].

The final major problem facing perovskite solar cells is degradation. $CH_3NH_3PbI_3$ is not vulnerable to degradation from oxidation, but it can easily degrade back to PbI_2 by reacting with water or some metals. Keeping water out of a perovskite solar cell is comparatively easy with modern encapsulation techniques. But degradation from the metals is a significant problem because metal from the contacts of a perovskite solar cell will slowly diffuse through the HTM and into the $CH_3NH_3PbI_3$, causing it to degrade over time [55]. Because of this, perovskite solar cells with metal contacts degrade far too quickly to be commercially viable, even when stored in the dark under an inert atmosphere where no other degradation should occur. To combat this, some groups such as Mcghee et al. [56] used indium tin oxide (ITO) as a contact on both sides of the solar cell. ITO is a transparent conductor which is normally used only as a bottom contact (where it is essential to be able to let light in) because it is les conductive and more expensive than metal contacts. Due to its increased resistance, the overall efficiency of the device is slightly reduced when using ITO for both contacts, but the stability is dramatically increased. Not only is the ITO inert to the $CH_3NH_3PbI_3$, thus eliminating the major degradation pathway, but it also acts as an excellent barrier layer against water in the atmosphere. Because of this, perovskite solar cells can now withstand operation for thousands of hours, even in humid conditions under constant illumination [57]. This demonstrates that, with the right choice of materials, perovskite solar cells could be stable enough for use in commercial devices.

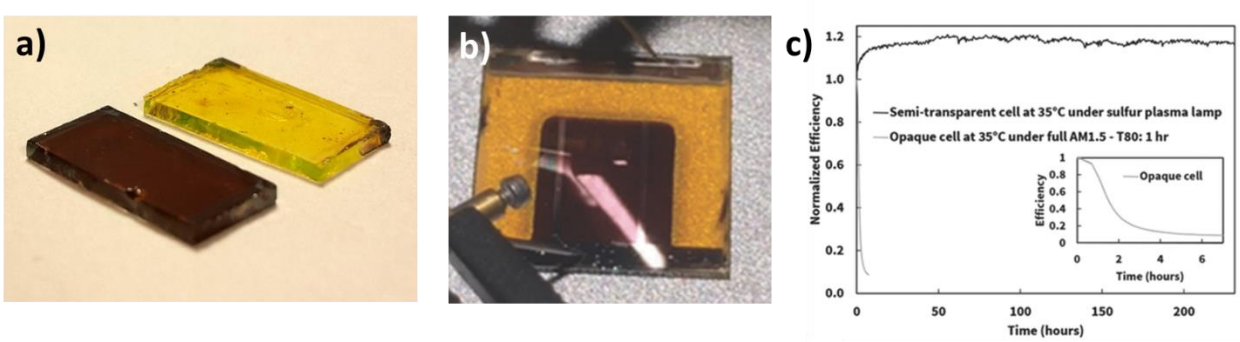

Figure 25 - Degradation in perovskites- a) A fresh perovskite film compared to one that has been left in atmosphere for 6 days, completely degrading it to PbI_2(image source [58]). b) A transparent solar cell incorporating ITO on both contacts.

Note that the area covered by the ITO is completely protected from degradation while the rest of the film is converted to PbI_2. [56] C) Compares the lifetime of a transparent solar cell to one containing metal contacts – the metal cell is completely degraded within hours, while the transparent cell remains unchanged after >250 hours [56].

Tuning perovskite properties

One of the reasons that the perovskite structure is so well studied in a wide range of fields is the versatility of the ABX_3 structure. The crystal's properties can be easily tuned by substituting the constituent ions with alternatives, provided these substitutions maintain charge balance and are the right size to fit in lattice. Methylammonium lead iodide is no exception to this, and there are a wide range of substitutions one can make to optimise the properties for device applications. We shall categorise the various substitutions by the site they occupy, and they have the following general effects. Substitutions to the A site strongly affect the stability, conductivity, and crystallinity of the material, and also have a modest tuning effect on the bandgap. As mentioned before, any substitution to the lead in the B site causes large changes in many properties of the material, almost all of which are detrimental to the device performance. Finally substitutions in the X site have a strong impact on the bandgap of the material.

A site substitutions

One of the factors which makes this class of perovskites interesting is their organic component. The presence of the $CH_3NH_3^+$ (MA) cation is one of the key reasons why perovskites are so easily solution processable, as it dramatically increases the crystal's solubility, but the presence of this cation also has some significant drawbacks. First the disorder introduced by having an asymmetrical and highly polar molecule inside the lattice complicates the material's physics significantly, making it challenging to create an accurate theoretical model of the system. Perhaps more importantly, the $CH_3NH_3^+$ cation is directly involved in many of the degradation pathways which reduce the lifetime of perovskite solar cells. It reacts strongly with water to form methylamine gas, which then escapes the film to leave behind a degraded perovskite, and the MA ion is also quite volatile. Because of the volatility of the $CH_3NH_3^+$ ion, $CH_3NH_3PbI_3$ will tend to decompose to PbI_2 if heated to temperatures close to 100 $^{\circ}$C by releasing vapours of CH_3NH_3I gas. A solar cell operating in a hot country can be expected to reach temperatures of at least 85 °C for extended periods, meaning that it seems unlikely that $CH_3NH_3PbI_3$ would ever be stable enough for long term commercial use.

To combat this, research groups started looking for possible substitutions for $CH_3NH_3^+$. However this is difficult because the MA ion occupies a sweet spot where any larger ions will be too big to fit in the lattice, while most metal ions will be too small for the resulting crystal to be stable. The two

substitutions which have seen the most success have been Cs^+ and $CH(NH_2)_2^+$. These both come with their own sets of problems, but together they have allowed perovskite solar cells to dramatically increase in both stability and efficiency.

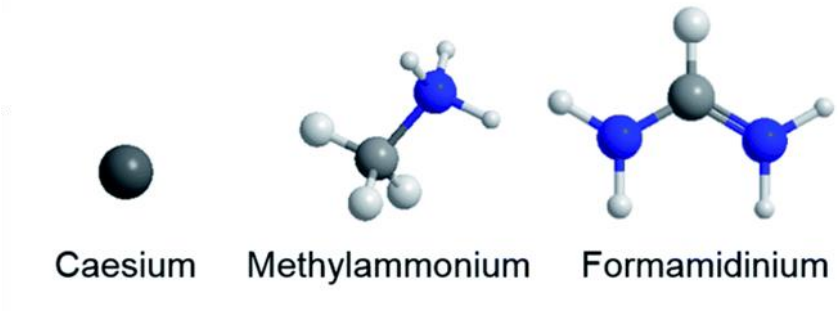

Figure 26- The different ion which can be used in the A site of hybrid perovskites(image source [59]).

$CH(NH_2)_2^+$, also known as formamidinium (FA) is a very similar ion to MA (see figure 26), with the exception that it has an extra NH_2 group attached. The effect of this change is a slight increase in effective ionic radius, a significant change in polarity, and a strongly reduced volatility. Because of this reduced volatility, a perovskite made from $FAPbI_3$ is much more resistant to thermal degradation than $MAPbI_3$ [59]. The slight change in ionic radius also causes the bandgap to be narrowed slightly to 1.43 eV, allowing the solar cell to produce a higher current. However the huge drawback of $FAPbI_3$ is that, due to the change in hydrogen bonding from the different A cation, it is not stable at room temperature. $FAPbI_3$ will slowly convert to a non-absorbing δ phase if left at room temperature, and will only remain stable in a useful form if held at temperatures above 100 °C. This process is reversible by heating, but makes pure $FAPbI_3$ all but useless for a solar cell in normal operation. To combat this, a compromise between the low volatility of the FA ion and the optimal bonding of the MA ion could be achieved by making a mixed cation perovskite of $MA_xFA_{(1-x)}PbI_3$. Across a variety of groups an x value of roughly 0.6 was found to be optimal, yielding a device with enhanced stability and slightly improved efficiency [60].

At the same time as this, other groups were also working on replacing the MA ion with Cs^+ to create $CsPbI_3$ - a completely inorganic perovskite. Caesium is a completely spherical ion, which greatly simplifies the physics of the resulting perovskite structure. The resulting structure has improved conductivity and a slightly widened bandgap of 1.76 eV compared to the 1.6 eV for $CH_3NH_3PbI_3$. Additionally the completely inorganic nature of $CsPbI_3$ makes it extremely resistant to thermal and chemical degradation [61]. However in spite of these advantages the Cs^+ ion has many of the same disadvantages of FA. Firstly the Cs precursor salts are far less soluble than the organic precursors, meaning that solutions are limited to low concentrations of up to 0.4 M. This means that the thickness of pure $CsPbI_3$ is very limited when compared to MA or FA cations, which can easily

achieve concentrations greater than 1.2 M. $CsPbI_3$ also has the same problem as FA in that pure $CsPbI_3$ is highly unstable at room temperature due to its tendency to switch to a yellow δ phase. Thus a compromise once again has to be reached by creating a mixed cation perovskite of $MA_xCs_{(1-x)}PbI_3$ or $FA_xCs_{(1-x)}PbI_3$. Indeed, the highest performing perovskite solar cells to date actually consist of a triple cation perovskite made from a highly optimised mixture of all three cations [62]. The resulting perovskite has far higher efficiency, stability, and reproducibility than its single cation counterparts.

B site substitutions

As mentioned earlier, most attempts at substituting the lead component from $MAPbI_3$ and its variants have resulted in structures with far worse properties than the original material. Tin is thus far the only substitution that has yielded any significant device efficiencies, with $MASnI_3$ devices achieving efficiencies as high as 6% [54], albeit with very low reproducibility. With a bandgap of 1.23 eV, $MASnI_3$ has a much narrower bandgap than $MAPbI_3$, placing it in a good region for the Shockley-Queisser limit. However $MASnI_3$ appears to be fundamentally a worse material than its lead counterpart. The PL spectrum of $MASnI_3$ is much broader than for $MAPbI_3$, indicating it has a much higher density of defects which could reduce the efficiency of a solar cell, and the Sn^{2+} ion is extremely vulnerable to oxidation into the Sn^{4+} state. Thus $MASnI_3$ solar cells are expected to be much less stable and efficient than solar cells made from $MAPbI_3$.

Other attempts to remove the lead component have revolved around the formation of double perovskites by using a 50:50 mix of a 1+ cation such as copper or silver with a 3+ cation such as bismuth or indium [63]. This could potentially open up a whole new area to explore and optimise with this class of material, but unfortunately it has thus far been impossible to use this method to create a stable material with a bandgap narrow enough for use in solar cells. Even if this were to be achieved, the commonly used 1+ ions such as silver, gold, and copper are many orders of magnitude less soluble than lead ions. This means that even if a good double perovskite were to be found it would not be solution processable – thus removing one of the key advantages that make it interesting.

X site substitutions

Controlling the bandgap of a perovskite solar cell is, in theory, very easy as one can just make a perovskite with a mix of halogens. $MAPbI_3$ has a bandgap of 1.6 eV while $MAPbBr_3$ and $MAPbCl_3$ have bandgaps of 2.3 eV and 3.2 eV respectively. Any bandgap in between these extremes can be achieved by making a mixture of $MAPbI_{3x}Br_{3(1-x)}$ or $MAPbBr_{3x}Cl_{3(1-x)}$, as shown on figure 27. Note that

a mixture of I and Cl does not work because the size difference is so large that the lattice is not stable when containing both ions.

This tuneablity is an excellent property because it could allow for perovskite LEDs at any colour of the rainbow, and also makes perovskites an ideal material for tandem cells. One of the more promising routes to commercialising perovskite solar cells is to work with competitors such as silicon rather than against them. Silicon has a bandgap which is on the narrow side of ideal for the Schockley-Queisser limit, while $MAPbI_3$ is on the wide side of optimal. However the two materials together have close to ideal bandgaps for making a tandem cell with high efficiency, and a silicon-perovskite tandem cell could have efficiency of 35-40% [64]for only a relatively small increase in cost. This would come close to halving the payback time for a solar photovoltaic installation and hugely increase its viability.

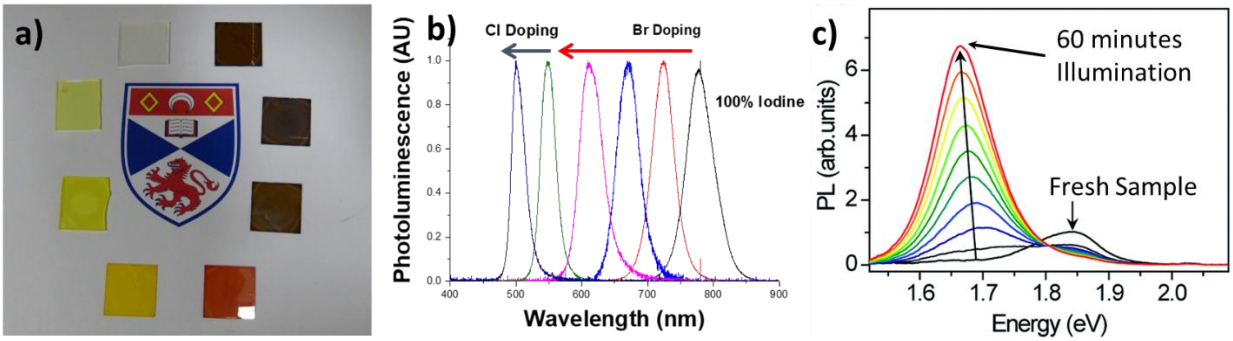

Figure 27 - Tuning the bandgap of perovskites. a) A range of mixed halide perovskites tuning from 100% Iodide, to 100% Bromide, and then 100% Chloride. b) How the PL spectrum of mixed halide perovskites as the bandgap is increased. c) The Hoke effect from the original paper by Hoke et al, where the emission a perovskite film with a bandgap of 1.9 eV red shifts over time due to halide segregation(reference [65]).

The ideal bandgap for a perovskite solar cell in this tandem configuration is 1.9 eV, which a mixture of 40% bromine and 60% iodine can provide easily, but unfortunately it is not quite as simple as this. When one increases the bandgap of a solar cell, you expect to get less current but more voltage. In perovskite solar cells, increasing the bandgap does indeed decrease the Jsc, but the Voc remains more or less constant, thus completely removing any advantage one gets from changing the bandgap. The reason for this is that the halide ions are quite mobile within the perovskite lattice, and when the perovskite is excited with light it becomes energetically favourable for them to phase separate into iodide-rich and bromide-rich regions. The iodide-rich regions have a lower bandgap than the bromide rich ones, and hence the charges tend to migrate towards the low bandgap regions, resulting in a lower Voc despite the overall increased bandgap. This is known as the Hoke

effect [65]. It is one of the main unsolved problems in perovskite solar cells, and its impact can be clearly seen in the PL spectrum of an illuminated sample over several minutes. Due to this effect, the closest stable bandgap to the ideal 1.9 eV that can be achieved with perovskites is 1.7 eV, and it also significantly reduces the number of available colours a perovskite light emitter can achieve. There are many works which claim to reduce the halide segregation effect, and it is generally agreed that the presence of caesium ions in the lattice can help pin the halogens in place [66], but thus far no work claiming to achieve a stable perovskite with 1.9 eV bandgap has been reliably reproduced by separate laboratories.

Light emitting devices from perovskites

The bulk of the work done on lead halide perovskites focuses on their use as a solar cell material, but perovskites also have great potential as a light emitting material. As discussed earlier, one of the key reasons for the excellent performance of perovskite solar cells is their ability to emit light, leading to a high Voc and hence a high efficiency. To illustrate this, some of the best perovskite solar cells can also be operated in forward bias to work as LEDs with efficiencies close to 1%[48]. This is a remarkable value in a non-optimised device with no blocking layers and very poor outcoupling. This combined with the excellent electrical properties, the absence of triplet excitons, and the good stability of perovskites makes them an ideal candidate for studying light emitting applications. Unfortunately the first attempts at making dedicated perovskite light emitting diodes yielded high brightness but very poor efficiency [67]. This poor efficiency could be largely attributed to the weak recombination rates in perovskites due to the complete absence of excitons. In a conventional OLED the charges would quickly form excitons which have a strong radiative recombination rate, meaning that the charges decay to emit light before non-radiative pathways can force them to lose their energy as heat instead of light. In a perovskite LED the excitons do not form, and hence an electron will only decay radiatively if it directly collides with a hole for it to recombine with, meaning that non-radiative pathways will usually decay a charge before it has a chance to recombine radiatively. This effect can be clearly seen in the intensity dependent PLQY of most perovskites [68].

An OSC will generally have a fairly constant PLQY regardless of excitation density because the recombination is mostly geminate – one photon creates one exciton which then recombines radiatively after a delay. In a perovskite the recombination is bimolecular – one photon creates an electron and hole which then will diffuse randomly until they find a counterpart to recombine with. If the number of excited charges is low, then a charge has low odds of finding a counterpart to recombine with before it decays non-radiatively. At higher excitation densities the probability of finding a counterpart increases, leading to a PLQY which increases roughly linearly with pump

density. The result of this is that perovskite light emitters will generally perform poorly at low powers but will be substantially improved at higher powers.

This phenomenon motivated research into making perovskites with crystal morphologies which could promote radiative recombination even at low intensities, and the solution was to create a perovskite with the smallest crystals possible – the exact opposite of the aim in perovskite solar cells. Since the charges move much more slowly across crystal boundaries, a well passivated crystal boundary will act as a wall confining the charge inside the crystal. If the crystals are small then the charges are confined inside a much smaller space, and hence they are far more likely to recombine than if they are trapped inside a large crystal as shown on figure 28. This can be seen in the intensity dependent PLQY becoming closer and closer to a flat line as the crystal size is reduced, and Tae Woo Lee et al exploited this to create green perovskite LEDs with 8.5% EQE and a very high brightness of 42 cdA^{-1} [69]. This is an impressive result given that the outcoupling efficiency of a perovskite LED will be very poor due to its high refractive index, and also shows that the absence of excitons allows perovskites to achieve higher efficiencies than fluorescent OSCs.

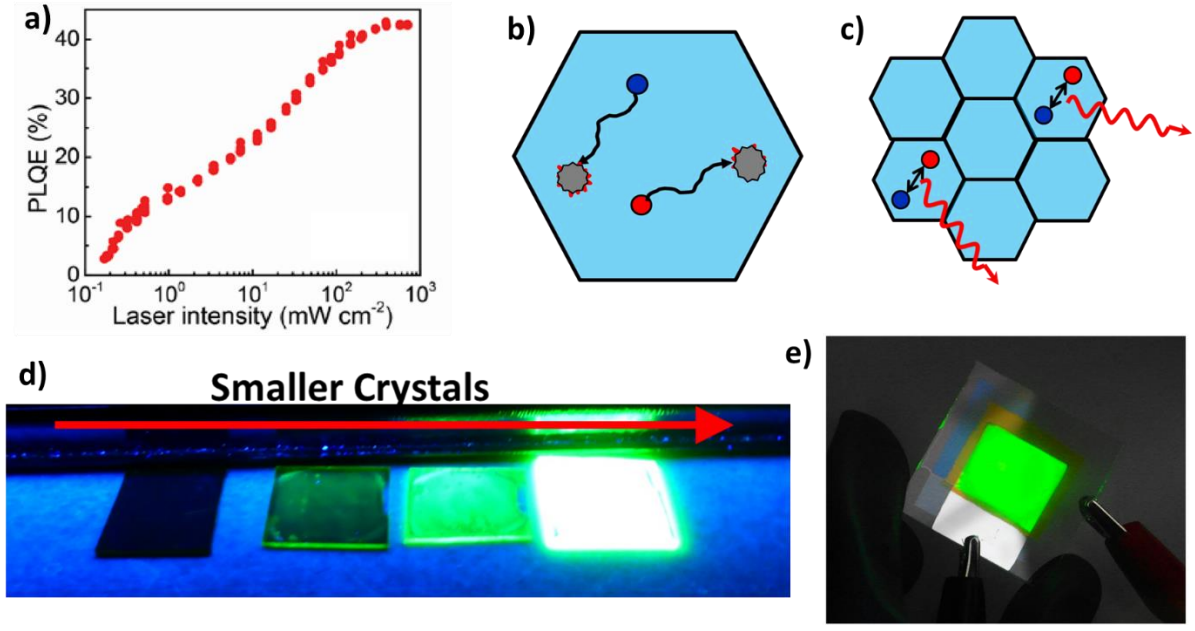

Figure 28 - a) An example of how the PLQY in a perovskite film varies with pump density(Image Source [69]). b) electrons and holes are unable to find each other to recombine in a large crystal. In c) the smaller crystals confine the charges and force them to recombine radiatively. d) Different films of $MAPbBr_3$ under UV light – the samples with the smallest crystals have the strongest PL. e) A large area LED made from $MAPbBr_3$ [69].

Perovskite lasers

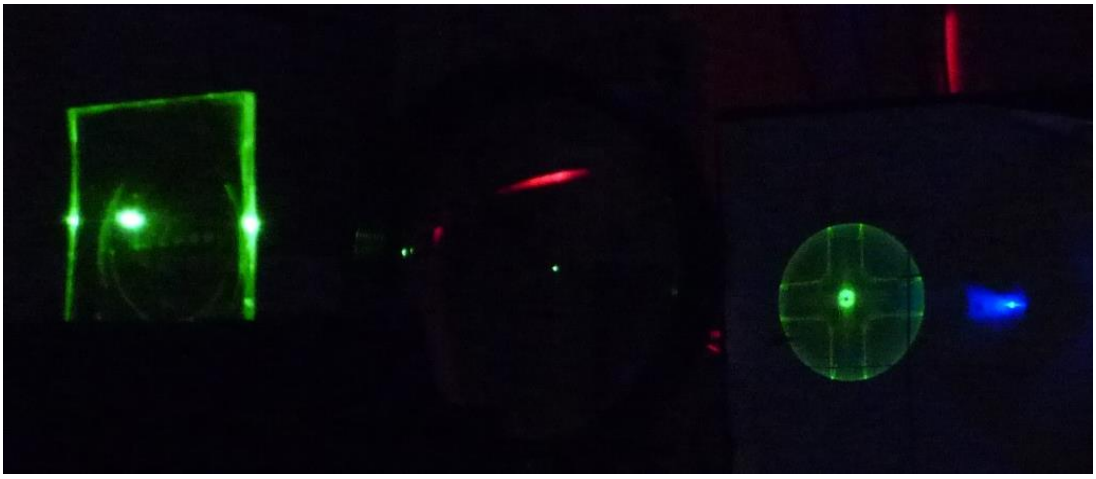

Figure 29 – An optically excited thin film laser made from $MAPbBr_3$ perovskite in St Andrews. The laser is deposited on a glass substrate on the left, with the beam output projected onto a screen on the right.

The intensity dependent PLQY is a significant problem in an LED, where the charge densities are generally very low, but it is not a problem in a laser which normally operates at much higher excitation densities. Amplified spontaneous emission (ASE) was first noticed in $MAPbI_3$ in 2015 [70], and since then there has been a large amount of work on using perovskites as a laser material. Lasers from perovskite nanowires were able to achieve thresholds as low as 220 $nJcm^{-2}$ [71], and a large number of Fabry-Perot lasers have now been reported [72]. Perovskites have a range of properties which make them ideal for this purpose, including their low threshold, the absence of triplet excitons, their solution processability, and their resistance to photooxidation.

Until now, the only solution processable laser materials were laser dyes and OSCs, these both achieve low thresholds and high performance but are also limited to pulsed operation in the solid state due to the accumulation of triplet excitons discussed earlier. In addition, both of these materials are easily degraded by photooxidation when operating at high pump powers, and they are not sufficiently conducting to allow electrical pumping. Perovskites as a material have the potential to overcome all of these issues whilst also being cheap and having an easily tuneable bandgap. It is important to note however that the Hoke effect still has a highly detrimental effect on perovskite lasers made from mixed halide perovskites. Although ASE can be achieved at almost any wavelength in the visible spectrum, the threshold for ASE increases dramatically when using mixed halides to tune the bandgap. All of these effects combine to make perovskite lasers a vibrant and highly promising field of research, and much of this thesis shall focus on efforts to use perovskite to make all solution processed thin film lasers.

Low dimensional perovskites

Due to the absence of excitons at room temperature, perovskites are generally unsuitable for studying polaritonic effects. Therefore some groups set about designing a perovskite with a high exciton binding energy in order to observe polaritons in a perovskite system. The result of this search was to create perovskites which effectively operated in 2,1 or even zero dimensions by making layered perovskites, perovskite nanowires, and perovskite nanocrystals respectively.

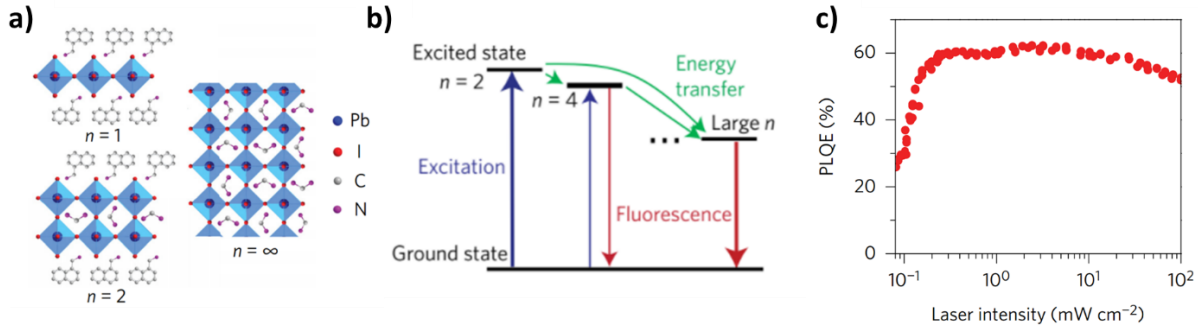

Figure 30 - a) The structure of n=1 and n=2 layered perovskites compared to the bulk 3D perovskite. b) Excited states in a sample with a material with a range of different n values will be funnelled into the crystal with the largest n, as this has the lowest bandgap. c) The PLQY of a layered perovskite vs pump intensity – it remains fairly constant due to the funnelling and confinement effects (Images sourced from [69]).

Layered perovskites are made by doping a normal perovskite with an A site ion that is much too large to fit in the normal lattice site, such as butylammonium (BA) or phenylethyalmmonium(PEA). The perovskite crystal rejects these larger ions and causes them to separate into layers in the way shown on figure 30, forming a Ruddlesden-Popper phase with the larger ions being excluded from layers of normal bulk perovskite. This is known as a layered perovskite, and they are classified by their composition and their n value. The n value of a layered perovskite defines the number of repeat units of a normal perovskite unit cell exist between each layer of the insulating larger cations. An n=3 perovskite will on average have 3 units of normal 3D perovskite between each layer of insulator, but in reality it will be a dispersion of some n=1,2,3,4 etc. layers with the total averaging out to 3. The narrower a layer is, the wider its bandgap and the more confined the charges are in the layer. This leads to a high exciton binding energy in layered perovskites because the charges are confined in a narrow region as is the case in an OSC. It also serves to create a material which has a multitude of layers each with different bandgaps, and so charges excited in a high bandgap region will be funnelled via quantum tunnelling into the layers with the widest bandgaps. This serves to concentrate the charges and provide a material with a high exciton binding energy and a high PLQY which does not vary with excitation density [69, 73].

Layered perovskites proved to be ideal for the study of polaritons, allowing for the effect of strong coupling to be clearly observed even at room temperature and opening up the possibility of a new route to achieving polariton lasing at room temperature. But in addition to being excellent for the study of polaritons, these layered perovskites proved to be excellent for making high efficiency light emitting diodes due to their intensity independent PLQY and excellent film quality. So long as the layers could be oriented to be perpendicular to the plane of the device, charges can easily flow along the planes in the perovskite. This, combined with the high PLQY values of the perovskite, allowed layered perovskite LEDs to achieve efficiencies up to 11% at any colour between 550 nm and 800 nm[69]. It is important to note that it is essential for the layers in a layered perovskite LED to be aligned perpendicular to the plane of the device. Otherwise the injected charges will be forced to repeatedly tunnel through many layers of insulator in order to pass through the device, causing it to have a very high resistance. It has not been made abundantly clear how the authors who achieved such high efficiency accomplished this, and hence these results cannot be reproduced independently until this is information is made public.

Figure 31 - A highly luminescent film of n=3 layered perovskite. b) Solutions of $CsPbX_3$ perovskite nanocrystals (Image source [74]).

Perovskite nanocrystals

Perovskite nanocrystals (PNCs) are a zero-dimensional analogue of the normal perovskites made in solar cells, and they have attracted great interest because they can achieve solution PLQY values of near unity [74] and do not appear to suffer from halide segregation to the same extent as the bulk perovskite. Because of their high PLQY, there has been great interest in using PNCs in LEDs or as laser materials, but this has so far proved difficult because the nanocrystals have to be surrounded by insulating ligands to prevent them quenching off of each other. These ligands keep the nanocrystals separate from each other, thus preventing exciton-exciton quenching and achieving a high PLQY, but they also make it difficult to excite the nanocrystals electrically. Thus the efficiency of

LEDs made from PNCs remain low, but they do remain a promising material for optically pumped lasing.

Conclusion

In conclusion, solution-processed OSCs have many advantages over their inorganic counterparts which could revolutionise the way we use electronics. Organic LEDs are already a popular commercial technology, while flexible solar cells and lasers from organics are constantly improving. Hybrid perovskites are a new class of material which combine the advantages of both organics and inorganics, and their excellent performance as a solar cell material so far makes them highly likely to see commercialisation in the near future. Finally the same properties which make perovskites an excellent solar cell material also make them highly promising as a light emitting material, and there are many exciting fields to explore where perovskites could prove to be the solution to many of the long-standing problems.

References

1. Kittel, C., *Introduction to Solid State Physics*. 2004: John Wiley & Sons.
2. Palik, E.D., *Handbook of Optical Constants of Solids lll*. 1985: Elsevier Science.
3. Klauk H., G.B., *An Introduction to Organic Semiconductors*. 2004: Springer.
4. *EXPO 2015: Field of polymer solar cells in the German Pavilion*. 2015 21/12/17]; Available from: http://www.plasticseurope.org/information-centre/news/news-2015/expo-2015-field-of-polymer-solar-cells-in-the-german-pavilion.aspx.
5. Kowalski, K., *Digital lighting goes organic.* 2014.
6. A. Swarup and P. Khare, *Organic Solar PV Cells: Promising Option for Meeting Future Energy Requirements,* 2015, available from: http://www.supersmartenergy.com/organic-solar-photovoltaic-cells-promising-option-for-meeting-future-energy-requirements/.
7. Green, M.A., *Improved value for the silicon free exciton binding energy.* AIP Advances, 2013. **3**: p. 112104.
8. Carsten Deibel, D.M., Julien Gorenflot, Achim Scholl, Stefan Krause, Friedrich Reinert, Daniel Rauh, Vladimir Dyakonov, *Energetics of Excited States in the Conjugated Polymer Poly(3-hexylthiophene).* Phys Rev B, 2010. **81**: p. 085202-085207.
9. Hoppe, H. and N.S. Sariciftci, *Organic solar cells: An overview.* Journal of Materials Research, 2004. **19**(7): p. 1924-1945.
10. Alexey Kavokin, J.J.B., Guillaume Malpuech, and Fabrice P. Laussy, *Microcavities*. 2007: Oxford Scholarship Online.
11. Su, R., et al., *Room-Temperature Polariton Lasing in All-Inorganic Perovskite Nanoplatelets.* Nano Letters, 2017. **17**(6): p. 3982-3988.
12. Oulton, R.F., et al., *Strong coupling in organic semiconductor microcavities.* Semiconductor Science and Technology, 2003. **18**(10): p. S419-S427.
13. Biard, T.M.O.a.J.R. *The first practical LED*. 2015 [cited 2018 30/07/2018]; Available from: http://www.edisontechcenter.org/lighting/LED/TheFirstPracticalLED.pdf.
14. U. Giovanella, M.P., and C. Botta, *Organic Light-Emitting Diodes (OLEDs): Working Principles and Device Technology.* Applied Photochemistry, 2016. **92**: p. 145-196.
15. Baldo, M.A., et al., *Excitonic singlet-triplet ratio in a semiconducting organic thin film.* Physical Review B, 1999. **60**(20): p. 14422-14428.

16. Youtian Tao, C.Y., Jingui Qin *Organic host materials for phosphorescent organic light-emitting diodes* Chemical Society Reviews, 2011. **40**: p. 2943-2970.
17. Zhiyong Yang, Z.M., Zongliang Xie, Yi Zhang, Siwei Liu, Juan Zhao, Jiarui Xu, Zhenguo Chi, Matthew P. Aldred, *Recent advances in organic thermally activated delayed fluorescence materials* Chemical Society Reviews, 2017. **46**: p. 915-1016.
18. Energy, O.o.E.E.a.R. *World Record White OLED Performance Exceeds 100 lm/W*. Available from: https://energy.gov/eere/ssl/world-record-white-oled-performance-exceeds-100-lmw.
19. Dong Ryun Lee, B.S.K., Chil Won Lee, Yirang Im, Kyoung Soo Yook, Seok-Ho Hwang, Jun Yeob Lee, *Above 30% External Quantum Efficiency in Green Delayed Fluorescent Organic Light-Emitting Diodes.* Applied Materials & Interfaces, 2015. **7**(18): p. 9625-9629.
20. Hammerschmidt, C. *Infrared LED prototype sets efficiency record*. 2012 21/12/17]; Available from: http://www.eenewseurope.com/news/infrared-led-prototype-sets-efficiency-record.
21. Reineke, S., et al., *White organic light-emitting diodes with fluorescent tube efficiency.* Nature, 2009. **459**(7244): p. 234-U116.
22. Lin, H.Y., et al., *Patterned microlens array for efficiency improvement of small-pixelated organic light-emitting devices.* Optics Express, 2008. **16**(15): p. 11044-11051.
23. Tae-Wook Koh, J.A.S., Kyung Min Lee, Craig B. Arnold, Barry P. Rand, *Enhanced Outcoupling in Organic Light-Emitting Diodes via a High-Index Contrast Scattering Layer.* ACS Photonics, 2015. **2**(9): p. 1366-1372.
24. Chung-Chih Wu, W.-K.L., Min Jiao, Chun-Yang Lu *Enhance Light Out-Coupling of OLEDs: Low-Index Active Materials and Horizontal Dipole Emitters* OSA Technical Digest (online) 2016.
25. Daniel Ping-Kuen Tsang, T.M., Chihaya Adachi, *Operational stability enhancement in organic light-emitting diodes with ultrathin Liq interlayers.* Scientific Reports, 2016. **6**: p. 22463.
26. Nicholson, P.G. and F.A. Castro, *Organic photovoltaics: principles and techniques for nanometre scale characterization.* Nanotechnology, 2010. **21**(49).
27. William Shockley, H.J.Q., *Detailed Balance Limit of Efficiency of p-n Junction Solar Cells* Journal of Applied Physics, 1961. **32**: p. 510.
28. Christiana Honsberg, S.B. *Shunt Resistance*. 2018 [cited 2018 16/03/2018]; Available from: http://www.pveducation.org/pvcdrom/solar-cell-operation/shunt-resistance.
29. Green, M.A., *Radiative efficiency of state-of-the-art photovoltaic cells.* Progress in Photovoltaics, 2011. **20**(4): p. 472-476.
30. Hak-Beom Kim, Y.J.Y., Jaeki Jeong, Jungwoo Heo, Hyungsu Jang, Jung Hwa Seo, Bright Walker, Jin Young Kim *Peroptronic devices: perovskite-based light-emitting solar cells.* Energy & Environmental Science, 2017. **10**: p. 1950-1957.
31. Harrison K. H. Lee, Z.L., James R. Durrant, Wing C. Tsoi, *Is organic photovoltaics promising for indoor applications? .* Applied Physics Letters, 2016. **108**: p. 253301.
32. Paul Shaw, A.R., Ifor D W Samuel, *Exciton Diffusion Measurements in Poly(3-hexylthiophene).* Advanced Materials, 2008. **20**(18): p. 3516-3520.
33. Hedley, G.J., et al., *Determining the optimum morphology in high-performance polymer-fullerene organic photovoltaic cells.* Nature Communications, 2013. **4**.
34. Karl, M., et al., *Flexible and ultra-lightweight polymer membrane lasers.* Nature Communications, 2018. **9**.
35. Samuel, I.D.W. and G.A. Turnbull, *Organic semiconductor lasers.* Chemical Reviews, 2007. **107**(4): p. 1272-1295.
36. Ghafourishiraz, H. and C.Y.J. Chu, *Distributed Feedback Lasers - an Overview.* Fiber and Integrated Optics, 1991. **10**(1): p. 23-47.
37. Wang Y, T.G., Kanibolotsky AL, Skabara PJ, Samuel ID, Turnbull GA, *Nanoimprinted polymer lasers with threshold below 100 W/cm2 using mixed-order distributed feedback resonators.* Optics Express, 2013. **21**(12): p. 14362-14367.
38. Y. Yang, G.A.T., I.D.W. Samuel, *Hybrid optoelectronics: A polymer laser pumped by a nitride light-emitting diode* Applied Physics Letters, 2008. **92**: p. 163306.

39. Ifor D W Samuel, G.A.T., *Polymer lasers: recent advances.* Materials Today, 2004. **7**(9): p. 28-35.
40. Aurelien M. A. Leguy, J.M.F., Andrew P. McMahon, Victoria Garcia Sakai, W. Kockelmann, ChunHung Law, Xiaoe Li, Fabrizia Foglia, Aron Walsh, Brian C. O'Regan, Jenny Nelson, João T. Cabral, Piers R. F. Barnes, *The dynamics of methylammonium ions in hybrid organic–inorganic perovskite solar cells.* Nature Communications, 2015. **6**: p. 7124.
41. Akihiro Kojima, K.T., Yasuo Shirai, Tsutomu Miyasaka, *Organometal Halide Perovskites as Visible-Light Sensitizers for Photovoltaic Cells.* Journal of the American Chemical Society, 2009. **131**(17): p. 6050-6051.
42. Mingzhen Liu, M.B.J., Henry J. Snaith, *Efficient planar heterojunction perovskite solar cells by vapour deposition.* Nature 2013. **501**: p. 395-398.
43. Atsuhiko Miyata, A.M., Paulina Plochocka, Oliver Portugall, Jacob Tse-Wei Wang, Samuel D. Stranks, Henry J. Snaith & Robin J. Nicholas, *Direct measurement of the exciton binding energy and effective masses for charge carriers in organic–inorganic tri-halide perovskites.* Nature Physics, 2015. **11**: p. 582-587.
44. Krzysztof Galkowski, A.M., Atsuhiko Miyata, Paulina Plochocka, Oliver Portugall, Giles E. Eperon, Jacob Tse-Wei Wang, Thomas Stergiopoulos, Samuel D. Stranks, Henry J. Snaith, Robin J. Nicholas, *Determination of the exciton binding energy and effective masses for the methylammonium and formamidinium lead tri-halide perovskite family.* Energy & Environmental Science, 2016. **9**: p. 962-970.
45. Thomas M. Brenner, D.A.E., Andrew M. Rappe, Leeor Kronik, Gary Hodes, David Cahen, *Are Mobilities in Hybrid Organic-Inorganic Halide Perovskites Actually "High"?* Journal of Physical Chemistry Letters, 2015. **6**: p. 4754-4757.
46. Samuel D. Stranks, G.E.E., Giulia Grancini, Christopher Menelaou, Marcelo J. P. Alcocer, Tomas Leijtens, Laura M. Herz, Annamaria Petrozza, Henry J. Snaith, *Electron-Hole Diffusion Lengths Exceeding 1 Micrometer in an Organometal Trihalide Perovskite Absorber.* Science, 2013. **342**(6156): p. 341-344.
47. Kristofer Tvingstedt, O.M., Andreas Baumann, Carsten Deibel, Henry J. Snaith, Vladimir Dyakonov, Henk J. Bolink, *Radiative efficiency of lead iodide based perovskite solar cells.* Scientific Reports, 2014. **4**: p. 6071.
48. Dongqin Bi, W.T., M. Ibrahim Dar, Peng Gao, Jingshan Luo, Clémentine Renevier, Kurt Schenk, Antonio Abate, Fabrizio Giordano, Juan-Pablo Correa Baena, Jean-David Decoppet, Shaik Mohammed Zakeeruddin, Mohammad Khaja Nazeeruddin, Michael Grätzel, Anders Hagfeldt, *Efficient luminescent solar cells based on tailored mixed-cation perovskites.* Science Advances, 2016. **2**(1).
49. Laboratory, N.R.E. *Best Solar Cell Efficiencies*. 2017 [cited 2017; Available from: https://www.nrel.gov/pv/assets/images/efficiency-chart.png.
50. Tejas S. Sherkar, C.M., Lidón Gil-Escrig, Jorge Ávila, Michele Sessolo, Henk J. Bolink, and L. Jan Anton Koster, *Recombination in Perovskite Solar Cells: Significance of Grain Boundaries, Interface Traps, and Defect Ions.* ACS Energy Letters, 2017. **2**(5): p. 1214-1222.
51. Jin-WookLee, S.-H., NicholasDe Marco, Yao-TsungHsieh, ZhenghongDai, YangYang, *The role of grain boundaries in perovskite solar cells.* Materials Today, 2017.
52. inc., O. *Perovskite Precursor Ink (for Air Processing)*. 2018; Available from: https://www.ossila.com/products/perovskite-ink-air.
53. Park, N.-G., *Methodologies for high efficiency perovskite solar cells.* Nano Convergence, 2016. **3**(15).
54. Maria Konstantakou, T.S., *A critical review on tin halide perovskite solar cells.* Journal of Materials Chemistry A, 2017. **5**: p. 11518.
55. Konrad Domanski, J.-P.C.-B., Nicolas Mine, Mohammad Khaja Nazeeruddin, Antonio Abate, Michael Saliba, Wolfgang Tress, Anders Hagfeldt, Michael Gratzel, *Not All That*

Glitters Is Gold: Metal-Migration-Induced Degradation in Perovskite Solar Cells. ACS Nano, 2016. **10**(6): p. 6306-6314.

56. Kevin A. Bush, C.D.B., Ye Chen, Andrea R. Bowring, Wei Wang, Wen Ma, Tomas Leijtens, Farhad Moghadam, Michael D. McGehee, *Thermal and Environmental Stability of Semi-Transparent Perovskite Solar Cells for Tandems Enabled by a Solution-Processed Nanoparticle Buffer Layer and Sputtered ITO Electrode.* Advanced Materials, 2016. **28**: p. 3937-3943.
57. Kevin A. Bush, A.F.P., Zhengshan J. Yu, Mathieu Boccard, Rongrong Cheacharoen, Jonathan P. Mailoa, David P. McMeekin, Robert L. Z. Hoye, Colin D. Bailie, Tomas Leijtens, Ian Marius Peters, Maxmillian C. Minichetti, Nicholas Rolston, Rohit Prasanna, Sarah Sofia, Duncan Harwood, Wen Ma, Farhad Moghadam, Henry J. Snaith, Tonio Buonassisi, Zachary C. Holman, Stacey F. Bent & Michael D. McGehee, *23.6%-efficient monolithic perovskite/silicon tandem solar cells with improved stability.* Nature Energy, 2017. **2**: p. 17009.
58. Dunning, H. *Scientists discover why next-gen solar cells break down in days*. 2015 Available from: http://www3.imperial.ac.uk/newsandeventspggrp/imperialcollege/newssummary/news_27-5-2015-11-1-52.
59. Giles E. Eperon, S.D.S., Christopher Menelaou, Michael B. Johnston, Laura M. Herza, Henry J. Snaith, *Formamidinium lead trihalide: a broadly tunable perovskite for efficient planar heterojunction solar cells* Energy & Environmental Science, 2014. **7**: p. 982-988.
60. O. J. Weber, B.C., M. T. Weller, *Phase behaviour and composition in the formamidinium–methylammonium hybrid lead iodide perovskite solid solution* Journal of Materials Chemistry A, 2016. **4**: p. 15375-15382.
61. Fengjun Ye, W.Y., Deying Luo, Rui Zhu, Qihuang Gong, *Applications of cesium in the perovskite solar cells.* Journal of Semiconductors, 2017. **38**(1): p. 011003.
62. Michael Saliba, T.M., Ji-Youn Seo, Konrad Domanski, Juan-Pablo Correa-Baena, Mohammad Khaja Nazeeruddin, Shaik M. Zakeeruddin, Wolfgang Tress, Antonio Abate, Anders Hagfeldt, Michael Grätzel, *Cesium-containing triple cation perovskite solar cells: improved stability, reproducibility and high efficiency.* 9, 2016(1989-1997).
63. George Volonakis, A.A.H., Rebecca L. Milot, Weng H. Sio, Marina R. Filip, Bernard Wenger, Michael B. Johnston, Laura M. Herz, Henry J. Snaith, Feliciano Giustino, *Cs2InAgCl6: A new lead-free halide double perovskite with direct band gap.* Journal of Physical Chemistry Letters, 2017. **8**(4): p. 772-778.
64. YiLiang Wu, D.Y., Jun Peng, The Duong, Yimao Wan, Sieu Pheng Phang,Heping Shen, Nandi Wu, Chog Barugkin, Xiao Fu, Sachin Surve, Dale Grant, Daniel Walter, Thomas P. White, Kylie R. Catchpole, Klaus J. Weber, *Monolithic perovskite/silicon-homojunction tandem solar cell with over 22% efficiency.* Energy & Environmental Science, 2017. **10**: p. 2472.
65. Eric T. Hoke, D.J.S., Emma R. Dohner, Andrea R. Bowring, Hemamala I. Karunadasa Michael D. McGehee *Reversible photo-induced trap formation in mixed-halide hybrid perovskites for photovoltaics* Chemical Science, 2015. **6**(1): p. 613-617.
66. David P. McMeekin, G.S., Waqaas Rehman, Giles E. Eperon, Michael Saliba, Maximilian T. Hörantner, Amir Haghighirad, Nobuya Sakai, Lars Korte, Bernd Rech, Michael B. Johnston, Laura M. Herz, Henry J. Snaith, *A mixed-cation lead mixed-halide perovskite absorber for tandem solar cells.* Science, 2016. **351**(6269): p. 151-155.
67. Zhi-Kuang Tan, R.S.M., May Ling Lai, Pablo Docampo, Ruben Higler, Felix Deschler, Michael Price, Aditya Sadhanala, Luis M. Pazos, Dan Credgington, Fabian Hanusch, Thomas Bein, Henry J. Snaith, Richard H. Friend, *Bright light-emitting diodes based on organometal halide perovskite.* Nature Nanotechnology, 2014. **9**: p. 687-692.
68. Himchan Cho, S.-H.J., Min-Ho Park, Young-Hoon Kim, Christoph Wolf, Chang-Lyoul Lee, Jin Hyuck Heo, Aditya Sadhanala, NoSoung Myoung, Seunghyup Yoo, Sang Hyuk Im, Richard H. Friend, Tae-Woo Lee, *Overcoming the electroluminescence efficiency limitations of perovskite light-emitting diodes.* Science, 2015. **350**(6265): p. 1222-1225.

69. Nana Wang, L.C., Rui Ge, Shuting Zhang, Yanfeng Miao, Wei Zou, Chang Yi, Yan Sun, Yu Cao, Rong Yang, Yingqiang Wei, Qiang Guo, You Ke, Maotao Yu, Yizheng Jin, Yang Liu, Qingqing Ding, Dawei Di, Le Yang, Guichuan Xing, He Tian, Chuanhong Jin, Feng Gao, Richard H. Friend, Jianpu Wang, Wei Huang, *Perovskite light-emitting diodes based on solution-processed self-organized multiple quantum wells.* Nature Photonics, 2016. **10**: p. 699-704.
70. Samuel D. Stranks, S.M.W., Konrad Wojciechowski, Felix Deschler, Michael Saliba, Hitesh Khandelwal, Jay B. Patel, Steve J. Elston, Laura M. Herz, Michael B. Johnston, Albertus P. H. J. Schenning, Michael G. Debije, Moritz K. Riede, Stephen M. Morris, and Henry J. Snaith, *Enhanced Amplified Spontaneous Emission in Perovskites Using a Flexible Cholesteric Liquid Crystal Reflector.* Nano Letters, 2015. **15**(8): p. 4935-4941.
71. Haiming Zhu, Y.F., Fei Meng, Xiaoxi Wu, Zizhou Gong, Qi Ding, Martin V. Gustafsson, M. Tuan Trinh, Song Jin, X-Y. Zhu, *Lead halide perovskite nanowire lasers with low lasing thresholds and high quality factors.* Nature Materials, 2015. **14**: p. 636-642.
72. Brandon R. Sutherland, E.H.S., *Perovskite photonic sources.* Nature Photonics, 2016. **10**: p. 295-302.
73. Mingjian Yuan, L.N.Q., Riccardo Comin, Grant Walters, Randy Sabatini, Oleksandr Voznyy, Sjoerd Hoogland, Yongbiao Zhao, Eric M. Beauregard, Pongsakorn Kanjanaboos, Zhenghong Lu, Dong Ha Kim, Edward H. Sargent, *Perovskite energy funnels for efficient light-emitting diodes.* Nature Nanotechnology, 2016. **11**: p. 872-877.
74. Loredana Protesescu, S.Y., Maryna I. Bodnarchuk, Franziska Krieg, Riccarda Caputo, Christopher H. Hendon, Ruo Xi Yang, Aron Walsh, Maksym V. Kovalenko, *Nanocrystals of Cesium Lead Halide Perovskites (CsPbX3, X = Cl, Br, and I): Novel Optoelectronic Materials Showing Bright Emission with Wide Color Gamut.* Nano Letters, 2015. **15**(6): p. 3692-3696.

Chapter 3 – Experimental

Sample Preparation

Spin Coating

One of the main things that makes OSCs and lead halide perovskites interesting is that they are solution processable. This makes it very quick and simple to make devices from them on the laboratory scale, whilst also making them cheap to produce on the commercial scale. The most common process, which is used chiefly for creating small scale devices, is spin-coating. Spin coating works by dissolving the material in the required solvent, and then covering a substrate such as glass with the resulting solution. The substrate is then spun at speeds between 1000 and 8000 RPM, where centrifugal force throws most of the solution off the substrate as shown in figure 1. A combination of friction and viscosity allows a very thin and flat layer of solution to remain on the substrate, which then forms a film of the material as the solvent evaporates. This is a simple and effective method that reliably gives smooth and high-quality films in under 60 seconds, but has notable drawbacks in that most of the (often expensive) material is wasted, and it is not easily applicable to large area mass production. Hence it is more common for industrial manufacturers to use processes such as spray coating [1, 2], blade coating [3, 4], or slot-die coating [5], which are out of the scope of this thesis.

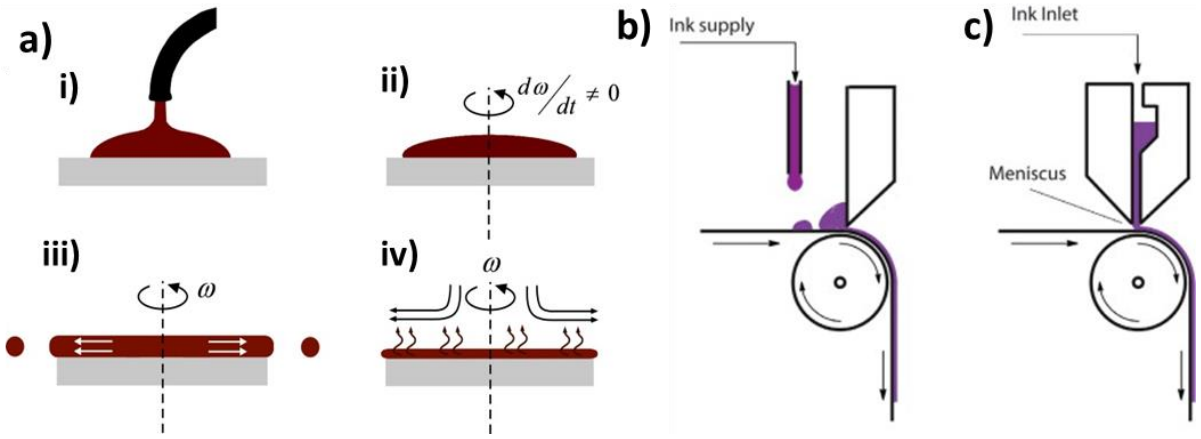

Figure 1 - a) The steps of the spin-coating process - i) The solution is deposited on the substrate, ii) The substrate is accellerated up to speed, iii) Most of the material flies off and a flat layer of liquid forms, iv) The polymer film forms as the solvent evaporates (image source Hellstrom et al.) [6]. b) and c) Examples of industrial scale blade coating and slot die coating respectively (image source Krebs et al.) [7]

With spin-coating, the thickness of the resulting films can be easily controlled by changing either the spin speed or the concentration of the solution, and it is empirically found that the film thickness very roughly obeys the following equation [8]:

$$Film\ thickness \propto \frac{Concentration^2}{\sqrt{Spin\ Speed}}.$$

Note that the film quality drops dramatically when the spin speed is reduced below 1000 RPM, and so the maximum film thickness we can make of a given material is limited by its solubility in the available solvents. Faster spin speeds also generally lead to higher quality films, and so more soluble materials will be able to work with higher spin speeds to get the same thickness. Hence a spin-coating material will ideally be as soluble as possible. The most commonly used solvents for dissolving OSCs are toluene and chlorobenzene(CB), but toluene is generally preferred because halogenated solvents are much less environmentally friendly. If higher solution concentrations are required, the solubility of most OSCs can often be increased by using more aggressive solvents such as chloroform (CF) or dichloromethane(DCM). However, spin-coating with these solvents is very difficult because CF and DCM are both extremely volatile, meaning that they will start to evaporate before the spin-coating has even begun. This makes it harder to achieve films with consistent thickness and high quality.

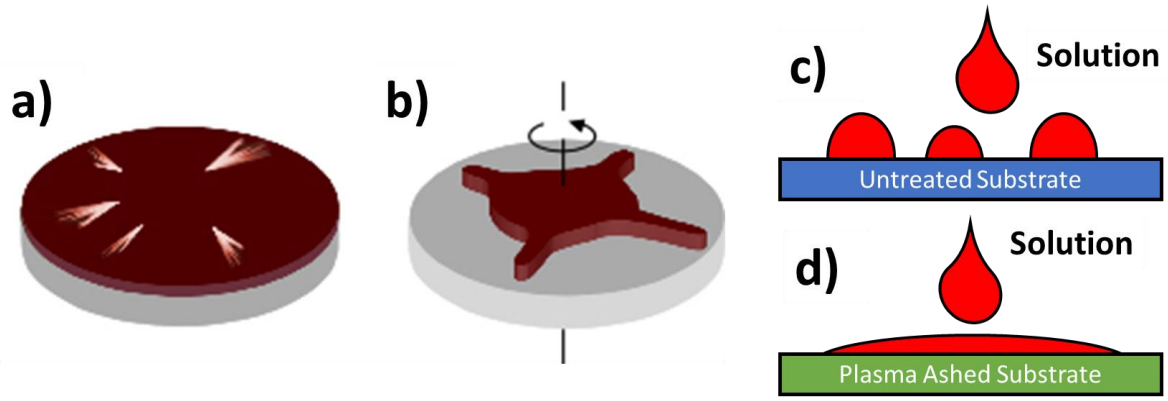

Figure 2 - a) Streak patterns on a film caused by dust particles, b) Poor spin-coating result caused by the solution not wetting to the substrate (image source [6]). c) Solutions will often aggregate to form droplets with incomplete coverage on an untreated substrate. d) Solutions get much better coverage and wettability on a plasma ashed substrate

When spin-coating with most OSCs, the resulting films are in the order of 100 nm thick, while dust particles in a room can be up to 100 microns across. This means that our substrate must be extremely smooth and clean because any particles of dust on the surface will easily poke through the film, creating a shorting pathway in the device and leaving a streak pattern on the surface of the film like the ones shown in figure 2 (a). To combat this, all spin-coating is done in a cleanroom environment, and all substrates are pre-cleaned before any spin-coating occurs. The substrates are

first scrubbed in order to remove any large particles, before being sonicated in a bath of acetone. Sonication involves using high frequency sound waves to dislodge any dust from the surface, and the particles are then dissolved in the acetone. The sonication is then repeated in a bath of isopropanol (IPA) and the samples are dried with a high-pressure nitrogen gun. Finally, the samples are cleaned by plasma ashing, where they are placed in a vacuum and exposed to oxygen radicals. This vaporises any remaining dust particles and also makes the sample surface extremely hydrophilic due to the adherence of oxygen ions to the substrate. This further enhances the quality of the spin-coating because the solution will prefer to cover the entire substrate rather than aggregating into droplets.

Optoelectronic Device Fabrication Procedure

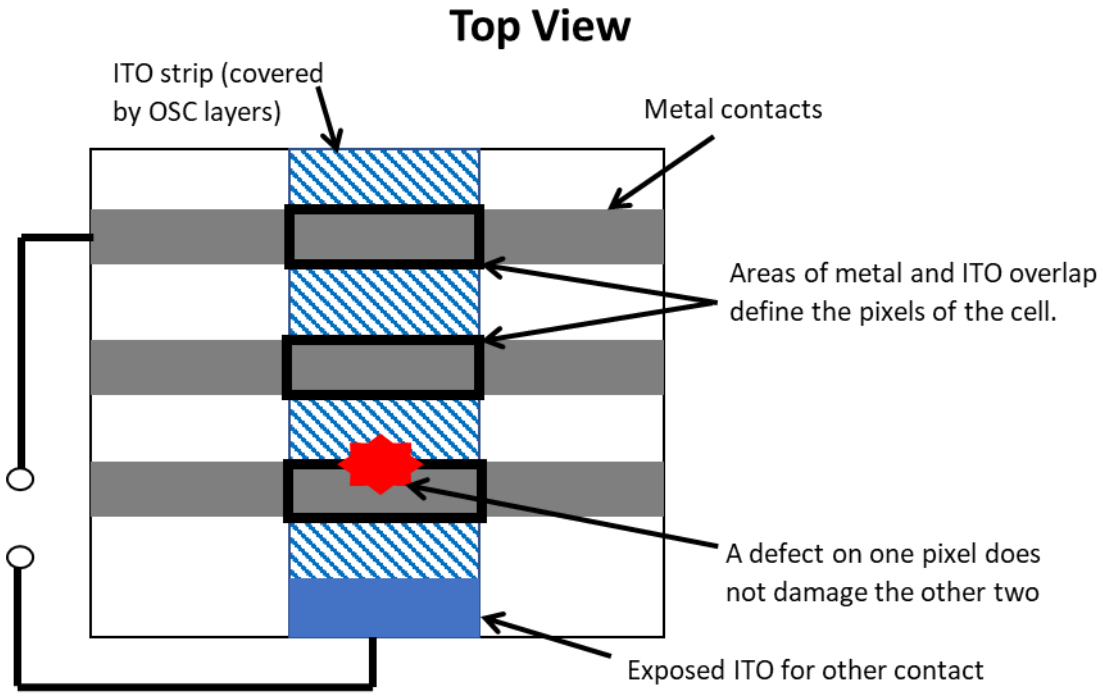

Figure 3 – A top-down view of the layout of devices for an OLED or solar cell

As mentioned in the previous chapter, all devices we work with in this thesis follow a monolithic architecture. This makes fabrication simple because devices can be made simply by spin-coating the required layers sequentially on top of each other. However, it also introduces a major design constraint in that we cannot use the same solvent for two adjacent layers – otherwise the solvent for the new layer will dissolve the previous layer and destroy the device. Therefore the bottom layer has to be made out of something reasonably tough, such as polyethylene dioxythiophene: polystyrene sulphonate (PEDOT:PSS) (which is soluble in water but insoluble in most other solvents) or titanium dioxide (TiO_2) (which is formed from solution but then baked at high temperatures to become completely insoluble). The active layer can then be deposited with few design constraints,

while the top layer and metal contacts are often deposited by vacuum evaporation. Vacuum evaporation works by placing the material and samples together in a vacuum and heating the material until it starts to sublime. The gas particles in the vacuum will follow ballistic trajectories and will adhere to the sample when they hit it, forming a thin and uniform layer of material. This is an expensive and time-consuming process, but it allows the final layers to be deposited with high precision and quality without adversely affecting the active layer.

The final layout of devices on the substrate of either an OLED or a solar cell has the design shown on figure 3, with the bottom contact (ITO) being made of a strip down the middle of the device, which is accessed by scraping away some of the OSC material at the edge of the sample. The metal contacts are then made of 3 strips perpendicular to the ITO strip, which separates the device into 3 pixels – one at each point where the ITO and metal overlap. If the sample was used to make one large pixel instead of three small pixels, then it would only take a single dust particle to kill the entire device, while in the split device we will still have at least two working pixels even if one is completely ruined.

Encapsulation

Any device which is sensitive to water or oxygen will usually be fabricated entirely within a nitrogen filled glovebox, but it must be encapsulated in order to protect it from atmosphere when being used in the outside world. For our studies we used a simple encapsulation technique, using a UV cured epoxy to glue a layer of glass onto the sample which completely covers all the pixels. Although glass is effectively a perfect barrier to water and oxygen [9], this is not by any means a perfect method of encapsulation because water and O_2 can still leak through the epoxy and the OSC film. However, it is more than sufficient for doing simple tests on the timescale of a few days.

Measuring Samples

Measuring Solar Cells

The defining measure of a solar cell is its current density – voltage (J-V) curve, which is measured using a Keithley 2400 source-meter. The solar cell is placed in a holder with spring-loaded pins to act as contacts, and a mask to ensure that an area slightly smaller than the area of the pixel is exposed. The mask is important because it provides a clearly defined area to produce accurate measurements of current density. Without the mask it will be possible for some charges created outside the device area to diffuse to the contacts [10], meaning that the setup will measure a higher current density than the solar cell is actually producing, and hence we will overestimate the efficiency. The solar cell is first measured in the dark as a baseline, and then under illumination from an AM 1.5G solar simulator lamp. This is a xenon lamp with a series of filters designed to mimic the industry standard

AM 1.5 G solar spectrum as closely as possible. Before each measurement, the lamp is calibrated with a silicon reference solar cell incorporating a KG5 short pass filter to ensure that the intensity is exactly one sun. The short pass filter changes the spectral response of the silicon cell to more closely match the response of the solar cells we plan to measure, and the exact spectral response of the silicon reference cell was calibrated by ORIEL to ensure an accurate measurement [11]. Once the lamp intensity has been confirmed to be one sun, the J-V curve of the sample cell is measured by applying a source voltage and measuring the current through the device. The raw current value is converted to current density by dividing by the device area to get an overall efficiency. The setup also includes a torch with variable intensity for doing intensity dependent J-V curve measurements. Note that for certain classes of solar cells (particularly in perovskites) there is known to be a degree of hysteresis in the J-V curves [10, 12], and so it is important to always perform both a forward (negative to positive voltage) and a backward scan (positive to negative) to ensure that both possibilities are displayed. The precise reasons for the hysteresis seen in perovskite solar cells is a hotly debated topic, but the prevailing consensus is now that it is due to ion migration during measurement [13].

Another important parameter of a solar cell is its incident photon to charge collected electron efficiency (IPCE), also known as the external quantum efficiency (EQE). This is a measure of how many charges are created per absorbed photon of a given wavelength incident on the solar cell when it is operating at short circuit. To measure the IPCE spectrum, light from a xenon lamp was passed through a Bentham monochromator (spectral width less than 1 nm) and is then directed onto the solar cell via an optical fibre. The solar cell is held in short circuit and the current from the cell is measured as the wavelength is changed to get a graph of current vs input wavelength. Since the absolute intensity of the lamp at any given wavelength is unknown, a single measurement is not sufficient to get an absolute IPCE without something to compare it to. Therefore, the measurement was repeated on a reference cell with known IPCE in order to get a useful comparison. The reference cell was calibrated by the National Physics Laboratory (NPL) of the UK. Knowing the IPCE of a solar cell gives crucial insight into how the solar cell is operating and where the current is coming from. But it is also useful as a second verification of device efficiency - the Jsc of any given solar cell can in theory be calculated indirectly by multiplying its IPCE spectrum with the solar spectrum and then integrating the result [10]. Thus, it provides an excellent way to independently verify that the current measured from your J-V curve is accurate.

PLQY setup

Another important factor for determining the quality of a material is its photoluminescence quantum yield (PLQY), which is the number of photons which are emitted for every photon absorbed. As mentioned before, a high PLQY is vital for getting high voltage in a solar cell, but knowing the PLQY also provides crucial insight into a material's important parameters such as its radiative and non-radiative recombination rates. The basic equation for PLQY is simply:

$$PLQY = \frac{\text{photons emitted}}{\text{photons absorbed}}$$

On the surface this would seem like a very simple measurement. Counting the number of absorbed photons should be easy as long as we know the absorbance and the input power, but accurately counting the number of photons emitted can often prove to be quite difficult because PL photons are always emitted randomly in all directions. Therefore a single detector will never be able to catch all of them, and we will not ever be sure we have the correct PLQY. To overcome this, the measurement is carried out in an integrating sphere, where all light from the sample is scattered randomly inside the sphere. This effectively collects all the photons and provides a uniform intensity which can be measured with a photodiode or a CCD, however this alone cannot be used to calculate PLQY because the process is far from being 100% efficient. Many photons are eventually absorbed or escape the sphere before reaching the photodiode, so we can measure a PL spectrum through the sphere, but we do not know exactly how many photons it corresponds to. To make matters worse, the sphere and the detector will have a spectral response - the efficiency of the integrating sphere and photodiode will depend on wavelength, meaning that the normalised PL spectrum will look different before and after it has been passed through the sphere.

As mentioned earlier, one of the main issues with measuring the PLQY of perovskites is that their PLQY strongly increases with intensity, meaning they require high input intensity in order for their PL to be measureable. Therefore, for measuring perovskites we created an in-house PLQY setup which used laser excitation so as to provide high pump powers. The in-house setup had the design shown in figure 4, and uses the design principles laid out by Greenham et al in 1995 [14]. 405 nm laser excitation was provided by a Kimmon IK series continuous wave helium-cadmium (HeCad) laser with a maximum power of 42 mW, which could be attenuated by a series of neutral density (ND) filters. The input power was measured with a Coherent FieldMaster power meter, and then coupled into an integrating sphere. Light in the integrating sphere was measured using a fibre coupled ANDOR UV-enhanced calibrated CCD, with a baffle to prevent light from direct reflections reaching the detector. The combined spectral response of the sphere, fibre, and CCD was calculated by measuring the

spectrum of a calibrated tungsten lamp through the sphere and working out the correction factor required to regenerate the original spectrum.

To measure the PLQY, a sample is placed in the path of the laser beam at a slight angle to ensure no light was reflected directly out of the sphere. Once the spectral response of the system has been accounted for, the PLQY is calculated by the following equation:

$$PLQY = \frac{X_{sample} - (R+T)X_{sphere}}{(1-R-T)X_{Laser}},$$

where R is the measured reflectance of the sample and T is the measured transmission of the sample at the laser wavelength. X_{laser} is the integrated spectrum of the laser peak when fired into an empty integrating sphere, thus giving a measure of how many photons are incident on the sample. The total number of photons absorbed can then just be calculated from $(1 - R - T)X_{Laser}$. X_{sample} is the integrated counts of the PL spectrum when the sample is placed in the path of the laser beam, while X_{sphere} is the integrated PL counts when the sample is inside the sphere but the laser beam does not hit it directly.

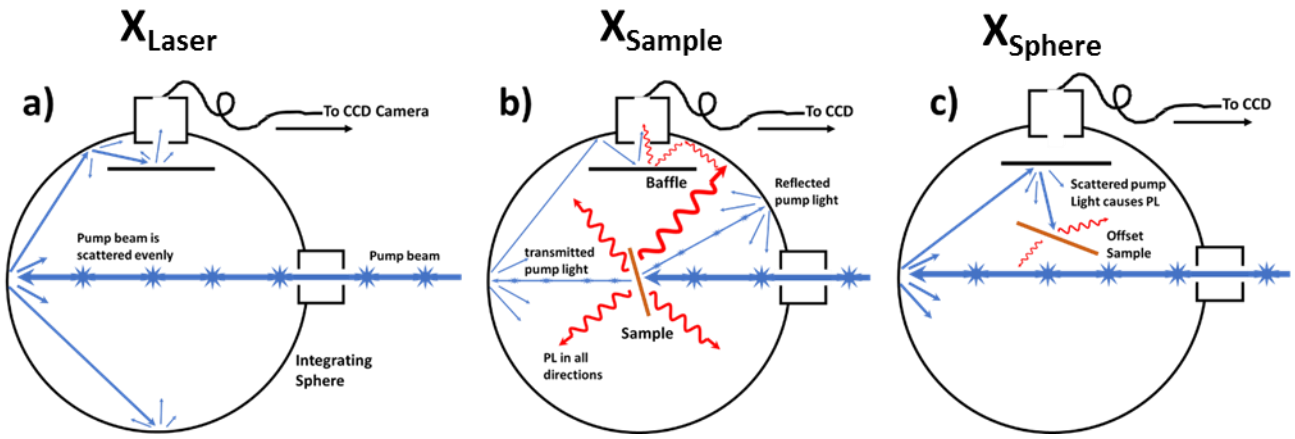

Figure 4- configurations for measurement in the integrating sphere setup. a) X_{laser}, where the signal from the raw pump beam is measured b) X_{sample}, where PL from direct absorption is measured c) X_{sphere} - the measurement which allows us to account for second-pass absorption.

At first glance, one would expect the term for photons emitted to just be X_{sample}, but we have to add a correction factor of $(R+T)X_{sphere}$ to account for absorption which does not occur in the first pass of the pump beam. If the sample is not perfectly absorbing, then transmitted and reflected photons will bounce around the sphere before eventually being absorbed by the sample. Thus causing our calculation term of $(1-R-T)X_{laser}$ to underestimate the total number of photons absorbed. The extra $(R+T)X_{sphere}$ term accounts for this by removing any PL counts that can be attributed to second cycle absorption. As a final calibration, the accuracy of the setup was checked by taking measurements of

glass filters with known PLQY values and comparing the known value to the outcome of the measurement.

For experiments where even higher intensity excitation was required, pumping was provided with a pulsed source from a Laser Compact Group LCS-DTL-374QT frequency tripled Nd:YAG laser emitting at 355 nm with 1 ns pulses. This could be used to provide a relative measure of PL strength vs intensity, but could not be used to accurately measure photoluminescence quantum yield because the tungsten lamp used for calibration was too weak to provide useful calibration at this wavelength.

In our research group, most PLQY measurements are taken using a Hamamatsu C9920-02 commercial setup, which uses an extremely well calibrated integrating sphere of known efficiency and spectral response. Any measured spectra can then be corrected by the known spectral response to get a "real" spectrum. First a zero measurement is taken, where the pump light is incident on a blank sample, thus providing a measure of the number of photons incident on the sample. When the desired sample is measured in the next step, a portion of the incoming photons are absorbed. This causes the pump peak in the spectrum to be reduced while emission due to the PL can also be measured. The exact details of the algorithm used to calculate the PLQY from this are not discussed, but as a rough guide the system calculates the photons absorbed by measuring the difference in area under the pump peak before and after the sample is placed in the sphere, while the photons emitted is calculated by integrating the PL part of the spectrum. The Hamamatsu setup has the advantage that measurements are extremely quick to perform, allowing a high throughput of samples to be easily measured. But for our purposes it has a major disadvantage in that it uses a monochromated lamp excitation, which gives it very low power, making it unsuitable for measuring perovskite samples.

Lasers

Laser measurements

The first step in creating a thin film laser from a new material is to check that it can support amplified spontaneous emission (ASE), which is a precursor to lasing. If the material does not have ASE at a reasonable threshold then it will not be worthwhile trying to use it to make a laser. Creating ASE in a semiconductor film requires the waveguided light to see gain [15]. The gain is provided by exciting the sample with a pulsed pump laser. The most common pump used for this purpose is 355 nm light in 1 ns pulses at 1 kHz from a CryLaS FTSS355Q4_1k laser (known as the CryLaS). The CryLaS provides excellent pulse stability in a compact source, but is limited to only work at 355 nm with a

low maximum power. If greater power or a specific wavelength is needed, then pumping is provided with a Continuum Surelite I-20 optical parametric oscillator (OPO) setup operating at 20 Hz at any wavelength between 355 nm and 1000 nm. The OPO can provide high power at almost any wavelength, but the pulse energy is much less stable than when using the CryLaS, making it less suitable for certain measurements where the pump power must be kept exactly constant.

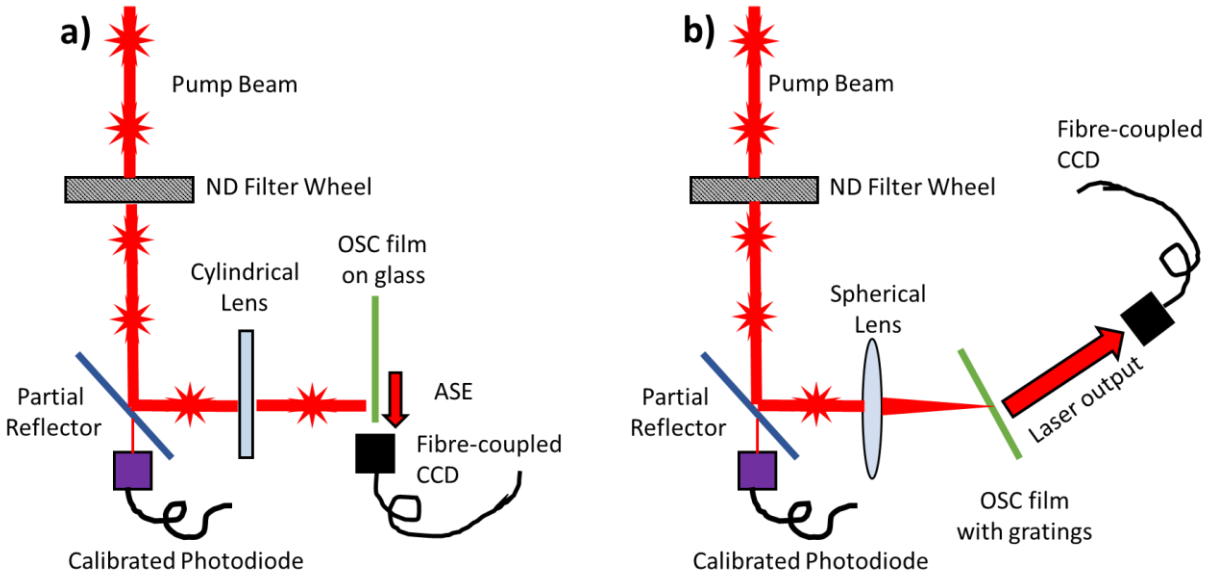

Figure 5- Simplified laser measurement setup. a) shows the configuration for measuring ASE. b) Shows the configuration for DFB lasers

To measure ASE, the pump laser spot is focussed with a cylindrical lens to form a stripe of excitation in the setup shown on figure 5. Light which is waveguided in the direction of the stripe will be amplified to create ASE, while light propagating in other directions will not. The emission spectrum of the sample is measured with an ANDOR fibre coupled CCD camera, and the input end of the coupling fibre is placed at the point where the stripe meets the edge of the film. Therefore, the CCD will only pick up light which has been waveguided down the stripe. The intensity of the pump beam is varied using an ND wheel, and a small portion of the pulse is removed from the beam with a partial reflector for measuring the pulse energy (in μJ). The pulse energy is measured with a calibrated photodiode supplied by Coherent, which is protected from being saturated by several more ND filters to attenuate the beam. Note that these ND filters will reduce the value of the measured pulse fluence, and the partial reflector will only couple $\frac{1}{10.7}$ of the light into the photodiode. Hence corrections for these factors are included when calculating pulse energy

$$Pulse\ energy\ (\mu J) = \frac{E_{Photodiode}}{T_{Filter}T_{reflector}},$$

where $E_{photodiode}$ is the pulse energy measured by the photodiode, T_{filter} is the fraction of light which is passed through the shielding filters, and $T_{reflector}$ is the fraction of light coupled to the photodiode through the partial reflector (0.093 in the case of our setup). The emission spectrum from the film is then repeatedly measured as the pulse energy is increased, and a graph of integrated intensity and full width half maximum (FWHM) of the spectrum vs pulse energy is plotted. The ASE threshold can be clearly seen at the point where the spectrum collapses to a much narrower peak, resulting in a sudden drop in FWHM, and a sudden increase in slope of the integrated counts vs pulse energy. After the measurement, the beam area is measured with a beam profiler to get absolute value for the threshold in pulse fluence (μJcm^{-2}), which can be calculated by dividing pulse energy by minimum beam area. The overall pulse fluence is calculated with the following equation.

$$Pulse\ fluence\ (\mu Jcm^{-2}) = \frac{Pulse\ Energy\ (\mu J)}{Beam\ Area\ (cm^2)}$$

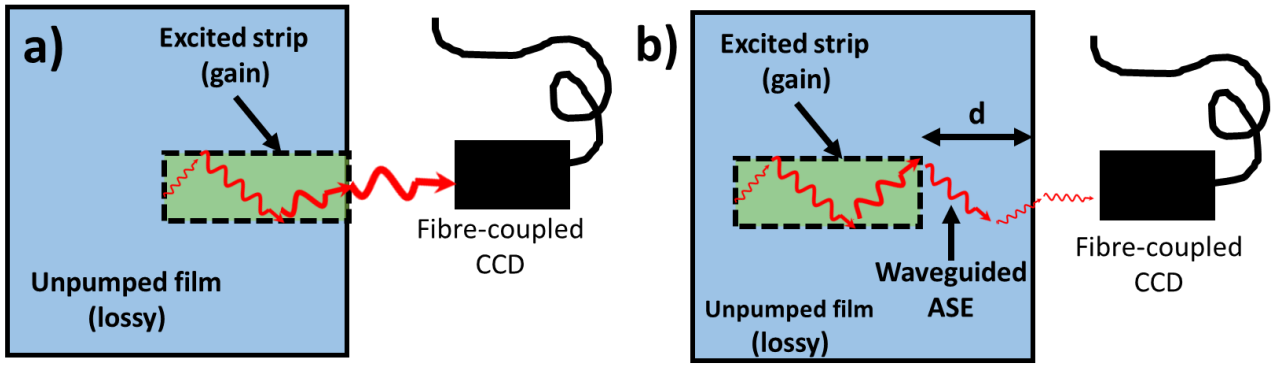

Figure 6 - a) Normal ASE measurement where the sample is excited at the edge. b) Loss measurement where the strip is moved through the sample - waveguided ASE must travel a distance d through the unpumped film to reach the CCD, and it is attenuated by waveguiding losses as a result.

The threshold for ASE is the point at which waveguiding gain becomes greater than loss, and hence one of the best ways to reduce lasing threshold is to minimise the waveguide loss. Waveguide loss is measured by forcing waveguided light to propagate through the film without excitation, and observing how the intensity of the escaping light varies with the length of the waveguide. To do this, a large area film of the laser material is placed on a moving stage and excited above threshold with a stripe in the same way as in the ASE measurement [16]. The detector is placed on the same stage so that the sample remains the same distance from the detector. The emission from the edge is observed in the same way as before, but the sample stage is moved so that the stripe moves along the sample away from the measured edge. The result is that, once the stripe has separated from the

edge of the film, the waveguided light must propagate an increasing distance through non-excited film before reaching the CCD (see figure 6). Therefore, as the stage first begins to move we will see an increase in the integrated CCD counts of the spectrum because the effective length of the stripe is increasing, but once the stripe edge leaves the sample edge the spectrum should fall off on an exponential curve. Fitting the exponential will give a decay constant with units of cm^{-1}, which we call the loss coefficient [16]. This should be as low as possible in a good lasing medium.

Distributed Feedback Gratings

Once a material is known to have a good ASE threshold, the next step is to try making a distributed feedback laser. This is achieved simply by spin-coating the gain material on top of a grating of the required period, but first the ideal grating has to be designed and fabricated. The ideal grating period for a laser depends on the effective refractive index of the system, which is defined by the refractive index of the materials in the laser, and the thickness of the gain medium. The system is modelled as a 3 layer slab waveguide (see figure 7d), with the bottom cladding layer usually being the grating material (n=1.52), and the upper cladding layer being air (n=1) or an encapsulant (n=1.33). The refractive index of the gain medium is usually between 1.7 and 2.3, and it must be sufficiently thick that the effective refractive index of the mode is greater than the refractive index of both cladding layers. The resonance condition for the grating is when the effective wavelength of the lasing mode, which is assumed to be the wavelength of the ASE peak divided by the effective refractive index, is equal to the grating period.

Once an ideal grating period has been calculated, the next step is to fabricate the grating. First, a master structure is made on silicon via electron beam lithography, but this master structure is far too expensive to be used in a mass-produced device. To make devices on a useful scale, copies of this master structure are made using UV nanoimprint lithography (UV-NIL). UV-NIL works by making a negative copy of a silicon structure out of a polymer photo resist to create a soft stamp, which can then be used to repeatedly imprint the desired grating structure on cheap polymer substrates. The stamp is usually made on a glass substrate, and first an adhesion layer of a polymer called 3-(Trimethoxysilyl)propyl acetate (4045X) is spin coated on the glass at 2000 RPM and annealed at 100 ^{0}C for 60 seconds. This prevents the stamp from peeling off the glass after repeated use. The stamp itself is made from a trade protected polymer called MD700, supplied by Micro Resist Technology, which consists of a raised base with the imprint of the grating on the top. The base is made first by placing the substrate on a blank sheet of clean silicon, with it raised off the surface by three 1 mm washers. A few droplets of MD700 are placed on the silicon and the substrate, before they are pressed together to make a flat circle of MD700 exactly 1 mm thick. The polymer is then cured to

become solid by exposing it to UV light for 300 seconds in an EVG 620 photomask aligner with custom nanoimprint tooling. Once the exposure is finished the substrate is peeled off the silicon to create a glass substrate with a blank stamp.

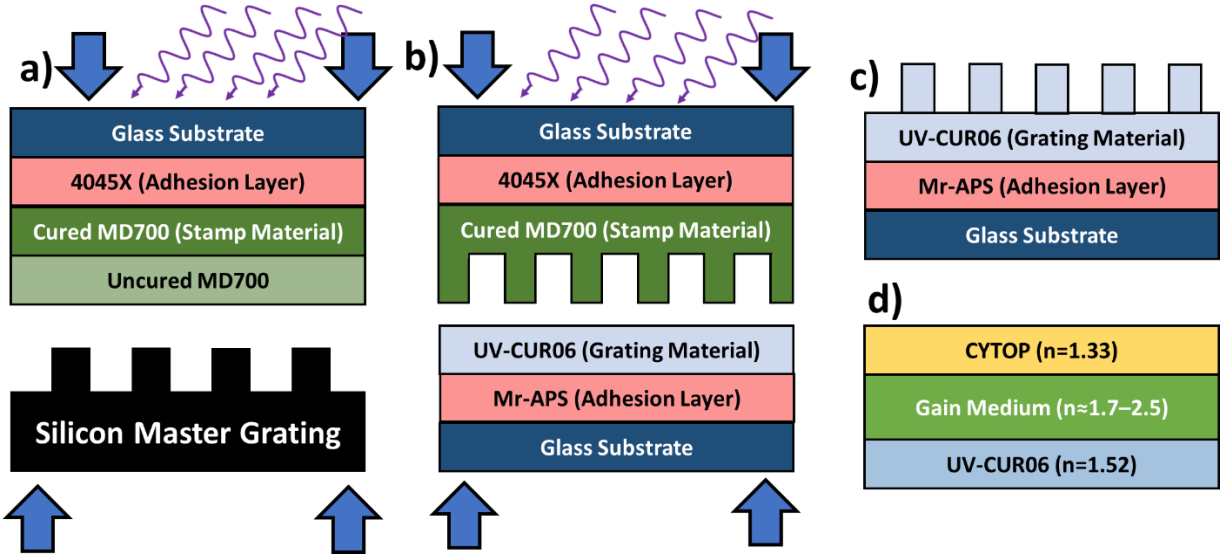

Figure 7- The UV nanoimprint lithography process. a) A stamp is made from MD700 by moulding it around the master structure and curing it with exposure to UV light, creating a negative of the structure. b) The grating is made by pressing the stamp onto a blank layer of UVcur06 or Mr-NIL210 and exposing it to UV light to solidify the structure. c) The final grating structure after the nanoimprint process is an exact copy of the master grating. d) The slab waveguide model used in simulations.

To give the blank a grating structure, more MD700 is then spin coated onto the stamp at 2000 RPM for 60s. The silicon master grating is placed face up in the UV curing chamber, and several drops of MD700 are placed on the grating structure. The stamp is then placed directly in contact with the silicon master grating, and the MD700 completely moulds to the shape of the grating (figure 7a). The pair are then left to cure under UV light for another 300 seconds, and the finished stamp is then peeled away from the silicon master structure. The new stamp and the master structure are both cleaned with IPA before storage for later use. The silicon master can be re-used almost indefinitely for making stamps, while the soft stamp must be replaced approximately once every 6 months.

Once a stamp has been created, it is fairly simple to create a laser grating. Once again, a glass substrate is cleaned and prepared for use, and an adhesion layer of mr-aps is spin coated on the substrate at 4000 RPM for 60 s and then annealed at 150 ^{0}C for 60 s. The mr-aps is a commercial polymer solution supplied by Micro Resist Technology, and once the adhesion layer has been applied, a resist layer of mr-NIL 210 or UV-CUR06 is then deposited by spin-coating at 4000 RPM for 60 s followed by annealing at 100 ^{0}C for 60 s. UV-CUR06 and mr-NIL 210 are a commercial blends also supplied by Micro Resist Technology. The blank grating is then placed in the EVG chamber along

with the soft stamp, and by a standard machine procedure the two samples are pressed together under vacuum and exposed to UV light for 300 s (figure 7b). Once the curing is complete, the stamp and the blank can be separated, leaving a perfect copy of the original grating imprinted on the cured mr-NIL 210 (figure 7c), while the stamp can be reused after a quick cleaning in IPA. This process can be used to quickly and easily produce a large number of gratings which can be turned into lasers by simply spin-coating with a gain material of the correct thickness on top. Prior to spin-coating, the gratings are often plasma ashed on low power for 30 seconds to enhance wettability and improve film quality, but it is important that the gratings are not exposed to oxygen plasma for any longer than 30 seconds or the plasma will destroy the gratings.

Once the grating has been made, the gain medium is deposited on top via spin-coating, and an encapsulant cladding layer such as CYTOP^{TM} is deposited on top of that. CYTOP is an excellent barrier to water but a poor barrier to oxygen, and so lasers incorporating gain media which are vulnerable to photooxidation must be kept in a vacuum in order to keep them stable long enough for useful measurements to be made.

Lasing Measurements

Once a laser has been fabricated, we measure its threshold in a very similar way to measuring ASE. The grating area is pumped with a circular spot (using a spherical lens to focus the pump beam) and a graph of output counts and spectrum FWHM is plotted vs input pulse fluence. The key differences are that the light is now outcoupled perpendicular to the film rather than out of the edge of the sample, and we expect the FWHM to collapse to less than 1 nm rather than the ~5 nm normally seen in ASE. The plot of integrated intensity vs time should in theory follow a straight line below threshold and then rapidly converge on a second steeper line above threshold. The absolute value for the threshold can then be calculated as the pulse fluence where the two extrapolated straight lines cross, which should also be at approximately the same point when the FWHM collapses.

Provided the laser is of sufficient quality, the output light should conform to a coherent output beam which can be easily studied. The shape of the output beam can be easily measured using a beam profiler, and its polarisation can be studied by passing the beam through linear and circular polarising plates. Another measure of beam quality is the M^2 value of the beam, which defines the smallest spot which the beam can be focussed down to. A perfect single mode gaussian beam has an M^2 value of 1, meaning that its minimum spot size is diffraction limited. Any other beam profile will always have an M^2 value greater than this. We measure the M^2 value by passing the beam through a spherical lens and measuring its beam radius vs distance from the lens. A beam profiler is placed on a moving stage, and a beam profile is taken at every position point to get a beam radius. As the

beam is focussed down its intensity increases, and so it must be attenuated with a series of ND filters to ensure that it does not saturate the pixels of the beam profiler. Once a graph of beam radius vs position has been plotted, the curve is fitted to the following function to calculate M^2.

$$w = w_0 \sqrt{1 + \frac{M^2 \lambda z}{\pi {w_0}^2}}$$

Where w is the beam radius, w_0 is the beam waist radius, λ is the beam wavelength, and z is the distance from the beam waist [17].

Characterising Films

Absorbance and Reflectance Measurements

Knowing the absorbance and reflectance of one's materials is very important for determining their bandgap, assessing their worth as a solar cell material, and for calculating their PLQY. These parameters are measured using a Varian CARY 300 absorption spectrometer, which works by passing monochromated light from a lamp source through the sample, and comparing the transmitted amount to a reference beam. The setup has a tungsten lamp for measuring the visible range and a deuterium lamp for measuring the UV range. To remove any contributions from the substrate, a reference measurement is taken where the substrate material (usually glass) is placed in front of both the reference beam and the sample beam to give a 100% transmission measurement. Next a substrate coated with the desired material is placed in front of the sample beam to give a measurement of the transmission spectrum of the sample.

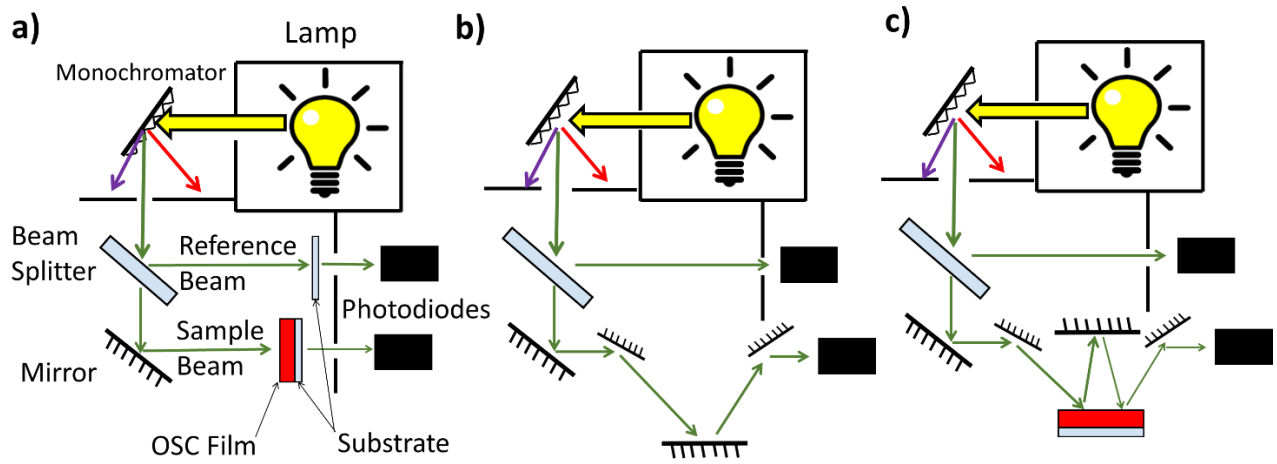

Figure 8- a) CARY 300 Absorption spectrometer setup. b) Reflection Setup in 100 % reflectance calibration. c) Reflection setup measuring sample. A 0% reflection calibration is taken by removing the sample and allowing all light to escape..

Reflectance is measured with a slightly different setup where the sample beam is reflected off several mirrors and then into the sample at an angle as close to normal incidence as possible (see figure 8). To account for the imperfect reflectance of the mirrors in the setup, first a 100% transmission measurement is taken with the setup in figure 8b, where all the light should get through to the detector. Second a 0% reflection measurement is taken, with the measuring sample being absent, in order to remove any background signal. Finally the sample is measured by placing it in the path of the beam so that the beam is reflected twice off the sample. The reflectance spectrum of the material can then be calculated by measuring the amount of light that reaches the detector. If we assume that there is no scattering in the film (which is usually quite easy to spot due to its strong $\frac{1}{\lambda^4}$ dependence), then it is straightforward to calculate the absorbance of the sample by assuming the following equation holds true:

$$Absorbance + Transmission + Reflection = 1.$$

PL Lifetime measurements

When a sample is excited with a short pulse, a number of excited states are generated which will then decay exponentially. This exponential decay has a time constant known as the photoluminescence lifetime (PL lifetime). The PL lifetime is a crucial parameter of any semiconducting material because it gives key insight into the way excited charges behave in the material. At its core, the PL lifetime gives the total rate of recombination, which is the sum of the radiative (k_{rad}) and non-radiative (k_{nonrad}) rates respectively. Knowing k_{rad} is useful because it gives a measure of the strength of the emissive transition in the material, while k_{nonrad} gives information about the number and type of trap states in the material. Combining knowledge of the PL lifetime and the PLQY of a sample allows us to know these two quantities individually by using the following equations [18]:

$$PL\ lifetime\ (\tau) = \frac{1}{k_{rad}+k_{nonrad}} \quad , \qquad PLQY = \frac{k_{rad}}{k_{rad}+k_{nonrad}}.$$

The PL lifetime is measured using one of two methods – a streak camera, or time correlated single photon counting (TCSPC). For TCSPC, an Edinburgh instruments FLS 980 fluorimeter is used, which excites the sample with a pulsed laser with picosecond pulse duration. The emitted photons are collected using photomultiplier tubes and are binned according to their delay time – that is the time it takes them to be emitted after the laser pulse is absorbed. The result is a plot of the number of PL counts vs time after excitation which, provided the response time of the instrument is known, can be fitted with an exponential to give a quantitative value for the PL lifetime.

TCSPC measurements can accurately give the PL lifetime on scales ranging from 2 ns 50 µs with a resolution of approximately 500 ps. However, it has some disadvantages in that the setup is limited to using only low power from a low power laser, and it is very time consuming to measure how the PL spectrum evolves with time. If these issues are significant, a streak camera is used which can quickly measure the time evolution of a PL spectrum over a range of 200 ps to 2 ns with 2 ps resolution, while using a much more intense power source. The sample is excited with 515 nm, 200 femtosecond laser pulses from a Light Conversion™ optical parametric amplifier. The resultant PL is collected with a wide area lens and the excitation light is then filtered out. The PL is then focussed into the slit of a Hamamatsu C10910 streak camera where it is reflected off a diffraction grating to give spectral resolution, and then impacted onto a photocathode. The electrons from the photocathode then impact a phosphor screen where they are detected. To give temporal resolution, the electrons from the photocathode are subject to a time dependent electric field which will alter what pixel on the screen they hit depending on their time of arrival [19]. This results in the excitation forming a "streak" on the screen which gives the streak camera its name. Each pixel will receive a set number of counts after each pulse, which allows a 2D plot of the light emission to be created - with the horizontal axis giving spectral resolution and the vertical axis giving temporal resolution. In this setup the sample being studied is usually stored in an Oxford Instruments™ cryostat to allow measurements at low temperatures and high vacuum.

Air Photoemission - Measuring HOMO and LUMO levels

One of the most important parameters when designing an electronic device is the position of the energy levels in the materials being used. If the energy levels are not properly aligned then the charges will experience barriers preventing them from moving through the structure, meaning the device will not work efficiently. In this thesis we use a KP technology APS03 setup to measure both the work function and the HOMO level of materials because it provides accurate and reproducible results on thin films with a simple setup.

The APS03 setup has the design shown in figure 9 and uses air photoemission to measure the HOMO value of a material, which involves illuminating the film with monochromatic UV light (generated from a deuterium lamp) and measuring electrons ejected from the sample via the photoelectric effect [20-22]. If a UV photon with more energy than the depth of the HOMO is absorbed by the sample, it promotes an electron all the way to the vacuum level, meaning it escapes the material. The electron is then collected by the probe tip and measured as a current signal. If the photon has less energy than the HOMO then the sample will absorb the photon, but the electron will remain within the sample and no photocurrent signal is detected. The HOMO level can be determined by

varying the photon energy and determining the point at which the photoemission turns on. In most semiconductors the number of available states below the HOMO level approximately goes with the excess energy cubed, and so above photoemission threshold the measured photocurrent should obey the following equation [20-22].

$$Photoemission\ Counts\ \propto (E_{photon} - E_{HOMO})^3$$

The measured photoemission counts are then corrected for the known intensity spectrum of the excitation lamp, and then plotted on a cube root scale. The cube root scale turns the plot of photoemission counts into a straight line, from which the HOMO level can be easily calculated by extrapolating to the x axis crossing point.

This setup is very versatile and can work in atmosphere on a wide range of materials. The key constraints are that the sample must be a good photoemitter, allowing a good signal to noise ratio, and it must be grounded to compensate for the loss of charge from photoemission. If the sample is not grounded then it will become positively charged as it emits photoelectrons, making it harder for the electrons to escape the surface and causing the signal to decay over time. Hence films are usually measured on an ITO substrate in order to facilitate an easy contact to ground. The measurement will receive photoelectrons from up to 100 nm depth inside the sample. This means that we can be sure that the majority of the signal is coming from the bulk sample, and not the substrate or surface states, provided that the film is sufficiently thick.

It is worth noting that the mean free path of the photoelectrons in air is in the order of 100 nm, which should be nowhere near long enough to reach the detector at ~100 microns from the sample surface. To combat this, most measurements of this class are usually done under ultra-high vacuum, which can be very expensive and time consuming. However the APS03 setup can still achieve a strong signal under ambient conditions because the electrons will ionise the air around the sample, creating a cloud of charged ions that can be easily collected by applying a small (+70 V) potential to the measuring tip.

Kelvin Probe – Measuring the Fermi Level

In addition to providing direct measurements of the HOMO level of a material, the APS03 setup can also be used for measuring a material's fermi level [20]. Thus providing a measure of how strongly doped a material is and how the bands are bending in the device. The fermi level is calculated by using the setup in a kelvin probe configuration. The film to be measured is grounded in the same way as before, and the tip is held at ~100 microns from the sample. Because the sample and the tip have different work functions, there will be a potential difference across the air gap, causing some

charge to accumulate on the end of the tip. This is called the contact potential difference (CPD) and it allows the probe tip and the sample to essentially form a parallel plate capacitor which obeys the following equations.

$$V = \frac{Q}{C} \quad and\ C = \frac{\varepsilon_0 A}{d}$$

A simple measurement of the work function would be to measure the charge generated, and apply a voltage to zero it. The value of this cancelling voltage will give us the difference in work function between the tip and the sample. However this measurement is slow, and very susceptible to background noise or charging effects. Therefore it is better to use an oscillating measurement which is much easier to separate from the background. If the tip is oscillated up and down by a small amount, it will change the capacitance of the setup, which will in turn change the voltage across the capacitor since the charge should remain constant. This produces a clear signal in the form of an oscillating voltage, and the magnitude of the signal will be directly proportional to the potential difference between the tip and the sample. Most setups will then apply a cancelling voltage until they find a voltage which sets the amplitude of the signal to zero [23]. However this gives a large error margin because the signal disappears into the background noise as the optimal cancelling voltage is approached. A better method is to apply a large positive and negative voltage (in the range of ±7 V) and measuring the signal magnitude at each point. The difference in work function between the tip and the sample can then be extrapolated by fitting a straight line between the two points and finding where it crosses the x axis.

To ensure that the measured value is correct, and not due to random charging effects, the measurement is repeated once per second and plotted on a graph of contact potential difference vs time. A good quality measurement on a well-grounded sample will be stable and drift-free over a 30 s scan, whilst also having a standard deviation from the mean of less than 3 mV. Measurements which do not meet these criteria are discarded and the sample is realigned to ensure proper grounding before repeating the measurement. The absolute value for the work function can be extrapolated from the contact potential difference by adding the value to the work function of the measuring tip. To ensure accurate measurements, the work function of the tip is measured before each measurement by calibration against a gold reference sample with known work function, allowing absolute values of a material's work function to be accurately measured.

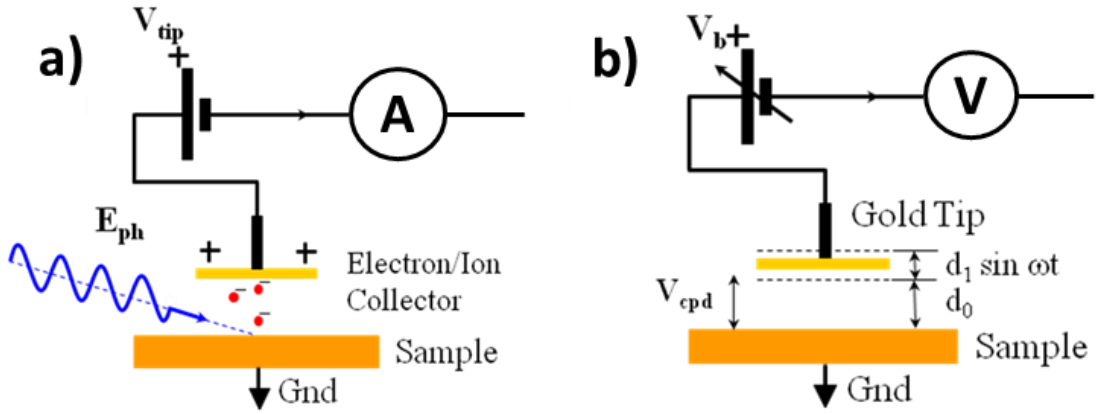

Figure 9- a) Air Photoemission Setup - photoelectrons are collected by the tip and measured as a current. b) Kelvin Probe setup - an oscillating potential is measured on the tip with amplitude proportional to the difference in work function between the tip and the sample.

Film Quality and Thickness Measurements

When making a thin film of material, it is vital to be able to accurately measure their thickness and surface roughness. A rough film with incomplete coverage of the substrate is useless for devices as it allows shorting pathways to ruin the device operation, and the thickness of a film will strongly affect the conductivity, light absorbance, and light outcoupling of a device. To assess film quality, samples are usually imaged with a Hitachi S4800 scanning electron microscope. As long as the sample material is sufficiently conductive, images of sub-100 nm resolution can be taken on a film, allowing any pinholes or poor coverage to be clearly identified.

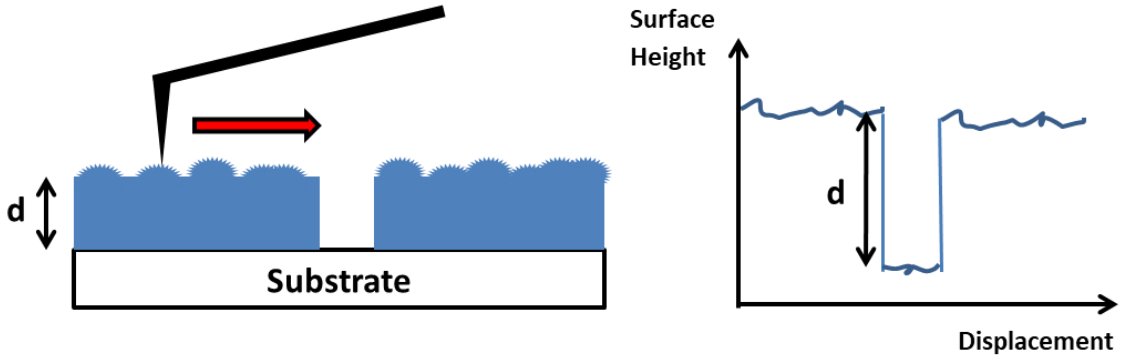

Figure 10 - a) A Dektak surface profilometer measuring a rough thin film. b) A typical data output from this measurement.

A film's thickness and roughness are measured using a Veeco Dektak surface profilometer, which drags a stylus along the surface of a sample and measures the height of the stylus against position using the force on the tip. This gives a one-dimensional scan of the surface profile of the sample, allowing the roughness to be clearly determined from the root mean square (rms) deviation from the mean. The thickness can also be measured using this instrument by drawing a clean scratch in

the film all the way down to the substrate. Thus when the stylus crosses the scratch it will leave a clear step in the surface profile which corresponds to the thickness exactly.

References

1. Mei, Y.C., et al., *High Mobility Field-Effect Transistors with Versatile Processing from a Small-Molecule Organic Semiconductor.* Advanced Materials, 2013. **25**(31): p. 4352-4357.
2. Chen, L.M., et al., *Multi-Source/Component Spray Coating for Polymer Solar Cells.* Acs Nano, 2010. **4**(8): p. 4744-4752.
3. Zhong, Y.F., et al., *Blade-Coated Hybrid Perovskite Solar Cells with Efficiency > 17%: An In Situ Investigation.* Acs Energy Letters, 2018. **3**(5): p. 1078-1085.
4. Lee, W.Y., et al., *High-Mobility Air-Stable Solution-Shear-Processed n-Channel Organic Transistors Based on Core-Chlorinated Naphthalene Diimides.* Advanced Functional Materials, 2011. **21**(21): p. 4173-4181.
5. Shin, D., et al., *Slot-die coating of organic thin films for active-matrix organic light-emitting diode displays.* Thin Solid Films, 2016. **619**: p. 179-186.
6. S.L.Hellstrom. *Basic Models of Spin Coating*. 2007 ; Available from: http://large.stanford.edu/courses/2007/ph210/hellstrom1/.
7. RoarSøndergaard, M., DechanAngmo, Thue T.Larsen-Olsen, Frederik C.Krebs, *Roll-to-roll fabrication of polymer solar cells.* Materials Today, 2012. **15**(1-2): p. 36-49.
8. Ossilla. *Spin Coating: A Guide to Theory and Techniques*. 2018 Available from: https://www.ossila.com/pages/spin-coating.
9. Hannes Klumbies, P.S., Markus Hähnel, Aarti Singh, Uwe Schroeder, Claudia Richter, Thomas Mikolajick, Christoph Hoßbach, Matthias Albert, Johann W. Bartha, Karl Leo, Lars Müller-Meskamp, *Thickness dependent barrier performance of permeation barriers made from atomic layer deposited alumina for organic devices.* Organic Electronics, 2015. **17**: p. 138-143.
10. J.A. Christians, J.S.M., P.V. Kamat, *Best Practices in Perovskite Solar Cell Efficiency Measurements. Avoiding the Error of Making Bad Cells Look Good.* The Journal of Physical Chemistry Letters, 2015. **6**(5): p. 852-857.
11. Ebenhoch, B., *Organic Solar Cells: Novel Materials, Charge Transport, and Plasmonic Studies*, in *School of Physics and Astronomy*. 2015, University of St Andrews.
12. Henry J. Snaith, A.A., James M. Ball, Giles E. Eperon, Tomas Leijtens, Nakita K. Noel, Samuel D. Stranks, Jacob Tse-Wei Wang, Konrad Wojciechowski, and Wei Zhang, *Anomalous Hysteresis in Perovskite Solar Cells.* The Journal of Physical Chemistry Letters, 2014. **5**(9).
13. Meloni, S., et al., *Ionic polarization-induced current-voltage hysteresis in CH3NH3PbX3 perovskite solar cells.* Nature Communications, 2016. **7**.
14. N.C.Greenham, I.D.W.S., G.R.Hayes, R.T.Phillips, Y.A.R.R.Kessener, S.C.Morattic, A.B.Holmes, R.H.Friend, *Measurement of absolute photoluminescence quantum efficiencies in conjugated polymers.* Chemical Physics Letters, 1995. **241**(1-2): p. 89-96.
15. M. Anni, S.L., *Organic Lasers: Fundamentals, Developments, and Applications*. 2018: CRC Press.
16. Tsiminis, G., et al., *Low-threshold organic laser based on an oligofluorene truxene with low optical losses.* Applied Physics Letters, 2009. **94**(24).
17. O. Svelto, D.H., *Principles of Lasers*. 5th ed. 2010: Springer Science.
18. Greenham, N.C., et al., *Measurement of Absolute Photoluminescence Quantum Efficiencies in Conjugated Polymers.* Chemical Physics Letters, 1995. **241**(1-2): p. 89-96.
19. Photonics, H. *Guide to Streak Cameras*. 2008 [cited 2018; Available from: https://www.hamamatsu.com/resources/pdf/sys/SHSS0006E_STREAK.pdf.

20. Iain D.Baikie, A.C.G., JamesSutherland, JamieLaw, *Dual Mode Kelvin Probe: Featuring Ambient Pressure Photoemission Spectroscopy and Contact Potential Difference.* Energy Procedia, 2014. **60**: p. 48-56.
21. Iain D. Baikie, A.G., James Sutherland, Jamie Law, *Near ambient pressure photoemission spectroscopy of metal and semiconductor surfaces.* Physica Status Solidi, 2015. **12**(3): p. 259-262.
22. Iain D.Baikie, A.C.G., JamesSutherland, JamieLaw, *Ambient pressure photoemission spectroscopy of metal surfaces.* Apploed Surface Science, 2014. **323**: p. 45-53.
23. Zisman, W.A., *A new method of measuring contact potential differences in metals.* Review of Scientific Instruments, 1932. **3**(7): p. 367-370.

Chapter 4 - Solar Cells, Energy Levels, and Doping

The initial aim of this PhD was to use advanced techniques such as Kelvin probe and time resolved photoluminescence to study the properties of perovskite solar cells and identify avenues for their improvement. The end goal was to design alternative perovskite structures with superior properties, or without the toxic lead component present in the most common perovskite solar cell materials. The first step on achieving this goal was to create solar cells which could match literature performance, which would then be used as a platform for further improvement. This proved to be much more difficult than first anticipated because perovskite processing methods suffer from very poor reproducibility due to the unusual way the film is formed. When spin-coating with an OSC, the polymer is simply falling out of solution as the solvent dries, meaning a similar quality film will form in a wide range of processing conditions. When spin-coating a perovskite solution, a polycrystalline film is formed by a chemical reaction. The size and shape of the crystals in the film are strongly controlled by the rate and nature of this reaction, and as such the film quality is strongly affected by a wide range of factors such as humidity, temperature, solvent choice, and any contaminants in the atmosphere. The usual outcome of these effects is to cause the perovskite to aggregate into large, micron-sized crystals with very poor surface coverage, and the processing must be extremely well optimised in order to produce a continuous film which is of sufficient quality for device applications.

Initial Work on Solar Cells

Spin-coating in Atmosphere

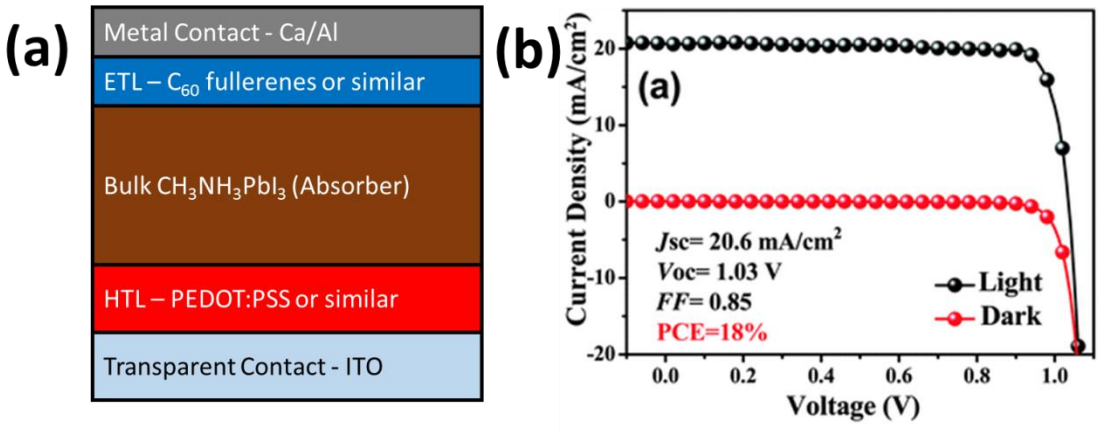

Figure 1 - (a) The structure of an inverted perovskite solar cell. (b) J-V curve of the best solar cell of this design, reported by Gratzel et al [1].

The first attempts at perovskite solar cells used the inverted planar heterojunction (PHJ) structure consisting of Indium tin oxide (ITO) as a bottom contact, polyethylenedioxythiophene:polystyrene sulphonate blend (PEDOT:PSS) as a hole transporter, $CH_3NH_3PbI_3$ as the active layer, phenyl – C_{60} – butyl methyl ester (PCBM) as the electron transporter and calcium/aluminium contacts (see figure 1). PEDOT:PSS was spin-coated from a low conductivity Clevios™ AL4083 solution at 4000 RPM for 60 s, followed by annealing at 110 °C for 10 minutes, resulting in a 40 nm thick film. The PCBM was spin-coated from a 20 $mgml^{-1}$ solution in chlorobenzene at 1000 RPM for 60 s inside a glovebox to give a 50 nm film. The perovskite precursor solution consisted of a 1:1 molar mixture of lead iodide and methylammonium iodide at a total concentration of 600 $mgml^{-1}$ in dimethyl formamide (DMF). Initially, the solution was spin-coated on top of the PEDOT:PSS film in 50% humidity atmosphere at 2000 RPM, before annealing at 100 °C for 30 minutes. However the high humidity caused the perovskite to form films which were completely unsuitable for devices. Figure 2 shows a microscope image of the resulting film, along with a comparison of surface profilometer traces of an OSC film and the resulting perovskite film. It can be clearly seen that the film has aggregated into micron sized crystals with large areas of the surface completely uncovered by perovskite. Devices made with these films were completely shorted, with J-V curves closely resembling resistors with 0% power conversion efficiency (PCE).

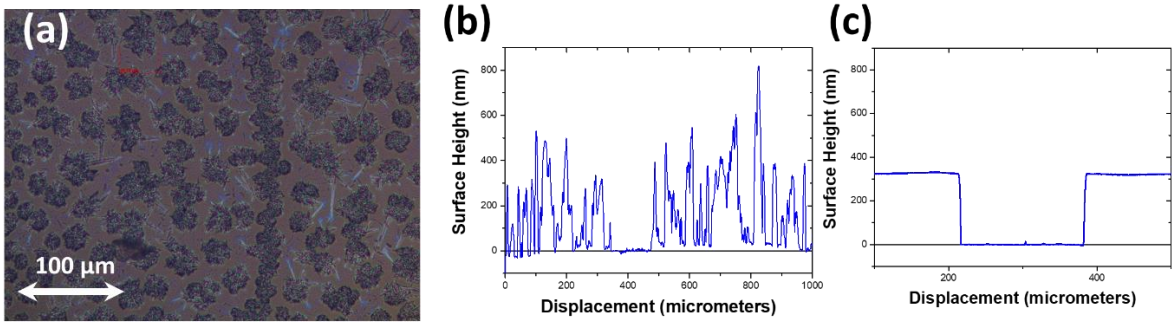

Figure 2 - (a) Optical microscope image of a perovskite film deposited on glass in air – the film has clearly aggregated into large crystals with no continuous film. (b) A dektak surface profile trace of the same film, demonstrating very high roughness and incomplete coverage. (c) A dektak trace of a high quality organic thin film for comparison.

It is a known effect that high humidity is extremely detrimental to the formation of perovskite films [2-4], and hence most groups perform their fabrication in a nitrogen filled glovebox to combat this. However some groups, particularly Yang Yang and co-workers, have found that the presence of oxygen or even a small amount of water can often improve film quality [5]. Hence they perform their fabrication in glove boxes filled with dry air, or at fixed humidity of 30 %. Since we did not have the facilities to perform spin-coating in a controlled humidity environment, all spin-coating of perovskites in the rest of this thesis was done in a nitrogen filled glovebox with <0.1 ppm O_2 and H_2O

unless stated otherwise. Spin-coating the same lead iodide perovskite film in a glovebox resulted in somewhat enhanced film formation, but the overall quality remained very inconsistent, resulting in low quality devices that never exceeded 2 % PCE.

Mixed Halide Method

In an attempt to improve efficiency and reproducibility, we switched to a different perovskite precursor solution known as the mixed halide method. This precursor route, first reported by Stranks et al. [6] consists of a 3:1 mix of methylammonium iodide and lead chloride in DMF at a concentration of 660 mgml^{-1}. The reaction for this route follows the below equation:

$$3CH_3NH_3I_{(s)} + PbCl_{2(s)} \rightarrow CH_3NH_3PbI_{3-x}Cl_{x(s)} + 2CH_3NH_3Cl_{(g)},$$

where x is a very small number. The size difference between I^- and Cl^- ions is so large that they cannot coexist in the lattice, and so any Cl^- ions are rejected and slowly escape the film as CH_3NH_3Cl gas when the film is annealed. The excess CH_3NH_3Cl is not very volatile, and hence the film must be annealed at high temperatures (~150 °C) for long periods (~ 2 hours) in order to completely remove the CH_3NH_3Cl and convert the other precursors into a perovskite film. Despite the longer annealing time, this method was often considered to be a superior method because it formed higher quality perovskite crystals and ultimately achieved higher performance than its pure iodide counterpart. To make films, the solution was spin-coated in a glovebox at 2000 RPM for 60 s, before being left at room temperature for 30 minutes and then annealed for two hours at 100 °C. The films were observed to turn from yellow to orange over the room temperature step and then slowly turned dark brown over the course of the annealing step. Films made from this route had greatly improved quality over films from the pure PbI_2 route, but quality was still poor by comparison to organic semiconductors. Surface profile plots of the sample as seen in figure 3 (a) show a film with complete coverage at a thickness of ~ 500 nm, but with a high roughness of ±100 nm. This high roughness could be explained by looking at microscope images of the resulting films, as can be seen in figure 3(b), which showed a dense network of large pinholes in the film which are formed as the CH_3NH_3Cl gas escapes. As a result of these pinholes, the device efficiency and reproducibility still remained low, with a maximum efficiency of 4.1 % (figure 3c). The key limiting factor on their efficiency was a very low fill factor of 44%, which was unsurprising given that the pinholes can be expected to introduce a high density of shunting pathways into the device, which would strongly reduce the fill factor. Attempts to improve upon these results would need to achieve films with a low density of pinholes.

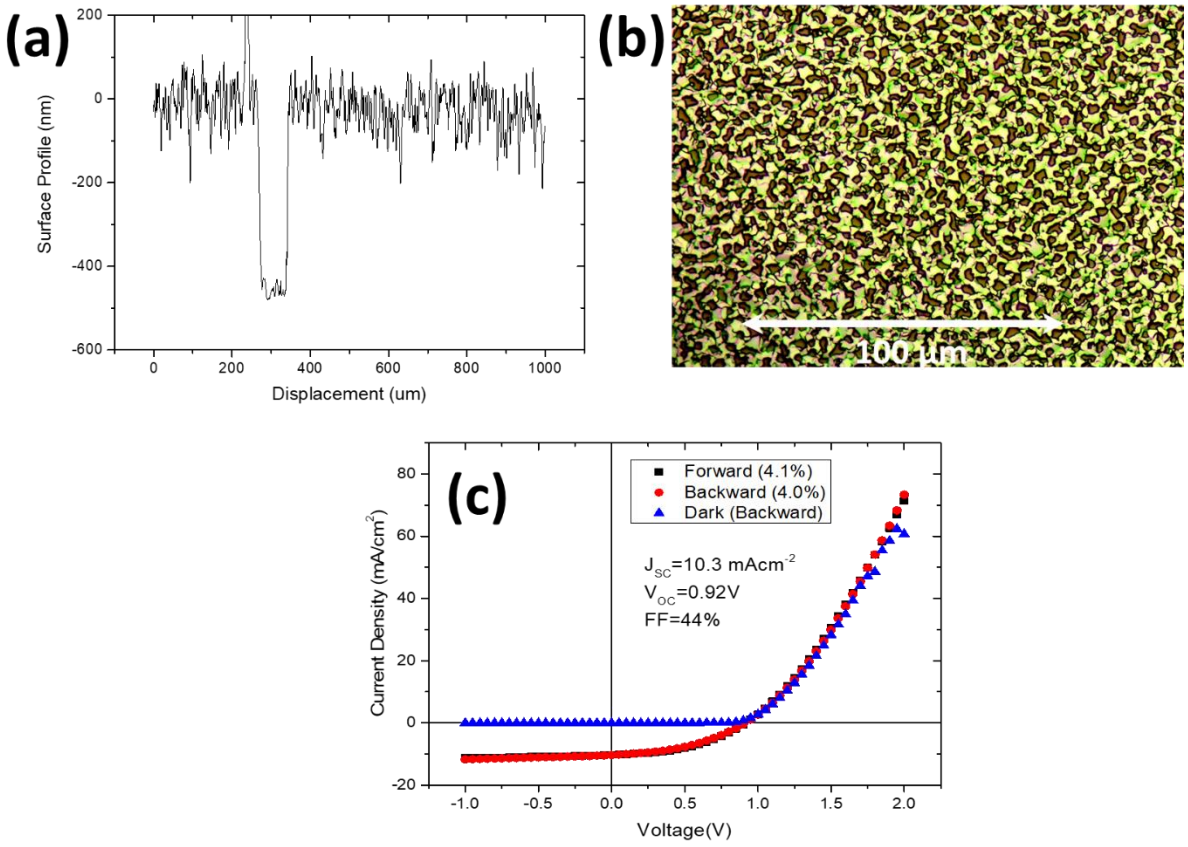

Figure 3 - (a) Surface profile scan of $CH_3NH_3PbI_{3-x}Cl_x$ film, (b) Optical microscope image of the same film, showing a uniform but high density of pinholes. (c) J-V curve of the best cell made using this method the dark spots are pinholes.

Note that a common problem with perovskite solar cells, first reported by Snaith et al, is that they can often have hysteresis in their J-V curves [7]. The J-V curve of a perovskite solar cell scanned from negative to positive bias (forward scan) can often be significantly different to a scan of the same cell from positive to negative bias (reverse scan). This can lead to inaccurate measures of the efficiency. For reasons which are still not entirely clear, the problem is much prevalent in perovskite solar cells with the non-inverted architecture, but even when using the inverted architecture, it is important to show scans in both directions to prove that there is no hysteresis. Hence all J-V curves in this thesis will contain a dark scan, a forward scan, and a reverse scan.

Sequential Deposition

Another attempt to improve the quality and reproducibility of the films was to deposit the film via sequential deposition. This route, first reported by Grätzel and co-workers [8, 9], allows for much easier optimisation of the processing by separating the film formation into two steps. First a pure PbI_2 layer is deposited via spin-coating at 3000 RPM from a 461 $mgml^{-1}$ solution of PbI_2 in DMF. The film is then dried by annealing at 110°C for 10 minutes before it is exposed to solution of MAI dissolved in isopropanol (IPA) to convert it to $CH_3NH_3PbI_3$. This exposure is done either via dip

coating, where the sample is submerged in the solution for 60 s before being removed and rinsed, or via spin-coating. In the spin-coating method the PbI_2 film is set to spin at 2000 RPM, and the IPA is dropped slowly onto the spinning film. The resultant perovskite film is then annealed at 100 °C for 10 minutes in order to complete the conversion.

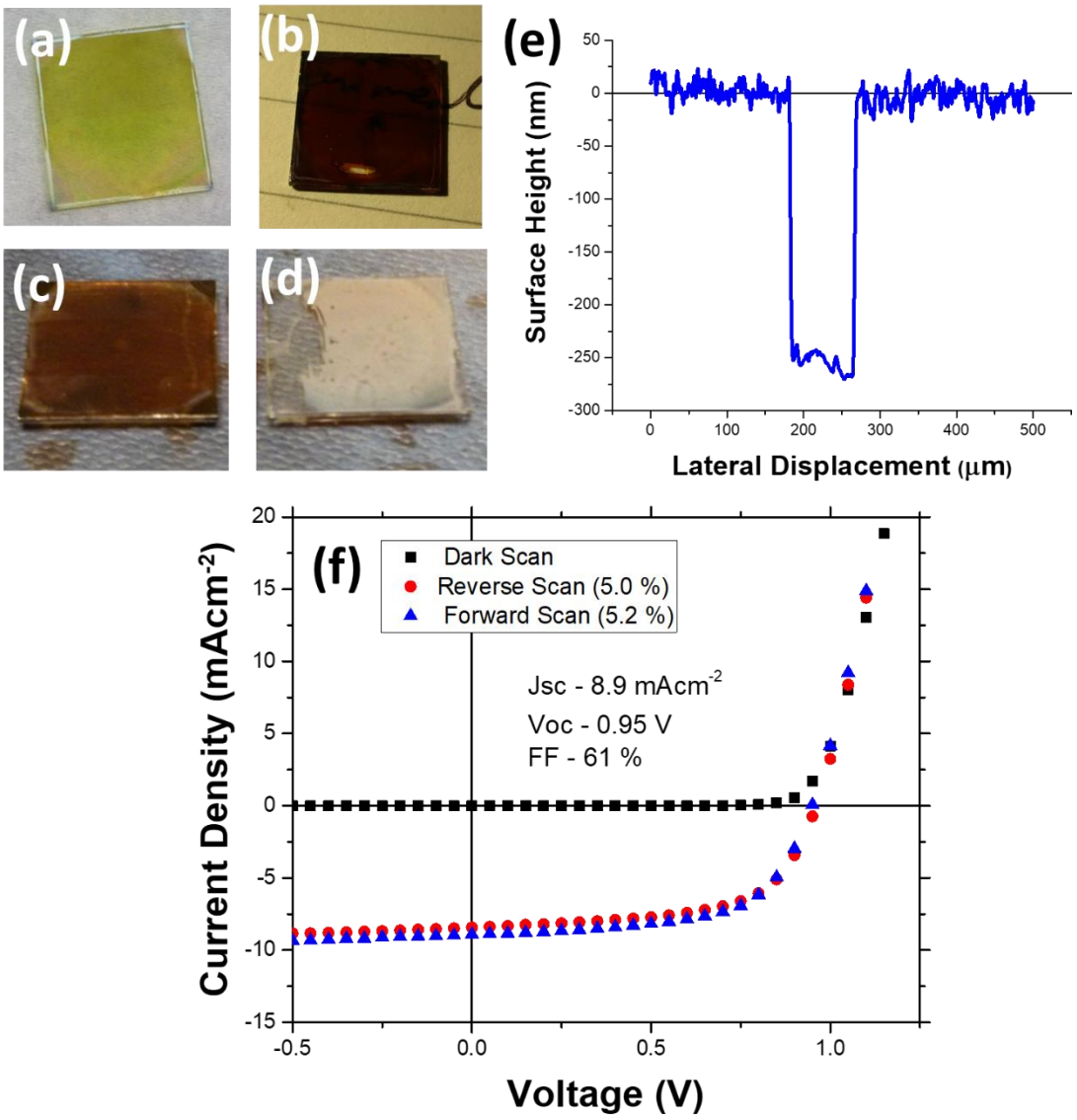

Figure 4 - (a) A high quality PbI_2 film (b) a good quality $CH_3NH_3PbI_3$ film formed using the sequential deposition method (c) and (d) $CH_3NH_3PbI_3$ films which achieved poor conversion. (e) A surface profile of a high quality $CH_3CH_3NH_3PbI_3$ film. (f) The best J-V curve that was achieved using this method.

This method has been reported to give efficiencies as high as 18% using the same device architecture used here [1]. But the recipe for the optimal method varies wildly between publications. The ideal concentration of MAI solution varies from 10 $mgml^{-1}$ to 50 $mgml^{-1}$ [1, 8, 9], and some groups incorporate additives into the PbI_2 layer in order to achieve better film quality [1].

This method is reported to have very good reproducibility and stability, however despite this we were never able to reproduce the results reported in these works. The key problem was that, assuming a good quality film of PbI_2 was produced (i.e. dense crystals with no pinholes), complete conversion of the PbI_2 into $CH_3NH_3PbI_3$ was rarely achieved because the MAI could not penetrate into all of the film for reaction. This could be clearly seen in the "milky" or translucent appearance of the perovskite films, as shown on figure 4. The degree of conversion had large sample-to-sample variation, even on films fabricated under ostensibly identical conditions, and hence the efficiency of solar cells produced by this route could vary by up to an order of magnitude within a single batch. Films which happened to achieve good conversion showed a film thickness of 250 nm with a low roughness of ± 25 nm, and devices from this route had a significantly enhanced fill factor over the mixed halide route (see figure 4). This would indicate that better quality films with fewer shunting pathways were being formed. However, the maximum efficiency was still limited to ~5 % due to all of the cells having a low short circuit current of <9 $mAcm^{-2}$, as opposed to ~20 $mAcm^{-2}$ which is achieved in literature devices. Low current density proved to be a recurring issue among all inverted solar cells produced in this group, and this is discussed in more detail in the next chapter.

Nanocrystal Pinning

One of the key problems with spin-coating perovskites is that there is very little control over how the crystallites form. Dimethyl formamide (DMF) and dimethyl sulphoxide (DMSO), the usual solvents for perovskites, have very high boiling points and as such they evaporate extremely slowly during spin-coating. This results in larger crystals with a strong tendency to form islands with poor surface coverage. A solution to this, first reported by Sang il Seok and coworkers, is to force the crystals to form quickly by washing the sample with a poor solvent (antisolvent) such as toluene shortly after the start of the spin-coating [10-12]. The antisolvent completely displaces the DMF or DMSO and forces the perovskite precursors to crash out of solution, rapidly forming a dense network of smaller crystals with very low roughness and a complete absence of pinholes.

A typical recipe for this method is a to make a 1:1 molar ratio mixture of PbI_2 and MAI at a total concentration of 371 $mgml^{-1}$ (0.6 M) in DMSO. The sample is spin-coated at 3000 RPM for 60 seconds, and the sample is washed with toluene approximately 10 s into the spin-coating step. The film is quickly observed to turn from clear yellow to dark brown. The sample is then annealed at 100 °C for 10 minutes, causing the film to darken further as the reaction completes. This recipe gives extremely reproducible and high-quality perovskite films with a thickness of ~140 nm, which should be more than sufficient to achieve a high efficiency.

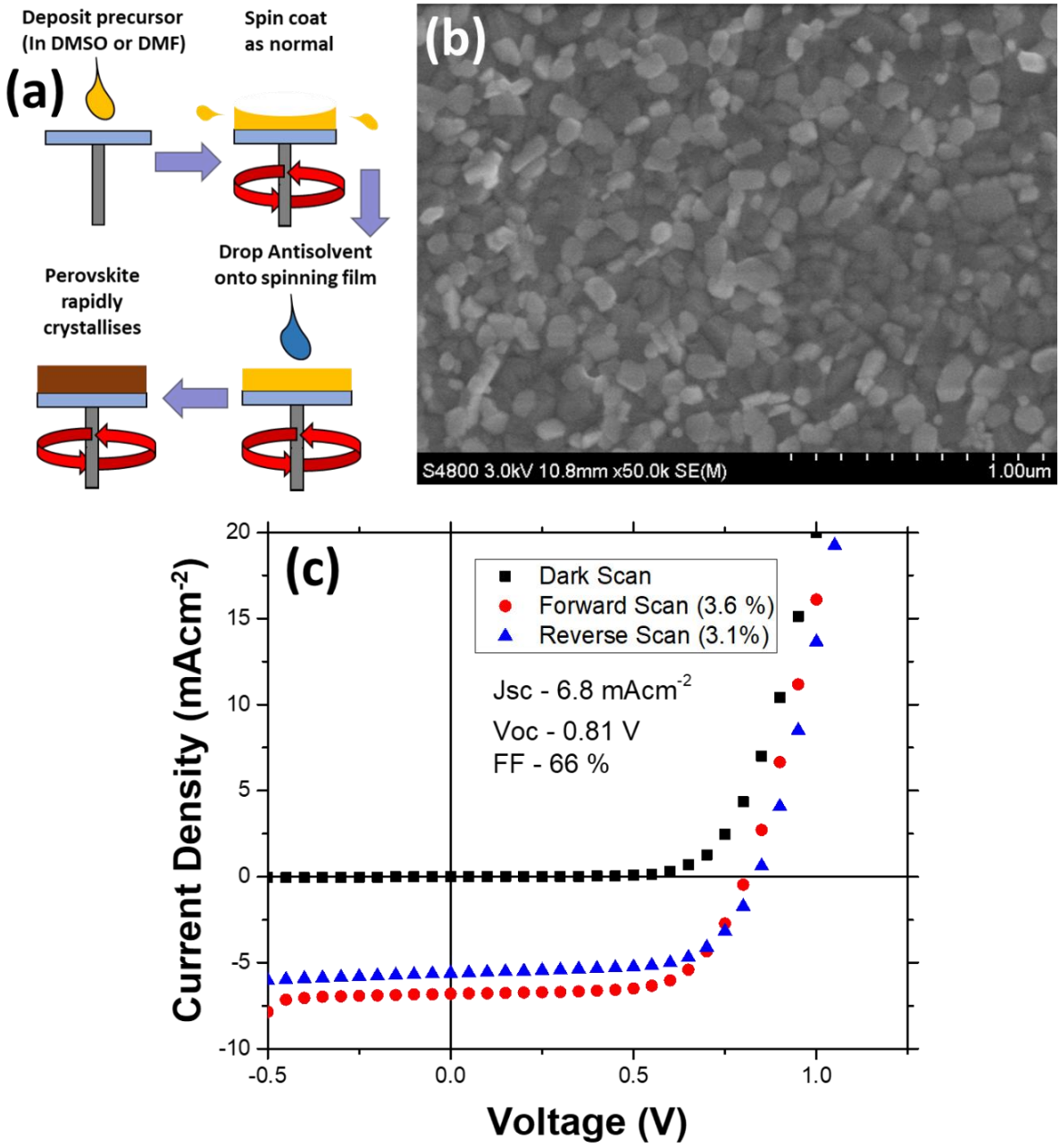

Figure 5- (a) The nanocrystal pinning process (b) A scanning electron microscope image of a $CH_3NH_3PbI_3$ film formed by nanocrystal pinning. Note the dense crystals with no pinholes. (c) J-V curve of the best cell made via this route in St Andrews, note that a small amount of hysteresis is visible in this device

Unfortunately the efficiency of solar cells made from this method remained extremely low, despite the excellent film quality. The best devices achieved only ~3.5 % PCE, as shown on figure 5, and most devices had less than 2% PCE. The reasons for this low efficiency remain unclear, since the quality of this perovskite film is significantly better than the films shown in many papers which report greater than 10 % PCE [3]. The devices we report show a good fill factor, indicating a good quality film with few pinholes or defects, but the efficiency is severely limited by a mediocre voltage and a very low current for this class of cells. A good perovskite solar cell of this type should get a short circuit

current density (Jsc) in the region of 20 $mAcm^{-2}$, but most of the cells produced in our lab have Jsc values less than 5 $mAcm^{-2}$. Both the PCBM and PEDOT layers are known to be of good quality because identical solutions were used in a separate project to produce organic solar cells with high efficiency, so the problem must lie in the perovskite layer. However there is no obvious reason for this perovskite layer to have a problem. Our best hypothesis is that our processing environment leads to differences in the films which are detrimental to performance.

Lead Acetate Route

For some time, the mixed halide route was the most popular method for creating perovskite films. But it had some significant drawbacks in that it required very long annealing times and it formed many pinholes as the CH_3NH_3Cl gas escaped the film. Both of these problems are caused by the fact that the CH_3NH_3Cl takes a long time to escape the film due to its low volatility. The formation of perovskite is strongly inhibited when CH_3NH_3Cl is present in the film, and so it forms extremely slowly as the gas escapes. A solution to this proposed by Zhang et al. [13] was to use lead acetate, which shall be referred to as $Pb(ac)_2$, instead of lead chloride as a precursor. The resulting chemical reaction is as follows

$$Pb(ac)_{2(s)} + 3CH_3NH_3I_{(s)} \rightarrow CH_3NH_3PbI_{3(s)} + 2CH_3NH_3(ac)_{(g)}$$

This is an identical reaction to the chloride route, with the exception that the by product is methylammonium acetate (MA(ac)) instead of methylammonium chloride. MA(ac) is much more volatile than methylammonium chloride, and as such it completely escapes the film after just 5 minutes of annealing at 100 °C. This means that the perovskite film can form much more rapidly and does not have as much time to form pinholes as in the chloride route. This allows the acetate route to produce films of extremely high quality with a very small number of pinholes, a low surface roughness, and a low sample – to – sample variation.

To learn the details of this method, we made a visit to Prof. Snaith's laboratory in Oxford, where Dr Zhang demonstrated the technique to us on the non-inverted solar cell structure (shown in figure 6). The non-inverted structure uses titanium dioxide (TiO_2) as an electron transporter on the base of the cell, and 2,2',7,7'-tetrakis[N,N-di(4-methoxyphenyl)amino]-9,9'-spirobifluorene (Spiro-OMeTAD) as a hole transporter. The top contact was made from thermally evaporated silver, while the bottom contact was made from fluorine doped tin oxide (FTO). FTO is used instead of ITO because the TiO_2 layer requires an annealing step of 500 °C in its fabrication, which would cause the ITO layer to crack and lose its conductivity. FTO is more expensive than ITO, but it can withstand the 500 °C annealing step with little loss in conductivity.

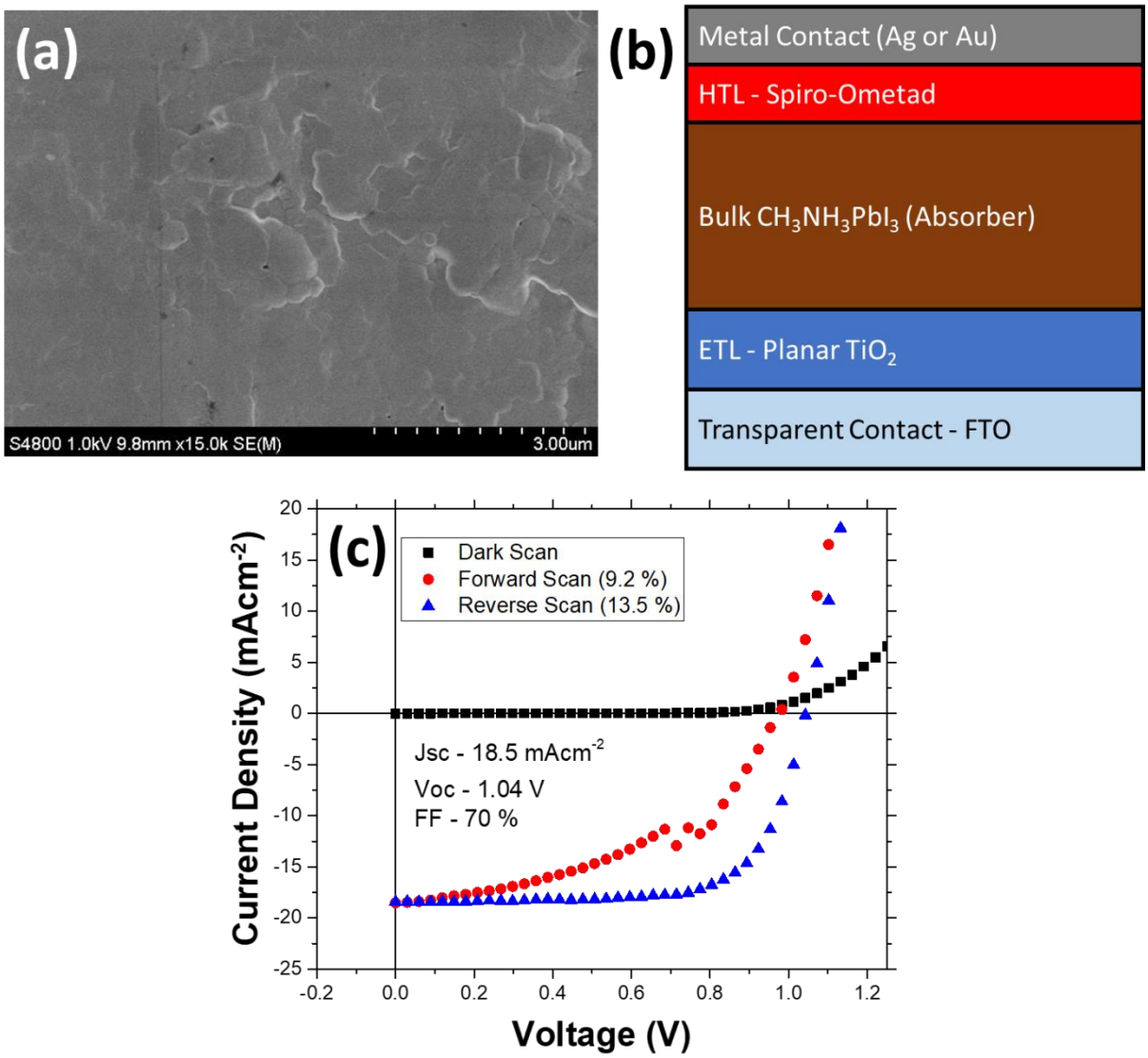

Figure 6- (a) A scanning electron microscopy image of a $CH_3NH_3PbI_3$ film formed by the lead acetate route. Note the smooth landscape with only very small pinholes. (b) The structure of the non - inverted cell. (c) J-V curve of the best solar cell of this structure made in oxford.

The full recipe for the process is as follows. Patterned FTO substrates from XinYan Technology Ltd are cleaned, and a TiO_2 precursor solution was spin-coated on the sample in air at 1500 RPM. The precursor solution was made from a mildly acidic 1:10 volume ratio solution of titanium isopropoxide and ethanol, with the acidity being provided by the addition of a small amount of ethanoic acid. The TiO_2 layer was then completed by annealing the samples at 500 °C for 30 minutes and then leaving them to cool down overnight. The $CH_3NH_3PbI_3$ precursor solution was made from methylammonium iodide and lead acetate at a 3:1 molar ratio dissolved in DMF at a total concentration of 400 mg ml^{-1}. It had also been found that the addition of a small amount (3 µl per ml) of hypophosphoric acid to the solution provided enhanced performance [14], which was quickly dissolved by 5 minutes of vigorous shaking. To form the perovskite films, the solution was spin-

coated at 2000 RPM for 45 s in a nitrogen filled glovebox, before being left at room temperature for 10 minutes then annealed at 100 °C for 5 minutes. The resultant perovskite layer was 150 nm thick, which is slightly thinner than optimal but still allows for the absorption of ~90% incoming light. For the HTL, Spiro-OMeTAD was deposited from an 80 mg ml^{-1} solution in chlorobenzene containing additives of 11.6 µl per ml tert-butyl pyridine and 33.2 µl per ml of 0.61 M bis(trifluoromethane) sulfonimide lithium (Li-TFSI) solution in acetonitrile. These additives enhance the solubility and conductivity of the Spiro-OMeTAD layer. Finally, silver contacts were evaporated on top of the sample to complete the solar cell.

Using this method in Prof. Snaith's lab, we were able to reproduce the high efficiencies reported, with a best efficiency of 13 % PCE and an average of ~ 10 % PCE, as shown in figure 6. However, on reproducing this method in St Andrews the efficiency dropped significantly to an average of ~6% with a best efficiency of 10 %, as shown in figure 7(a). It is unclear what the cause for this drop in efficiency could be, given that the materials used for the Oxford batch were from the same batch as what is used in St Andrews, but it seems likely that our perovskite films form differently in the environment we have available in St Andrews.

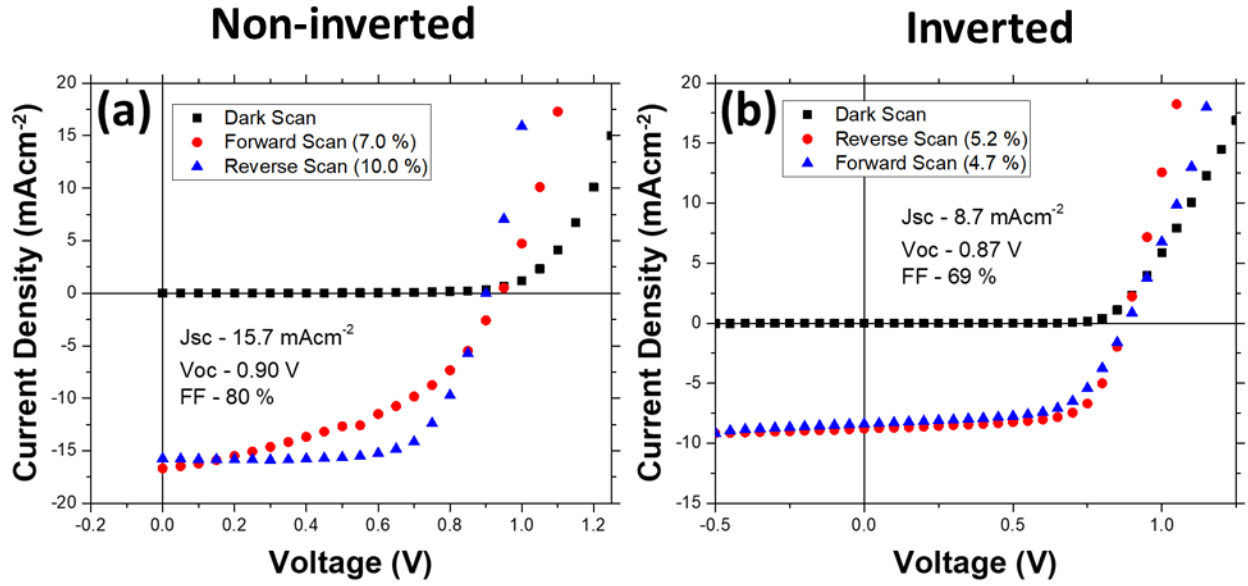

Figure 7 - (a) Best non-inverted $CH_3NH_3PbI_3$ cell made in St Andrews, (b) - Best inverted solar cell made with the acetate route.

This lower efficiency became even worse when the lead acetate route was attempted with the inverted PEDOT:PSS/$CH_3NH_3PbI_3$/PCBM structure, with a wildly varying efficiency which would vary between 2 and 5% PCE, once again with a good fill factor but the main limiting parameter being a poor Jsc. This leads to the conclusion that the inverted structure is significantly more difficult to

optimise than the non-inverted structure, and so the non-inverted structure was chosen for further study with Kelvin probe in the next section.

A final point to note, which was discovered near the end of this PhD, is that in many of the routes described here the purity of the lead iodide precursor is a crucial factor. We observed that "Perovskite grade" lead iodide, which is extra dry and has undergone an extra purification step over standard lead iodide, has dramatically improved solubility over its standard counterpart. This is in spite of the fact that both classes of lead iodide are rated to the same purity standard of 99.999 %. The precise reasons for this are currently poorly understood -it is difficult to see how such a small impurity could have such a profound impact on a material's solubility, and dryness should not be a factor since it is common practice to include a small amount of water as an additive in perovskite solutions [1]. It will be discussed in later chapters that the performance of light emitting perovskites are strongly enhanced if ultra-pure precursors are used, but preliminary measurements performed on solar cells by Natalie Mica showed little to no improvement over the use of standard lead iodide, indicating that the solubility of the lead iodide was likely not the main factor contributing to our low solar cell performance.

Energy Levels in a Perovskite Solar Cell

The non-inverted structure is by far the most commonly used device architecture in perovskite solar cells, and as such it is important to get a detailed map of the energy levels in this structure in order to identify any weaknesses or avenues for improvement in the structure. As mentioned before, the correct alignment of energy levels is crucial for a device to achieve the best performance possible, as the structure must have minimum barriers for the desired charge transport whilst also not wasting excessive energy as charges fall to lower energy levels. This is already a subject of intense interest, and there are many papers which try to map the HOMO, LUMO, and Fermi levels in a perovskite system [15-18]. However none of these are able to get a reliable and complete map from a single instrument. The key parameters to note are the HOMO and LUMO level of the perovskite active layer, the HOMO level of the Spiro-OMeTAD layer, and the LUMO level of the TiO_2 Layer. It is also important to know the position of the Fermi levels in each of these materials, as well as how they change when the sample is illuminated with light. Our KP technology APS03 setup allowed us to study almost all of these parameters in one instrument under real-world conditions, making it an ideal platform for an in-depth study into the workings of the solar cell.

Measuring HOMO Levels

Accurate knowledge of the HOMO and LUMO levels in devices has been a crucial factor in the construction of organic optoelectronic devices for many years, and thus far most measurements of this parameter are done using cyclic voltammetry (CV) in solution. CV is a simple and widely used method, but it is known to have several significant drawbacks. First, there is a significant margin of error in the measurement due the measurement having a strong hysteresis with most materials. More importantly, CV is usually done on materials in solution rather than solid state. It is well known that the HOMO levels of a material in solution can be significantly different to its HOMO in solid state [19], and so it is a major concern that incorrect HOMO levels are being quoted when building devices. Air photoemission, as described in chapter 3, provides a quick and easy way of measuring a film in its natural state whilst also being much more reliable than CV. The LUMO of the material can then be determined using the material's bandgap which, in a semiconductor such as $CH_3NH_3PbI_3$, is very easily measured from its absorption spectrum.

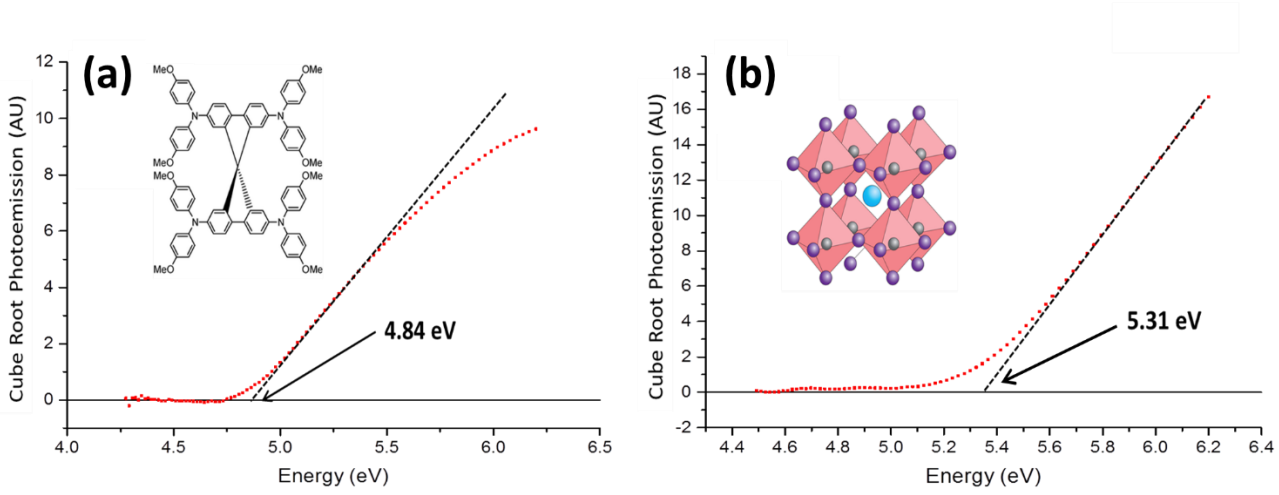

Figure 8 - Air photoemission spectra for (a) Spiro-OMeTAD, and (b) $CH_3NH_3PbI_3$ deposited via the acetate route. Figures taken from our paper [20].

Figure 8 shows plots of air photoemission vs photon energy for bare films of Spiro-Ometad (with all of its usual dopants) and $CH_3NH_3PbI_3$ (fabricated via the acetate route) deposited on FTO glass. The data is plotted on a cube root scale to turn the curves into straight lines, which are then extrapolated to the x axis to give a value for the HOMO level. The data gives a HOMO level of −5.31 ± 0.05 eV for $CH_3NH_3PbI_3$, and −4.84 ± 0.1 eV for Spiro-OMeTAD. No photoemission spectrum from TiO_2 could be obtained, as its known HOMO of −7.4 eV [21] is deeper than our UV source was able to excite.

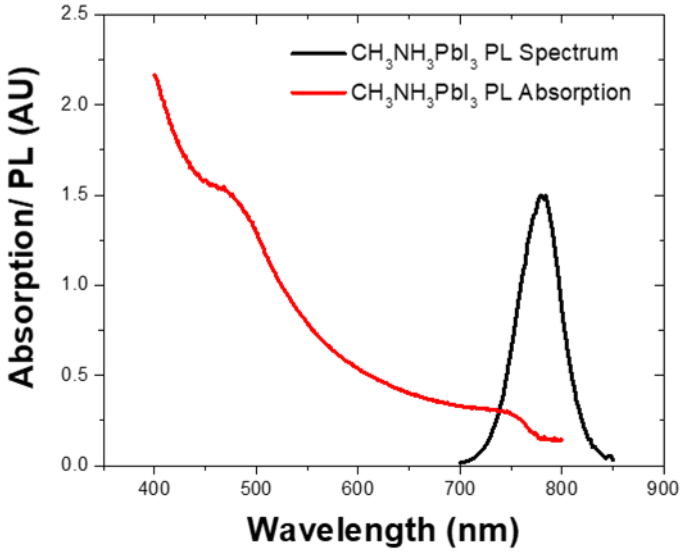

Figure 9 – Absorption and normalised photoluminescence spectrum of $CH_3NH_3PbI_3$

Our measurement of $CH_3NH_3PbI_3$ agrees closely with results obtained previously via ultra-high vacuum UV photoemission spectroscopy (UPS), which give a HOMO level between -5.4 eV [22] and -5.3 eV [23]. This is encouraging as it shows that the HOMO level of perovskite is not significantly affected by measurement under ambient pressure, and even with the possibility that there is a small amount of degradation on the surface of the sample we can conclude that it does not directly affect the HOMO of the bulk system. Of more interest is our measurement of Spiro-OMeTAD, which differs significantly from literature results from CV. Solution CV measurements on Spiro-OMeTAD report values for the HOMO level between -5.0 eV [24] and -5.2 eV [25, 26], leaving a large discrepancy with our value of -4.84 eV. Our thin film measurement is much more relevant to device operation, and leads to the conclusion that the HOMO of Spiro-OMeTAD may not be as well matched to the HOMO of $CH_3NH_3PbI_3$ as previously thought. It can therefore be concluded that there may be scope for a new material to achieve even better performance through better matching of the energy levels by deepening its HOMO without altering its other excellent properties.

By combining these measurements with bandgap measurements of $CH_3NH_3PbI_3$, and literature measurements on TiO_2, we can construct a full diagram of the energy levels in the solar cell. The LUMO of $CH_3NH_3PbI_3$ can be obtained from adding its bandgap energy to the HOMO level, and the LUMO level of TiO_2 has been widely studied in previous literature [21]. Measuring the absorption spectrum of $CH_3NH_3PbI_3$ gives a clear absorption onset of 790 nm, corresponding to a bandgap of 1.6 eV and a LUMO of 3.7 eV, which is offset from the LUMO of TiO_2 (4.1 eV) by roughly the same amount that Spiro-OMeTAD is offset from the HOMO. Note that obtaining the LUMO level via the bandgap is a viable strategy on $CH_3NH_3PbI_3$ because it has a very clearly defined absorption edge,

and only a small shift between the PL peak and the absorption edge. In many other materials (particularly OSCs), the bandgap is not as clearly defined and so it cannot be used to accurately determine the LUMO level.

Measuring Fermi Levels – Single Layers

To investigate the position of the Fermi levels in the system, films of each layer deposited directly onto FTO were measured using the APS03 setup in Kelvin probe contact potential difference (CPD) configuration. First the work function of the tip was calibrated against a gold reference sample and found to have a value of -4.87 eV. All measurements in CPD are relative to the work function of the measurement tip, and gave values of +100 mV, +229 mV, and −284 mV for Spiro-OMeTAD, $CH_3NH_3PbI_3$, and TiO_2 respectively. This corresponds to Fermi Levels of -4.97 eV, -5.10 eV, and -4.59 eV respectively. For Spiro-OMeTAD, this shows that the Fermi level lies almost exactly on top of the HOMO level, indicating strong p doping as we would expect for a good hole transporter. This result also agrees closely with literature reports from X-Ray photoelectron spectroscopy, which show that the Fermi level is strongly shifted towards the HOMO by the presence of the Li-TFSI salt which is added to Spiro-OMeTAD. Thus giving it its hole transporting properties.

Material	**HOMO Level (eV)**	**LUMO Level (eV)**	**Stable Fermi Level (eV)**
FTO (Cleaned)	-4.9	N/A	-4.9
TiO_2 (on FTO)	-7.4	-4.1	-4.6
$CH_3NH_3PbI_3$ (on FTO)	-5.3	-3.7	-5.1
$CH_3NH_3PbI_3$ (on TiO_2)	-5.3	-3.7	-4.7
Spiro-OMeTAD (on FTO)	-4.9	-1.9	-4.9
Spiro (on $CH_3NH_3PbI_3$)	-4.9	-1.9	-4.9

Table 1 – Summary of all HOMO, LUMO, and Fermi levels as measured by CPD and air photoemission. HOMO data for TiO_2 is taken from Liu et al. [21]

The Fermi level of TiO_2 (−4.6 eV) is close to the known LUMO of −4.1 eV, indicating a mild n doping which is unsurprising given that it is an electron transporter, while $CH_3NH_3PbI_3$ has its Fermi level at −5.10 eV. This deviates significantly from the bandgap centre of −4.65 eV and indicates that it is mildly p doped. This is of interest because the Fermi level of $CH_3NH_3PbI_3$ has been found to vary

strongly with the choice of processing route, and it has been previously found that $CH_3NH_3PbI_3$ films made with lead chloride have fairly strong n doping with a Fermi level of around -4.2 eV [27]. The reason the Fermi level is so variable with preparation route is due to the inherent ambipolar nature of $CH_3NH_3PbI_3$. $CH_3NH_3PbI_3$ can easily conduct both electrons and holes, and which carrier is in excess tends to be determined by the dominant vacancy in the crystal. It has been shown that vacancies of – $CH_3NH_3^+$ and Pb^{2+} tend to lead to p doping while I^- vacancies result in n doping [28, 29]. The lead acetate route uses a 3:1 ratio of methylammonium iodide to lead acetate, and as such the methylammonium and Iodide ions are likely to be the ones in excess. Hence Pb^{2+} vacancies are likely to dominate and thus perovskites from this route will tend to be p doped, as we observe here. The addition of the hypophosphorous acid to the precursor solution was also shown by Zhang et al to help reduce the presence of metallic lead in the material [14], as well as to passivate trap states which normally form at the grain boundaries. This could also have an impact on the work function, so it is unsurprising that the observed Fermi level is significantly different to that from other routes.

Multilayer KP – Fermi level pinning

One factor to be aware of when measuring the work function of the materials is that the energy levels will bend to meet the layer below them, creating a depletion region in the material where the work function will differ from that of the bulk material. The size of this depletion region will vary with carrier concentration, and in a thin film of material with a low carrier concentration the depletion region can extend all the way to the surface of the film. As a result of this, the apparent work function of the top layer will be "pulled" towards the work function of the layer below [30]. To investigate this effect in the solar cell structure, two more samples of FTO/TiO_2/$CH_3NH_3PbI_3$ and FTO/$CH_3NH_3PbI_3$/Spiro-OMeTAD were measured with the Kelvin probe setup. Putting perovskite on TiO_2 causes the observed Fermi level to shift from -5.10 eV on bare FTO, to -4.65 eV on TiO_2 – a change of roughly 0.45 eV. Since the Kelvin probe setup only measures work function on the surface, this would indicate that the depletion region of the TiO_2/$CH_3NH_3PbI_3$ interface has extended all the way to the surface of the perovskite and has "pulled" the work function of the perovskite towards that of the TiO_2. Therefore we can conclude that the TiO_2 forms an excellent interface with the perovskite layer, and that the depletion region from this contact will be at least 190 nm thick (i.e. greater than the thickness of the sample). An interesting experiment to get an exact measure of the thickness of the depletion region would be to perform this experiment on varying thicknesses of $CH_3NH_3PbI_3$, with the maximum depletion layer thickness where the work function returns to that of the isolated $CH_3NH_3PbI_3$. This was not possible in this case because the lead acetate fabrication route cannot be used to make films thicker than 190 nm. But a separate study by Jiang et al using Kelvin

probe force microscopy found the depletion region to be roughly 300 nm thick (using a different depostition method to achieve a thicker film), which is consistent with what we observe here. [31]

Similar, but less pronounced results are observed in the FTO/$CH_3NH_3PbI_3$/Spiro-OMeTAD structure in that the Fermi level of the spiro-OMeTAD is "pulled" towards the Fermi level of the $CH_3NH_3PbI_3$ by approximately 55 mV (as opposed to a shift of ~400 mV in the previous case). This indicates that a depletion region is still forming, but it is much narrower than in the former case because the carrier density in spiro-OMeTAD is much higher. From these results it becomes clear that it is important to check that, when measuring materials with very low carrier concentrations, the Fermi level of the sample is not being strongly affected by the material below it. Indeed, Tengstedt et al observed that, due to their low carrier concentration, the Fermi level of certain conjugated polymers would never be deeper than the work function of their conducting substrate because the band bending effects would "pin" the Fermi level to the energy of the substrate [30]. The samples measured in this thesis do not go to this extreme due to their high conductivity and carrier density, but it is still an important concern to take note of.

Surface Photovoltage

Thus far all measurements of the work function/Fermi level have been performed under dark conditions, but it is also of great interest to see how this changes when samples are illuminated. As a first test for this, a stack of FTO/TiO_2/$CH_3NH_3PbI_3$/Spiro-OMeTAD – essentially a complete solar cell without a top contact – was fabricated and its work function was repeatedly measured over time. Once it was certain that the work function was stable, the sample was illuminated with intense white light from a quartz tungsten halogen (QTH) lamp source. Once illuminated, the work function of the sample dropped rapidly from -5.05 eV in the dark to -3.98 eV under illumination – a change of more than 1050 mV. The work function remained very stable under this condition, but would rapidly rise back towards its initial value once the illumination was switched off. There is a long tail of about 10 s duration in the final part of the recovery which we hypothesise is due to the slow removal of trapped charges on the surface of the device. In a single sample this whole process was found to be completely reversible and repeatable, with the work function reaching identical values every time the illumination was repeated. Repeating this measurement on 5 separately made samples yielded similar results in each case, with the key difference being that the absolute magnitude of the work function shift had a variation in the same way as the open circuit voltage of a solar cell. Low quality samples would experience a shift as low as 750 mV, and only the best samples would achieve the maximum of 1050 mV.

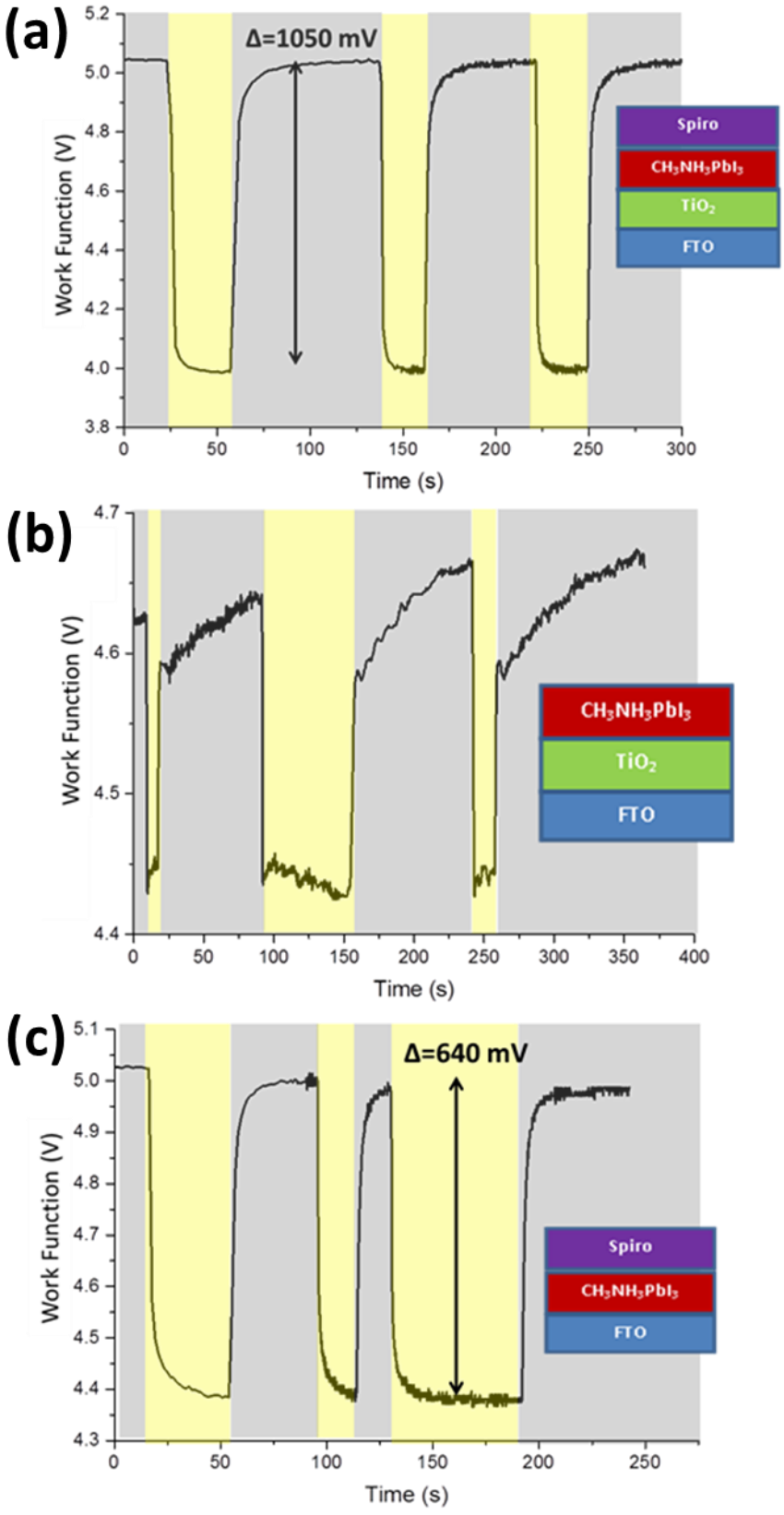

Figure 10 - Measured work function vs time for (a) a full solar cell stack, (b) a stack with the Spiro - OMeTAD layer removed, (c) a stack with the TiO_2 layer removed. Measurements under illumination are highlighted yellow, and measurements in dark are grey. Figures taken from our paper [20].

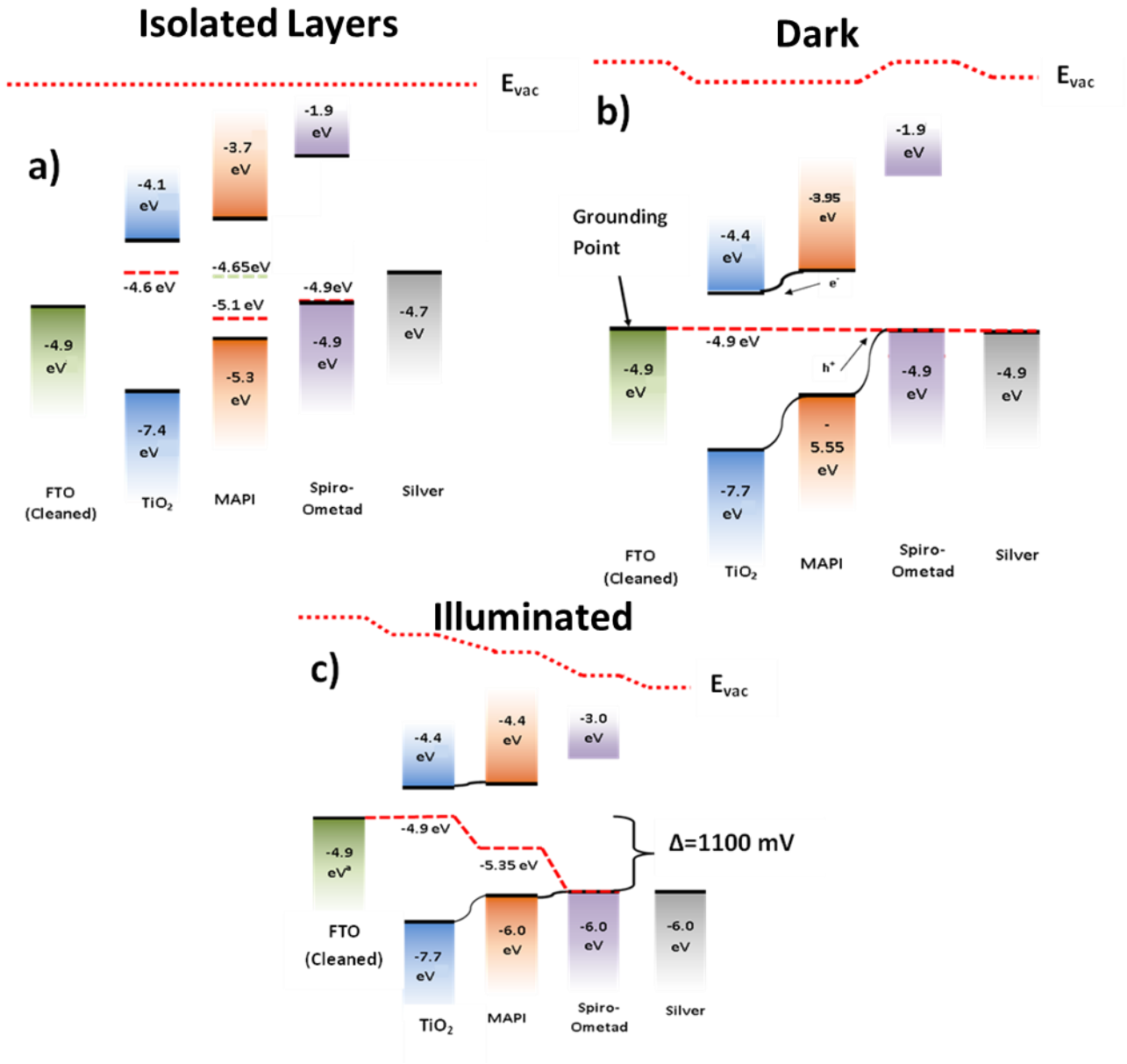

Figure 11- (a) A summary energy level diagram of the perovskite solar cell if each layer is considered in isolation. Fermi levels measured in isolation are shown with dashed red lines, while the green dashed line shows the Fermi level for $CH_3NH_3PbI_3$ when on a TiO_2 substrate. (b) Band bending diagram for the solar cell under dark conditions –the Fermi levels all align to be equal, causing shifts in the HOMO, LUMO, and vacuum levels to accommodate this. The resulting offset between LUMO levels causes a potential gradient for electrons to flow to the TiO_2, and the offset in HOMO levels create a gradient for holes to flow to the Spiro-Ometad. (c) Band bending diagram for the cell under illumination – the accumulation of charge will cause the Fermi levels to shift until HOMO and LUMO offsets are completely flattened and the potential gradient for the flow of electrons and holes is removed. This occurs after a Fermi Level shift of 1100 mV. Figures taken from our paper [20].

It seems reasonably clear that this photovoltage is caused by charges being separated in the stack and accumulating at opposite ends of the sample, which essentially leads to the stack mimicking the open circuit voltage of the cell. Measurements of a single perovskite layer on FTO show a light

response magnitude of less than 150 mV, while the transporting layers such as Spiro-OMeTAD have very slow and weak responses that are more likely due to heating effects than the motion of charge. Hence it can be can concluded that the large shift observed in the solar cell stack only happens as a result of all three layers working together to separate the charge, and so it is of interest to see how the magnitude of this shift changes when certain layers are removed from the full solar cell structure. Figure 10 shows scans on stacks of FTO/TiO_2/$CH_3NH_3PbI_3$ and FTO/$CH_3NH_3PbI_3$/Spiro-OMeTAD (TiO_2 removed) under pulses of illumination. It can be seen that in the sample without TiO_2 the work function shifts by ~640 mV, while the sample without Spiro-OMeTAD has a shift of ~200 mV. Note that sample without Spiro-OMeTAD has a much slower recovery time than the other stacks with a spiro-OMeTAD capping layer, and also has a slight increase in its dark work function after every light pulse – indicating a small amount of degradation from the intense heat of the excitation lamp. This shows that the Spiro-OMeTAD layer is playing an important role in both allowing the swift removal of charge from trap states in the perovskite, whilst also providing a capping layer to protect it from degradation by the lamp source. It is important to emphasise that this degradation was only observed under the accelerating conditions of the intense light illumination, and that the bare $CH_3NH_3PbI_3$ showed no evidence of degradation under dark Kelvin probe or air photoemission measurements.

The measured photovoltage of these stacks can be predicted using the energy level diagrams of the solar cell. Figure 11a shows a summarised energy level diagram of the full solar cell using the isolated energy values measured in this work, while figure 11(b) shows the equilibrium energy levels when electrically connected. Without illumination there is no potential difference across the sample, meaning that the energy levels in the stack will bend in order to keep the Fermi level constant across the entire sample. Since the FTO layer is grounded, its Fermi level cannot change and so the Fermi levels of each layer are “pinned” to that of the FTO, resulting in the bands bending to form the energy level diagram on figure 11b. This places the effective HOMO level $CH_3NH_3PbI_3$ to be much deeper than that of Spiro-OMeTAD, and so holes generated in the $CH_3NH_3PbI_3$ will experience a strong potential gradient to move to the Spiro-OMeTAD. The inverse is true for electrons in the LUMO at the interface between $CH_3NH_3PbI_3$ and TiO_2, meaning that under illumination the charges will be separated by this internal potential gradient and accumulate at opposite ends of the cell. This accumulation of charge is what builds up the observed photovoltage, and in an ideal world it will continue to build up until the electric field induced by the charge build up exactly cancels out the potential gradient and flattens the bands – as is shown in figure 11(c). Looking at figure 11c, the bands will flatten completely once the Fermi level of the TiO_2 is shifted by 450 mV, and the Fermi level of the Spiro-OMeTAD is shifted by 650 mV. This leads to a theoretical maximum open circuit

voltage for the solar cell of 1100 mV. In a real sample there will be other competing factors such as recombination losses which will prevent one from reaching this point, but our best samples and the best cells reported in the literature can come remarkably close to this value at 1050 and 1070 mV respectively. This model is further backed up by the fact that the photovoltage of our FTO/$CH_3NH_3PbI_3$/Spiro-OMeTAD stack has a magnitude of 640 mV, which closely matches the predicted open circuit voltage if just the interface between the Spiro-OMeTAD and the $CH_3NH_3PbI_3$ is considered. This indicates that this model can closely reproduce experiment in ideal cases with no degradation or trap states to provide competing loss mechanisms.

Perovskite Doping

Bismuth Doping

One of the key aims of us studying perovskite solar cells in detail was to find an alternative to the toxic lead component of $CH_3NH_3PbI_3$. An attractive candidate for this purpose is bismuth, which is cheap, non-toxic, and has a similar electronic orbital structure to lead. However it has a key difference from lead in that it forms a 3+ ion instead of a 2+ ion, meaning that a simple substitution is not possible because it does not conserve charge balance. This is not a complete disaster as there is no reason to conclude that bismuth could not form a similar structure to $CH_3NH_3PbI_3$ by using slightly different partner ions. But as a first feasibility test we aimed to dope the normal $CH_3NH_3PbI_3$ structure with a small amount of bismuth ions to see how the presence of bismuth affects the performance. The excess charge of the Bi^{3+} ion will mean that, for every Bi^{3+} ion in the place of a Pb^{2+} ion, one $CH_3NH_3^+$ ion will need to be removed from the lattice, leading to the presence of vacancies in the A site of the structure. Films of bismuth doped perovskite were fabricated using identical methods for fabricating $CH_3NH_3PbI_3$, with the exception that the stoichiometry of the solutions was modified to exactly give perovskite of the formula $(CH_3NH_3)_{1-x}Pb_{1-x}Bi_xI_3$, where x is the doping fraction.

Bismuth proved to have similar levels of solubility to lead, allowing solutions to be easily made and spin-coated in the same way as standard perovskites. But even a small bismuth component was found to turn the precursor solutions from a clear yellow colour to a dark red, indicating that the bismuth component was very strongly absorbing in the green and blue parts of the spectrum. Films made from these precursors maintained their dark red colour, and X-Ray diffraction measurements performed by Dr Julia Payne from the department of chemistry in St Andrews showed that the material would keep its perovskite structure up to a doping level of 30 %.

Despite these promising characteristics, further measurements showed that the presence of even a small amount of bismuth was highly detrimental to the performance of the perovskite. Absorption measurements of films taken with the CARY absorption spectrometer show that the absorption edge at 780 nm, corresponding to the strong direct bandgap of $CH_3NH_3PbI_3$, completely disappears when even a small amount of bismuth is incorporated into the structure. As can be seen in figure 12 (a), the absorption edge is replaced by a linearly increasing absorbance, indicative of a strong scattering component. There is also a broad absorbance peak around 480 nm. The size of this peak increases with increasing bismuth concentration, indicating that it is either due to absorption from the Bi^{3+} ion, or some impact of the vacancies. But even if this material were to have good semiconducting properties it is now useless as a solar cell material because the sample only usefully absorbs at wavelengths shorter than 500 nm, which will result in a very low efficiency because only a small fraction of the energy from the sun is in the spectral region.

The issues become worse when one looks at the photoluminescence properties – pure $CH_3NH_3PbI_3$ has a strong photoluminescence (PL) peak at 790 nm with a narrow full width half maximum of roughly 30 nm, indicating it has a low density of trap and defect states. However it was found that even a small amount of bismuth would quench the PL completely. This meant that no spectrum could be measured with any of our instruments, and indicated that bismuth was unlikely to perform well as a solar cell material.

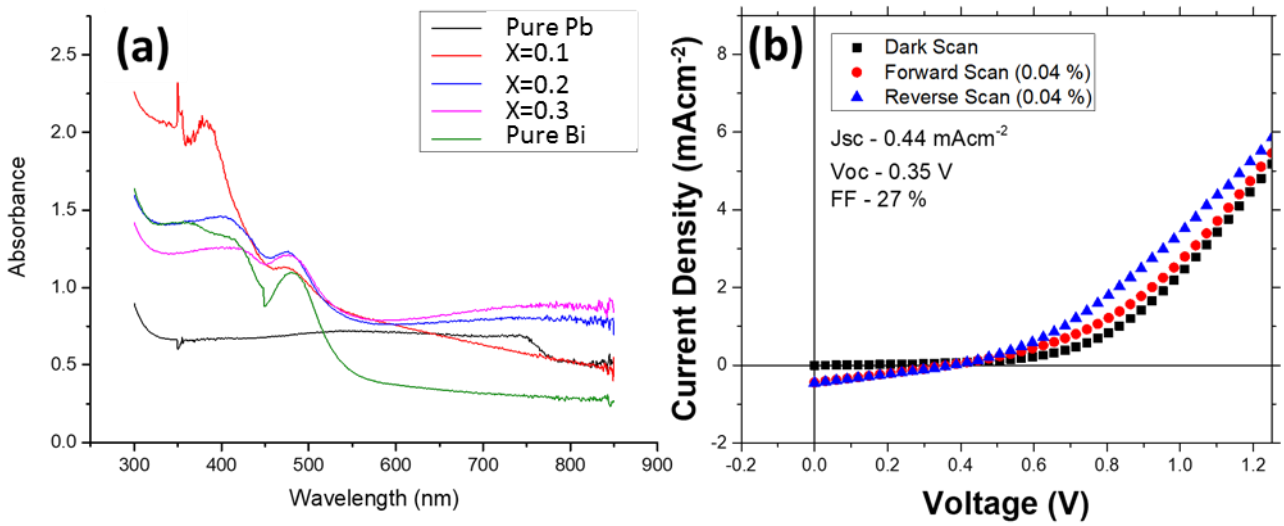

Figure 12 - (a) Absorption measurements of $(CH_3NH_3)_{(1-x)}Pb_{(1-x)}Bi_xI_3$ with varying x values. (b) J-V curve for the best cell made using x=0.1 doped perovskite from the acetate route in Prof. Snaith's laboratory.

To confirm these conclusions, a batch of solar cells made from 10% bismuth doped $(CH_3NH_3)_{1-x}Pb_{1-x}Bi_xI_3$ was fabricated alongside a control batch of normal $CH_3NH_3PbI_3$. The cells were made whilst visiting Prof. Snaith's lab in Oxford and used the non-inverted structure with the lead acetate route (with bismuth acetate substituted in for the doped cells). Cells made from the standard $CH_3NH_3PbI_3$

achieved an average efficiency of ~10%, with a best of 13%, while cells made from $(CH_3NH_3)_{0.9}Pb_{0.9}Bi_{0.1}I_3$ were all less than 0.1% efficient. The best J-V curve is shown in figure 12 (b), and the weak light response of the cells can be clearly seen. The $(CH_3NH_3)_{0.9}Pb_{0.9}Bi_{0.1}I_3$ were made in the same batch as the 11% cells, so the discrepancy can only be due to the change in active layer, and they all demonstrated diode-like J-V curves meaning that the low performance cannot be attributed to an error in fabrication. This leads us to the unfortunate conclusion that bismuth doping is not a viable route for achieving low toxicity perovskite solar cells

Diamine doping – other ways to introduce vacancies

One question which arose from the bismuth doping experiment was whether the poor optoelectronic charachteristics was due to the presence of the A site vacancies, or whether it was something intrinsic to the Bi^{3+} ion. To resolve this, Dr Julia Payne designed a precursor compound that could introduce vacancies to the perovskite structure without replacing any of the lead component. This would allow us to isolate the effects of the vacancies from any other effects the bismuth doping may have introduced. To do this, a portion of the methylammonium iodide would be replaced with ethylenediammonium diiodide ($H_3NC_2H_4NH_3I_2$), which forms a 2+ ion instead of a 1+. The resulting structure would have the formula $(CH_3NH_3)_{1-2x}(H_3NC_2H_4NH_3)_xPbI_3$, and could be made using any of the standard methods for fabricating $CH_3NH_3PbI_3$ films, provided that the stoichiometry of the films was adjusted to give the desired doping level. X-Ray diffraction measurements performed by Dr Payne found that the resulting crystal underwent two phase transitions as the doping concentration was increased – going through a tetragonal to cubic transition at a doping constant (x) of 0.1, and going from cubic to mixed phase above a doping constant of 0.2.

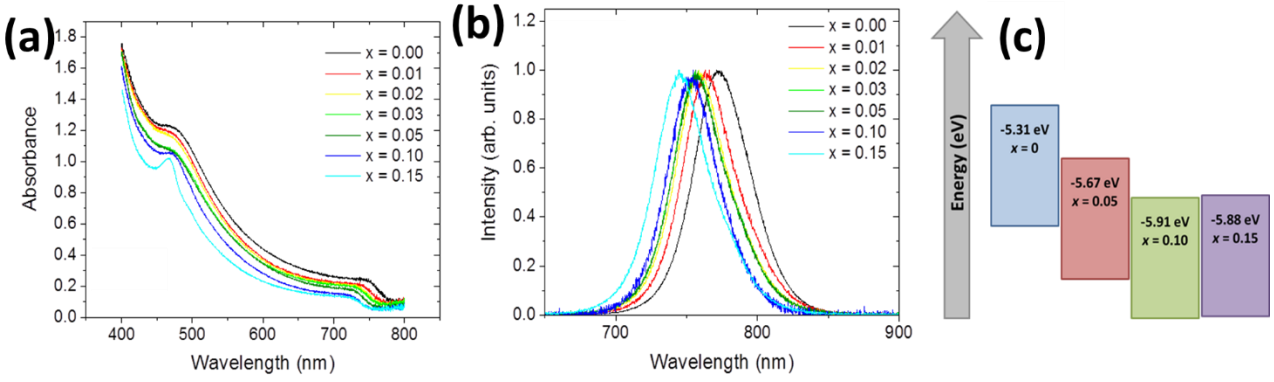

Figure 13 - (a) Absorption spectra for $CH_3NH_3PbI_3$ with varying fractions of diamine doping. (b) PL spectra for the same films. (c) HOMO level measurements on films with varying doping levels.

Absorption and photoluminescence measurements on the resulting doped films found that the introduction of vacancies resulted in somewhat reduced properties, but did not have anywhere near as significant an impact as the bismuth doping in the previous section. Absorption measurements seen on figure 13(a) show that the absorption onset of the resulting films is slowly blue shifted as the doping concentration is increased, indicating that this doping is increasing the bandgap of the material. Photoluminescence data shown on figure 13(b) supports this conclusion, as the PL spectrum can be seen to blue shift from 770 nm at x=0.00 to 740 nm at x=0.20 – a similar rate to the absorption spectrum and an overall shift of ~0.06 eV. Looking back at the absorbance, it can also be seen that the steepness of the absorption onset is gradually reduced as the doping is increased. This is generally bad for devices as it indicates the presence of sub – bandgap states trap states which will reduce performance, but it is nowhere near as detrimental as the complete removal of the absorption onset seen in the bismuth doping. Additionally, the previously observed peak in absorption at 480 nm is seen to appear here too at high doping concentrations, leading to the conclusion that this peak is due to effects from the vacancies rather than the Bi^{3+} ion itself.

Air photoemission measurements on the films indicate that the HOMO level of the perovskite structure is drastically affected by the addition of the vacancies. The HOMO level deepens sharply with increasing doping constant before flattening out at -5.9 eV at around x=0.10, as shown on figure 13(c). This represents a shift of 0.6 eV – 10 times greater than the shift in bandgap, and is likely to cause issues in device fabrication because the LUMO level of the perovskite will be poorly aligned with any electron transporting layer. To investigate this, Dr Lethy Jagadamma from our research group in St Andrews fabricated some inverted solar cells using the nanocrystal pinning method from x=0.10 $(CH_3NH_3)_{1-2x}(H_3NC_2H_4NH_3)_xPbI_3$, as well as a control batch of standard $CH_3NH_3PbI_3$. The resulting J-V curves are shown in figure 14 and show a clear drop in performance from (7.5% PCE to 4.5%), though not to the same extent as observed with the bismuth doping (13% to 0.04%). The open circuit voltage is improved by ~0.06 eV, as would be expected from the widened bandgap, but the short circuit current is significantly reduced. This is in part due to the reduced absorption from the widened bandgap, but transfer matrix simulations of the structure using public software released by McGhee et al [32] revealed that the reduced absorption can only account for about half of the reduction in Jsc. The rest of the drop in Jsc will be due to losses induced by the vacancies which have been introduced. This can also be clearly seen in the incident photon to charge conversion efficiency (EQE) curves of the solar cells, where the doped cell has reduced conversion efficiency across the entire spectrum, in addition to its blue shifted absorption onset. However, the main conclusion which can be drawn from this is that the perovskite still works remarkably well when A site vacancies are introduced.

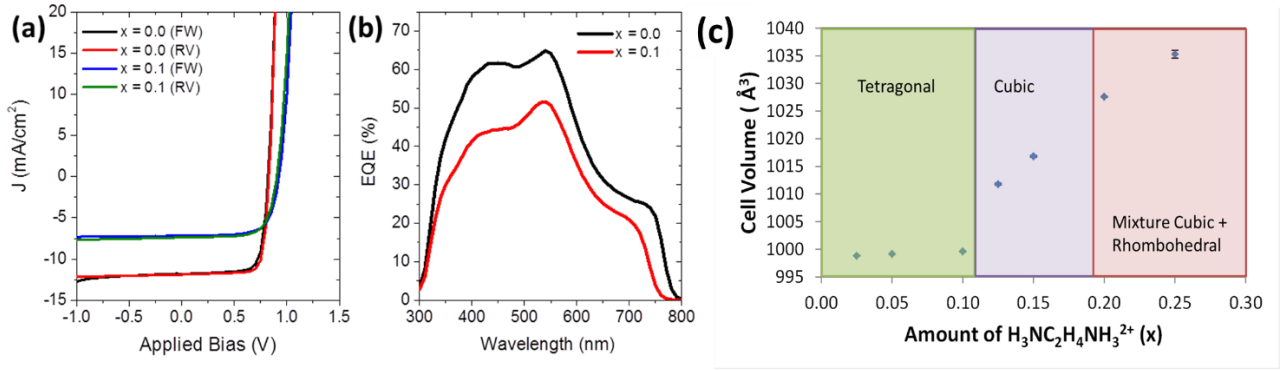

Figure 14 - (a) J-V curves for inverted solar cells made from pure $CH_3NH_3PbI_3$(red), and x=0.1 diamine doped perovskite (blue). Note that the doped curve has reduced Jsc but increased Voc. (b) EQE curves for the undoped (black) and x=0.1 (red) materials. The shift in bandgap can be clearly seen, and the x=0.1 material has overall worse conversion efficiency. (c) Cell volume vs doping fraction for diamine doped $CH_3NH_3PbI_3$. Measurements for (a) and (b) were taken by Dr L. Jagadamma, while (c) was made by Dr J. Payne.

Although these results clearly indicate that the introduction of vacancies is definitely not desirable for optimised performance, they also show that these vacancies are far less detrimental to the performance than the effect of the bismuth doping from the previous section. This leads us to the conclusion that it was the Bi^{3+} ion itself that was ruining the performance of the Bismuth doped perovskite solar cells, and so attempting to replace the lead component of perovskites with bismuth is unlikely to lead to a material with useful optoelectronic applications.

Conclusion

In conclusion, this chapter describes the fine details of how perovskite films were fabricated, and the steps we took trying to achieve high performance perovskite solar cells. High quality perovskite films can now be easily achieved, but the efficiency of most devices fabricated in our laboratory remains poor for reasons we have not been able to ascertain. We also used Kelvin probe and air photoemission to perform an advanced study on the energy levels in the most common perovskite solar cell structure, and used these data to form a detailed and effective model of the solar cell's operation. Finally, we have discussed our attempts at designing low toxicity perovskite materials, and our investigation into the effect of A site vacancies on the performance of the material leads us to the conclusion that perovskites containing Bi^{3+} ions are unlikely to be of significance for optoelectronic devices.

References

1. Wu, C.G., et al., *High efficiency stable inverted perovskite solar cells without current hysteresis.* Energy & Environmental Science, 2015. **8**(9): p. 2725-2733.

2. Sharenko, A. and M.F. Toney, *Relationships between Lead Halide Perovskite Thin-Film Fabrication, Morphology, and Performance in Solar Cells.* Journal of the American Chemical Society, 2016. **138**(2): p. 463-470.
3. Eperon, G.E., et al., *The Importance of Moisture in Hybrid Lead Halide Perovskite Thin Film Fabrication.* Acs Nano, 2015. **9**(9): p. 9380-9393.
4. Gao, H., et al., *Nucleation and Crystal Growth of Organic-Inorganic Lead Halide Perovskites under Different Relative Humidity.* Acs Applied Materials & Interfaces, 2015. **7**(17): p. 9110-9117.
5. You, J.B., et al., *Moisture assisted perovskite film growth for high performance solar cells.* Applied Physics Letters, 2014. **105**(18).
6. Stranks, S.D., et al., *Electron-Hole Diffusion Lengths Exceeding 1 Micrometer in an Organometal Trihalide Perovskite Absorber.* Science, 2013. **342**(6156): p. 341-344.
7. Henry J. Snaith, A.A., James M. Ball, Giles E. Eperon, Tomas Leijtens, Nakita K. Noel, Samuel D. Stranks, Jacob Tse-Wei Wang, Konrad Wojciechowski, and Wei Zhang, *Anomalous Hysteresis in Perovskite Solar Cells.* Journal of Physical Chemistry Letters, 2014. **5**(9): p. 1511-1515.
8. Burschka, J., et al., *Sequential deposition as a route to high-performance perovskite-sensitized solar cells.* Nature, 2013. **499**(7458): p. 316-+.
9. Chiang, C.H., Z.L. Tseng, and C.G. Wu, *Planar heterojunction perovskite/PC71BM solar cells with enhanced open-circuit voltage via a (2/1)-step spin-coating process.* Journal of Materials Chemistry A, 2014. **2**(38): p. 15897-15903.
10. Jeon, N.J., et al., *Solvent engineering for high-performance inorganic-organic hybrid perovskite solar cells.* Nature Materials, 2014. **13**(9): p. 897-903.
11. Jung, J.W., S.T. Williams, and A.K.Y. Jen, *Low-temperature processed high-performance flexible perovskite solar cells via rationally optimized solvent washing treatments.* Rsc Advances, 2014. **4**(108): p. 62971-62977.
12. Xiao, M.D., et al., *A Fast Deposition-Crystallization Procedure for Highly Efficient Lead Iodide Perovskite Thin-Film Solar Cells.* Angewandte Chemie-International Edition, 2014. **53**(37): p. 9898-9903.
13. Zhang, W., et al., *Ultrasmooth organic-inorganic perovskite thin-film formation and crystallization for efficient planar heterojunction solar cells.* Nature Communications, 2015. **6,**6142.

14. Zhang, W., et al., *Enhanced optoelectronic quality of perovskite thin films with hypophosphorous acid for planar heterojunction solar cells.* Nature Communications, 2015. **6,** 10030 .
15. Barnea-Nehoshtan, L., et al., *Surface Photovoltage Spectroscopy Study of Organo-Lead Perovskite Solar Cells.* Journal of Physical Chemistry Letters, 2014. **5**(14): p. 2408-2413.
16. Jimenez-Lopez, J., et al., *Charge Injection, Carriers Recombination and HOMO Energy Level Relationship in Perovskite Solar Cells.* Scientific Reports, 2017. **7,**6101.
17. Chang, J.J., et al., *Elucidating the charge carrier transport and extraction in planar heterojunction perovskite solar cells by Kelvin probe force microscopy.* Journal of Materials Chemistry A, 2016. **4**(44): p. 17464-17472.
18. Chi, W.J., Q.S. Li, and Z.S. Li, *Exploring the electrochemical properties of hole transport materials with spiro-cores for efficient perovskite solar cells from first-principles.* Nanoscale, 2016. **8**(11): p. 6146-6154.
19. Bredas, J.L., *Mind the gap!* Materials Horizons, 2014. **1**(1): p. 17-19.
20. J. R. Harwell, T.K.Baikie., I. D. Baikie, J. L. Payne, C. Ni, J. T. S. Irvine, G. A. Turnbull, I. D. W. Samuel *Probing the energy levels of perovskite solar cells via Kelvin probe and UV ambient pressure photoemission spectroscopy* Physical Chemistry Chemical Physics, 2016. **18**: p. 19738-19745
21. Liu, G.M., et al., *XPS and UPS characterization of the TiO2/ZnPcGly heterointerface: Aligmment of energy levels.* Journal of Physical Chemistry B, 2002. **106**(23): p. 5814-5819.
22. Schulz, P., et al., *Interface energetics in organo-metal halide perovskite-based photovoltaic cells.* Energy & Environmental Science, 2014. **7**(4): p. 1377-1381.
23. Docampo, P., et al., *Efficient organometal trihalide perovskite planar-heterojunction solar cells on flexible polymer substrates.* Nature Communications, 2013. **4,** 2761.
24. Leijtens, T., et al., *Hole Transport Materials with Low Glass Transition Temperatures and High Solubility for Application in Solid-State Dye-Sensitized Solar Cells.* Acs Nano, 2012. **6**(2): p. 1455-1462.
25. Song, Y.K., et al., *Energy level tuning of TPB-based hole-transporting materials for highly efficient perovskite solar cells.* Chemical Communications, 2014. **50**(96): p. 15239-15242.
26. Li, H.R., et al., *A Simple 3,4-Ethylenedioxythiophene Based Hole-Transporting Material for Perovskite Solar Cells.* Angewandte Chemie-International Edition, 2014. **53**(16): p. 4085-4088.
27. Miller, E.M., et al., *Substrate-controlled band positions in CH(3)NH(3)PbI(3) perovskite films.* Physical Chemistry Chemical Physics, 2014. **16**(40): p. 22122-22130.

28. Frolova, L.A., N.N. Dremova, and P.A. Troshin, *The chemical origin of the p-type and n-type doping effects in the hybrid methylammonium-lead iodide (MAPbI(3)) perovskite solar cells.* Chemical Communications, 2015. **51**(80): p. 14917-14920.
29. Wang, Q., et al., *Qualifying composition dependent p and n self-doping in CH3NH3PbI3.* Applied Physics Letters, 2014. **105**(16).
30. Tengstedt, C., et al., *Fermi-level pinning at conjugated polymer interfaces.* Applied Physics Letters, 2006. **88**(5).
31. Jiang, C.S., et al., *Carrier separation and transport in perovskite solar cells studied by nanometre-scale profiling of electrical potential.* Nature Communications, 2015. **6,** 8397.
32. Burkhard, G.F., E.T. Hoke, and M.D. McGehee, *Accounting for Interference, Scattering, and Electrode Absorption to Make Accurate Internal Quantum Efficiency Measurements in Organic and Other Thin Solar Cells.* Advanced Materials, 2010. **22**(30): p. 3293-3297.

Chapter 5 - Infrared Perovskite Laser

Making a Perovskite Laser

ASE from $CH_3NH_3PbI_3$

As mentioned in chapter 2, a good solar cell must be a strong light emitter, and hybrid perovskites are no exception to this rule. Many of the best solar cell films reported in the literature were found to have a high PLQY [1], and so studying the PL of our films was deemed to be a good route to finding a possible reason for the low efficiency of our solar cell devices. However, studying the PL of perovskites proved more difficult than expected due to their intensity dependent PLQY [2]. Our most advanced setups for measuring PL predominantly used a low intensity lamp source for excitation, and so no signal could be measured from films of $CH_3NH_3PbI_3$ deposited via the acetate route. PLQY measurements using a Hamamatsu integrating sphere with lamp excitation gave 0% PLQY with no spectrum visible above the background, and so we switched to pulsed laser excitation for further study of the material. This switch allowed the material to operate in an intensity regime where the light emission was much more efficient, thus allowing clear photoluminescence spectra to be recorded. However it became clear that, under the right conditions, the light emission could be much stronger than first anticipated. While attempting to map the dependence of the photoluminescence versus excitation intensity, the emission from a sample of $CH_3NH_3PbI_3$ deposited via the acetate route [3, 4] was suddenly observed to dramatically increase once the excitation laser power reached a certain threshold, and the emission spectrum collapsed to a narrow peak of ~10 nm full width half maximum (FWHM). The spectrum of this emission compared to the normal PL is shown in figure 1, and this unexpected result indicated that waveguided light in the $CH_3NH_3PbI_3$ film was undergoing amplified spontaneous emission (ASE).

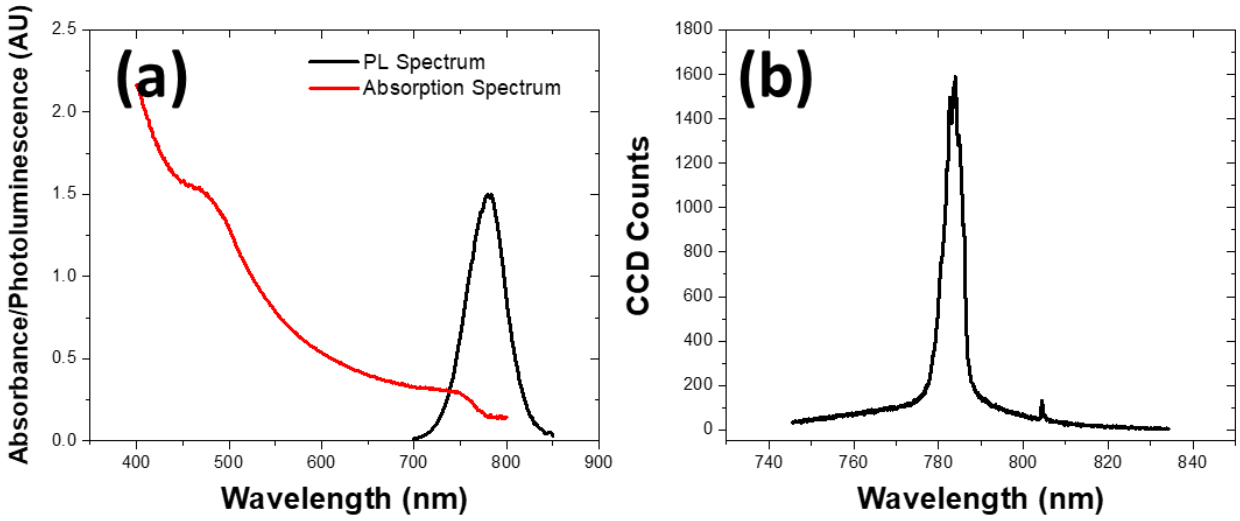

Figure 1 - (a) Absorption and photoluminescence spectrum of $CH_3NH_3PbI_3$. (b) Emission spectrum of $CH_3NH_3PbI_3$ when excited above its ASE threshold with 355 nm light. The normal PL spectrum can be weakly seen in the baseline.

The presence of ASE in $CH_3NH_3PbI_3$ had very recently been demonstrated by Stranks et al [5], using cholesteric liquid crystal reflectors to provide mode confinement, and so the demonstration of ASE from a simple thin film of $CH_3NH_3PbI_3$ was not an especially interesting discovery in itself. However, what it did show for us was that $CH_3NH_3PbI_3$ was an excellent candidate material for the production of distributed feedback lasers. Achieving gain in a thin film would allow for laser operation in an identical manner to that used in organic thin film lasers, and enable the properties of perovskite lasers to be comparable with their organic counterparts. Firstly, the exciton binding energy of $CH_3NH_3PbI_3$ (<5 meV at room temperature) [6, 7] meant that excitons would be dissociated almost immediately in a perovskite film. This absence of excitons in the film would mean that pulse duration would not be limited by the accumulation of triplet excitons in the material, since no singlet excitons would exist to be converted via intersystem crossing. This could open up a route to a new generation of high power thin film lasers which can operate in the continuous wave (cw) rather than pulsed regime [8]. Secondly, $CH_3NH_3PbI_3$ has an ambipolar(i.e. for both electrons and holes) charge mobility several orders of magnitude higher than most OSCs [9], meaning that an electrically pumped perovskite device could conceivably reach the very high current densities required to reach electrically pumped lasing – a major milestone on the road to making thin film lasers a commercial viability. Additionally, perovskites are cheap, solution processable, and have easily tuneable properties, meaning that commercial devices could be easily mass produced on a large scale at low cost. Finally, the refractive index of hybrid perovskites tends to be far higher than what is seen in most organic semiconductors(~2.6 [10] compared to ~1.9 [11] in polymers). This is a big disadvantage for making light emitting diodes because they will be much worse at outcoupling their

light. But it is a useful feature when making lasers because the high refractive index will allow stronger mode confinement in a thinner film. In light of these advantages, we set out to prove these concepts by producing an all solution-processed perovskite distributed feedback laser using easily scalable techniques.

Competing with Scattered ASE

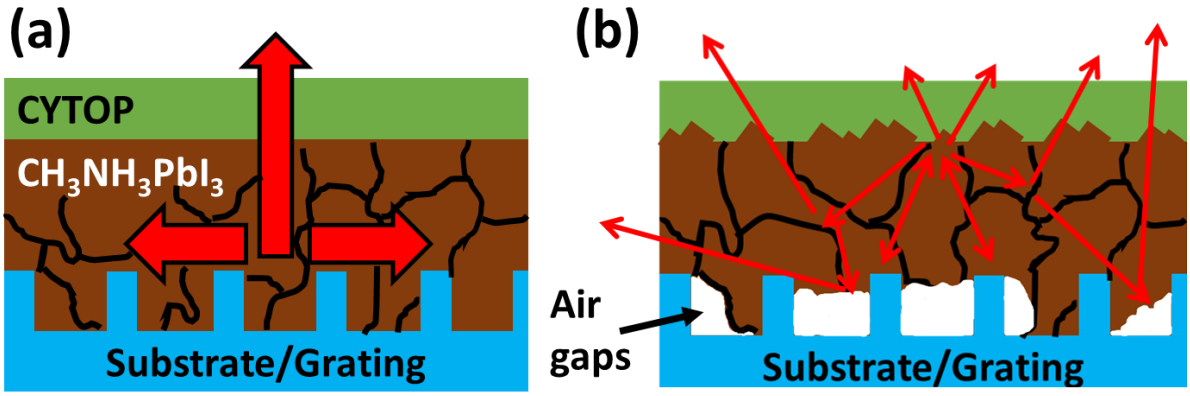

Figure 2- (a) A schematic of the ideal $CH_3NH_3PbI_3$ laser –the crystals conform to the grating structure to make a smooth capping layer with minimal scattering off the grain boundaries, allowing strong distributed feedback to occur. (b) A more likely scenario where the $CH_3NH_3PbI_3$ does not conform to the grating, leaving a rough film with air gaps. Scattering off the imperfections and the grain boundaries eclipses any feedback from the grating structure.

In spite of their advantages, achieving distributed feedback in a perovskite film would present some major challenges. Firstly, it was not clear how the perovskite would behave when being deposited on a distributed feedback (DFB) grating. To operate effectively, the perovskite would need to completely conform to the grating structure without leaving any air gaps in the ~200 nm wide troughs in the grating, whilst also ideally leaving a completely flat capping layer on the top. Since perovskite films form via crystallisation, it could not be guaranteed that the crystals would grow to fill the gaps. Instead the crystals might simply lie randomly on top of the structure without conforming to it, resulting in the situation shown in figure 2. Secondly, the multicrystalline nature of the films would be highly likely to introduce large scattering losses to the film. If the scattering from the crystal boundaries became stronger than the scattering from the feedback grating then the DFB lasing mode would be eclipsed by random lasing modes, which would compete with the DFB mode for gain, thus ruining the device. In order to minimise these issues, we would need to produce perovskite films with a very low surface roughness to minimise scattering, and small crystals to aid conformity with the grating structure. For this, the lead acetate route (see chapter 4, pg 88) was selected due to its excellent and highly reproducible film quality with weakly defined crystal boundaries. Hence this route is used in all $CH_3NH_3PbI_3$ film depositions for lasers in this chapter.

When designing a DFB laser, one must pick the grating period so that it satisfies the Bragg equation

$$2n_{eff}\Lambda = m\lambda_{laser},$$

where λ_{laser} is the wavelength the laser is expected to operate at, n_{eff} is the effective refractive index of the waveguide, Λ is the period of the grating, and m is the order of diffraction (which is 2 in the case of second order gratings). The master grating structures are very expensive to make, and so usually it is easier to tune the effective refractive index of the waveguide to match the grating periods that are readily available. A simple way to calculate the effective refractive index is to treat the laser as a slab waveguide and use the approximation

$$n_{eff} = n_1 \cos\theta$$

Where n_1 is the refractive index of the lasing medium and θ is the propagation angle of the light in the slab waveguide. The angle of propagation is iteratively calculated by satisfying the phase relation for the waveguide. That is calculating the phase change in one cycle through the waveguide, and finding the propagation angle where the phase change is an integer factor of 2π. This allows us to accurately model the effective refractive index of any thin film. Assuming the cladding layers are the grating material (n=1.52) and either air (n=1) or an encapsulant (n=1.33), the main factors which control the n_{eff} of the waveguide are the refractive index of the gain material and the thickness of the gain layer (which was measured by Dr Guy Whitworth, from our group at the University of St Andrews, using ellipsometry to be n=2.46 at 783 nm). Since the gain medium's refractive index is constant, that leaves only the thickness as a means to control n_{eff}. Our most advanced mixed order gratings (which could achieve the lowest threshold) had a period of 350 nm, which would require the $CH_3NH_3PbI_3$ layer to be at least 250 nm thick to meet the feedback condition. To achieve this thickness, the lead acetate precursor solution was set to a concentration of 550 $mgml^{-1}$ and the solution was spin-coated on distributed feedback gratings at 2000 RPM in an N_2 glovebox with the usual annealing parameters. The gratings were fabricated via the method described in chapter 3, and the complete devices were encapsulated with a layer of the fluoropolymer CYTOP™ to prevent degradation of the perovskite by water.

To test the laser devices, they were excited with 1 ns pulses of 355 nm laser light from a diode pumped CryLas solid state laser with a spot size of ~100 microns and a repetition rate of 100 Hz. The output light was collected with a fibre coupled Andor CCD spectrograph in the setup shown in figure 3. The resulting devices showed a clear threshold in output, but did not have any of the spatial or temporal coherence normally associated with lasing. The emission linewidth remained at ~5 nm

instead of the <1 nm expected for lasing, and the emission could be detected from the film at all angles. These results indicated that the effect of random scattering was stronger than the feedback from the grating, meaning that structure was simply producing scattered ASE rather than lasing. Looking back at the quality of the films produced by this method, the surface roughness was still below the noise threshold of the Dektak surface profilometer (~10 nm). However visual inspection revealed a "cloudy" appearance to the films, which suggested that the optical quality of the films was dropping with the increased thickness and introducing extra scattering. Attempts to improve film quality whilst maintaining this film thickness (by varying the spin speed, annealing conditions, and solution concentration) all produced the same, poor quality results, and so we were forced to conclude that the lead acetate route could not be used to produce films of sufficient quality for our advanced gratings.

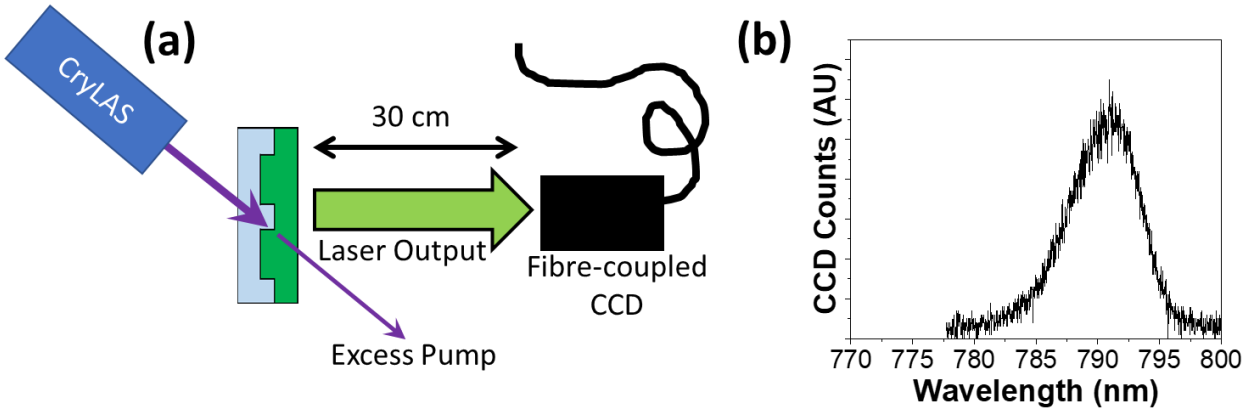

Figure 3 - (a) A simplified diagram of the setup used to measure DFB lasers. The laser is pumped at a slight angle to prevent excess pump light being coupled into the CCD. (b) The emission spectrum from the laser, indicating that the sample is only emitting scattered ASE. This spectrum was seen from the samples at all angles, and is too spectrally wide to be considered single mode coherent emission.

Achieving Distributed Feedback Lasing

In general, it is easier to achieve smooth and high-quality films if the film thickness is reduced, so in order to improve film quality we aimed to build a laser incorporating a thinner $CH_3NH_3PbI_3$ film. This would not meet the resonance condition of the main gratings we planned to use, so instead we switched the master grating structure to a tuneable array of 2D feedback gratings. This structure consisted of a 6x6 array of 2D 2nd order gratings with period varying between 250 and 425 nm in 5 nm steps. These gratings would achieve a worse lasing threshold than the mixed order gratings we had planned to use, but it could be guaranteed that at least one of the gratings would meet the resonance condition to provide distributed feedback so long as the layer was thicker than the cut-off thickness (which can be as low as 70 nm for $CH_3NH_3PbI_3$ due to its high refractive index). This increased freedom in layer design allowed us to reduce the concentration of the lead acetate

precursor solution from 550 $mgml^{-1}$ to 400 $mgml^{-1}$. When spun at 2000 RPM, this created films of ~190 nm thickness with greatly improved optical quality. The waveguiding loss coefficient of these films was measured using the procedure described in chapter 3 to be roughly 6 cm^{-1}, which is average by the standard of organic semiconductor films [12], meaning it should have sufficiently low losses to provide distributed feedback lasing. Solving the phase relationship equation for a stack with this thickness gave an effective refractive index of 2.14 which, assuming a lasing mode of 785 nm, should provide lasing on a 365 nm grating.

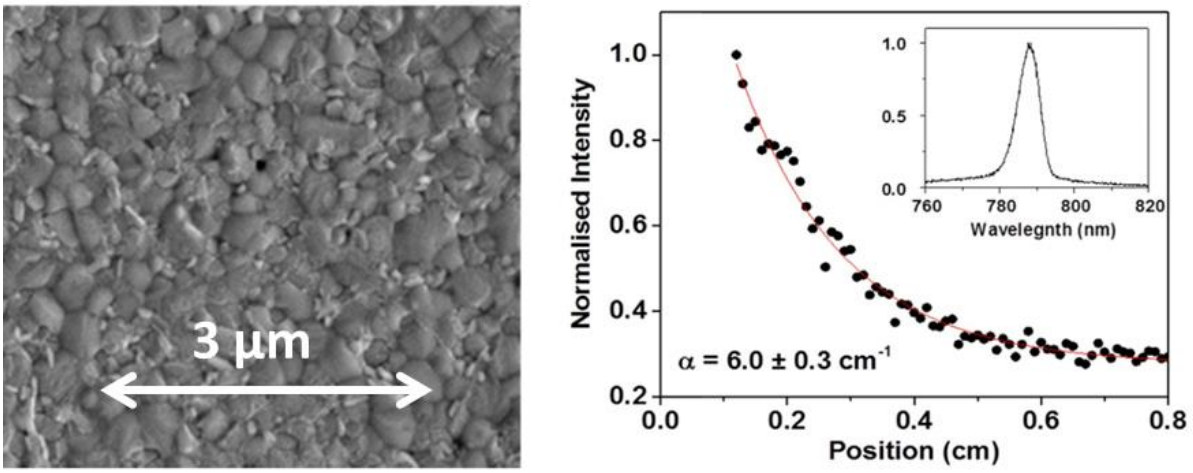

Figure 4 - (a) Scanning electron microscopy image of the high quality $CH_3NH_3PbI_3$ film deposited via the acetate route. Note the dense films with only a very small number of pinholes. (b) Waveguiding loss measurement on a similar film. Images are taken from our paper [13]

In order to see how the perovskite film coated the grating, one device from the batch was made without the CYTOP encapsulation layer, and was studied using an FEI Scios™ DualBeam focussed ion beam/ scanning electron microscopy setup operated by David Miller at the department of Chemistry, University of St Andrews. Prior to measuring, a thin layer of gold (1-10 nm) was sputtered on top of the $CH_3NH_3PbI_3$ layer using a Quorum Q150R ES sputterer to prevent charging effects on the material surface to aid imaging. Figure 4 shows an image of the resulting $CH_3NH_3PbI_3$ layer on a planar part of the substrate. Note that the material shows a complete and uniform coverage with an average crystallite size of ~300 nm. To ensure that the $CH_3NH_3PbI_3$ was completely conforming to the grating, a region of the $CH_3NH_3PbI_3$ on the grating was milled away using the focussed ion beam to reveal the polymer structure underneath. Figure 5b shows an angled (52°) SEM image of this sample, which clearly shows the perovskite forming a high quality planar film over the grating structure with a number of small pinholes visible in the film.

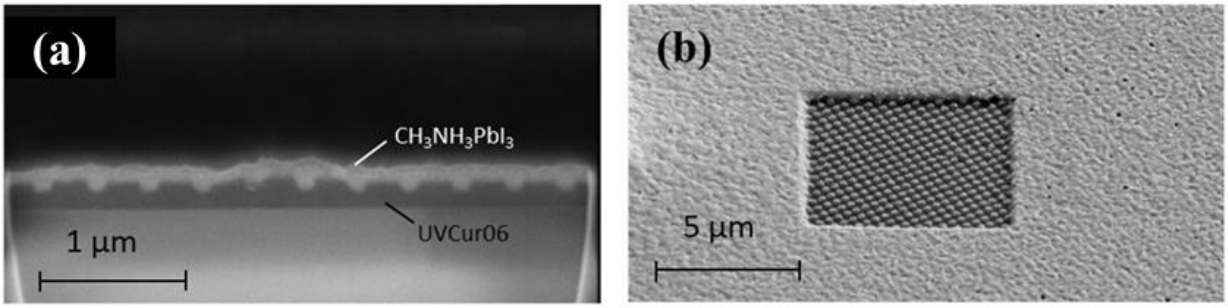

Figure 5- (a) Transverse SEM image of $CH_3NH_3PbI_3$ laser. The perovskite can be clearly seen to fill in the grating, leaving a smooth capping layer with no gaps. (b) Angled SEM image of the same laser with a square of $CH_3NH_3PbI_3$ milled away to reveal the grating underneath. Images are taken from our paper [13]

Finally a transverse SEM image of the grating was taken by digging a trench in the sample using the focussed ion beam and imaging the sample at a steep angle. A layer of carbon was sputtered onto the sample prior to milling to assist in achieving a clean vertical cut while also providing a strong contrast with the perovskite layer to produce a clear image. Figure 5a shows the resulting image, and it can be clearly seen that the $CH_3NH_3PbI_3$ has completely filled in the gaps in the grating, leaving no air pockets or voids. The grating has a depth of 80 nm with a planar capping layer of ~145 nm on top. This shows that the resulting structure should provide high quality distributed feedback to the lasing mode, although we can still expect some scattering losses due to the pinholes and small non-uniformities which are also visible.

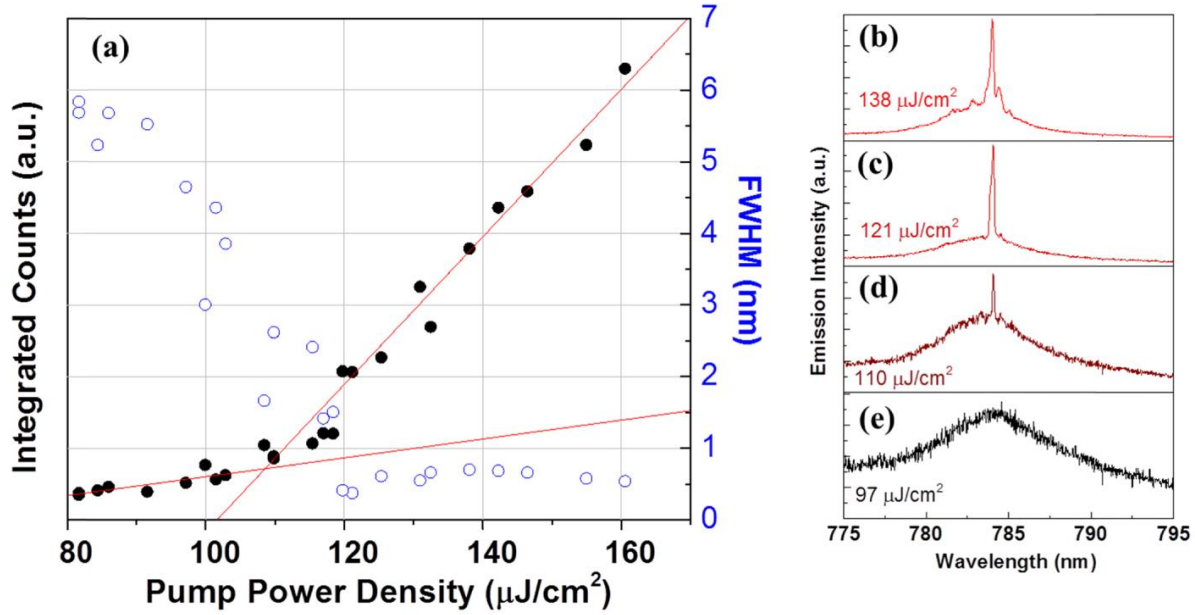

Figure 6 - (a) Threshold Measurement of the $CH_3NH_3PbI_3$ laser. PL counts are on a linear scale. (b),(c),(d), and (e) The emission spectrum at varying pump fluences. Clear single mode lasing can be seen between 110 and 121 µJcm^{-2}, but there is evidence of extra modes appearing at 138 µJcm^{-2}. Images are taken from our paper [13]

Upon testing under the same conditions as the previous batches, these devices were measured by Dr Guy Whitworth, and above a certain thereshold the emission spectrum from the 365 nm grating was observed to abruptly collapse to a FWHM of less than 0.4 nm, as shown in figure 6. This would indicate strong temporal coherence in the emission, and the spectrum was only measurable directly perpendicular to the substrate, indicating a clear beam was formed. Note that an image of the beam could not be seen directly because the emission wavelength of 785 nm is at a wavelength where the human eye has very weak response. Plotting the output counts against input fluence on figure 6 (a) shows a clear threshold behaviour, and extrapolating the two straight line parts to the intersection gives a clear lasing threshold of 110 μJcm^{-2} for the grating.

Although distributed feedback lasing had been achieved thanks to the improved film quality, competing modes due to scattering still remained a problem for the devices. As the pump fluence was increased further, the laser started to operate at multiple modes simultaneously. These modes were very closely spaced, meaning that the modes appear to merge to form a single broad peak unless the spectrum was examined in close detail. Zooming in on the spectrum would reveal the broad peak was made up of a series of narrow peaks with ~0.2 nm spacing. To confirm that these were lasing modes and not random noise, Dr Whitworth took repeated measurements of the spectrum over two minutes and compiled all the spectra into a 2D colour plot (figure 7a). It can be clearly seen that these individual peaks are stable with time, meaning that we can conclude that they are stable lasing modes and not the result of random lasing or noise.

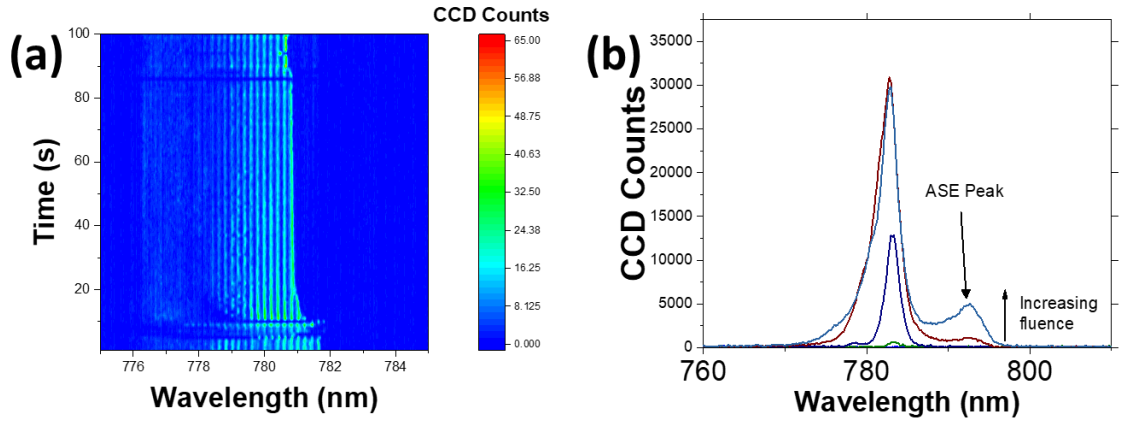

Figure 7- (a) A 2D colour plot of emission from the $CH_3NH_3PbI_3$ laser vs time. Multiple modes which are stable with time can be seen at a 0.2 nm spacing. (b) Spectra of the laser operating at high powers. As the pump fluence is increased an ASE peak is seen to appear at 790 nm. Figures made by Dr Guy Whitworth

At very high powers we observed that a scattered ASE peak, spectrally separated from the multimode lasing described earlier, would appear and compete for gain with the lasing modes

(figure 7b). This shows that scattering is still a problem in this device, and if the gain becomes too high then emission from the random scattered modes will become favourable over the coherent scattering from the grating. Therefore, we conclude that there is still room to improve on the scattering losses and film quality in these devices, and if these could be improved then the lasing threshold and output quality could be dramatically enhanced.

Pumping in the fs Regime

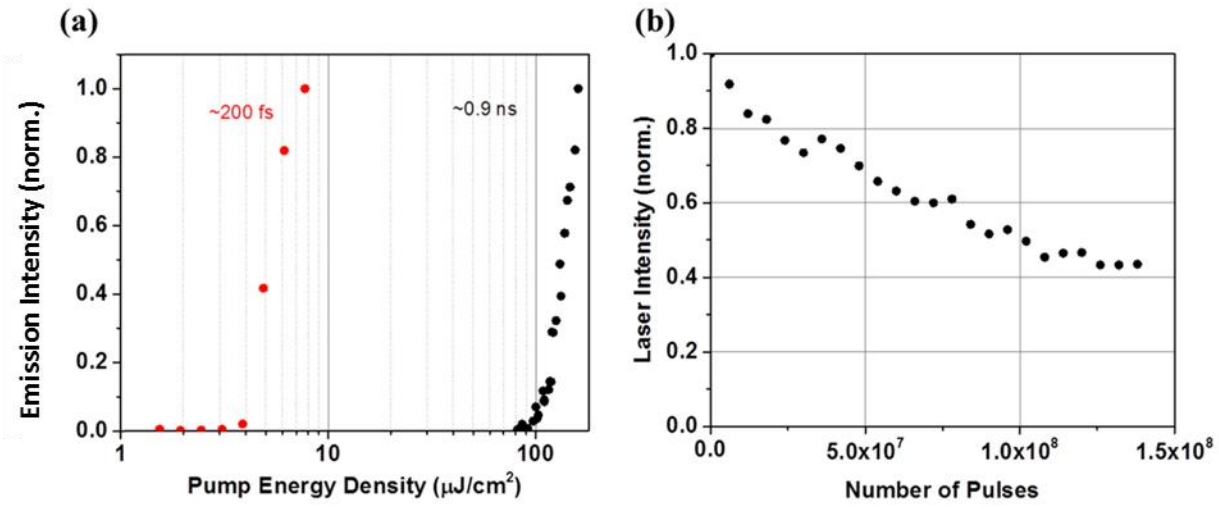

Figure 8– (a) A comparison of lasing threshold between nanosecond and femtosecond pumping. The threshold is drastically reduced in the fs regime. (b) The output intensity of the laser vs time when under 100 kHz excitation. The device falls to half its normal output after ~10^8 pulses. Images are taken from our paper [13]

It is known in that the threshold pump fluence of a laser can be significantly reduced if ultrashort (fs) pulsed lasers are used as a pump source instead of ns pulses [14]. This is because a fs pulse will create a high carrier density, and thus a high population inversion, in a very short period of time before any loss pathways can remove them. To investigate this effect in perovskite DFB lasers, the CryLas pump source was replaced with 515 nm, 200 fs pulses from the second harmonic of a PHAROS regenerative amplifier with a pulse rate of 100 kHz. The perovskite laser spectrum was measured using a fibre coupled Ocean Optics USB spectrometer, and the laser output vs input fluence is plotted on figure 8. The lasing threshold was observed to drop down from ~ 80 μJcm^{-2} to ~4 μJcm^{-2}, which corresponds to a reduction of almost two orders of magnitude. This high repetition rate was also the ideal environment for testing the laser stability, and it was found that the $CH_3NH_3PbI_3$ laser exhibited a device half-life of ~ 10^8 pulses when left under excitation in atmosphere. This is far longer than would be typical for an organic laser in air, indicating that $CH_3NH_3PbI_3$ does not seem to be as vulnerable to the thermal degradation and photooxidation

processes which normally cause degradation in organics [15], and suggesting a possible advantage of perovskite lasers.

Approach to Quasi CW Regime

After observing such high stability in the $CH_3NH_3PbI_3$ lasers under fs pumping at 100 kHz, it was a natural progression to see if they could operate under ultra-high repetition rates of 80 MHz. This is known as the quasi CW regime because the pulse separation becomes shorter than the fluorescence lifetime of most materials. A key problem with this is that, assuming the threshold fluence remains constant, a jump from 100 kHz to 80 MHz will require an 800x increase in average pump power. A major block for achieving quasi CW lasing in most organic lasers is that the gain medium will quickly photodegrade in these conditions, but since our perovskite lasers showed high stability then this might not be a problem. Giebink et al recently observed stable lasing from a $CH_3NH_3PbI_3$ sample under long pulse continuous wave pumping at low temperatures [16], and so we aimed to see if this phenomenon still worked when approaching the CW regime using short pulses.

To view the operations of the $CH_3NH_3PbI_3$ laser in this regime, PL spectra and kinetics were measured with a Hamamatsu streak camera C10910-05 with S-20ER photocathode coupled to an Acton SP-2358 imaging spectrograph. The lasers were pumped with 515 nm, 180 fs pulses at either 100 kHz or 80 MHz by using light from a Pharos (Light Conversion) amplifier or oscillator respectively. The streak camera would measure emission wavelength, strength, and delay time and would plot them on a 2D heat map to simultaneously show the spectrum and lifetime of the light emission.

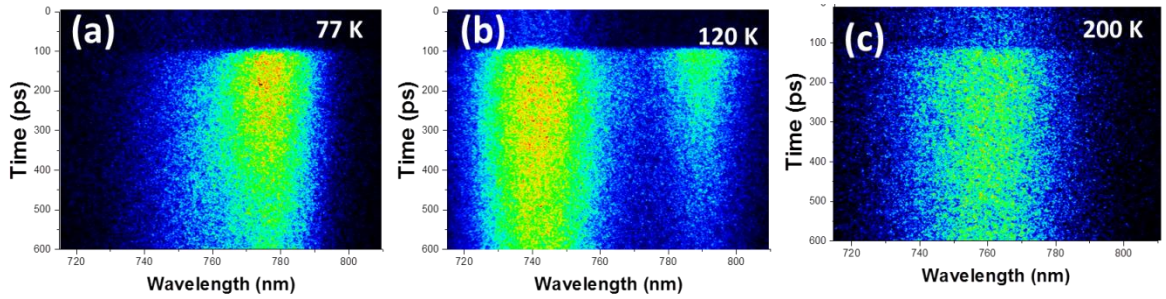

Figure 9 - Streak camera images of PL emission from a $CH_3NH_3PbI_3$ laser under 2.4 μJcm^{-2} pulse fluence at 100 kHz repetition rate with a temperature of (a) 77 K, (b) 120 K, and (c) 200 K. The images are 2D colour plots where the colour of each pixel represents the number of counts at that time and wavelength. Increasing counts go from black to blue to green to red.

As a first test on the effect of cooling on the $CH_3NH_3PbI_3$ laser, we pumped the DFB gratings at a range of different temperatures with 100 kHz pulses from the amplifier, focussed down to a 100 micron spot size. The sample was tested at 77 K, 120 K, and 200 K, and the PL spectrum below lasing

threshold was seen to drastically shift with temperature, as shown on figure 9. At 200 K, above the tetragonal to orthorhombic phase transition, the PL peak was at 790 nm. At 77 K, the PL was much stronger and had a strong blue shift to 750 nm, while at 120 K the sample appeared to be emitting from a 2 phase region and so two peaks were observed at 730 and 780 nm. As the intensity of the beam was increased, lasing could be clearly observed as the PL spectrum collapsed to a narrow peak and the emission decay dropped to less than 20 picoseconds, as can be clearly seen on figure 10.

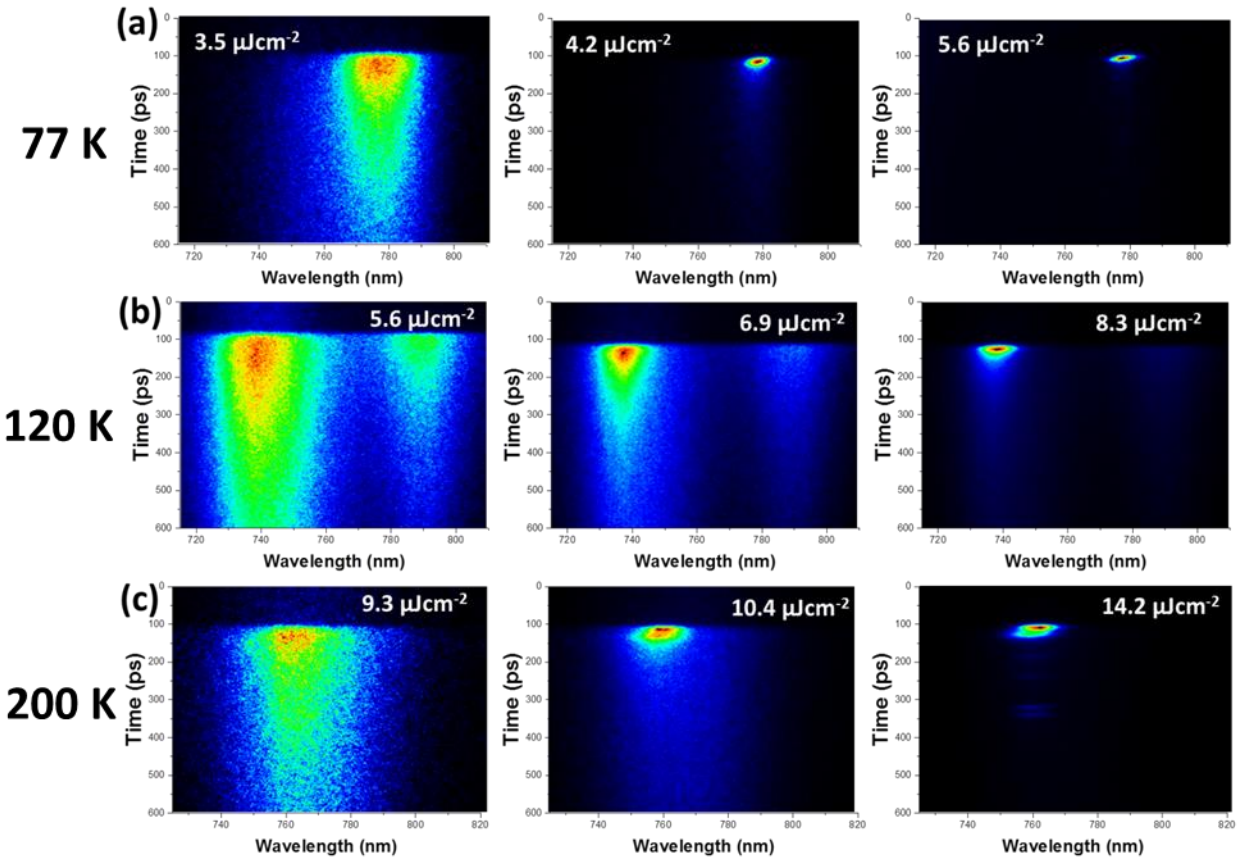

Figure 10 – Streak camera images of emission from a $CH_3NH_3PbI_3$ laser grating at a range of pump fluences when set at different temperatures. Set (a) is at 77 K, (b) is at 120 K, and (c) is at 200 K. Lasing is achieved when the emission linewidth abruptly narrows.

It is worth noting that the minimum FWHM of the lasing peaks was strongly limited by the spectral resolution of the streak camera to about 5 nm, so the exceptionally narrow linewidth emission typical of a DFB laser cannot be directly observed. But the sudden spectral narrowing and extremely short emission lifetimes provide sufficient evidence that lasing is taking place. The lasing threshold of these samples was found to be strongly affected by the temperature, with lasing thresholds of 4 μJcm^{-2}, 8 μJcm^{-2}, and 10 μJcm^{-2} being observed for 77 K, 120 K, and 200 K measurements respectively. This reduction in threshold with reduced temperature is not surprising since the

strength of the PL has been repeatedly observed by ourselves and others to dramatically increase at low temperatures [17]. Hence the sample will have more gain and therefore a lower threshold.

Switching to high repetition rate excitation, we were able to achieve a maximum pulse fluence of 12.5 μJcm^{-2}, which should be more than be sufficient to observe lasing from the samples. However, our streak camera images shown on figure 11 present no signs of ASE taking place at any temperature. Even at 77 K, where we should be a factor of 3 above threshold, the spectra showed no sign of narrowing and the emission decay remained in the hundreds of picoseconds. A possible reason for this lack of lasing was that the pump beam was heating the $CH_3NH_3PbI_3$ to the point where it could no longer provide optical gain. This hypothesis was backed up by the fact that the PL spectrum and lifetime had a tendency to shift significantly when the pump spot was moved, indicating that the beam is changing the parameters of the sample somewhat.

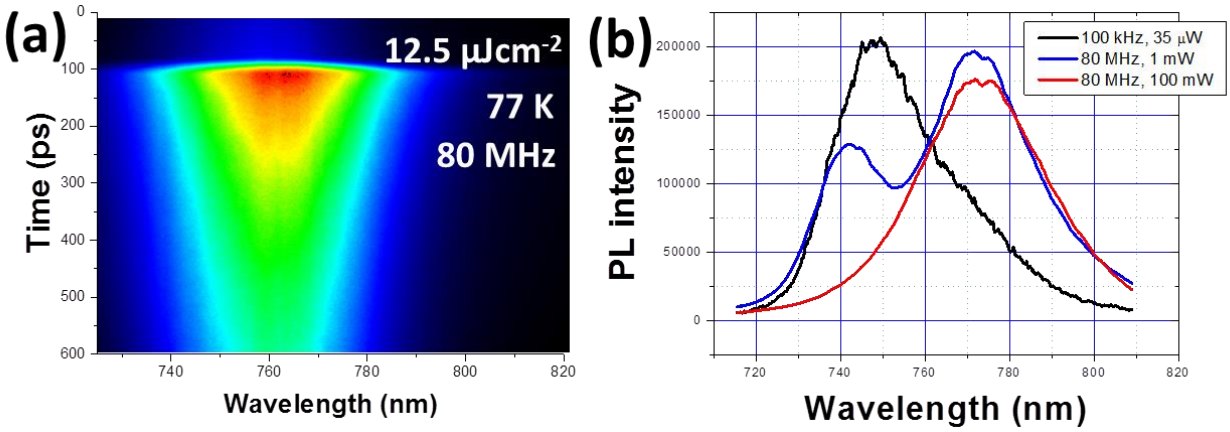

Figure 11 - (a) Streak camera image of emission from the $CH_3NH_3PbI_3$ laser structure under maximum power excitation at 80 MHz. The sample emits bright PL, but the spectrum linewidth is still wide, indicating that no ASE or lasing is taking place. (b) Evidence of sample heating – the PL spectrum from the 100 kHz excitation is significantly different from the 80 MHz excitation. The difference increases as the average power is increased, indicating that this is likely a heating effect.

To test this, we moved to a fresh spot and excited it with the oscillator beam at 1% of its maximum power. The spectrum was measured, and then remeasured under maximum power excitation. Comparing these results to the 77 K spectrum from the 100 kHz pump source, the spectra show increasing dissimilarities as the pump power is increased (see figure 11 b). This effect was reversible, and spots which had experienced the high power pumping would still lase at the same threshold as fresh spots, meaning that the effect we observe is not due to degradation. Hence we conclude that the high pump powers used in the quasi CW regime are causing undesirable heating effects which prevent the films from producing optical gain. It is known that $CH_3NH_3PbI_3$ has a very low thermal conductivity, and so in retrospect it is not surprising that this became an issue. However future work could improve upon this by performing measurements on a more conductive substrate, such as

sapphire, in order to conduct heat away from the beam centre and hopefully keep the $CH_3NH_3PbI_3$ at a temperature where it can support lasing.

Acetonitrile Deposition

The general conclusion from all of these results is that highly luminescent films of excellent optical quality are the key to achieving low threshold lasing from perovskite films. Therefore, it greatly captured our interest when a new method of producing perovskite films using acetonitrile was reported by Noel et al. [18] A big problem when depositing perovskites is that the only solvents which can dissolve the lead salts in perovskite precursors (DMF and DMSO) have very high boiling points and viscosity. This means that the solvents will tend to evaporate very slowly during spin-coating, meaning the crystallisation of the film will tend to be very uneven and sensitive to external factors. The nanocrystal pinning and lead acetate methods are both attempts to circumvent this issue by replacing parts of the solution with something more volatile in order to make the crystals form more quickly, thus hopefully resulting in smoother films. However, it would be much more preferable to use a low boiling point solvent. Acetonitrile is an excellent candidate for this because it has a low boiling point and a high polarity, but it still cannot dissolve the lead salts to the required concentrations.

It had previously been shown that methylamine gas was able to dissolve $CH_3NH_3PbI_3$ films into a clear liquid, which would then crystalise back into $CH_3NH_3PbI_3$ perovskite once the gas was removed [19, 20]. Zhou et al [20] exploited this to improve the performance of perovskite solar cells by exposing $CH_3NH_3PbI_3$ films to a post treatment of methylamine gas which, in optimal conditions, would recrystalise the perovskite to achieve much higher quality films with dramatically improved performance. Nikita et al used this phenomenon to make acetonitrile a valid solvent by attempting to dissolve CH_3NH_3I and PbI_2 in a 1:1 molar ratio to a concentration of 0.4 M in acetonitrile. The result was a black precipitate of $CH_3NH_3PbI_3$ crystals in the acetonitrile solution, but they found that the black crystals could be dissolved completely by bubbling methylamine gas through the solution for several minutes. Spin-coating the resulting solution using a simple one step method would then reliably create films with exceptionally low roughness with strong PL and very high uniformity. Films made in this way showed dramatic improvement in solar cell performance over all other deposition methods, but it was the low roughness and strong PL that was of interest to us because it would

seem to be an ideal method for making perovskite lasers.

Figure 12 - Images from Noel et al **[18]**. *(a) Attempting to dissolve $CH_3NH_3PbI_3$ in acetonitrile, resulting in a black precipitate which dissolves completely after bubbling with methylamine gas. (b) The resulting perovskite films are extremely smooth and reflecting. (c) An SEM image of the resulting films*

To reproduce Noel's results, we mixed high purity PbI_2 and CH_3NH_3I in a 1:1 molar ratio at 0.4 M concentration in acetonitrile. Once the black crystals had formed, we passed methylamine gas through the solution by bubbling an N_2 carrier gas through a solution of methylamine dissolved in water to cause outgassing, and the resulting methylamine/nitrogen mixture was passed through a drying tube and into the acetonitrile mixture. Following this we then spin-coated the solution in a nitrogen glovebox at 2000 RPM for 60 s before annealing the film at 100 ^{o}C for 60 minutes. The resulting films were by far the highest quality we had yet come across, with a mirrored surface and completely uniform coverage. Dektak measurements showed a film thickness of ~300 nm and, SEM images of the resulting films (figure 13) show a highly dense network of ~200 nm crystallites with a complete absence of pinholes. This is somewhat smaller than what Noel et al reported (observing ~1 µm crystals), but our methods consistently produced similar sized crystals in a variety of conditions. Switching the processing between an N_2 atmosphere and dry air made very little difference, and adjusting the annealing time seemed to affect the conductivity but not the crystal size. It was much harder to get clear SEM images of samples with only 5 minute annealing time as opposed to 60 minutes, indicating that the shorter annealing time had severely reduced the conductivity, but the observed crystals were roughly the same size.

It is worth noting that this method does not work for $CH_3NH_3PbBr_3$ films because the methylamine gas does not affect the bromide perovskite in the same way that it works for the iodide. Exposing $CH_3NH_3PbBr_3$ films to methylamine gas makes them become very rough, and they permanently lose their colour and luminescence. Attempting to dissolve bromide salts in acetonitrile seems promising at first because it results in a precipitation of bright orange $CH_3NH_3PbBr_3$ crystals, and bubbling the mixture with methylamine gas does cause the crystals to dissolve. However the solutions will tend to produce a white precipitate after only a few hours, and spin-coating from these solutions resulted in

colourless films with very poor coverage and a high roughness. Hence this method is only suitable for depositing exactly $CH_3NH_3PbI_3$.

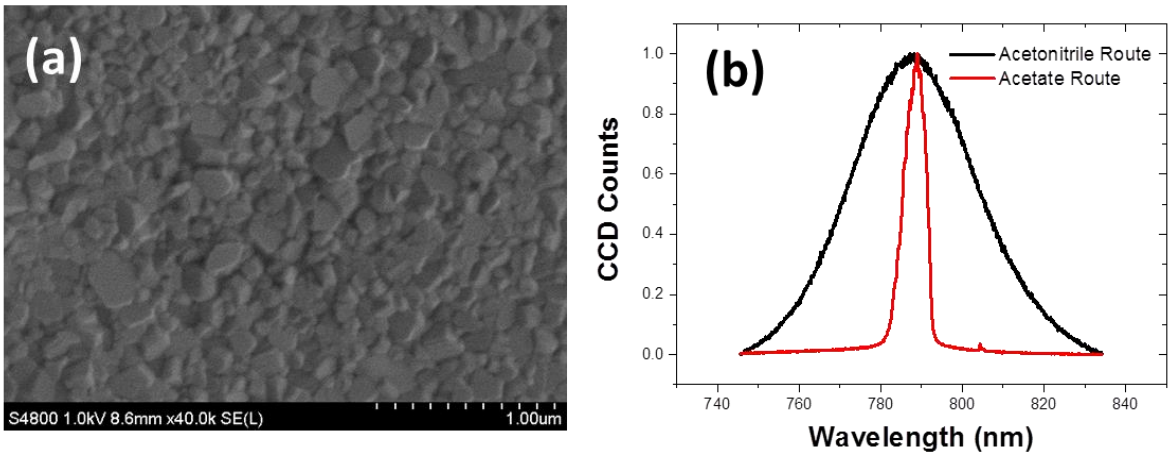

Figure 13 – (a) SEM image of the $CH_3NH_3PbI_3$ films formed by the acetonitrile route in St Andrews. (b) Comparison of the normalised emission spectra from $CH_3NH_3PbI_3$ deposited via the acetate and acetonitrile routes at ~400 μJcm^{-2}.

The high film quality would suggest that $CH_3NH_3PbI_3$ films from this method should have ASE at an extremely low threshold. However, we found that films from this route would not produce ASE even at the maximum power of the CryLas, as can be clearly seen in figure 13 (b). Switching to 400 nm excitation with 4 ns pulses from an optical parametric oscillator allowed us to achieve pump fluences in excess of 1000 μJcm^{-2}, but even at these powers the films would only emit bright PL in all directions, with no sign of stimulated emission. We spent a significant amount of time altering the parameters of this method by adjusting annealing times, modifying the stoichiometry of the precursor solutions, and spin-coating in humid, dry, and nitrogen atmospheres. But in all cases the films would emit strong PL but no ASE.

To investigate the reasons for this, we performed a comparison of time resolved PL measurements on films from both the acetate and acetonitrile route using the EI fluorimeter (see chapter 3 for details). Measuring films from the acetate route, the PL decay cannot be fitted with a single exponential because the slope changes with time. As can be seen on figure 14 (a), it starts with a steep slope of roughly 60 ns lifetime, and over time it tends towards a pure exponential with 300 ns lifetime. But overall it decays by $\frac{1}{e^4}$ in 1000 ns, giving a very rough average for the lifetime of 250 ns. This is in good agreement with reports on this route by Zhang et al, which would indicate that this deposition route is working as planned.

The total rate of recombination in a film is the sum of the radiative and non-radiative rates in the material. Since the radiative rate of a given material does not tend to change much between different materials, a longer PL lifetime is generally a very good thing because would indicate that

there has been a reduction in traps and other non-radiative pathways in the film. Films from the acetonitrile route were reported by Noel et al to have a clear single exponential decay with a lifetime of roughly 676 ns, suggesting that they have greatly reduced loss pathways in the material and should make an excellent gain medium. However, when we measured our films using the EI fluorimeter we found that the films had a very non-exponential decay with a maximum lifetime of 20 ns (figure 14b). This would explain the lack of ASE from the films, since it is clear that our acetonitrile films have much higher non-radiative losses than films from the acetate route. But it is not clear to us why our results diverge so much from the literature reports. We found that this short lifetime would occur regardless of the solution stoichiometry and processing conditions, so it is likely that there is another hidden factor that is proving detrimental to this method. In any case, this is a very surprising result and certainly warrants further investigation into the photophysics of films from different processing routes.

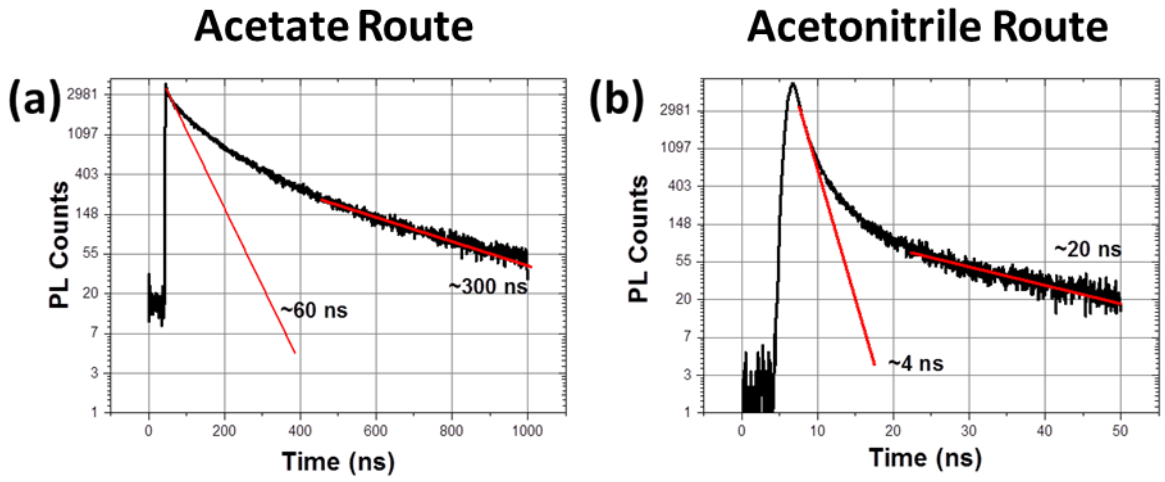

Figure 14 - Time resolved PL measurement of films from (a) the acetate route and (b) the acetonitrile route. Note that the acetate route has a much longer lifetime.

Conclusion and Next Steps

In conclusion, this section describes the use of the lead acetate perovskite deposition route to produce the first all solution-processed distributed feedback laser. We show that perovskites have many favourable properties which are perfectly suited for use in thin film lasers, but the multicrystalline nature of their films remains their biggest weakness. We found that the quality of the perovskite film must be extremely high in order to prevent scattering modes from eclipsing the feedback mode, and so the thickness of useful lasing films is limited by fall-off in film quality with

increased thickness. Even once these parameters were optimised, we found that scattering was still a major factor increasing lasing threshold and causing multimodal operation.

Despite the issues with scattering, $CH_3NH_3PbI_3$ lasers were found to have a threshold which is competitive with many organic materials, whilst having some very different properties. In particular, $CH_3NH_3PbI_3$ proved to have very good stability in comparison to most organic films, and its low exction binding energy and high charge mobility make it a very exciting candidate for CW operation and electrical pumping. In addition, the fact that $CH_3NH_3PbI_3$ emits in the infrared is a very unusual property in thin film lasers, since it is very unusual to find a good light emitting OSC with a bandgap narrower than 700 nm. Although this property makes $CH_3NH_3PbI_3$ lasers considerably more difficult to work with on the experimental side, it does make them of significant interest for certain applications where organic DFB lasers have been previously overlooked. The most notable of these is light assisted medical applications, where the infrared emission of the $CH_3NH_3PbI_3$ laser results in much less scattering and absorption in human tissue, thus allowing much greater tissue penetration than in lasers operating in the visible spectrum.

After observing high stability of perovskite lasers under fs excitation, we performed an investigation into the behaviour of $CH_3NH_3PbI_3$ lasers under high repetition rates. We found that the perovskite was able to withstand the extremely high powers experienced when approaching the quasi CW regime, but there appears to be a secondary heating effect that prevents the sample from lasing when under an 80 MHz pump source. If these heating effects could be overcome, then perovskite lasers could prove to be an excellent material for quasi CW laser sources. Finally, we performed an investigation into the use of acetonitrile as a solvent for perovskites in an attempt to improve threshold. Although the film quality was very promising, our films made via this route had very poor light emission properties and were therefore unsuitable for lasing. In light of all the above results, perovskite lasers have proven themselves to have great potential as a lasing medium, and definitely warrant further study to see if they can be pushed towards commercial viability.

References

1. Dongqin Bi, W.T., M. Ibrahim Dar, Peng Gao, Jingshan Luo, Clémentine Renevier, Kurt Schenk, Antonio Abate, Fabrizio Giordano, Juan-Pablo Correa Baena, Jean-David Decoppet, Shaik Mohammed Zakeeruddin, Mohammad Khaja Nazeeruddin, Michael Grätzel, Anders Hagfeldt, *Efficient luminescent solar cells based on tailored mixed-cation perovskites.* Science Advances, 2016. **2**(1), 1501170.
2. Nana Wang, L.C., Rui Ge, Shuting Zhang, Yanfeng Miao, Wei Zou, Chang Yi, Yan Sun, Yu Cao, Rong Yang, Yingqiang Wei, Qiang Guo, You Ke, Maotao Yu, Yizheng Jin, Yang Liu, Qingqing Ding, Dawei Di, Le Yang, Guichuan Xing, He Tian, Chuanhong Jin, Feng Gao, Richard H.

Friend, Jianpu Wang, Wei Huang, *Perovskite light-emitting diodes based on solution-processed self-organized multiple quantum wells.* Nature Photonics, 2016. **10**: p. 699-704.
3. W Zhang, M.S., D.T Moore, S.K Pathak, M.T Horantner, T Stergiopoulos, S.D Stranks, G.E Eperon, J.A Alexander-Webber, A Abate, A Sadhanala, S.H Yao, Y.L Chen, R.H Friend, L.A Estroff, U Wiesner H.J Snaith, *Ultrasmooth organic-inorganic perovskite thin-film formation and crystallization for efficient planar heterojunction solar cells.* Nature Communications, 2015. **6,** 6142.
4. W Zhang, S.P., N Sakai, T Stergiopoulos, P.K Nayak, N.K Noel, A.A Haghighirad, V.M Burlakov, D.W deQuilettes, A Sadhanala, W.Z Li, L.D Wang, D.S Ginger, R.H Friend, H..J Snaith, , *Enhanced optoelectronic quality of perovskite thin films with hypophosphorous acid for planar heterojunction solar cells.* Nature Communications, 2015. **6,** 10030.
5. S.D Stranks, S.M.W., K Wojciechowski, F Deschler, M Saliba, H Khandelwal, J.B Patel, S.J Elston, L.M Herz, M.B Johnston, A.P.H.J Schenning, M.G Debije, M.K Riede, S.M Morris, H..J Snaith, , *Enhanced Amplified Spontaneous Emission in Perovskites Using a Flexible Cholesteric Liquid Crystal Reflector.* Nano Letters, 2015. **15**(8): p. 4935-4941.
6. Askar, A.M., Shankar, K., *Exciton Binding Energy in Organic-Inorganic Tri-Halide Perovskites.* Journal of Nanoscience and Nanotechnology, 2016. **16**(6): p. 5890-5901.
7. A Miyata, A.M., P Plochocka, O Portugall, J.T.W Wang, S.D Stranks, H.J Snaith, R.J Nicholas, , *Direct measurement of the exciton binding energy and effective masses for charge carriers in organic-inorganic tri-halide perovskites.* Nature Physics, 2015. **11**(7): p. 582-U94.
8. M Cadelano, V.S., N Sarritzu, D Marongiu, F Chen, R Piras, R Corpino, C.M Carbonaro, F Fuochi, M Saba, A Mura, G Bongiovanni, *Can Trihalide Lead Perovskites Support Continuous Wave Lasing?* Advanced Optical Materials, 2015. **3**(11): p. 1557-1564.
9. B Maynard, Q.L., E.A Schiff, M..J Yang, K Zhu, R Kottokkaran, H Abbas, V.L. Dalal, , *Electron and hole drift mobility measurements on methylammonium lead iodide perovskite solar cells.* Applied Physics Letters, 2016. **108**(17),173505.
10. P Loper, M.S., B Niesen, J Werner, M Filipic, S.J Moon, J.H. Yum, M Topic, S De Wolf, C Ballif, , *Complex Refractive Index Spectra of CH3NH3PbI3 Perovskite Thin Films Determined by Spectroscopic Ellipsometry and Spectrophotometry.* Journal of Physical Chemistry Letters, 2015. **6**(1): p. 66-71.
11. P.O Morawska, Y.W., A Ruseckas, C Orofino-Pena, A Kanibolotsky, R Santhanagopal, N Frohlich, M Fritsch, S Allard, U Scherf P.J Skabara, I.D.W Samuel, G.A. Turnbull, , *Side-Chain Influence on the Mass Density and Refractive Index of Polyfluorenes and Star-Shaped Oligofluorene Truxenes.* Journal of Physical Chemistry C, 2015. **119**(38): p. 22102-22107.
12. G Heliotis, D.D.C.B., G.A. Turnbull, I.D.W Samuel, *Light amplification and gain in polyfluorene waveguides.* Applied Physics Letters, 2002. **81**(3): p. 415-417.
13. Guy L. Whitworth, J.R.H., David N. Miller, Gordon J. Hedley, Wei Zhang, Henry J. Snaith, Graham A. Turnbull, and Ifor D. W. Samuel *Nanoimprinted distributed feedback lasers of solution processed hybrid perovskites* Optics Express, 2016. **24**(21): p. 23677-23684.
14. Yakunin, S., et al., *Low-threshold amplified spontaneous emission and lasing from colloidal nanocrystals of caesium lead halide perovskites.* Nature Communications, 2015. **6**.
15. Sandanayaka, A.S.D., et al., *Toward continuous-wave operation of organic semiconductor lasers.* Science Advances, 2017. **3**(4).
16. Y.F Jia, R.A.K., A.J Grede, B.P Rand, N.C Giebink, , *Continuous-wave lasing in an organic-inorganic lead halide perovskite semiconductor.* Nature Photonics, 2017. **11**(12): p. 784-+.
17. K.W Wu, A.B., C Ma, M.Y Du, Y Yang, L Li, T Wu, *Temperature-dependent excitonic photoluminescence of hybrid organometal halide perovskite films.* Physical Chemistry Chemical Physics, 2014. **16**(41): p. 22476-22481.
18. N.K Noel, S.N.H., B Wenger, M.T Klug, M.T Horantner, M.B Johnston, R.J Nicholas, D.T Moore, H.J Snaith, *A low viscosity, low boiling point, clean solvent system for the rapid*

crystallisation of highly specular perovskite films. Energy & Environmental Science, 2017. **10**(1): p. 145-152.
19. H Yu, X.D.L., Y.J Xia, Q.Q Dong, K.C Zhang, Z.W Wang, Y Zhou, B Song, T.F Li, *Room-temperature mixed-solvent-vapor annealing for high performance perovskite solar cells.* Journal of Materials Chemistry A, 2016. **4**(1): p. 321-326.
20. Z.M Zhou, Z.W.W., Y.Y Zhou, S.P Pang, D Wang, H.X Xu, Z.H Liu, N.P Padture, G.L Cui, *Methylamine-Gas-Induced Defect-Healing Behavior of CH3NH3PbI3 Thin Films for Perovskite Solar Cells.* Angewandte Chemie-International Edition, 2015. **54**(33): p. 9705-9709.

Chapter 6 – Optimising PL for Green Perovskite Lasers with Enhanced Threshold

Motivation

The work in the previous chapter provided a clear demonstration of the potential of perovskites as a lasing medium, but it was also clear that there was significant room for improvement. A key point of this was that, while the lasers showed good stability, their threshold of 110 μJcm^{-2} under ns pumping was still significantly higher than the best organic semiconductors (OSCs). Some OSCs can achieve thresholds of less than 200 $nJcm^{-2}$ under 4 ns pumping [1], and perovskite lasers will need to at least be competitive with this if they are to achieve commercial viability or electrical pumping. If a perovskite laser could match this threshold, it would allow them to be pumped via pulsed light emitting diode s[2] – a much more compact and practical pump source than the lasers we use in the lab. Additionally, it would be of significant commercial interest if we could exploit the tuneable bandgap of hybrid perovskites to achieve laser emission in the "green gap" region of the spectrum that is currently unavailable to commercial inorganic lasers. Commercial indium gallium nitride lasers can access wavelengths up to 525 nm, while aluminium gallium indium phosphide lasers can cover wavelengths above 635 nm, but finding materials which can usefully emit laser light in the yellow-green part of the spectrum remains a major challenge which hybrid perovskites could overcome.

Electrically pumped green emission is currently achieved by using a diode laser to pump a Nd:YAG laser that emits at 1064 nm. A frequency doubling crystal is then placed inside the lasing cavity with the Nd:YAG crystal, which doubles the 1064 nm light to 532 nm, which appears as a pure green. This has proven to be effective and commercially viable, but it does not have the compactness and easy scalability that conventional diode lasers have.

To achieve the low threshold objective, we aimed to further optimise two key parameters in the perovskite films – scattering losses and PLQY. In the last chapter, we found that a perovskite film must be as smooth as possible in order to reduce scattering from the multicrystalline film. It would also seem logical that films with smaller crystals and less clearly defined boundaries would be less

likely to scatter the waveguided mode, thus achieving lower threshold. The importance of this was highlighted previously, where it was found that the laser would not operate at all if the scattering was too high. Of possibly more significance is the PLQY of perovskites. The best performing OSC laser materials all have PLQY values exceeding 80 % at most intensities [3], while the PLQY of most perovskites is close to zero for low intensities and only becomes significant under high powers [4]. With this in mind, it is indeed impressive that the lasing thresholds in perovskites are as low as they are. But if the PL behaviour could be improved so that the PLQY reaches higher values at lower intensities it could enable perovskites to reach the lasing regime at much lower pump thresholds.

To achieve emission in the "green gap" part of the spectrum, we switched from $CH_3NH_3PbI_3$ to $CH_3NH_3PbBr_3$ – an exact analogue of the original material with the exception that it has a Br^- ion replacing the I^- ion. The smaller ionic radius of the Br^- ion causes the peak emission to shift from 790 nm to 550 nm, thus providing light emission in the "green gap" which also has the advantage of being near the peak response point of the human eye. A big problem with optimising the PLQY in $CH_3NH_3PbI_3$ is that it emits in the infrared, meaning that it is not possible to quickly determine if a sample is strongly light emitting by using the human eye, and measuring PLQY is also significantly more difficult as many sensors start to become less responsive in this region. Working with green-emitting $CH_3NH_3PbBr_3$ greatly streamlined this optimisation process, as it was possible to rapidly screen deposition methods by simply illuminating samples with a UV lamp immediately after fabrication to qualitatively assess the strength of their PL.

Exploring Different Deposition Methods

Acetate Route

$CH_3NH_3PbBr_3$ can be deposited using identical processing methods to $CH_3NH_3PbI_3$, so long as the molar ratios of the precursors are kept the same, and so a good point to begin studying the PL would be on films of $CH_3NH_3PbBr_3$ deposited via the lead acetate route, since this had proved to be successful in the previous chapter. To deposit films via this route, 154 mg methylammonium Bromide (MABr) was dissolved with 175.6 mg lead acetate (pbac) in 1 ml dimethyl formamide (DMF) with 3 µl of hypophosphorous acid (HPA) as an additive. Essentially an exact analogue of the route used in the previous chapter, with MABr replacing methylammonium iodide [5, 6]. The resultant solution was spin coated at 2000 RPM in an N_2 glovebox and then annealed for 5 minutes at 100 ^oC. The resulting films could be visually seen to have excellent optical quality with very little scattering, and surface profilometry found their thickness to be ~ 190 nm. To further assess their quality, the films were imaged using atomic force microscopy, and were found to have a low root mean square

(r.m.s) roughness of 15 nm over a 5x5 µm area, which is in good agreement with the observations of Zhang et al. when the method was first proposed. However, despite their high optical quality it was clear that films made via this route had a very low PLQY – no light emission visible to the human eye was observed when the samples were exposed to UV light from a lamp, and measurements using the Hamamatsu PLQY setup measured zero signal coming from the samples. In spite of this weak PL, ASE measurements taken by exciting the films in a stripe using the pulsed CryLAS laser found that the films could readily support ASE at a reasonable threshold of 125 µJcm^{-2}, as shown in figure 1.

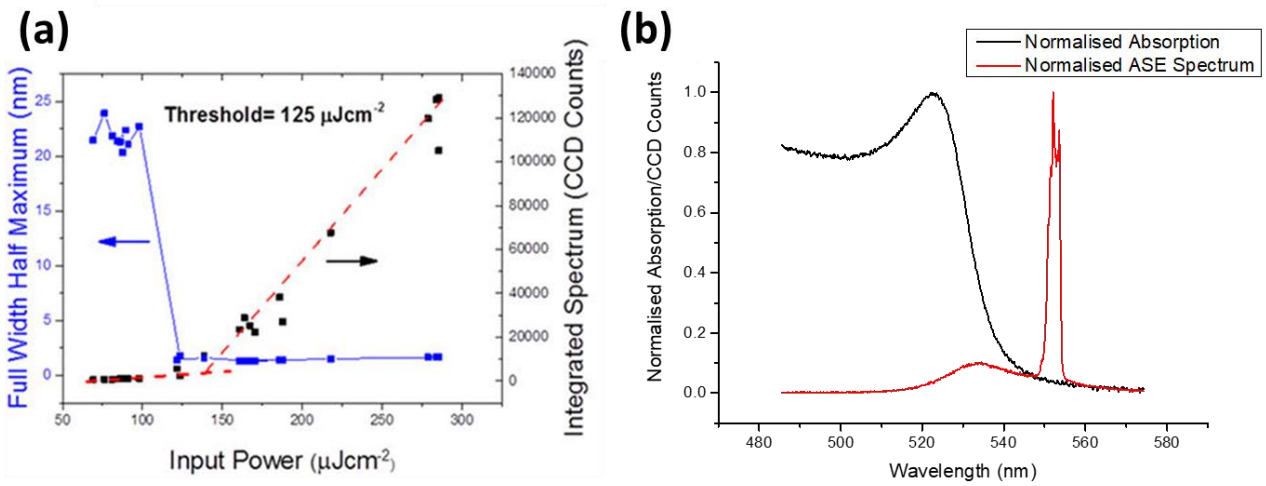

Figure 1 – (a) The ASE threshold of a film of $CH_3NH_3PbBr_3$ made via the acetate route. The PL counts deviate from linear and the FWHM drops dramatically at roughly 125 µJcm^{-2}. (b) The ASE and absorption spectra for $CH_3NH_3PbBr_3$ fims. The ASE peak is between 546 nm and 556 nm. Images taken from our paper [7].

From these results it is clear that, while the PLQY of these $CH_3NH_3PbBr_3$ films is very poor at low intensities, it must increase significantly as the ASE regime is reached. To study this further, I worked with Iain Harrison, a final year undergraduate project student, to perform intensity dependent PL measurements on $CH_3NH_3PbBr_3$ films. The overall aim of this was to excite the films with a 355 nm pulsed DPSS laser (1 ns pulses, 2.5 KHz rep rate, 2 mm beam diameter) and measure the PLQY as a function of the beam intensity. This would be done using the PLQY setup described in chapter 3 [8], with a series of ND filters being used to alter the intensity of the pump beam. Unfortunately, taking absolute PLQY measurements of the films proved to be too difficult when using a 355 nm pump source because we could not perform a sufficiently accurate calibration of the spectral response of the system at wavelengths as short as 355 nm. The calibration light source was a Bentham calibrated tungsten lamp, which did not have sufficient intensity at 355 nm to provide a good calibration, meaning that any PLQY measurements would have unacceptable error margins in their results. Since 355 nm was the only pulsed laser source readily available to us, we were forced to take relative measurements on a given sample within the integrating sphere, but without a complete calibration

for the spectral response of the sphere. These measurements could be accurately used to compare results from the same film at different intensities, but could not be used to get quantitative measurements of absolute quantum yields. Since the aim of the experiment was to observe trends rather than absolute values, this was deemed sufficient for our purposes.

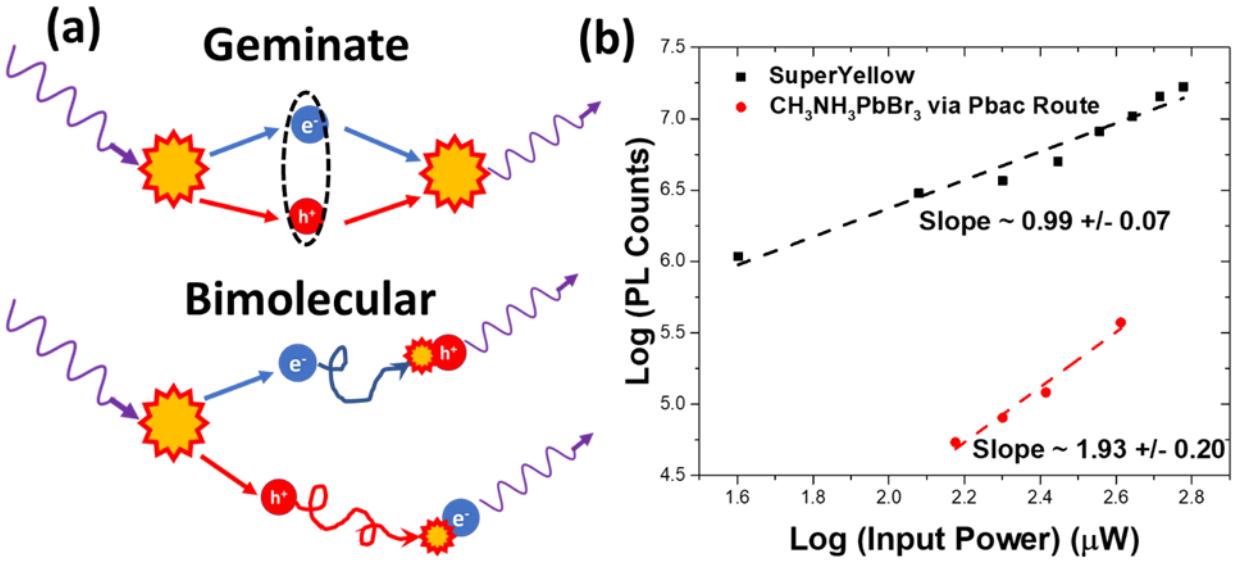

Figure 2 - (a) The difference between bimolecular and geminate recombination. In the geminate case an electron will recombine with the same electron it came from, effectively making the recombination a single particle process, while in bimolecular recomnbination the pair complely separates amd the charges will find other electrons and holes to recombine with, making it a 2 particle process. (b) shows a log-log plot of PL counts vs input power for SuperYellow and $CH_3NH_3PbBr_3$ films. Note that the $CH_3NH_3PbBr_3$ film could not be measured at very low powers because the signal to noise ratio became too high for accurate measurements.

Measuring the PL strength as a function of pump pulse fluence, one would expect a material with an intensity independent PLQY to follow a trend where PL counts are directly proportional to pump fluence. In organic semiconductors, this is exactly what is observed because the radiative recombination tends to be geminate – that is an absorbed photon creates a bound electron and hole pair (exciton), which will then recombine to create light in the way shown in figure 2. Since the excitons do not need other excitons to help them recombine radiatively, the efficiency of recombination should remain constant except at extremely high intensities where higher order effects such as Auger recombination (which are usually bad) start coming into play. Many inorganic semiconductors are the opposite case to this, where the absorbed photons create free electrons and holes which must then find each other again if they are to recombine radiatively. In this case, the efficiency will increase with excitation density because more excited charges means more potential for a hole to quickly find an electron and recombine before they fall back down via a trap state or

other non-radiative pathway. This is known as bimolecular recombination, and in this case the PL should be proportional to the excitation density squared.

Using our setup, we were able to measure the PL from films of SuperYellow (a commonly used organic light emitting polymer) at pump fluences between 0.4 and 6 μJcm^{-2}. The data on a log-log curve follows a straight line, and the slope indicates the power law which the PL vs pump fluence curve follows. The data, plotted in figure 2 (b), shows that SuperYellow has a slope very close to unity. This indicates that the recombination in this film is geminate in nature, which is exactly as expected for a polymer with a strong exciton binding energy. Comparing this to a film of $CH_3NH_3PbBr_3$ deposited via the lead acetate route, which has a slope of 1.9, it becomes clear that the $CH_3NH_3PbBr_3$ films have strong bimolecular behaviour. This explains why the PL is so weak at low intensities because the charges are unable to find counterparts to recombine with. Therefore, most of them will decay non-radiatively through trap assisted recombination or similar processes, unless the excitation density is substantially increased.

Assisted Nanocrystal Pinning

If the problem with our films is that the bimolecular nature of the recombination means the material only works at very high powers, does that mean that the problem could be solved by making the recombination more geminate in nature? One method of achieving this, proposed by Tae Woo Lee and coworkers [9] was to develop a spin coating method that produced very small crystals. He proposed that the charges were much slower when crossing the crystal boundaries than moving through the bulk crystal, and so a small crystal would effectively confine the generated electron – hole pairs in a small space in the way shown on figure 3, thus forcing them to recombine in a manner which was closer to the geminate nature seen in organics. Creating small crystals in this way is then obviously a bad thing for solar cells, which aim to separate the charge, but it could be an excellent way of making films for perovskite LEDs and lasers. By following this logic, Lee was able to create perovskite light emitting diodes with external quantum efficiencies greater than 8.5 %, using an adapted version of the nanocrystal pinning technique.

The precursor solution for this assisted nanocrystal pinning (A-NCP) recipe was a 0.6 M solution of $PbBr_2$ and CH_3NH_3Br in a 1:1.05 molar ratio dissolved in DMSO. The bromide salts were generally much more soluble than the iodide salts, and the precursors would be completely dissolved after 5 minutes of vigorous shaking to form a colourless solution. The solution contained a slight excess of CH_3NH_3Br in order to minimise the amount of uncoordinated Pb^{2+} ions, which have been shown to be a major source of trap states in the perovskite films [10], thus helping to improve the light emission. The solution would then be spin coated in a nitrogen glovebox in a 2 step process, starting

at 500 RPM for 7 seconds to provide a thick coating followed by a 90 s step at 3000 RPM. During this second stage, the spinning sample would be washed with an antisolvent of dichloromethane (DCM) containing 5 $mgml^{-1}$ 2,2',2"-(1,3,5-Benzinetriyl)-tris(1-phenyl-1-H-benzimidazole) (TPBi). The addition of TPBi to the antisolvent was shown by Lee to substantially reduce crystal size, and we observed that the resulting $CH_3NH_3PbBr_3$ films were much more luminescent than films made without the additive. The exact timing of the washing step would vary from day to day due to fluctuations in room temperature due to changes in the solvent evaporation rate, but the optimal washing time to achieve high film quality was usually approximately 40 s into the 3000 RPM step. In each device run, several test samples would be spun to find the optimal timings before the main samples were fabricated. Following the spin coating the films were then annealed at 90 ^{o}C for 10 minutes.

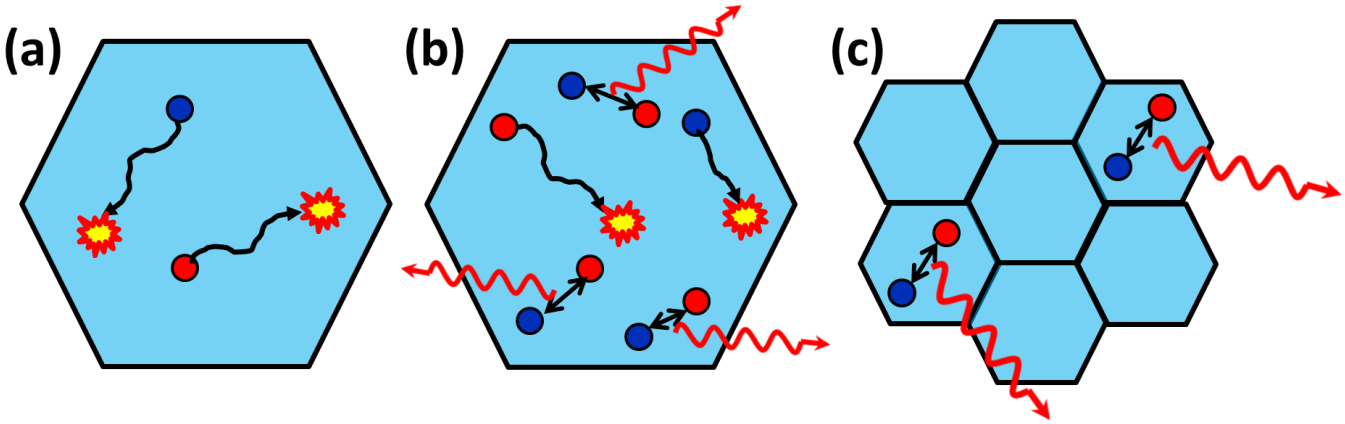

Figure 3 - (a) In large crystals the free charges cannot find each other to recombine, so strong PL is only seen at high intensities, as seen in (b) where there are many charges available for recombination. (c) In small crystals the charges are confined and forced to recombine radiatively.

As a first screening to observe their PL, the samples were illuminated with a UV lamp during the various stages of fabrication. The samples were observed to immediately glow bright green when the antisolvent was dropped on the film, indicating the immediate formation of highly luminescent $CH_3NH_3PbBr_3$ crystals. This PL was observed to grow weaker over the course of the spin coating and annealing steps, presumably due to the crystals growing to a larger-than-optimal size, but all samples would eventually stabilise to have a similar level of PL, which was still easily visible to the human eye – a much better result than seen with the acetate route. Attempts to prevent this initial decline in PLQY proved fruitless, as the film would always decay to be roughly the same brightness even if the annealing step was completely removed or the spin coating time reduced. Unannealed films were also found to be much more vulnerable to degradation than annealed films, and so it was concluded that the above conditions were optimal.

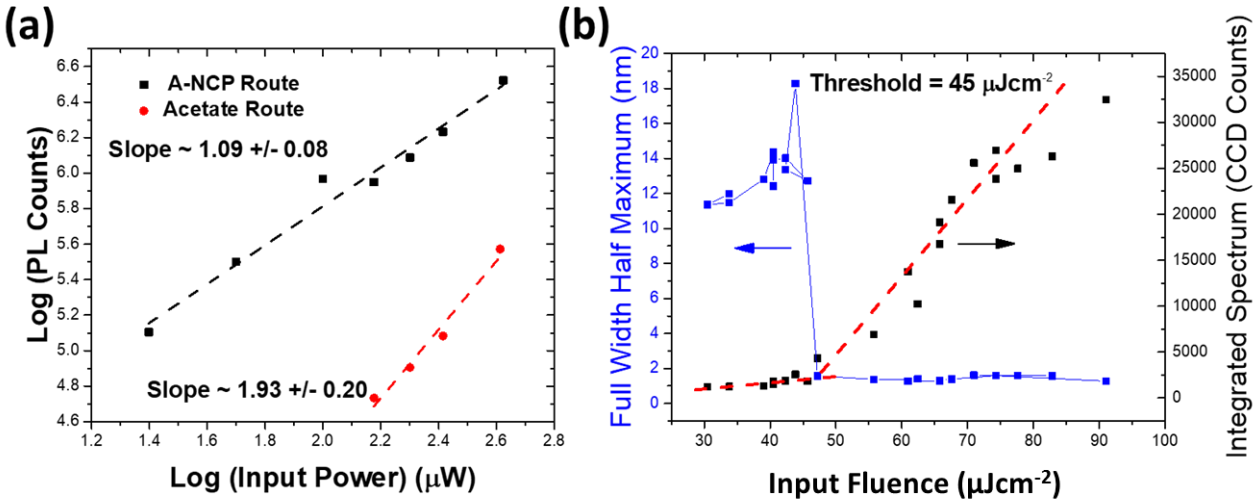

Figure 4 - (a) Log-Log plot of PL counts vs power for $CH_3NH_3PbBr_3$ from the acetate route (black) and the A-NCP route (red). Note that the A-NCP has a slope much closer to one, indicating recombination which is more geminate in nature. (b) ASE threshold of $CH_3NH_3PbBr_3$ made by the A-NCP route. The red dashed line is a guide to show the threshold. [7].

To provide a more quantitative comparison to the acetate route, we once again measured the intensity dependence of the PLQY. The log-log plot of the PL to excitation power shows a slope of 1.1 (see figure 4), indicating that the A-NCP route bringis the material very close to the geminate recombination seen in organic semiconductors. This is an excellent sign as it shows that control of the crystal size does indeed grant a measure of control over the nature of recombination in the film. Absolute PLQY measurements were also performed using continuous wave, 442 nm excitation from a helium-cadmium laser source at an intensity of 4.2 Wcm^{-2}, yielding a PLQY of 5 % while films from the acetate route could not produce a signal large enough to accurately measure (meaning a value of much less than 1 %). This substantial improvement in PL properties for the A-NCP route translated into a much lower ASE threshold of 45 μJcm^{-2} (shown in figure 4), which is a factor of 3 reduction over the acetate route (shown in figure 1). Hence, considering its high PLQY and low ASE threshold it appears likely that the A-NCP route would be the superior method for the production of perovskite lasers.

Film Quality and Scattering

While the PL measurements of the films provided a good measure of the gain which these films could provide, the scattering losses are of equal, if not greater importance because the scattering can completely destroy the distributed feedback. Best films from the two routes were measured for waveguiding loss using the method described in chapter 3. The results are shown in figure 6, and it was found that films from the acetate route have an exceptionally low loss coefficient of 2.5cm^{-1} while films from the A-NCP route have a loss of 8.7cm^{-1}. These values are both more than low

enough to be useful in DFB lasers, but looking at the visual appearance of the films it becomes clear why the acetate route is so much better in this regard. The acetate route gives clear, glassy films which provide pristine reflections of their environment, indicating extremely low scattering within the film. Films from the A-NCP route on the other hand are still smooth, but they have many visual imperfections within the film. These are likely caused by the much faster formation of the $CH_3NH_3PbBr_3$ crystals, and the result is a film which is much less reflective with some noticeable scattering.

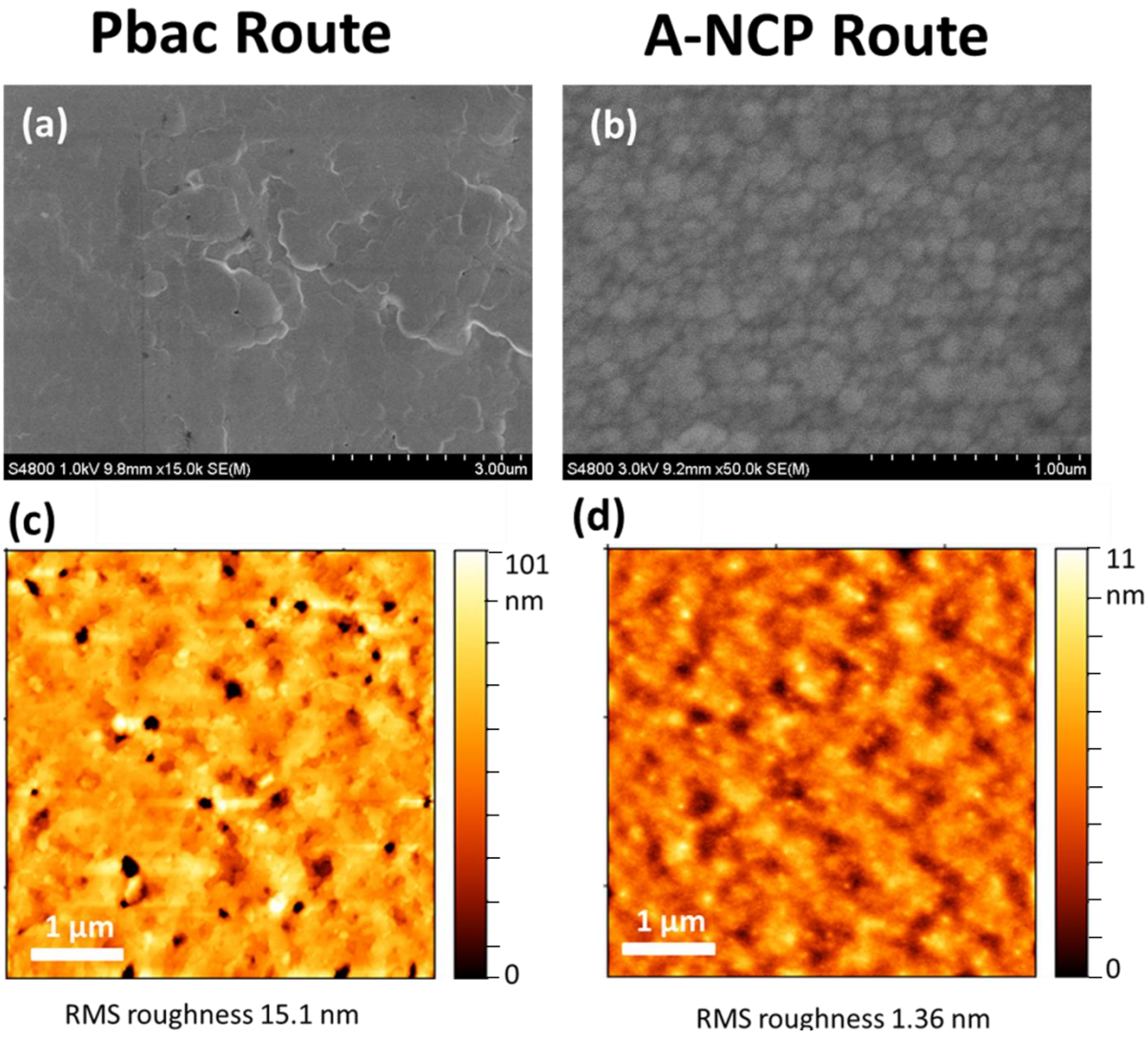

Figure 5 - SEM images of $CH_3NH_3PbBr_3$ films from (a) the acetate route and (b) the A-NCP route. (c) and (d) show 5x5 micron AFM roughness measurements of the acetate and A-NCP routes respectively. Images from our paper [7].

Part of the reason for this can also be seen from SEM images of the films shown in figure 5. Films from the A-NCP route show a dense network of clear crystals of ~300 nm size and a complete absence of pinholes, while the acetate route has a smooth landscape of weakly defined crystals with a small number of pinholes. The strong crystal boundaries are likely a major contributor to the

higher scattering coefficient of the films from the A-NCP route, while the small pinholes seen in the acetate route will be problematic for electrical devices but are too small and thinly spread to cause significant optical scattering. In spite of the higher scattering, one major surprise of the A-NCP route was that its root mean square (r.m.s) roughness was a factor of 10 lower than in the acetate route, despite the smoother visual appearance of the acetate route. Atomic force microscopy measurements on the films, seen in figure 5, showed that the acetate route had an r.m.s roughness of 15 nm on a 5x5 µm scan area, while A-NCP films showed an exceptionally low roughness of 1.3 nm on the same area. We attribute this discrepancy to the presence of pinholes in the acetate film which will go all the way through to the substrate. It can be seen in the AFM images that the roughness is mostly dominated by the presence of a small number of points which almost certainly correspond to pinholes, meaning that the average roughness is far higher than would be seen in the completely pinhole-free films made from the A-NCP route.

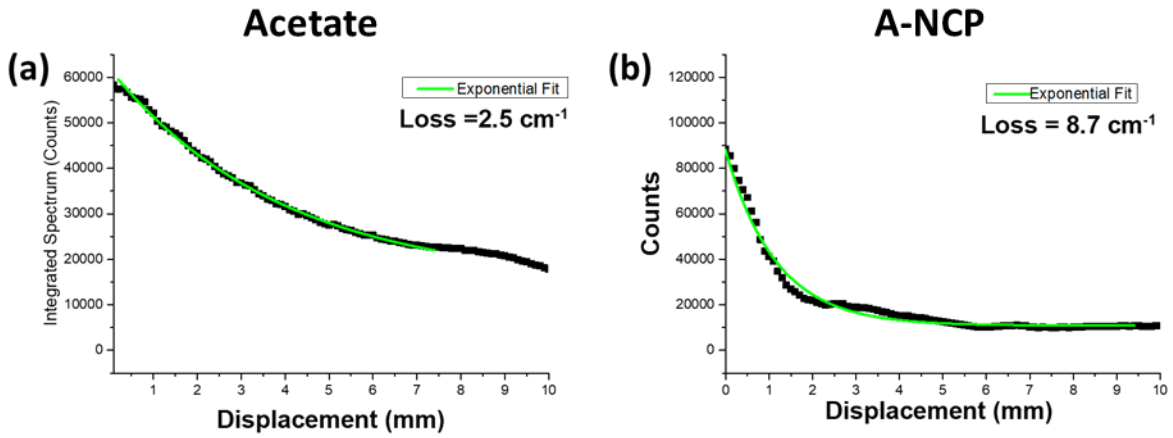

Figure 6 - Loss measurements on $CH_3NH_3PbBr_3$ films from (a) the acetate route, and (b) the A-NCP route. Images are from our paper [7].

Making a $CH_3NH_3PbBr_3$ Laser

Fabrication Process

Since the A-NCP route showed a dramatically improved threshold whilst keeping the scattering within acceptable bounds, this method was chosen for the production of green perovskite lasers. Surface profile measurements of the optimised films gave a film thickness of 140 nm, whilst the literature report the refractive index of $CH_3NH_3PbBr_3$ at its ASE peak of 550 nm to be 2.2 [11]. Modelling this film using the same logic applied in chapter 5 predicted that this waveguide would have an effective refractive index of ~ 1.91, indicating that a grating period of 290 nm should provide distributed feedback. To meet this condition, we once again used the tuneable 2D grating array of

with periods from 250 nm to 425 nm in 5 nm steps. The gratings were fabricated via UV nanoimprint lithography as described in chapter 3, and the finished gratings were pre-treated with a brief exposure in a plasma asher at low power to assist in spin coating. The $CH_3NH_3PbBr_3$ layer was then spin coated on top via the A-NCP method, and a layer of CYTOP™ amorphous fluoropolymer was added as an encapsulant via spin coating at 2000 RPM in the N_2 glovebox.

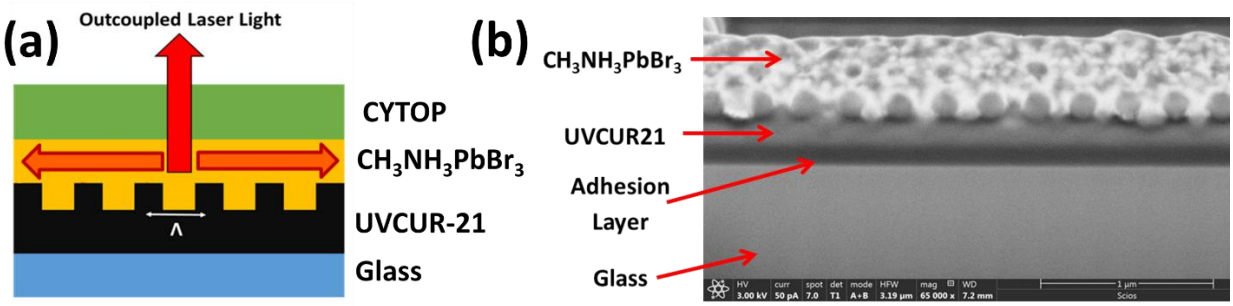

Figure 7 – (a) The basic structure of our $CH_3NH_3PbBr_3$ Lasers. (b) A transverse SEM image of a sample without a CYTOP capping layer. Images are from our paper [7].

Achieving Distributed Feedback Lasing

The completed device had a structure shown in figure 7, and a transverse SEM image of a spare sample without a CYTOP capping layer was taken to ensure that the perovskite was conforming to the gratings as expected. When the 300 nm period grating was excited with 355 nm, 1 ns pulsed light from the CryLas laser source it demonstrated clear single mode lasing emission above a pump threshold of 6 μJcm^{-2}. The emission from the sample was measured using a fibre-coupled CCD with the collection point approximately 20 cm from the sample. The pump beam was input at a 10 degree angle to ensure that no remnants of the pump were coupled into the CCD. Below threshold, the PL from the sample was weaker than the background noise in the CCD due to its high divergence, and so no measurable emission from the sample was observed. Above threshold, a clear spike in the spectrum at 547 nm appeared with a full width half maximum of ~0.2 nm. The nominal resolution of the CCD in this configuration is 0.03 nm. The emission spectrum and threshold measurement are shown on figure 8.

The exact wavelength of lasing could be tuned to a small degree (between 555 nm and 543 nm) by altering the grating period in the region between 285 nm and 305 nm, as shown on figure 9 (a), but the 300 nm grating was found to give the lowest threshold. Starting at the 285 nm grating, the lasing wavelength increased linearly with grating period up to 295 nm, where a mode hopping behaviour was observed from 555 nm to 543 nm. Above this period the lasing wavelength continued to increase linearly with grating period before disappearing in gratings of period 310 nm or larger. This

hop is attributed to a switch between TE and TM polarisations and will be discussed in more detail in the next subsection. Note that lasing could not be observed in gratings with periods greater than 305 nm or shorter than 285 nm because the feedback modes would lie outside of the region where gain was greater than loss in the perovskite film. A rough estimate of the region where gain exceeds loss can be taken from the ASE spectra of $CH_3NH_3PbBr_3$, and it can clearly be seen on figure 1 that this lies between 546 and 556 nm.

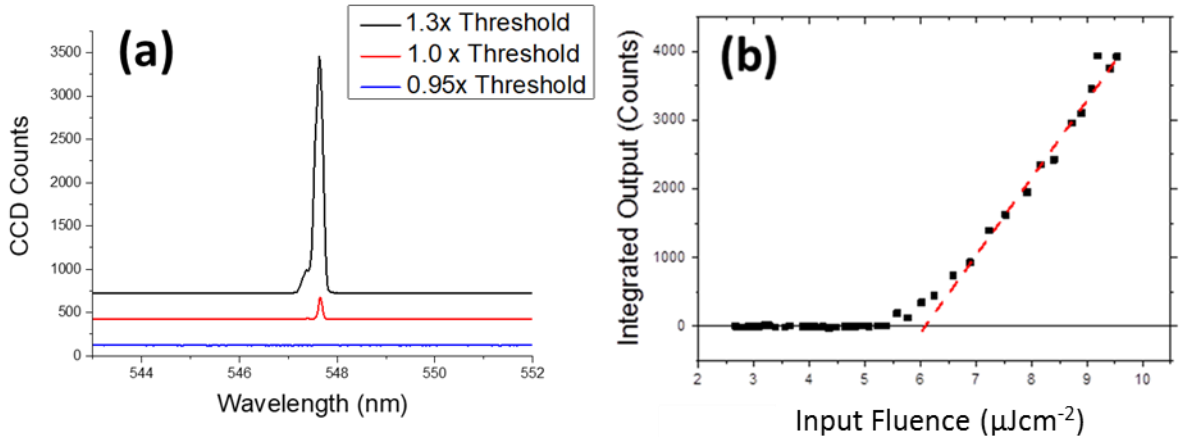

Figure 8 - (a) Emission spectra from $CH_3NH_3PbBr_3$ laser as threshold is crossed. (b) Measurement of lasing threshold of 300 nm grating. Images are from our paper [7].

It is worth noting that some, but not all of the devices made were able to sustain 2 lasing modes on the 295 nm grating – the point at which the mode hop occurs. An example of this is shown in figure 9 (b), where the laser clearly turns on at 544 nm above a pump fluence of 15 μJcm^{-2}, with a second mode at 555 nm appearing as the pump fluence was increased. This second mode appeared to have a much higher slope efficiency than the 544 nm mode, and by 35 μJcm^{-2} it dominated the spectrum. This double mode operation is caused by competition between two possible modes with similar resonance conditions (hence the hopping effect which will be further discussed later), and so if the exact conditions are met then both modes can be supported on the grating. Due to small sample to sample variations in thickness, this double mode behaviour was only observed in about 50 % of samples, indicating that there is a very narrow resonance condition for a grating to be able to support both modes simultaneously. Of more interest is why the 555 nm mode seems to grow faster with pump power than the 544 nm mode, despite the 544 nm mode having a lower threshold, since modes with a lower threshold tend to have a better slope efficiency. The results we observe contradict this general rule, and the most likely explanation for this is that the 544 nm mode has a lower surface emission loss than the 555 nm mode, which could lead to a lower threshold but weaker overall outcoupling.

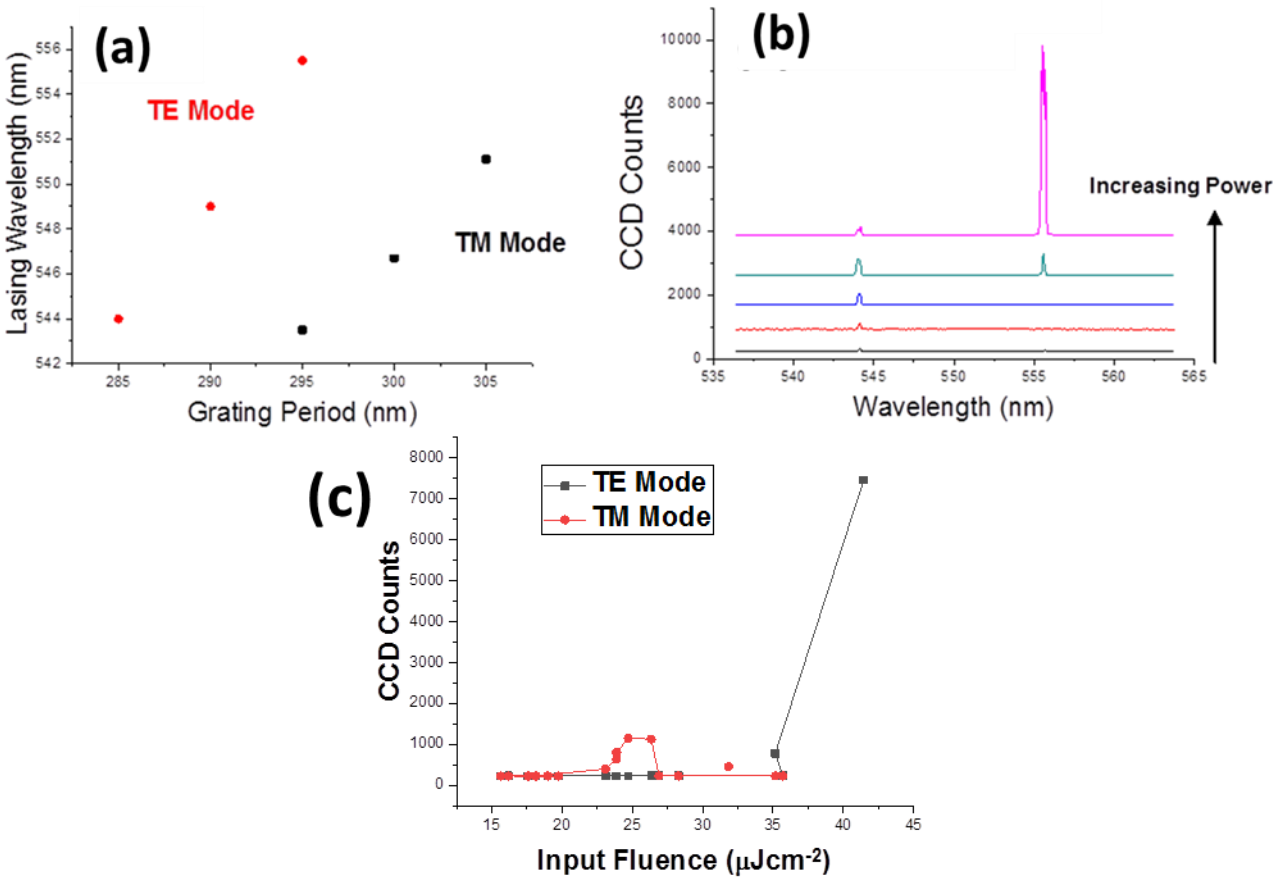

Figure 9 - (a) Lasing wavelength vs grating period. Note there is a "hop" in the lasing wavelength on the 295 nm grating. (b) Dual mode lasing from a 295 nm grating. Images are from our paper [7].(c) Graph of peak counts vs pump power for the two competing modes.

Beam Properties

A photograph of the laser emitting from the 300 nm grating is shown on figure 10 (a), while figures 10 (b) and 10 (c) show close ups of the emitted mode from the 290 nm grating and the 300 nm grating respectively – on either side of the mode hop. The lasing is clearly dominated by output from an annular transverse mode which we attribute to a 2D Bloch resonance supported by the two orthogonal grating vectors in the 2D micropillar grating array, thus creating a (1,1) output mode. Faint traces of the cross-like emission of the (1,0) and (0,1) modes can sometimes be seen in some gratings, but it is clear that the (1,1) mode dominates. This is interesting because the (1,1) mode is usually not visible in OSC lasers of identical design, suggesting that the high refractive index of the CH3NH3PbBr3 may strongly affect which modes are favourable. Other scattered light is also visible far from the centre which is due to the outcoupling of waveguided light by adjacent gratings, and the fact that these are clearly visible emphasises that this laser is achieving very low waveguide propagation losses.

Beam Properties

A photograph of the laser emitting from the 300 nm grating is shown in figure 10a, while figures 10b and 10c show close ups of the emitted mode from the 290 nm grating and the 300 nm grating respectively – on either side of the mode hop. The lasing is clearly dominated by output from an annular transverse mode which we attribute to a 2D Bloch resonance supported by the two orthogonal grating vectors in the 2D micropillar grating array, thus creating a (1,1) output mode. Faint traces of the cross-like emission of the (1,0) and (0,1) modes can sometimes be seen in some gratings, but it is clear that the (1,1) mode dominates. This is interesting because the (1,1) mode is usually not visible in OSC lasers of identical design, suggesting that the high refractive index of the $CH_3NH_3PbBr_3$ may strongly affect which modes are favourable. Other scattered light is also visible far from the centre which is due to the outcoupling of waveguided light by adjacent gratings, and the fact that these are clearly visible emphasises that this laser is achieving very low waveguide propagation losses.

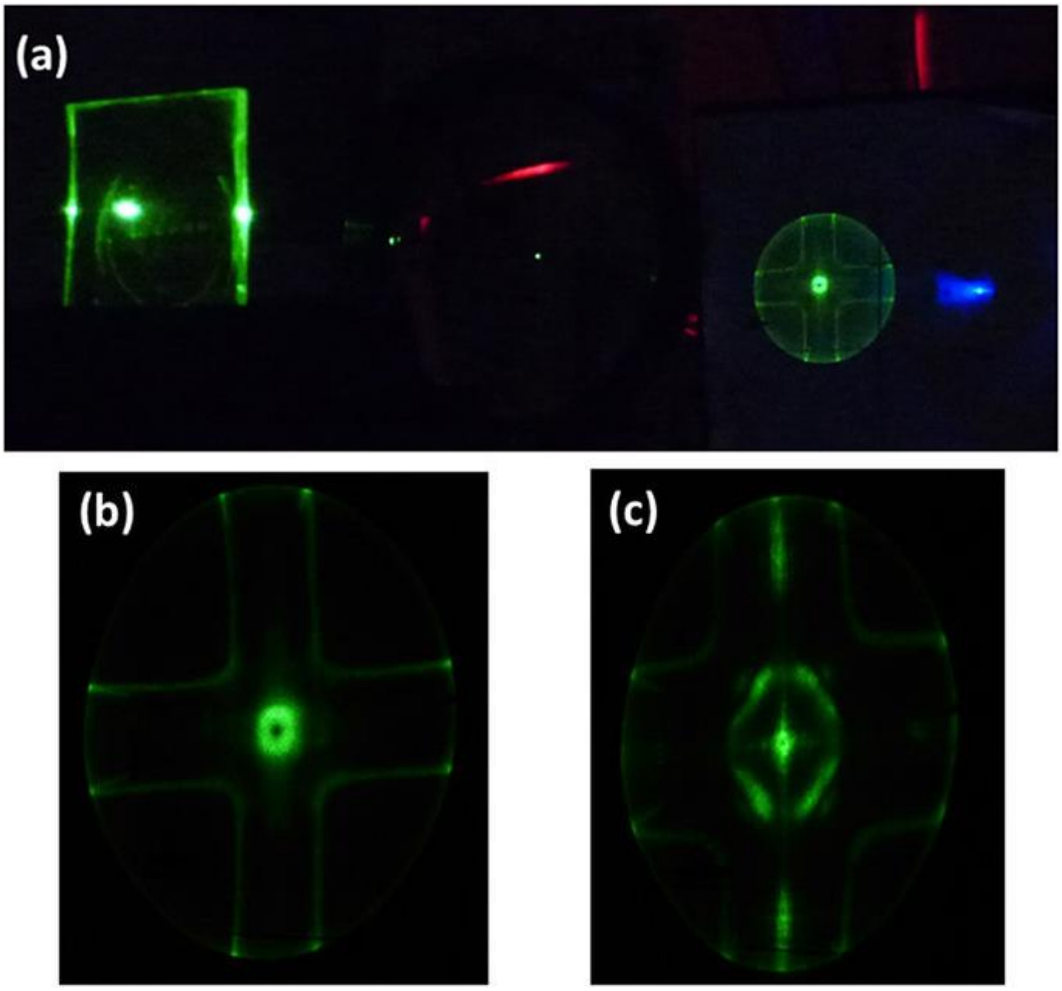

Figure 10 - (a) A photograph of a $CH_3NH_3PbBr_3$ Laser in operation. The surface emitted beam is refocussed with a collecting lens (not visible) and projected on a white screen. Remnants of the pump beam are visible to the right of the sample output. (b) A close up of the emission from a 300 nm grating and (c) a 290 nm grating. Images are from our paper [7].

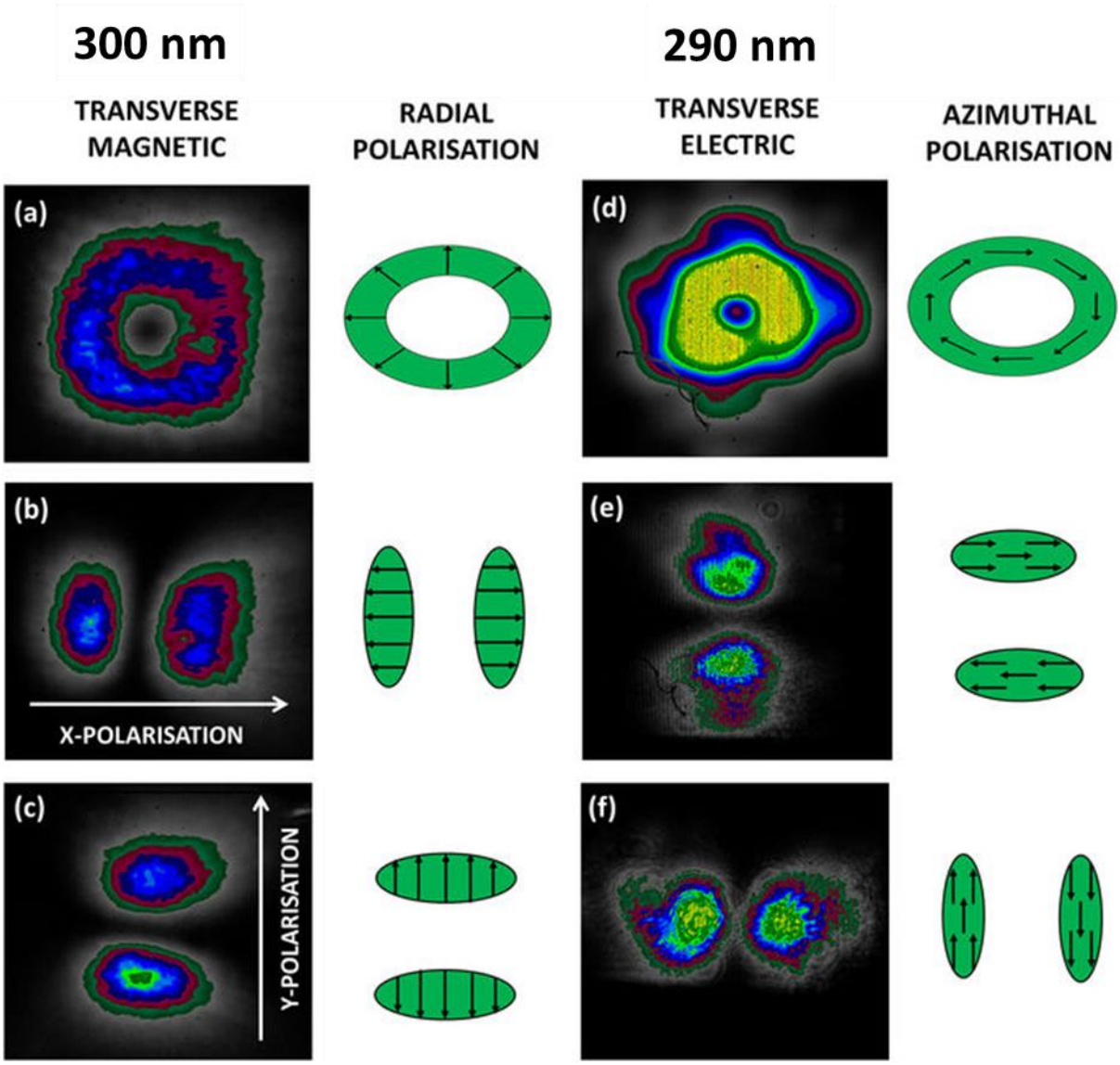

Figure 11 - Analysis of beams using a linear polariser. (a) and (d) show the unpolarised beam profiles of the 300 nm and 290 nm gratings respectively. (b) and (e) show the beams after passing through a horizontal polariser, while (c) and (f) show the vertically polarised beams. Applying this logic, we can conclude that the 300 nm grating mode is radially polarised while the 290 nm beam is azimuthally polarised. Images are from our paper [7].

Comparing the beams from the 300 nm and 290 nm grating, both beams have the same annular shape, but the beam from the 290 nm grating has a much smaller diameter. This rule holds across all gratings in that beams from gratings below 295 nm are much smaller than the beams from gratings above. This looks to be strongly linked to the mode hopping effect seen on the 295 nm grating, and so to investigate the effects of this mode hop further the beams were viewed using a Coherent™ beam profiler to examine their properties in more detail. As would be expected, the unpolarised beams have a clear annular shape when viewed through the profiler, but when the beams are passed through a linear polariser the beam switches to a double lobed (TEM_{10}-like) beam as shown on figure 11. Both the 290 nm and 300 nm gratings have this effect, with the only difference being

that the double lobed beam is rotated by 90 degrees between the two modes. Rotating the polariser by any angle would result in an identical rotation in the output beam by the same angle, showing that the polarisation of both beams has circular symmetry.

Using this information, we can conclude that the beam from the 290 nm grating is azimuthally polarised, as is the case for the TE output for most OSC lasers [12], while the output from the 300 nm grating is radially polarised. This would suggest that our mode hop is between TE and TM polarisations, which shows another major difference between perovskites and OSCs for DFB lasers because the TM mode is not normally visible in OSC lasers due to the strongly anisotropic nature of polymer films. In a polymer laser, the molecule chains are usually strongly orientated to be in the plane of the films, meaning that the TE and TM modes will see very different environments and hence will have very different refractive indexes [13]. Perovskites on the other hand have very little difference in refractive index for the two polarisations, and hence the resonance condition for the TE and TM mode have only a small separation compared to polymer lasers, which will usually only meet the resonance condition for the TE mode.

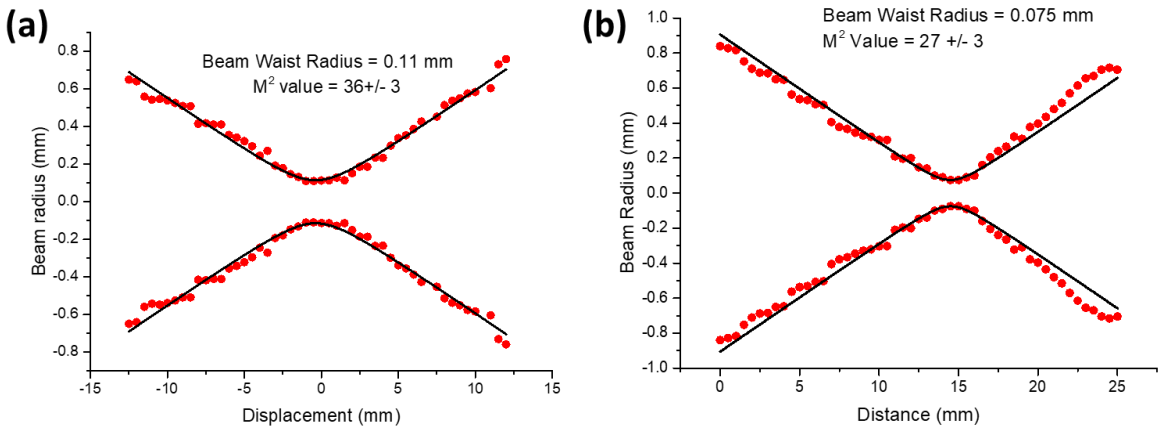

Figure 12 - M^2 measurements of beams from (a) the TM mode and (b) the TE Mode. Images are from our paper [7].

This easy switching between TE and TM modes could have sensing applications, where the laser would be tuned to be close to the hopping point so that a small change in local environment would cause a sudden shift in output polarisation, and achieving radially polarised emission could also be of interest because it has been hypothesised that a radially polarised beam could be focussed to a radius below the diffraction limit [14]. To test this, we took M^2 measurements of the beams from both gratings by focussing the output of the laser to a point using a spherical lens with 40 mm focal length, and measuring the beam radius with the beam profiler. The beam radius was then measured as a function of displacement, and the resulting curve was fitted to the beam radius equation

$w = w_0\sqrt{1 + \left(\frac{M^2\lambda z}{\pi {w_0}^2}\right)^2}$. The results are shown on figure 12, and show that the TM beam has an M^2 value of 36, while the TE beam has an M^2 of 26, indicating that we are very far from the diffraction limit in either of the beams. Having an M^2 value as high as this is quite surprising given that the beams appear to be of good quality with strong temporal coherence. The presence of the wide minimum in intensity on the axis of the surface emitted beam will certainly contribute to the poor value, but this cannot explain the whole problem because most Laguerre-Gaussian beams have a good M^2 whilst still having minimum in the centre.

FDTD simulations of Modes

Thus far, we have assumed that the radially polarised beam comes from a TM mode while the azimuthally polarised beam is TE. To confirm this, we performed further finite difference time domain (FDTD) simulations of the waveguides using software provided by Markus Karl from Prof. Gather's lab at the University of St Andrews, and detailed refractive index data of $CH_3NH_3PbBr_3$ reported by Alias et al [11]. The aim was to reproduce the lasing modes observed at 543.5 nm and 556.0 nm in the dual mode 295 nm grating, which we had assigned to the TM and TE modes respectively. The simulations were made more complex by the fact that $CH_3NH_3PbBr_3$ has a strong dispersion in its refractive index in the lasing region, meaning it is important to know the exact refractive index at each wavelength in order to get an accurate simulation.

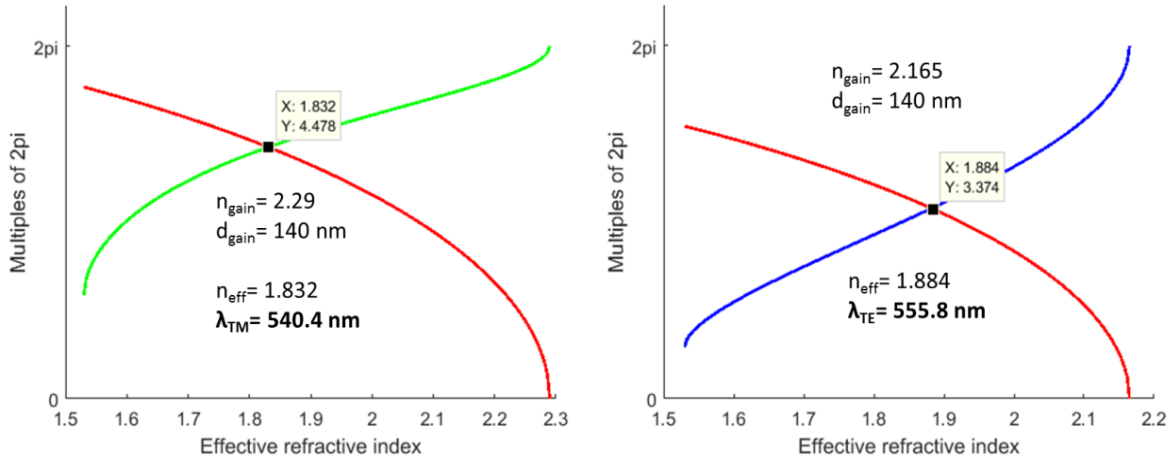

Figure 13 - FDTD simulation curves for (a) TM and (b) TE modes. The effective refractive index is defined as the point where the phase shift and geometric line cross. Calculations were performed assuming grating period of 295 nm, a perovskite layer thickness of 140 nm, and cladding layer refractive indices of 1.33 and 1.53 for CYTOP and the UVcur-21 grating respectively. Images are from our paper [7].

Modelling the laser as a slab waveguide and plugging in refractive index values for CYTOP (1.33), the grating material (1.53), and $CH_3NH_3PbBr_3$ at 556 nm (2.165) gives an effective refractive index for the

TE mode of 1.884. Multiplying this value by the grating period predicts a lasing wavelength of 556 nm, which is exactly what we observe in experiment. Thus we have external confirmation that the 556 nm mode, along with the azimuthally polarised modes observed on the 290 and 285 nm gratings, are indeed TE modes. Performing the same simulations for the TM mode, whilst being sure to account for the dispersion of the refractive index of $CH_3NH_3PbB_3$, gives a TM mode effective refractive index of 1.832. Plugging in the grating period of 295 nm predicts a lasing mode at 540 nm, which is 3 nm shorter than what we observe experimentally. The most likely reason for this small discrepancy is that the different film preparation route we use might result in slightly different dispersion relation to that seen by Alias et al. But the salient point is that the FDTD simulations predict the TM modes to be at a shorter wavelength than the TE, which agrees with the polarisations we initially assigned. This confirms that it is indeed correct to call the radially polarised modes TM and the azimuthal modes TE and shows that, in this case at least, the same polarisation logic applies to perovskite lasers as it does in polymer lasers.

Stability

One of the key challenges in the field of solution processed lasers is maintaining stability under high average pump powers. Even if the problems with triplet excitons are sorted, the ultimate aim of achieving continuous wave operation is unlikely if the material degrades quickly under these conditions. The main advantage of CW operation is the ability to achieve high average powers, but many organic semiconductors can be quickly degraded by photooxidation if pumped in this way. Perovskite solar cells have similar issues with stability, but their main catalysts for degradation are water and metals [15, 16], which are both far easier to exclude in a laser device than oxygen is. Whether oxygen is able to degrade perovskites is a matter of some debate, but in any case the rate of degradation due to oxygen is many times lower in perovskites than it is in organics, and in some cases it has even been shown to improve PL in $CH_3NH_3PbBr_3$ [17]. This means that the simple encapsulant of a CYTOP^{TM} capping layer, which is an excellent water barrier but a poor barrier to oxygen, could be sufficient to allow the perovskite laser to operate for extended periods of time.

Due to their high resistance to oxidation, we found that $CH_3NH_3PbBr_3$ laser devices remained operational even after several months of storage in ambient conditions at 50 % humidity, albeit with most devices having an increased threshold to as much as 50 μJcm^{-2} after storage. This stability made perovskite lasers very simple to work with, as a single grating could be studied while operating well above threshold for days at a time with no noticeable degradation in the beam output, allowing detailed characterisations to be easily performed. To assess this stability more quantitatively, a CYTOP^{TM} encapsulated laser was excited at roughly 2x threshold with 400 nm pulses from a 20 Hz

optical parametric oscillator source. The lasing output vs time was set to be repeatedly measured overnight, and it was found that the output power of the perovskite laser showed no downward trend even over the entire test duration of more than 15 hours. The results of this measurement are shown in figure 14.

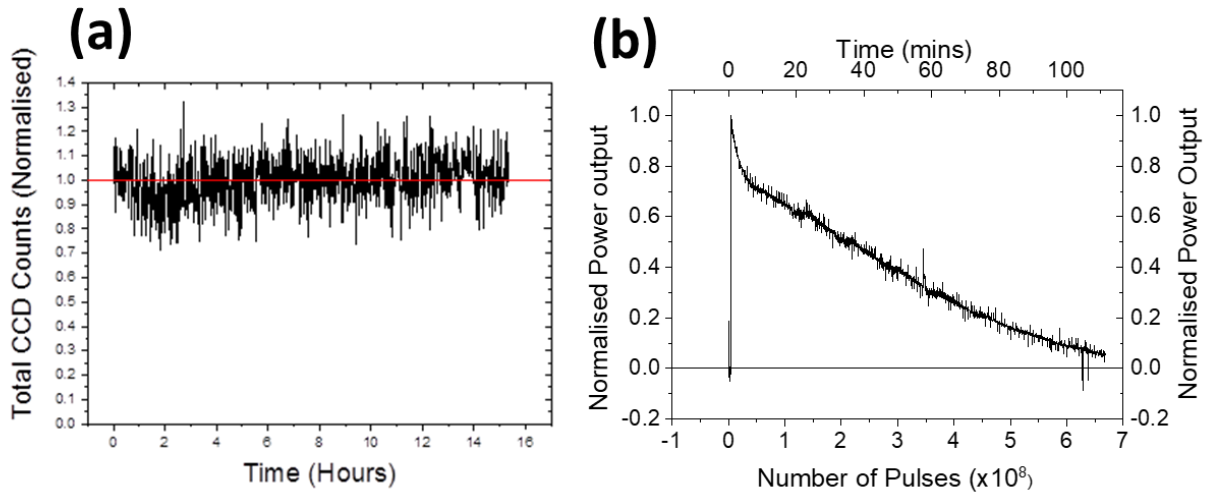

Figure 14 - (a) $CH_3NH_3PbBr_3$ laser stability under ns pumping at 2x threshold at 100 Hz. (b) Stability under high power(~200 μJcm^{-2}) fs pumping at 100 KHz. Images are from our paper [7].

In an attempt to stress the material to its limit, we tested the laser under very high power using 400 nm, 200 fs pulses from the second harmonic of an optical parametric amplifier which was pumped by a Light Conversion™ regeneratively amplified Pharos laser. The pump fluence was set to be several orders of magnitude above threshold at 200 μJcm^{-2} with a pulse rate of 100 kHz, resulting in an average intensity of 20 Wcm^{-2}. This represents 10000x more average power than used in the ns pumping experiments, but even under these extreme conditions the laser was able to withstand 80 minutes of continuous excitation before falling to 10 % of its initial value. These results show perovskite lasers have a stability far beyond that of most organic laser materials, which until recently were only reported to survive a maximum of ~10^6 pulses at 30 μJcm^{-2} in the literature [18]. Very recently, Adachi et al. showed great progress by reporting an organic laser which fell to 10% of its initial value after ~$7x10^9$ pulses [19], but due to its lower threshold the total energy absorbed by the perovskite laser still far exceeds that of the organic material ($1x10^{11}$ μJcm^{-2} versus $3.6x10^9$ μJcm^{-2} respectively). Our results definitely have scope for improvement with improved encapsulation or improved for lower thresholds, and we have therefore shown that perovskites have the potential to operate under high powers for very long periods of time.

Purity of Lead Salts

As mentioned in chapter 4, it was discovered towards the end of this PhD that the purity of the lead salt in the precursor solution is critical to achieving high performance in perovskite devices. All devices reported in this work were made using 99.999 % purity lead bromide ($PbBr_2$) from Sigma Aldrich (CAS 398853), but to provide comparison we made several batches of devices using their lower purity $PbBr_2$ which was rated to only 98 % (CAS 211141). The solubility issues reported earlier were not a problem because the bromide salts are much more soluble in DMSO than their iodide counterparts, meaning that the precursors were easily soluble even when using the low purity $PbBr_2$. However, the difference was clearly visible in the lasing threshold of the resulting devices. DFB lasers made using low purity $PbBr_2$ demonstrated a minimum lasing threshold of 50 μJcm^{-2} – an order of magnitude increase over the otherwise identical samples made from pure $PbBr_2$. We attribute this drop in efficiencies to impurities in the final perovskite causing a quenching of the PL, and it provides a clear demonstration of the impact that the purity of the precursor compounds can have when making perovskite devices.

Attempts to Reduce Threshold

Alternative Antisolvents for Nanocrystal Pinning

When finding the optimal deposition method for achieving low threshold $CH_3NH_3PbBr_3$ lasers, we tried many different choices and compositions for antisolvents in the NCP method before concluding that the TPBi in DCM solution was optimal. The general trend we found was that more volatile antisolvents gave better PLQY but were much harder to optimise to get a good film quality. Using antisolvents such as toluene or chlorobenzene would easily result in good films, with the exact timing of the solvent wash having a large window for optimal quality. However the samples would emit only very dim green light under a UV lamp, and had a PLQY of less than 1 % under laser excitation. Using more volatile antisolvents such as chloroform, dichloromethane, and diethyl ether in general resulted in films with much stronger photoluminescence. However the spin coating process proved much harder to optimise. If the antisolvent was dropped too early then the film would have spiral patterns on the surface, leading to films which were too scattery to be of use in lasers. However if the antisolvent was dropped too late then the PL from the sample would be weak and patchy. In chloroform, the optimal timing for the wash had a window of about 5 seconds. The more volatile the solvent, the stronger the PL but the narrower the optimal window, and so we found that DCM had a window of about 2 seconds while getting a good film using diethyl ether proved to be more luck than judgement. Thus making it unsuitable for achieving reproducible devices. The difference in threshold between films made using chloroform and DCM was found to

be fairly negligible, but we chose to stick with DCM since it was the most volatile solvent we could reliably get good films with.

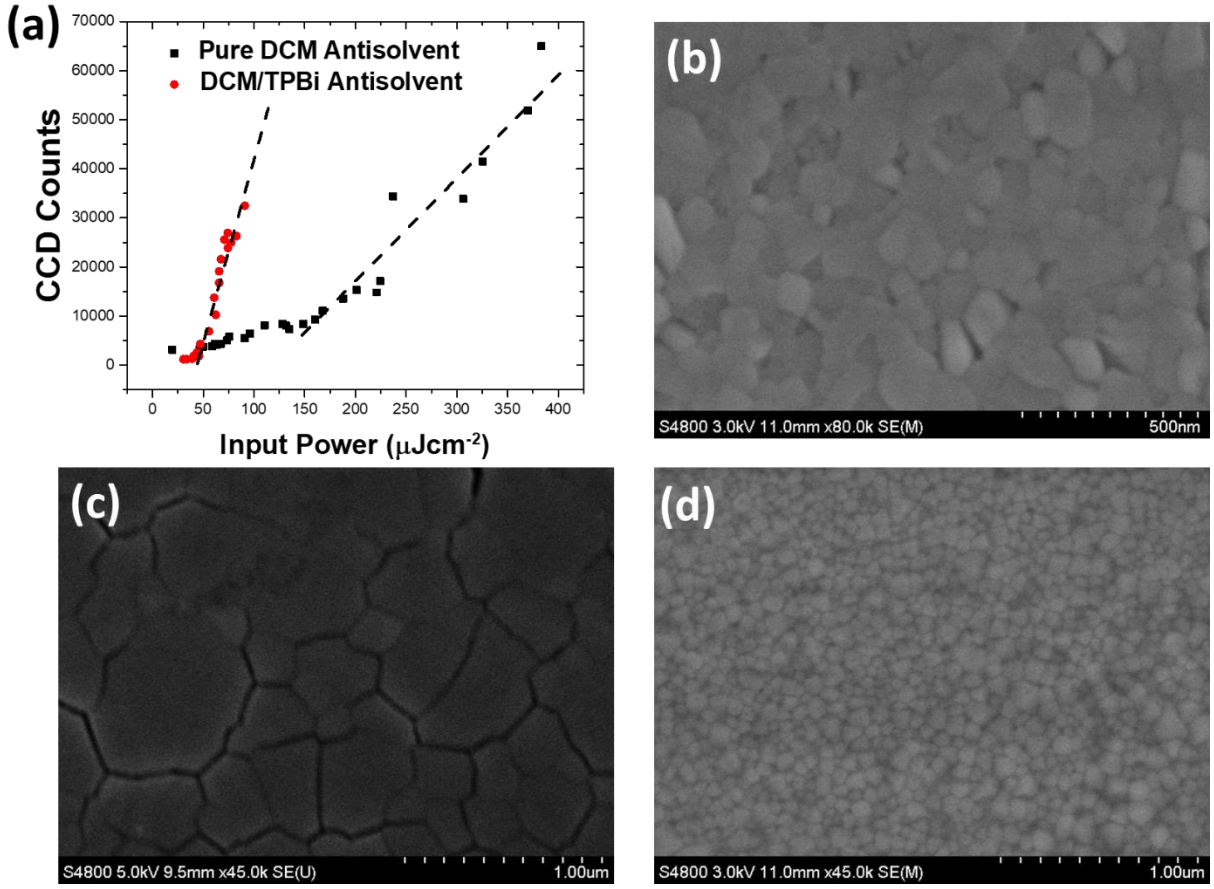

Figure 15- (a) Threshold measurement comparing ASE thresholds of films made with or without TPBi as an additive to the antisolvent. A comparisson of SEM images from samples made using (b) pure toluene, (c) pure chloroform, and (d) DCM with TPBi additive.

Adding TPBi to the solvent was found to dramatically enhance the PLQY of samples when using any antisolvent which would dissolve it, but it once again led to a trade-off between high PLQY and good film quality. If the concentration of TPBi was increased much beyond 5 $mgml^{-1}$ in DCM or chloroform the surface roughness was seen to visibly increase, and blue emission from the sample could be seen caused by the emission from the TPBi. We therefore decided to use the highest concentration we could get away with before visual reduction in film quality became evident, which is why 5 $mgml^{-1}$ was considered optimal. A point of interest is that TPBi was the only organic small molecule we could find which caused an improvement in performance. Adding other small molecules such as Bathocuproine (BCP), 4,4'-Bis(N-carbazolyl)-1,1'-biphenyl (CBP), or 1,3-Bis(N-carbazolyl)benzene (MCP) all resulted in films with only a small improvement in PL coupled with a far greater decrease in film quality than observed with TPBi. It is not clear why TPBi works so well in this case, or indeed

how Tae Woo Lee et al. discovered its utility, but it seems to be one of a very small subset of materials that works.

Ceasium and Formamidinium Perovskites

As a final step to optimisation of the lasing threshold, we decided to experiment with switching the A site cations in the perovskite structure. Both formamidinium (FA) and caesium (cs) have been shown to give improved performance in Iodide perovskite solar cells [20-22], so we aimed to make films of $FAPbBr_3$ and $CsPbBr_3$ for testing. It is worth noting that $FAPbBr_3$ and $CsPbBr_3$ are both stable at room temperature, while their iodide counterparts are not. This is because the ionic radius of Br^- is much better suited to forming a perovskite structure with these cations than the I^- anion. $FAPbBr_3$ films were made via an identical recipe to the A-NCP route, with the exception that the CH_3NH_3Br component was replaced with the same molar fraction of FABr. Spin coating with this solution tended to produce films of very poor quality with poor PL and many pinholes in the film. However it was found that the film quality could be improved greatly by adding a small amount (20 µl per ml) of hydrobromic acid (HBr) to the solution prior to spin coating. The addition of HBr made the solutions much more unstable, meaning that the solution had to be used in the same day or the solution would precipitate and give poor results, but the film quality was dramatically enhanced. Unfortunately, the same trade-off between PLQY and film quality cropped up again.

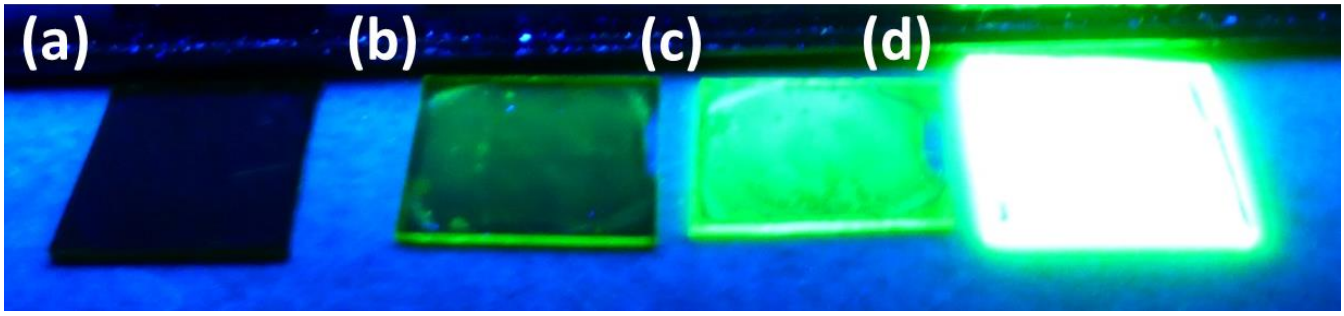

Figure 16- Perovskite films made via various routes, illuminated with UV light. The first three samples show $CH_3NH_3PbBr_3$ produced via (a) the acetate route, (b)the NCP route using chlorobenzene as an antisolvent, and (c) the A-NCP using TPBi in chloroform as an antisolvent. (d) shows $FAPbBr_3$ made via the A-NCP route using TPBi dissolved in chloroform as the antisolvent.

$FAPbBr_3$ samples spun using pure chloroform as an antisolvent produced excellent films made of densely packed grains with a complete absence of pinholes(see figure 17), but under UV excitation they would produce no photoluminescence at all, even under high powers. Films made when washed with a 5 $mgml^{-1}$ solution of TPBi in chloroform had much stronger PL than any other film made via this method, but the film quality and stability was very poor. Samples made in this way could be measured to have a PLQY of 1.3 % in the Hamamatsu PLQY machine using low intensity

excitation. This is still below the point at which the setup is considered trustworthy, but it is a major improvement on all $CH_3NH_3PbBr_3$ samples which were either unmeasurable or less than 0.5% when using powers as low as this. Pictures of the films from various routes are shown for comparison in figure 16, and SEM images of $FAPbBr_3$ films with and without the TPBi additive are shown on figure 17. Unfortunately, the bright $FAPbBr_3$ films had poor waveguiding properties due to their loosely packed crystals, and so the damage threshold of the films was reached before any ASE was observed.

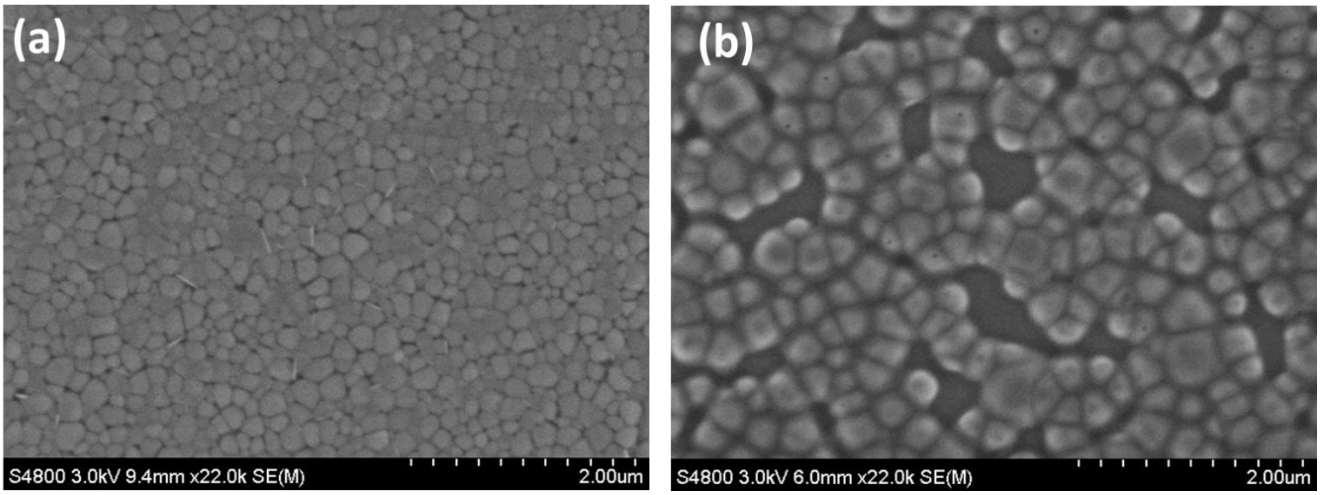

Figure 17- SEM images of FAPbBr3 spun using the A-NCP method using (a) Pure Chloroform as an antisolvent, (b) Using a 5 $mgml^{-1}$ solution of TPBi in Chloroform as an antisolvent. The addition of TPBi to the antisolvent dramatically enhances PL but results in extremely poor quality films.

Using $CsPbBr_3$ as a gain medium was a very attractive prospect because its completely inorganic nature made it extremely stable and resistant to degradation. To make films, we followed a recipe by Mcghee et al [22] - a 0.4 M solution of a 1:1 mixture of CsBr and $PbBr_2$ was prepared in DMSO, which was dissolved overnight by stirring at 100 ^oC. This lower concentration is because the CsBr is far less soluble than its organic counterparts, meaning we were limited to low concentrations. The films were formed by spin coating at 3000 RPM for 60 s and then annealing at 100 ^oC for 30 minutes. Despite reports of good film quality in the literature, we found this method gave poor surface coverage and films which were unsuitable for lasing. To rectify this, we introduced an antisolvent wash step approximately 30 seconds into the spin coating. We found that most antisolvents resulted in similarly poor film quality, but washing the films with pure toluene resulted in films which were of acceptable quality. However, despite their improved stability and smooth surface, our $CsPbBr_3$ films had very poor light emitting properties. The samples emitted PL at approximately 530 nm – a slight blue shift compared to $CH_3NH_3PbBr_3$ – but were significantly weaker even than $CH_3NH_3PbBr_3$ produced via the acetate route. The $CsPbBr_3$ films could be used to achieve ASE at a threshold of

approximately 150 μJcm^{-2}, but the ASE was unstable with poor reproducibility. ASE would usually only be observed if the excited strip was left under high power excitation (~500 μJcm^{-2}) for extended periods to "burn in". Samples under these conditions would initially show a simple PL spectrum, but over time an ASE peak would slowly grow from the spectrum over the course of several minutes. After the burn in, ASE could be observed at 150 μJcm^{-2} in the affected area of the sample, but it would quickly turn off if the excitation strip was moved to a fresh area. Attempts to ascertain a reason for this unusual effect were unsuccessful because the areas which had undergone burn in appeared to be completely indistinguishable from fresh areas by any other measurement. Areas which had been "burnt in" did not appear to have any increased PL when viewed under lamp excitation, and the PL part of the spectrum would always remain relatively constant even as the ASE peak started to appear, meaning that this effect is likely not due to an increase in PLQY. In any case, the relatively high ASE threshold, together with the unpredictable and undesirable burn in behaviour led us to conclude that $CsPbBr_3$ was an inferior medium for creating distributed feedback lasers. Hence it was not studied in further detail.

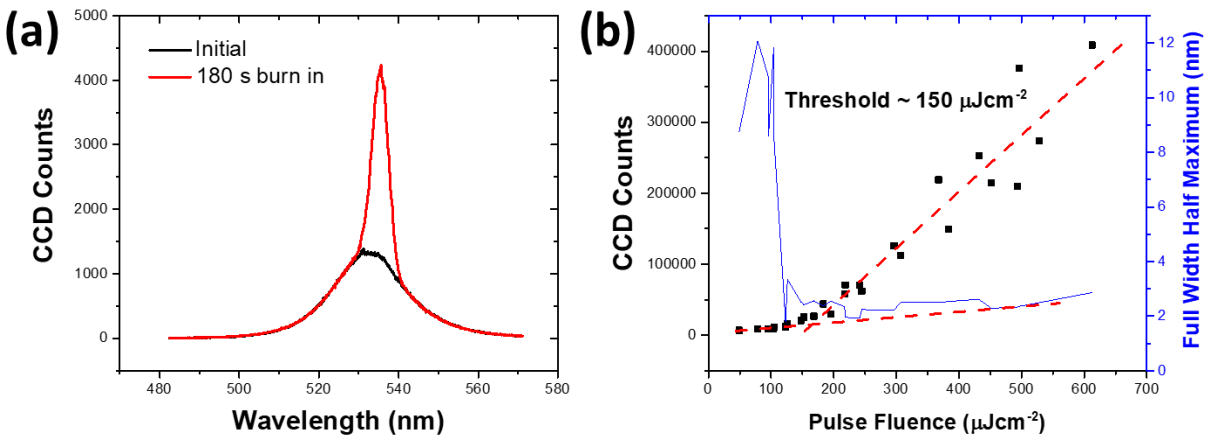

Figure 18 - (a) Emission spectra of a $CsPbBr_3$ film under excitation at 500 uJcm^{-2}. Initially only PL is observed, but after 180 s of exposure a clear ASE peak is observed. After burn in, threshold measurements could be taken, and the results are shown in part (b).

Conclusions

In conclusion, this chapter further develops halide perovskites as a laser material, and demonstrates a low threshold laser which emits highly stable and coherent light in the "green gap" part of the visible spectrum. We showed that the lasers have many interesting properties, being able to support multiple polarisations and modes, whilst also being stable and resistant to degradation. We performed a comparison between many different routes of producing $CH_3NH_3PbBr_3$ films, and found

that the A-NCP route was the best for confining the charges and bringing the material closer to geminate recombination. Thus optimising the trade-off between PLQY and film quality. Finally, we performed an investigation into other potential perovskites for supporting lasing, but unfortunately neither of the alternative structures we studied proved to have suitable properties.

References

1. Y Wang, G.T., A.L Kanibolotsky, P.J Skabara, I.D.W Samuel, G.A Turnbull, *Nanoimprinted polymer lasers with threshold below 100 W/cm(2) using mixed-order distributed feedback resonators.* Optics Express, 2013. **21**(12): p. 14362-14367.
2. Y Yang, G.A.T., I.D.W Samuel, *Hybrid optoelectronics: A polymer laser pumped by a nitride light-emitting diode.* Applied Physics Letters, 2008. **92**(16).
3. D.A Vithanage, A.L.K., S Rajbhandari, P.P Manousiadis, M.T Sajjad, H Chun, G.E Faulkner, D.C O'Brien, P.J Skabara, I.D.W Samuel, G.A Turnbull, *Polymer colour converter with very high modulation bandwidth for visible light communications.* Journal of Materials Chemistry C, 2017. **5**(35): p. 8916-8920.
4. Nana Wang, L.C., Rui Ge, Shuting Zhang, Yanfeng Miao, Wei Zou, Chang Yi, Yan Sun, Yu Cao, Rong Yang, Yingqiang Wei, Qiang Guo, You Ke, Maotao Yu, Yizheng Jin, Yang Liu, Qingqing Ding, Dawei Di, Le Yang, Guichuan Xing, He Tian, Chuanhong Jin, Feng Gao, Richard H. Friend, Jianpu Wang, Wei Huang, *Perovskite light-emitting diodes based on solution-processed self-organized multiple quantum wells.* Nature Photonics, 2016. **10**: p. 699-704.
5. W Zhang, M.S., D.T Moore, S.K Pathak, M.T Horantner, T Stergiopoulos, S.D Stranks, G.E Eperon, J.A Alexander-Webber, A Abate, A Sadhanala, S.H Yao, Y.L Chen, R.H Friend, L.A Estroff, U Wiesner H.J Snaith, *Ultrasmooth organic-inorganic perovskite thin-film formation and crystallization for efficient planar heterojunction solar cells.* Nature Communications, 2015. **6** 6142.
6. W Zhang, S.P., N Sakai, T Stergiopoulos, P.K Nayak, N.K Noel, A.A Haghighirad, V.M Burlakov, D.W deQuilettes, A Sadhanala, W.Z Li, L.D Wang, D.S Ginger, R.H Friend, H..J Snaith, , *Enhanced optoelectronic quality of perovskite thin films with hypophosphorous acid for planar heterojunction solar cells.* Nature Communications, 2015. **6,**10030.
7. J. R. Harwell, G.L.Whitworth., G. A. Turnbull, I. D. W. Samuel, *Green Perovskite Distributed Feedback Lasers.* Sci. Rep., 2017. **7**: p. 11727.
8. N.C Greenham, I.D.W.S., G.R Hayes, R.T Phillips, Y.A.R Kessener, S.C Moratti, A.B Holmes, R.H Friend, *Measurement of Absolute Photoluminescence Quantum Efficiencies in Conjugated Polymers.* Chemical Physics Letters, 1995. **241**(1-2): p. 89-96.

9. H.C Cho, S.H.J., M.H Park, Y.H Kim, C Wolf, C.L Lee, J.H Heo, A Sadhanala, N Myoung, S Yoo, S.H Im, R.H Friend, T.W Lee, , *Overcoming the electroluminescence efficiency limitations of perovskite light-emitting diodes.* Science, 2015. **350**(6265): p. 1222-1225.
10. N K Noel, A.A., S.D Stranks, E.S Parrott, V.M Burlakov, A Goriely, H.J Snaith, *Enhanced Photoluminescence and Solar Cell Performance via Lewis Base Passivation of Organic Inorganic Lead Halide Perovskites.* Acs Nano, 2014. **8**(10): p. 9815-9821.
11. M.S Alias, I.D., M.I Saidaminov, E.M Diallo, P Mishra, T.K Ng, O.M Bakr, B.S Ooi, *Optical constants of CH3NH3PbBr3 perovskite thin films measured by spectroscopic ellipsometry.* Optics Express, 2016. **24**(15): p. 16586-16594.
12. G.A Turnbull, P.A., W.L Barnes, I.D.W Samuel, *Operating characteristics of a semiconducting polymer laser pumped by a microchip laser.* Applied Physics Letters, 2003. **82**(3): p. 313-315.
13. B.L Lachut, S.A.M., H.A Atwater, M.J.A de Dood, A Polman, R Hagen, S Kostromine, *Large spectral birefringence in photoaddressable polymer films.* Advanced Materials, 2004. **16**(19): p. 1746-1750.
14. C.J.R Sheppard, A.C., *Annular pupils, radial polarization, and superresolution.* Applied Optics, 2004. **43**(22): p. 4322-4327.
15. J.M Frost, K.T.B., F Brivio, C.H Hendon, M van Schilfgaarde, A Walsh, *Atomistic Origins of High-Performance in Hybrid Halide Perovskite Solar Cells.* Nano Letters, 2014. **14**(5): p. 2584-2590.
16. A Guerrero, J.B.Y., C Aranda, Y.S Kang, G Garcia-Belrnonte, H.P Zhou, J Bisquert, Y Yang, *Interfacial Degradation of Planar Lead Halide Perovskite Solar Cells.* Acs Nano, 2016. **10**(1): p. 218-224.
17. H.H Fang, S.A., H.T Wei, J Yang, G.R Blake, J.S Huang, J Even, M.A Loi, *Ultrahigh sensitivity of methylammonium lead tribromide perovskite single crystals to environmental gases.* Science Advances, 2016. **2**(7), 1600534.
18. M Morales-Vidal, P.G.B., J.M Villalvilla, J.A Quintana, Q Yan, N.T Lin, X.Z Zhu, N Ruangsupapichat, J Casado, H Tsuji, E Nakamura, M.A Diaz-Garcia, *Carbon-bridged oligo(p-phenylenevinylene)s for photostable and broadly tunable, solution-processable thin film organic lasers.* Nature Communications, 2015. **6,** 8458.
19. A.S.D Sandanayaka, K.Y., M Inoue, C.J Qin, K Goushi, J.C Ribierre, T Matsushima, C Adachi, *Quasi-Continuous-Wave Organic Thin-Film Distributed Feedback Laser.* Advanced Optical Materials, 2016. **4**(6): p. 834-839.
20. M Saliba, T.M., J.Y Seo, K Domanski, J.P Correa-Baena, M.K Nazeeruddin, S.M Zakeeruddin, W Tress, A Abate, A Hagfeldt, M Gratzel, *Cesium-containing triple cation perovskite solar*

cells: improved stability, reproducibility and high efficiency. Energy & Environmental Science, 2016. **9**(6): p. 1989-1997.

21. G.E Eperon, S.D.S., C Menelaou, M.B Johnston, L.M Herz, H.J Snaith, *Formamidinium lead trihalide: a broadly tunable perovskite for efficient planar heterojunction solar cells.* Energy & Environmental Science, 2014. **7**(3): p. 982-988.
22. R.E Beal, D.J.S., T Leijtens, A.R Bowring, R.A Belisle, W.H Nguyen, G.F Burkhard, E.T Hoke, M.D McGehee, , *Cesium Lead Halide Perovskites with Improved Stability for Tandem Solar Cells.* Journal of Physical Chemistry Letters, 2016. **7**(5): p. 746-751.

Chapter 7: Low Dimensional Perovskites

In the previous chapters we demonstrated that many of the properties of perovskites which make them excellent materials for solar cells also make them an excellent gain medium in thin film lasers. We demonstrated that optimising the processing conditions for the perovskite films to promote high PLQY at low intensities, whilst also maintaining good film quality, was key to achieving a low lasing threshold in perovskite thin films. By applying this logic, we were able to make simple solution processed lasers which emitted in the green and near infrared parts of the spectrum with remarkable stability. The high stability, conductivity[1], and low exciton binding energy [2, 3] of the perovskite lasers give them some advantages over their OSC counterparts and make them excellent candidates for continuous wave or electrical pumping. However, our best threshold of 6 μJcm^{-2} is still an order of magnitude higher than the best performing organic polymer lasers[4], and we have yet to translate the easily tuneable bandgap of perovskites into lasing across the visible spectrum. In this chapter we attempt to improve upon these shortcomings by investigating the properties of low dimensional perovskites, which use their geometry to confine the charges to operate in a low dimensional regime. We shall first discuss our work with quasi-2D layered perovskites to produce high PLQY films for amplified spontaneous emission, before showing our results on using zero-dimensional perovskite nanocrystals (PNCs) to produce lasers and thin films with tuneable colours.

Layered Perovskites for Improved PLQY and high film quality

Theory of Layered Perovskites

In chapter 6, our improvements to the PLQY of $CH_3NH_3PbBr_3$ films certainly made a big difference to the threshold of the resulting lasers, but even our best performing films never had a PLQY larger than 5% under excitation from our He:Cd laser. Comparing this to the ~70 % PLQY seen in poly[2,5-bis(2',5'-bis(2''-ethylhexyloxy)phenyl)-*p*-phenylenevinylene] (BBEHP-PPV) polymer laser films[5] it is not surprising that polymer lasers can achieve a much lower threshold. We appear to have reached a local maximum in how far we can improve the PLQY of $CH_3NH_3PbBr_3$ films, and so without an obvious pathway to making further improvements it seems clear that we will need to significantly modify our material compositions to achieve PLQY values (and hopefully lasing thresholds) which are competitive with OSCs.

Layered perovskites offer an alternative way to get high PLQY films whilst still maintaining much of the favourable properties of perovskites. As mentioned in chapter 2, they work by confining the charges into 2 dimensions to increase the exciton binding energy, and the resulting excitons are all

funnelled into the lowest bandgap region where they can recombine with low loss. This significantly reduces the intensity dependence of the PLQY in the film because the recombination becomes mostly geminate in nature, and the charges are concentrated in a small region even at low intensities. Thus these materials can achieve high PLQY values at low intensities in a similar way to OSCs, but they have a broadly similar composition to normal $CH_3NH_3PbBr_3$. The only difference being that they incorporate a second (much larger) organic cation to separate the layers.

Layered perovskites were first developed for the study of polaritons in perovskites[6, 7] because the exciton binding energy in normal 3D perovskites was too low for strong coupling to occur[2]. The first attempts at this involved replacing the $CH_3NH_3^+$ (MA) ion in the perovskite with something much larger such as phenylethylammonium (PEA) or n-butylammonium (BA). The structure of these ions is shown in figure 1, and replacing MA with them created a series of 2D layers made from planes of PbI_6 octahedra, separated by the bulky organic cations. These materials showed a very strong exciton binding energy (~200 meV)[7], but they only had strong photoluminescence at low temperatures[8] due to exciton-phonon quenching[9]. Later attempts found that much better results could be obtained from a hybrid between the two extremes of 2D and 3D perovskites by creating several repeat units of the 3D perovskite within each layer[10-12]. Layers with many repeat units will have a bandgap approaching that of the bulk 3D perovskite, but the bandgap is strongly blue shifted for thinner layers. The average number of repeat units in each layer is referred to as the n value for the layered perovskite, with n=1 being single layers of PbI_6 octahedra and n=∞ being the bulk 3D perovskite, and any material with n=2 or greater will have a mixture of layer thicknesses which average out to the n value. Since the widest regions have the lowest bandgaps, all excitons are funnelled to these regions via quantum tunnelling through the layers, resulting in a high concentration of the charge even at low powers.

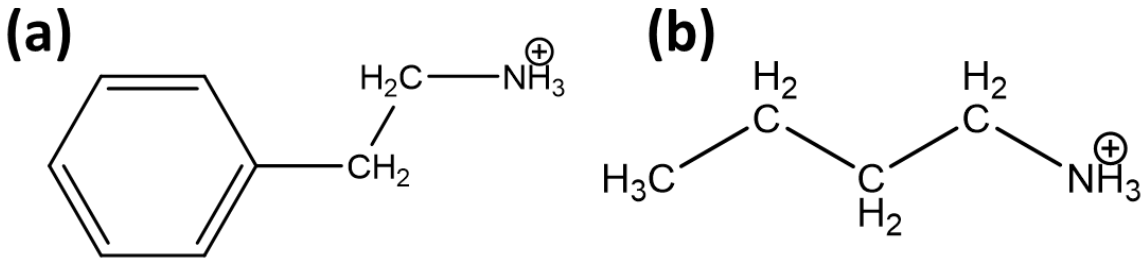

Figure 1 – The structure of the (a) Phenylethylammonium ion and (b) the n-butylammonium ion.

The n value of a layered perovskite is easily controlled by tuning the stoichiometry of its precursor solution, and samples between n=3 and n=7 tended to give the strongest PL in the literature. In 2016, two research groups (Huang et al and Sargent et al)[10, 11] simultaneously exploited these

properties to produce perovskite light emitting diodes with external quantum efficiencies up to 11.7 % - an extremely impressive result given the high refractive index of perovskite films. These LED results were impressive, but of particular interest to us was that in making these devices they reported that layered perovskites produced films with high stability, extremely low roughness, and PLQY values exceeding 60 % at most intensities. This was the exact goal we were aiming for in chapter 6, so if these results could be replicated then it could be the ideal route to achieving extremely low lasing thresholds in perovskite films.

Making Layered Perovskite Films

To make films of layered perovskites, we initially started following Sargent et al's route[11] to making films with phenylethylammonium iodide as the bulky cation to separate the layers. The recipe aimed to make films with the composition $(PEA)_2(MA)_{n-1}Pb_nI_{3n+1}$. The precursors were mixed in the specific stoichiometry to achieve the desired n value, and were then dissolved to a 1M concentration in DMSO. The correct stoichiometry of the solutions for a given n value could be calculated using the following recipe:

$$1M\ Lead\ Salt,$$

$$\frac{2}{n} M\ Phenylethylammonium\ Salt,$$

$$\left(1-\frac{1}{n}\right) M\ Methylammonium\ Salt.$$

For instance, an n=3 perovskite would require 1 M lead salt, 0.66 M PEA salt, and 0.66 M MA salt dissolved in DMSO. The solutions were then spin coated at 1000 RPM for 10 s before being ramped up to 5000 RPM, during which the sample was washed with a chlorobenzene antisolvent. The resulting films were then annealed at 70 ^{o}C for 10 minutes to improve crystallisation. In their paper, Sargent et al reported high quality films with a best PLQY of ~10 % at low intensities when using n=5 $(PEA)_2(MA)_{n-1}Pb_nI_{3n+1}$. However, our attempts to replicate these results gave rough films with a negligible PLQY for n=3, n=4, and n=5 variants of this material.

With the failure of this initial attempt, we designed a bromide version of this layered perovskite, $(PEA)_2(MA)_{n-1}Pb_nBr_{3n+1}$, whose green emission would hopefully allow better optimisation of the parameter space. The recipes remained identical, with the exception that PbI_2, PEAI, and MAI was replaced with $PbBr_2$, PEABr, and MABr. Films made in this composition still had a rough and scattery surface texture, but the films with n=3 stoichiometry showed dim blue-green PL when excited with a UV lamp. These films had a PLQY of ~4 % when measured under lamp excitation in the Hamamatsu setup. This is a significant improvement upon our previous materials, but still far below the values

we were hoping to achieve, and the films were too rough to be of any use in an optoelectronic device.

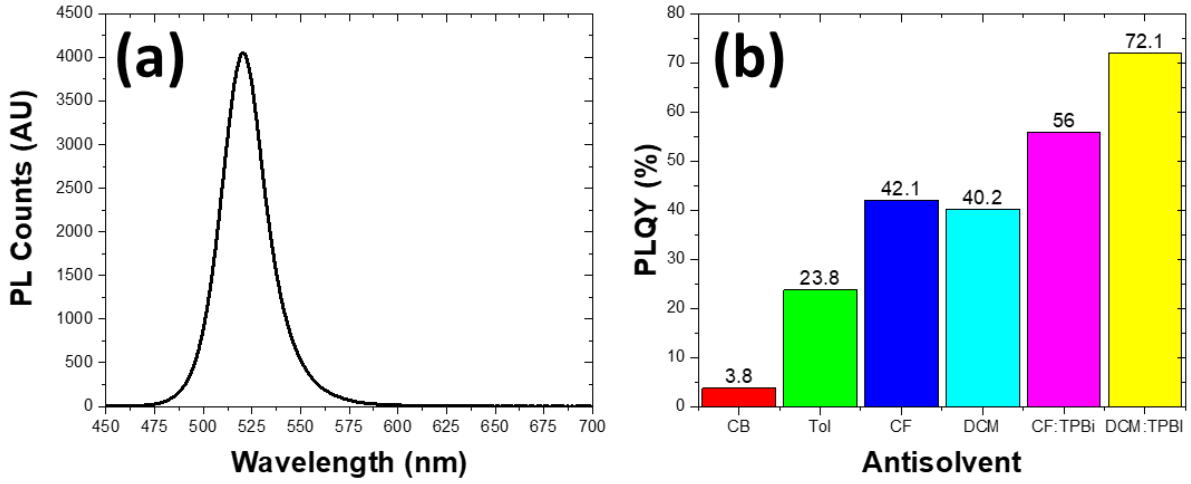

Figure 2 - (a) PL spectrum of n=3 $(PEA)_2(MA)_{n-1}Pb_nBr_{3n+1}$ formed using DCM:TPBi as an antisolvent, (b) A comparison of the best PLQY values achieved on n=3 $(PEA)_2(MA)_{n-1}Pb_nBr_{3n+1}$ films when using different antisolvents. The PLQY was measured under 400 nm excitation in the Hamamatsu setup.

To improve upon this, we investigated a range of different antisolvents and spin coating conditions. A comparison of the performance from each antisolvent is shown on figure 2, and we found that a method very similar to the A-NCP method used in chapter 6 proved to be optimal for simultaneously achieving high quality films and high PLQY. The solution was spin cast at 500 RPM for 7 seconds and then 3000 RPM for 90 seconds. An antisolvent of dichloromethane (DCM) containing 5 $mgml^{-1}$ TPBi (which we shall henceforth refer to as DCM:TPBi) was dropped on the sample after ~45s of spinning (optimal washing time could vary day to day). The final films were then annealed at 90 ^{o}C for 10 minutes to remove any remaining solvents. One point of interest was that the film quality issues seemed to be reversed when compared to spinning $CH_3NH_3PbBr_3$ previously. High boiling point antisolvents such as chlorobenzene or toluene would cause instant conversion to a rough film, whilst using chloroform (CF) or DCM would slowly convert the film over ~60 s to a much smoother film with very strong PL.

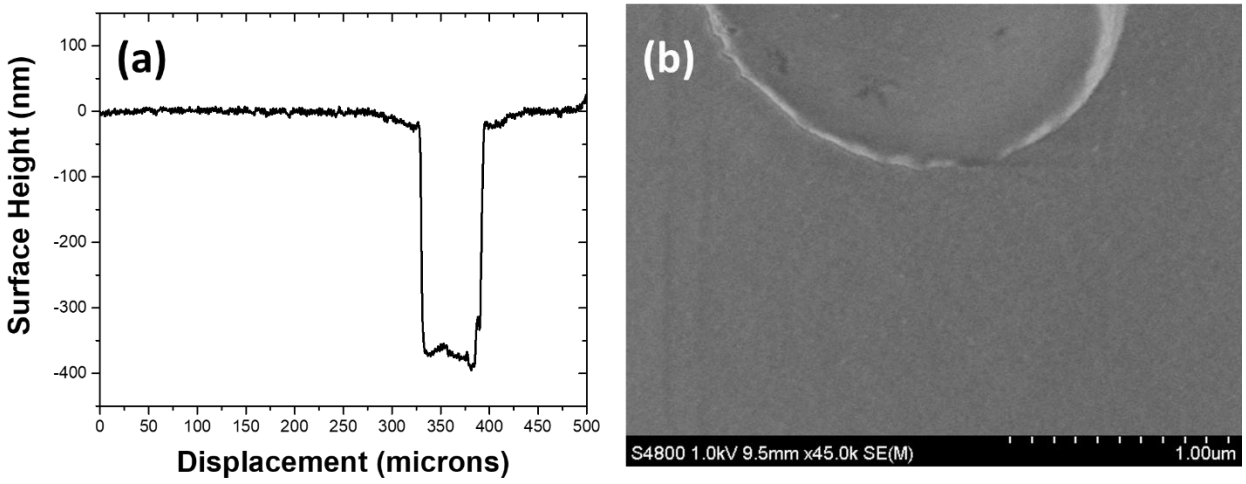

Figure 3 - (a) A Dektak trace of a scratch on a film of n=3 $(PEA)_2(MA)_{n-1}Pb_nBr_{3n+1}$. The scratch depth shows a total film thickness of 370 nm. (b) An SEM image of the same film. The scratch is included in the image to show that the sample is in focus.

A comparison of the PLQY values from all the antisolvent compositions investigated is shown on figure 2, and it is clear that the addition of TPBi to the solvent mixture improves the PLQY significantly. The best PLQY of 72 % is seen in films using DCM with TPBi, which we believe is the highest value reported for any perovskite film in the literature. The use of chloroform (CF) and dichloromethane (DCM) antisolvent blends once again achieved similar results, with the DCM:TPBi blend being harder timings to optimise but achieving a higher PLQY. The resulting films from this optimised method were of extremely high quality, with a thickness of ~370 nm and a roughness below the resolution of our Dektak (± 10 nm) as shown on figure 3. SEM images of the samples appear largely featureless, indicating that the sample is made up of either very small or very weakly defined crystals, meaning that these films are likely to have extremely low scattering losses. From the lessons we learned earlier, this combination of low scattering and high PLQY makes $(PEA)_2(MA)_2Pb_3Br_{10}$ look like an ideal laser material.

Once we had established the most reliable deposition route, we looked into how the PL changed with the n number of a given film. As can be seen on figure 4, the PL peak of the n=2 composition (485 nm) is strongly blue shifted from 550 nm peak of n=∞ $CH_3NH_3PbBr_3$. When the n value is increased to n=3 we see a large red shift in the PL to a peak of 515nm, coupled with a large increase in PLQY. As the n value is increased above n=3, the PL tends towards the spectrum of the bulk $CH_3NH_3PbBr_3$, and the PLQY gradually weakens with increasing n. These results are in good agreement with other literature, showing that films with narrower layers will have wider bandgaps, and they demonstrate that the n=3 perovskite is optimal for strong PL in this case.

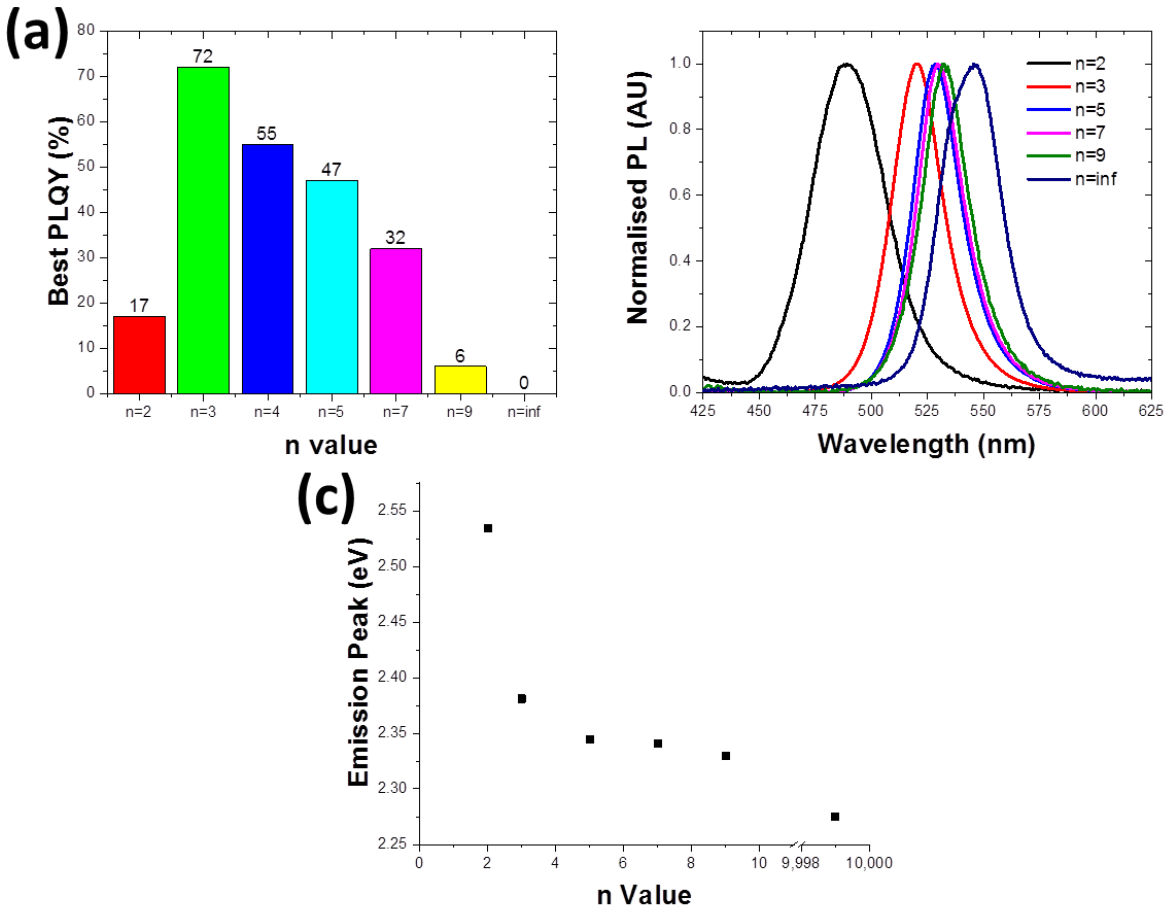

Figure 4 - (a) A comparison of the PLQY values observed for $(PEA)_2(MA)_{n-1}Pb_nBr_{3n+1}$ films of different n values in the Hamamatsu setup. (b) Normalised PL spectra for the same films measured in the Hamamatsu setup. Note that in order to get a measurable spectrum from the n=∞sample it was measured under 42 mW, 442 nm laser excitation from a He:Cd laser, under these conditions the n=∞ sample has a 5 % PLQY.(c) Peak emission energy vs n number. n=9999 is used to represent the bulk film which has n=infinity.

Film Formation

To gain some insight into why this method yields such good results, we observed the film formation in real time by illuminating the films with UV light while they were being spin coated. No PL is observed before the CF:TPBi antisolvent is dropped onto the sample, but when the antisolvent is dropped on, a large amount of brightly glowing solution is thrown off the sample. This would indicate that nanocrystals of the perovskite are forming in the excess chloroform mixture, and they seem to have an accelerated formation compared to the remaining material in the film. The PL from the excess solution quickly decays, which suggests that the nanoparticles are not stable in this state, but during their lifetime they change colour from blue to green before finally decaying.

This behaviour is mirrored to some extent in the film itself, which is seen in figure 5 to slowly shift from deep blue to cyan to light green over the course of 60 seconds, with the brightness of the PL

increasing in line with the colour shift. The final film does not decay in the same way as the excess solution, and after annealing it maintains its strong, pale green emission. The evolution of the PL in this way could not be observed quantitatively since it was not possible to get a spectrometer into the glovebox, but we hypothesise that what we are observing is the growth of the perovskite layers in real time.

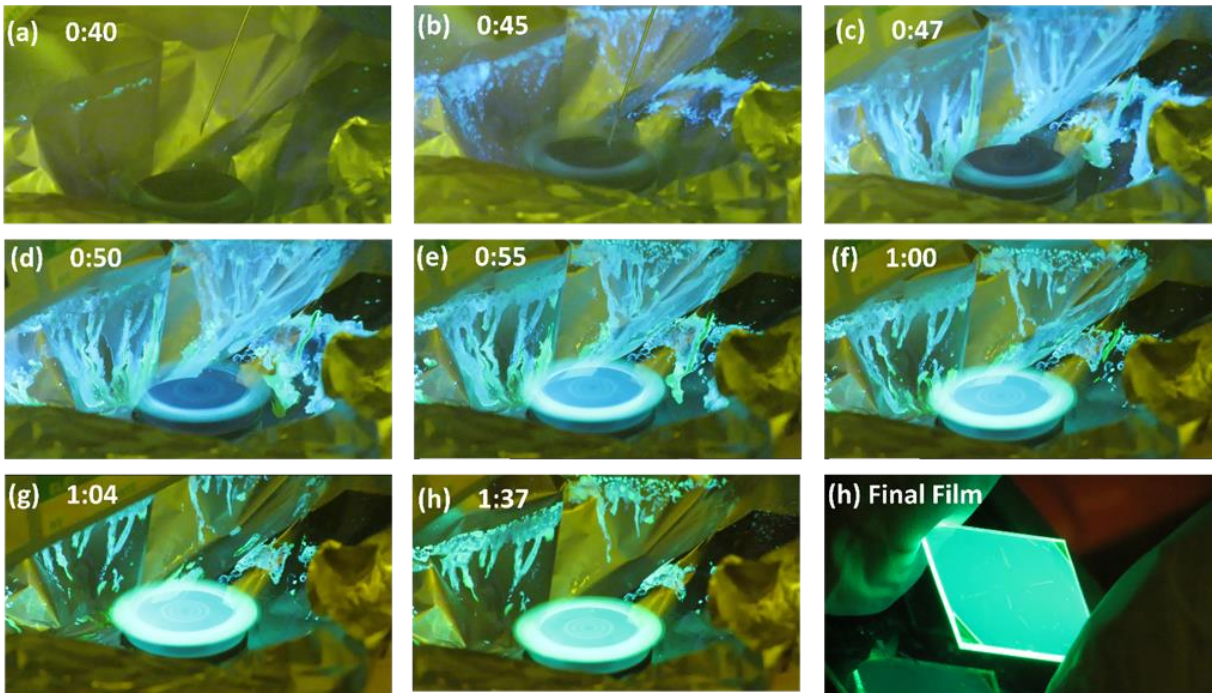

Figure 5 – A timelapse of the formation of an n=3 $(PEA)_2(MA)_{n-1}Pb_nBr_{3n+1}$ film. The film is illuminated with a UV lamp while spinning. (a) The film has no PL Before the antisolvent is dropped because the perovskite has not yet formed. (b) At 45 s the antisolvent is dropped on the film (c-h) The film gets brighter and changes colour as the perovskite forms. (h) The final film after annealing

From our studies varying the n value of the films, we found that narrower layers have a wider bandgap. This means that the early emission will be blue because it is dominated by the narrower layers, which will take less time to grow than the larger, green emitting layers. As the wide regions form, the charges in the narrow layers are funnelled into the wider layers which have a lower bandgap. Hence the emission will red shift towards the green as the layers grow, until emission from the wider layers dominates. It would certainly be interesting to prove this hypothesis by performing X-Ray diffraction measurements on the films as they formed, but the logistical challenges of performing real-time X-Ray measurements on a spinning sample inside a nitrogen filled glovebox made this impossible to realise.

Lead Purity

As a final note on film formation of these layered perovskites, it once again became clear that the purity of the lead salt is crucial to achieving high PLQY films. To test this issue, we made two

otherwise identical solutions of n=3 $(PEA)_2(MA)_{n-1}Pb_nBr_{3n+1}$ using high purity $PbBr_2$ (sigma Aldrich, 99.999 % grade) for one solution and low purity (sigma Aldrich, 98 % grade) $PbBr_2$ for the other. Films were made using the solutions under identical conditions, and the PLQY was found to drop from 72 % to 58 % when the lower purity $PbBr_2$ was used. This further emphasises that ensuring high purity of the precursor compounds is vital to achieving the best performance in this field.

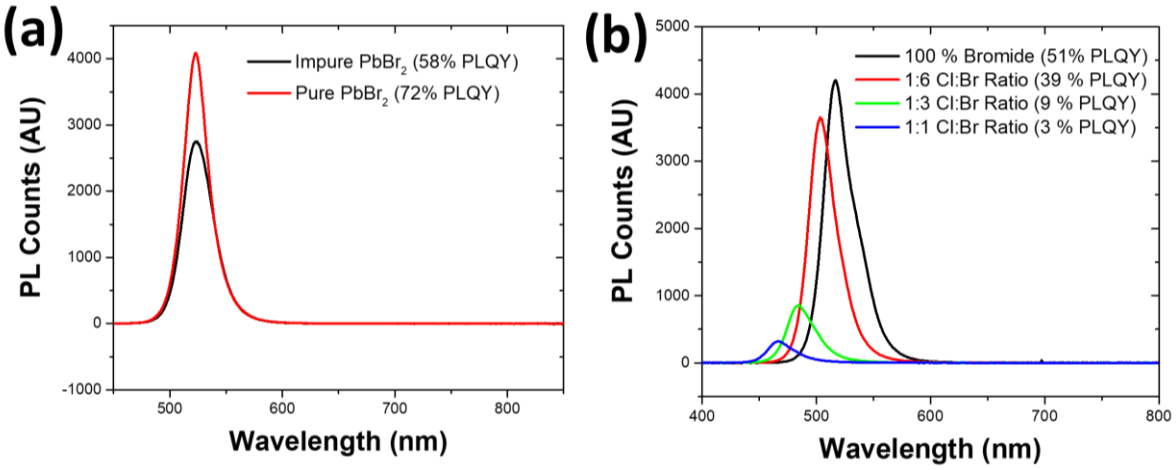

Figure 6 – (a) A comparison of PLQY measurements on n=3 $(PEA)_2(MA)_{n-1}Pb_nBr_{3n+1}$ when made using 98 % and 99.999 % purity $PbBr_2$. (b) The PL spectra and PLQY of n=3 $(PEA)_2(MA)_{n-1}Pb_nX_{3n+1}$ as the bandgap of the material is blue shifted by increasing the chloride content.

Colour Tuning

With a reliable method working for a pure bromide layered perovskite, we next tried to tune the colour by mixing the halides in our samples. To do this, we prepared three n=3 $(PEA)_2(MA)_{n-1}Pb_nX_{3n+1}$ solutions with X being Iodide, Bromide or chloride. Since PEACl was not commercially available, our chloride solution had PEABr occupying the PEA slot, thus making a solution which was 28 % Br and 72 % Br. Perovskite films of the desired halide composition could then be made by mixing the precursor solutions in the appropriate ratios (with the ratios for Cl mixtures adjusted to account for its Br component). Using this, we hoped to tune our emission into the blue by adding chloride to the compound, or tune it to the red by adding iodide.

Mixing bromide with chloride, we were able to tune our emission into the deep blue, but the PLQY dropped rapidly with increasing chloride component. As can be seen on figure 6, the PLQY dropped to as low as 3 % for a 50:50 Br:Cl mixture (emitting at 460 nm), and no PL could be observed in films with greater than 50 % chloride content. This is in line with works by other groups in that perovskites containing high chloride content tend to have very low PLQY values despite forming high quality films. The reasons for this phenomenon are hotly debated, but it is generally attributed to intrinsic

fixed energy defects in the perovskite structure which are shallow and above bandgap in red and green materials but become problematic as the bandgap is widened into the blue[13, 14].

Upon mixing the iodide and bromide samples it immediately became clear that there was a major problem with the iodide version of this structure. Mixing even a small amount of iodide solution with the bromide was found to completely quench all PL in the sample. This explains why we saw no emission in our early attempts to replicate Sargent's paper, but it is odd that our results differ so greatly. To confirm that the PL quenching was not due to an impurity in one of our iodide precursors, we then made three more solutions containing two bromide salts and one iodide salt, with the iodide salt being rotated between the Pb, PEA, and MA components in each of the solutions. If one of the precursors was causing problems, then it would become immediately evident because the solution with the problematic salt would be the only one not to emit PL. However, upon testing we found that none of the three solutions had any measurable photoluminescence, which would indicate that there is a serious underlying problem with the iodide version of this material rather than an issue with the purity of the precursor salts.

ASE from $(PEA)_2(MA)_{n-1}Pb_nBr_{3n+1}$

With a thickness of 370 nm, an extremely high PLQY, and a very low roughness, our films of $(PEA)_2(MA)_{n-1}Pb_nBr_{3n+1}$ would seem to be ideally suited for lasing. To prove this, we first tested our films for ASE under 1 ns pulses of 355 nm light from the CryLas laser using our standard ASE setup. However we found that the films would only emit bright PL in all directions, even under maximum power of the CryLas laser. This was a surprising result, since by our logic from the previous chapters these materials should have extremely low thresholds. Testing films with other n values yielded similar results, and so we switched to much higher powers by exciting with our optical parametric oscillator laser (OPO) (Continuum, 490 nm, 4 ns pulses). Under these conditions, we were able to observe ASE, but only at pump powers extremely close to the damage threshold of the material.

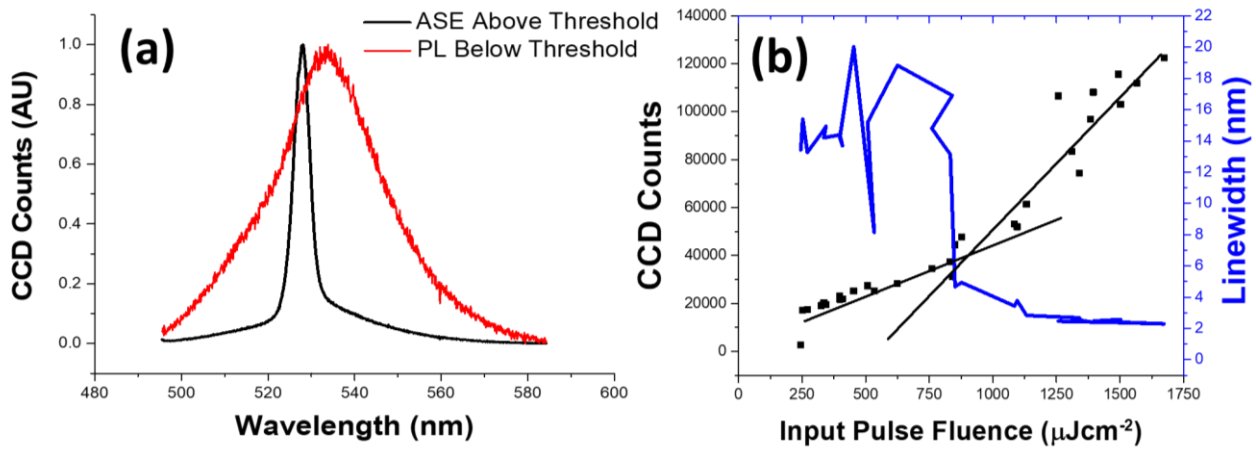

Figure 7 - (a) PL and ASE spectra of n=3 $(PEA)_2(MA)_{n-1}Pb_nBr_{3n+1}$. (b) shows the ASE threshold measurements for n=3 $(PEA)_2(MA)_{n-1}Pb_nBr_{3n+1}$ under 490 nm excitation.

Figure 7 shows a threshold measurement on a high-quality n=3 $(PEA)_2(MA)_{n-1}Pb_nBr_{3n+1}$. Comparing the ASE and PL spectra, this sample already appears to be quite unusual because the ASE peak is slightly blue shifted relative to the PL peak - most materials with a low stokes shift will tend to have their ASE peak on the red side of the PL as this is where losses due to self-absorption from the band edge will be at their minimum. However, of more pressing concern is that the sample has a clearly defined ASE threshold of ~ 800 μJcm^{-2}. This is an order of magnitude higher than the thresholds seen in the bulk 3D perovskites, meaning it will be of little to no use in any practical laser device. This is an extremely surprising result given the very promising PLQY and film qualities we observed before, and so to find possible explanations for this we next investigated the absorption spectra of the films.

Absorption Spectrum

In literature works on layered perovskites, the excitonic nature of material can be clearly seen in the absorption spectra of the material[7, 9, 10, 12]. A narrow spike in absorption, corresponding to an excitonic resonance, is commonly seen at the absorption edge of the material. This resonance can also be seen in the excitation spectra of the materials[10], where there is a spike in PL counts when exciting at the same wavelength as the absorption spike. This is a stark contrast to normal 3D perovskites such as $CH_3NH_3PbI_3$, where the absorption spectrum follows a simple step function with no evidence of an exciton peak[15]. The main exception to this rule is the films of $(PEA)_2(MA)_{n-1}Pb_nI_{3n+1}$ developed by Sargent et al[11], which show a series of much weaker peaks and a much slower absorption onset (see figure 8). To see if our material followed these rules, we measured the absorption spectrum of our best films using a CARY 300 spectrometer.

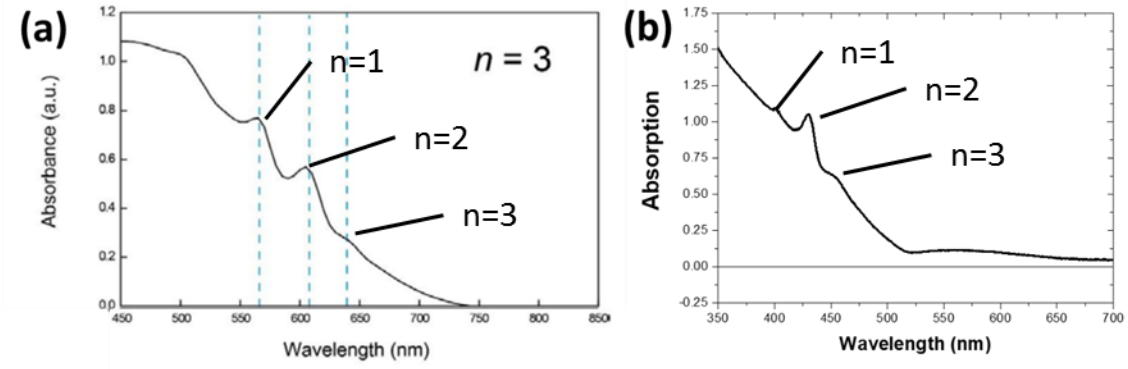

Figure 8 - (a) The absorption spectrum of n=3 $(PEA)_2(MA)_{n-1}Pb_nI_{3n+1}$ measured by Sargent et al[11], (b) The absorption spectrum of a 70 % PLQY film of n=3 $(PEA)_2(MA)_{n-1}Pb_nBr_{3n+1}$ measured in St Andrews on the CARY 300 spectrometer.

Measuring the absorption spectrum of n=3 $(PEA)_2(MA)_{n-1}Pb_nBr_{3n+1}$ (figure 8b), it becomes clear that our material more closely matches the results seen by Sargent et al, which is not unexpected because our material is a very close analogue to theirs. The bandgap of our material can be clearly seen at ~510 nm where the absorption suddenly starts to increase, and the bandgap is apparently not as well defined as in 3D perovskites (where the absorption is a step function at the band edge). This agrees with our hypothesis that the emission is dominated by the small fraction of the layers in the sample which have the lowest bandgap. In the n=3 mix, the average layer thickness will be 3, but there are many different layer thicknesses coexisting within the film. The peaks from the n=1, 2, and 3 layers can be clearly seen in the absorption spectrum on figure 8, but there will also be some layers of higher thickness which make up the lowest bandgap states. Since there are few layers which actually have this low bandgap, the density of available states is quite small at the band edge, and so the absorption onset will be a slow climb rather than a sudden step. The absorption will climb as more and more layers are able to be excited. This result seems quite logical, but of more concern is the fact there appears to be clear evidence of sub-bandgap absorption in the material between 525 and 650 nm. The absorbance here is small by comparison to the above bandgap absorption, but this absorption will be a major problem in a lasing film because it will greatly increase waveguiding loss. This explains why the ASE threshold of $(PEA)_2(MA)_{n-1}Pb_nBr_{3n+1}$ is so high, because the sample will need to provide a much larger gain to overcome the increased absorption losses, meaning a higher pump power is required. It also explains why the ASE peak of $(PEA)_2(MA)_{n-1}Pb_nBr_{3n+1}$ (525 nm) is on the blue side of the PL, as the ASE will exist in the part of the spectrum which has the lowest absorption losses, which can be seen to be minimal at roughly this point.

Although these results provide a good explanation for the high threshold, it is not clear what causes this sub bandgap absorption or why it is not observed in other literature reports. This phenomenon

is highly detrimental to lasing operation, but is much less of an issue in most other optoelectronic applications. Without a clear pathway to overcome this issue, in future work we shall focus on finding other uses for the otherwise excellent properties material in areas such as light emitting diodes and polaritons. Literature works have already demonstrated the great potential these materials have as LED materials, and their excitonic nature makes them very promising for the study of polaritons.

Perovskite Nanocrystals

Motivation

One of the major issues facing perovskite solar cells is the Hoke effect[16], where a mixed halide perovskite will be unstable to halide segregation under continuous illumination. This seriously limits the range of bandgaps that are available to perovskite solar cells despite their apparently easily tuneable bandgap. This halide segregation issue is also a significant problem for making colour tuneable perovskite lasers because the PLQY of mixed halide perovskites drops significantly compared to those of the pure halide materials. When working with $CH_3NH_3PbX_3$, it is possible to tune the PL to almost any colour in the visible spectrum by mixing the halides, and so in principle it should be straightforward to make perovskite lasers of any colour. However in practice the ASE threshold of perovskite films increases dramatically once the halides are mixed, and compositions tuned to the yellow/orange part of the spectrum do not emit ASE under any power. It is for this reason that the only lasers we have reported thus far emitted in the green and near infrared parts of the spectrum, as these are the wavelengths accessible using pure $CH_3NH_3PbI_3$ and $CH_3NH_3PbBr_3$.

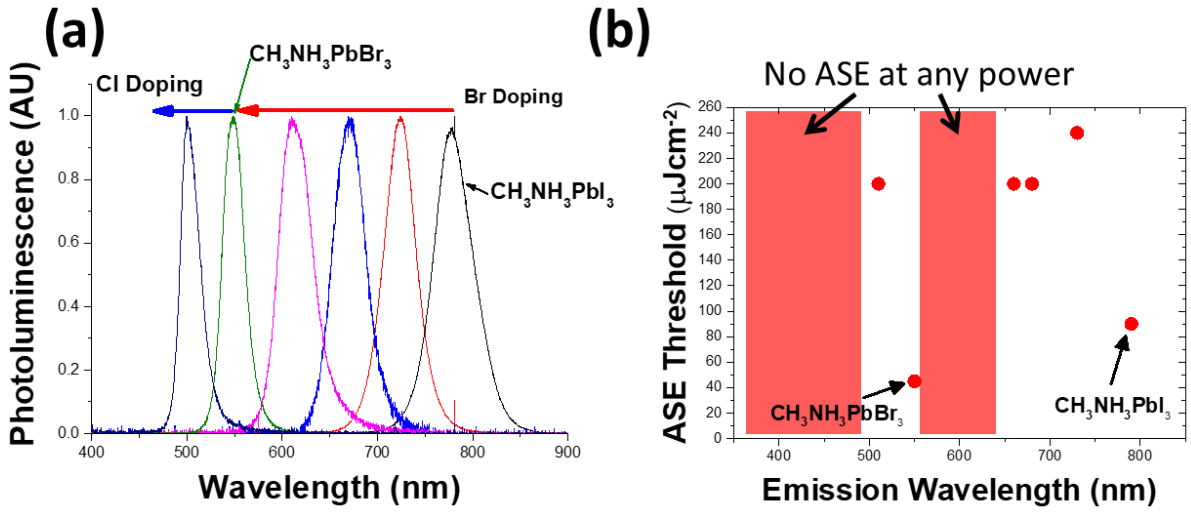

Figure 9 – (a) Normalised PL spectra for $CH_3NH_3PbX_3$ films as the bandgap is tuned via mixing the halides. Note that films with higher than 25% Cl content are not shown because the PL was too weak to get a clean spectrum. (b) ASE threshold vs

emission wavelength for different $CH_3NH_3PbX_3$ perovskites. Note that the threshold is dramatically increased for mixed halide materials, and no ASE at all is observed in certain regions.

A potential solution to this issue is to use $CsPbX_3$ perovskite nanocrystals (PNCs), which have been reported in the literature to have close to 100 % PLQY whilst being simple to fabricate and easily tuneable to any wavelength in the visible spectrum[17]. They are made from nanoparticles of $CsPbX_3$ surrounded by insulating ligands which are then dispersed in a poor solvent such as hexane. These nanocrystals are isolated from each other by their ligands, and they have not been reported to suffer from the Hoke effect in the same way as the bulk material, which may be in part due to their small size providing no scope for large scale halide segregation. Our initial plan was to disperse these nanoparticles in a Poly-9-vinyl carbazole (PVK) matrix in the way shown in figure 10 to make a smooth film which could operate in an identical way to an organic dye laser[18, 19]. The PVK matrix would prevent the nanoparticles from aggregating and causing concentration quenching, whilst also absorbing some of the excitation light and transferring the energy to the nanoparticles to increase PLQY. We would expect a laser of this design to have a higher threshold than a bulk perovskite laser because it will have a lower density of light emitting states, but the high PLQY and colour tuneability of the nanocrystals would outweigh these disadvantages.

Our supply of PNCs came from Dr Credgington's group at Cambridge university, and were fabricated by Nathaniel Davis using the method first reported by Kovalenko et al[17]. To make the nanocrystals, Cs_2CO_3 (0.814g, 99.9%) was loaded into 100 mL three-neck flask along with octadecene (ODE, 30 mL, 90%) and oleic acid (2.5 mL, OA, 90%), the mixture was then dried for 2 h at 120^{o}C under N_2. After drying, the solution temperature was lowered to 100^{o}C. ODE (75 mL), oleylamine (7.5 mL, OLA, 90%), and dried OA (7.5 mL) and a lead salt (2.82 mmol) such as PbI_2 (1.26 g, 99.99%), $PbBr_2$ (1.035g, 99.99%) or $PbCl_2$ (0.675g, 99.99%), were loaded into a 250 mL three-neck flask and dried under vacuum for 2 h at 120^{o}C. After complete solubilization of the PbX_2 salt, the temperature was raised to 170^{o}C and the Cs-oleate solution (6.0 mL, 0.125 M in ODE, prepared as described above) was quickly injected. After 10 s, the reaction mixture was cooled in an ice-water bath. For $CsPbCl_3$ synthesis, 5 mL of trioctylphosphine (TOP, 97%) was added to solubilize $PbCl_2$. The nanocrystals were transferred to an argon glovebox (H_2O and O_2 < 1 ppm) precipitated from solution by the addition of equal volume anhydrous butanol (BuOH, 99%) (ODE:BuOH = 1:1 by volume). After centrifugation, the supernatant was discarded and the nanocrystals were redispersed in anhydrous hexane (99%) and precipitated again with the addition of BuOH (hexane:BuOH = 1:1 by volume). These were

redispersed in hexane before being sent to St Andrews for experiments.

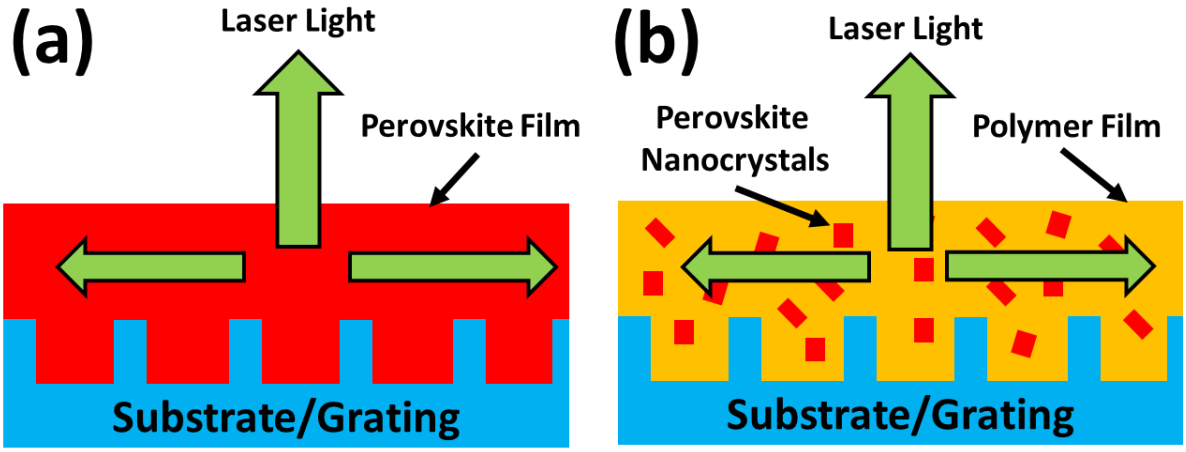

Figure 10 - (a) Normal design for a distributed feedback laser. (b) Our plan for a laser incorporating perovskite nanocrystals in a polymer matrix.

As a first batch they sent us three solutions of $CsPbBr_{1.5}Cl_{1.5}$, $CsPbBr_3$, and $CsPbBr_{1.5}I_{1.5}$ dispersed in hexane, which were measured to have solution PLQY values of 9 %, 81 % and 49 % respectively. A picture of the nanocrystal dispersions is shown on figure 11. PVK is not soluble in hexane, and so our first challenge was to move the nanocrystals from a hexane dispersion into a toluene dispersion. This was achieved by evaporating the 50 % of the solution with a nitrogen airflow, and then replacing the lost volume with toluene. The process was repeated 4 times to ensure that almost all of the new dispersion was toluene rather than hexane. The final concentration of the nanocrystal/toluene solutions could also be controlled by adjusting the final volume of toluene added to the solution. Once the nanocrystals were dispersed in toluene, we then combined the nanocrystal solutions with 35 $mgml^{-1}$ solutions of PVK dissolved in chlorobenzene (which is miscible with toluene) to make a PVK:Nanocrystal mixture. The mixtures could then be spin coated in the same way as a normal PVK film (2000 RPM, 60 s) and then measured using the Hamamatsu PLQY setup.

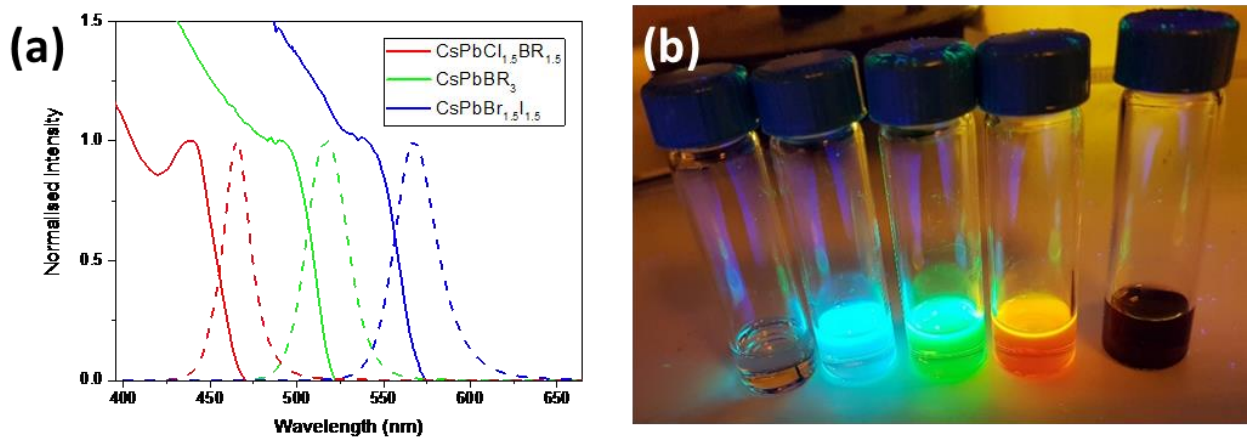

Figure 11- (a) Absorption (solid) and PL (dashed) spectra for $CsPbBr_{1.5}Cl_{1.5}$, $CsPbBr_3$, and $CsPbBr_{1.5}I_{1.5}$ nanocrystals. (b) Solutions of $CsPbCl_3$, $CsPbBr_{1.5}Cl_{1.5}$, $CsPbBr_3$, $CsPbBr_{1.5}I_{1.5}$, and $CsPbI_3$ nanocrystals dissolved in hexane. Figures created by Nathaniel Davis.

The resulting films showed weak absorbance and very poor PLQY values, with most samples having a PLQY of less than 5 %. However, during the optimisation process we found that higher concentration films generally performed much better. This was unexpected because the PNCs were expected to suffer from concentration quenching in the same way as organic laser dyes, where higher concentrations of dye will result in lower PLQY as the molecules come into contact with each other and induce exciton-exciton annihilation. However, in spite of this phenomenon we found that even the best performing mixture of 17 $mgml^{-1}$ PVK and 40 $mgml^{-1}$ $CsPbBr_3$ nanocrystals achieved a PLQY of less than 11 %, and none of the films made in this way were able to support ASE at any power.

Because the solutions seemed to improve with increasing nanocrystal concentration, as a last resort we tried spin coating the raw dispersions of PNCs in hexane onto glass substrates. We found that dropping ~ 50 µl of the raw dispersion onto a spinning substrate at 1000 RPM resulted in films with remarkably high optical quality, and PLQY values of up to 50 % for the $CsPbBr_3$ solution. By mixing the $CsPbBr_3$ solution with the $CsPbBr_{1.5}Cl_{1.5}$ solution in various ratios we were also able to tune the PL to 500 nm and 460 nm whilst maintaining a modest PLQY of 14 %, which is actually higher than the PLQY of these nanocrystals in solution. Scanning electron microscopy images, seen on figure 12, showed that the film was uniform and densely packed, with no pinholes or irregularities to speak of. This was quite unexpected for a film made of discrete nanoparticles, but it is excellent news from a laser standpoint because it means that they will be quite likely to conform well to a grating structure so long as the film is sufficiently thick.

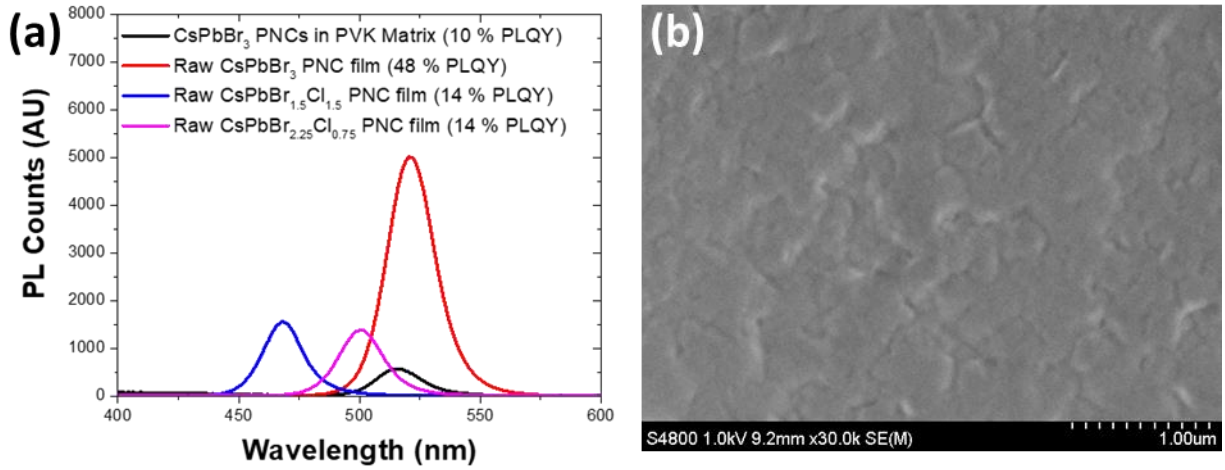

Figure 12 – (a) PLQY measurements of raw films of $CsPbBr_3$ nanocrystals with various levels of chloride doping. The best PLQY of $CsPbBr_3$ nanocrystals in a PVK matrix is shown in black. (b) SEM image of a raw $CsPbBr_3$ film.

Despite their high optical quality, the nanocrystal films were only very weakly bound to their substrate, meaning they would be easily wiped off by even the slightest touch. In most cases this was not a major problem because the films could be easily protected by depositing a layer of CYTOP™ on top of the films by dropping onto a spinning sample at 2000 RPM. However this weak packing made it very difficult to directly measure the thickness of the PNC films because the Dektak needle would dig a trench in the film, preventing us from viewing the surface profile. To resolve this, the films were measured via ellipsometry by Dr Arunandan Kumar on a J.A.Woollam EC400 ellipsometer.

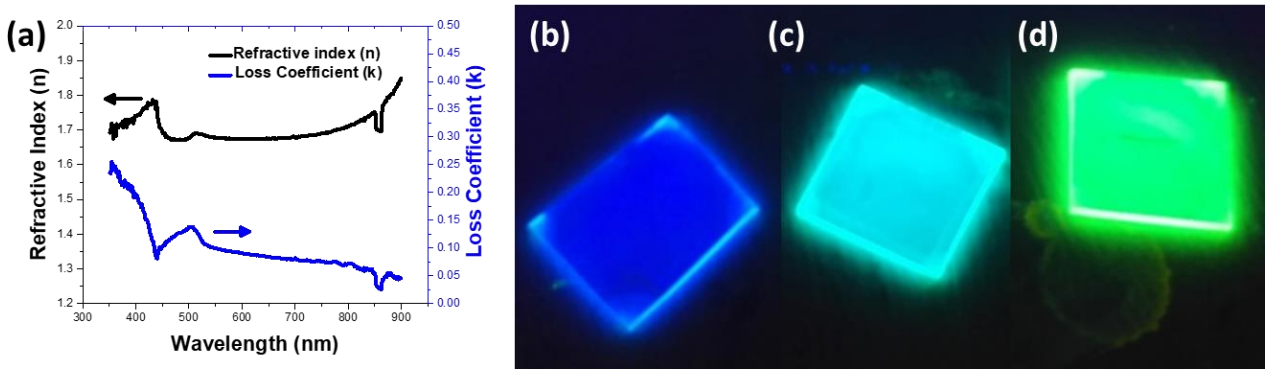

Figure 13 – (a) n and k values for a raw $CsPbBr_3$ film calculated from ellipsometry performed by Dr Arunandan Kumar. (b),(c),and (d) show photographs of raw films of $CsPbBr_{1.5}Cl_{1.5}$, $CsPbBr_{2.25}Cl_{0.75}$, and $CsPbBr_3$ nanocrystals.

The polarisation and phase shifts against wavelength and angle were measured, and a model of the thickness and refractive index of the film was iterated against the data until a good fit was achieved. By modifying the parameters to fit the data, the model produced n and k values for the PNCs and estimated a film thickness of 250 nm for $CsPbBr_3$ PNC films spun from 80 $mgml^{-1}$ concentration at 1000 RPM. The calculated n and k values are shown on figure 13. Note that it is considered bad

practice in ellipsometry to simultaneously calculate refractive index and thickness values from a single measurement because fitting two variables can increase the margin for error. But without any independent confirmation this was the only option available to us.

Looking at the refractive index data (figure 13 a), the $CsPbBr_3$ films have a refractive index of ~1.7 around their PL peak, which is very similar to the value seen in most OSCs and much lower than previously seen for bulk 3D perovskite films. Modelling the 250 nm films as slab waveguides gives an effective refractive index of ~1.6, and a cut-off thickness of ~100 nm. All this suggests that these PNC films should be able to support ASE under laser excitation, and so the films were tested for ASE under 355 nm, 1ns laser pulses from the CryLas in the standard ASE setup. The results are shown on figure 14, and it was found that the emission from pure $CsPbBr_3$ (green) NC films deposited from solution at 1000 RPM would collapse into a narrow ASE peak above a pump fluence of ~ 100 μJcm^{-2}. Films of $CsPbBr_{2.25}Cl_{0.75}$ (sky blue) were also found to have a similar ASE threshold when deposited under the same conditions, but films of $CsPbBr_{1.5}Cl_{1.5}$(deep Blue) did not show any ASE.

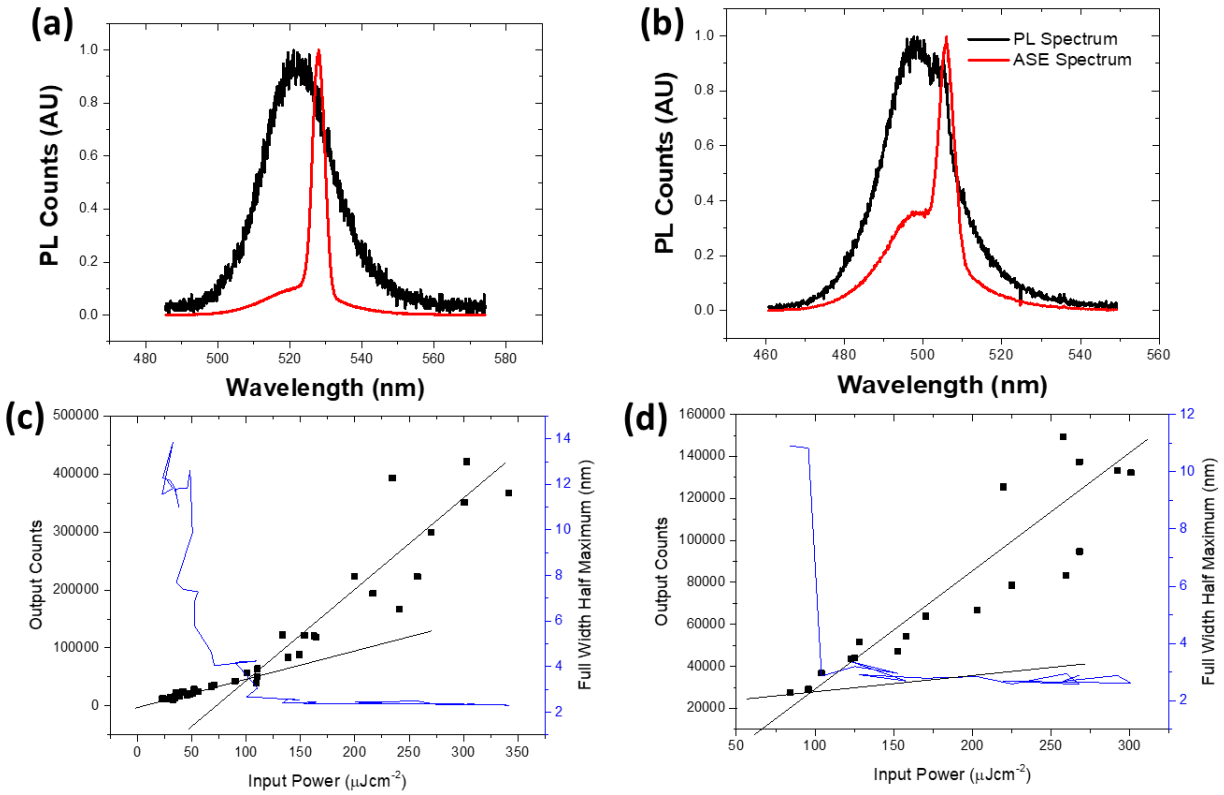

Figure 14 – PL and ASE spectra for raw nanocrystal films of (a) $CsPbBr_3$ and (b)$CsPbBr_{2.25}Cl_{0.75}$. (c) and (d) show ASE threshold measurements of the same CsPbBr3 and $CsPbBr_{2.25}Cl_{0.75}$ films respectively.

We next attempted to reduce the ASE threshold of the CsPbBr3 films by increasing spin speed, thus improving the film quality and hopefully reducing scattering losses. However it was found that increasing the spin speed to 4000 RPM resulted in a 25 % increase in lasing threshold to 125 μJcm^{-2},

and samples deposited at speeds faster than this gave no ASE at all. To investigate the reasons for this, we measured the loss coefficients of both the 4000 RPM film and the 1000 RPM film, and the results are shown on figure 15. We found that the 4000 RPM film had a loss of ~8 cm^{-1} while the 1000 RPM film had an extremely low loss of ~3 cm^{-1}, which is on par with the highest quality 3D perovskite films we had made thus far. At first glance it would seem counterintuitive that the film with the faster spin speed would have more waveguide loss, but if one assumes that the films roughly obey the spin coating thickness rule of $\text{thickness} \propto \frac{\text{concentration}^2}{\sqrt{\text{Spin speed}}}$ then we can estimate the films to be ~ 125 nm thick, which is getting very close to the cut-off thickness so we can expect the waveguide mode to become leaky. This also explains why films from faster speeds were not able to support ASE, as they would be thinner than the cut-off thickness.

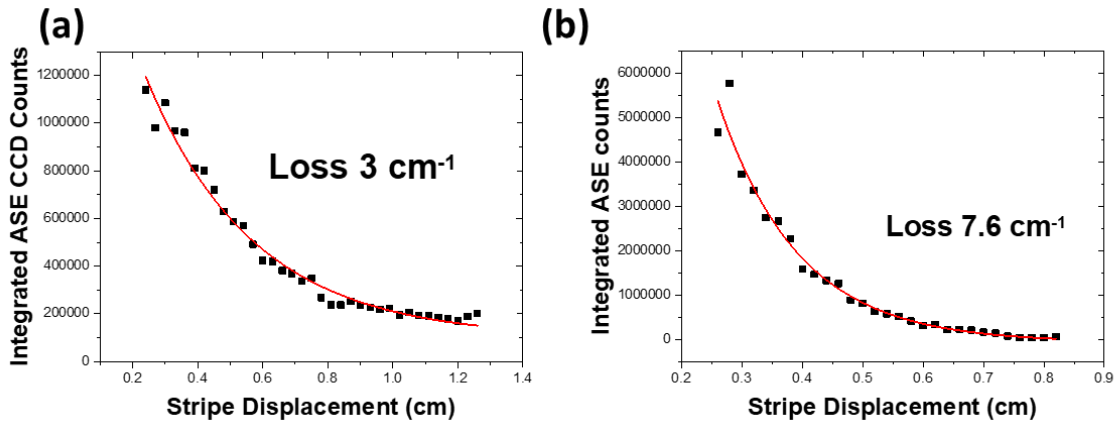

Figure 15 – Waveguiding loss measurements on $CsPbBr_3$ nanocrystal films spun at (a) 1000 RPM and (b) 4000 RPM

The lower refractive index of the PNC films is a significant advantage to us because it allows the resonance condition of the film to overlap with our more advanced mixed order gratings, which were originally designed for OSCs. The effective refractive index of 1.6 should in theory provide distributed feedback at ~340 nm, and as a first test for lasing we deposited the $CsPbBr_3$ PNC films onto 2D second order gratings of the same design used in chapter 6. The gratings were fabricated from mr-NIL210 polymer via UV nanoimprint lithography (described in chapter 3), and a CYTOP encapsulant was spin coated on top of the PNC capping layer to provide protection.

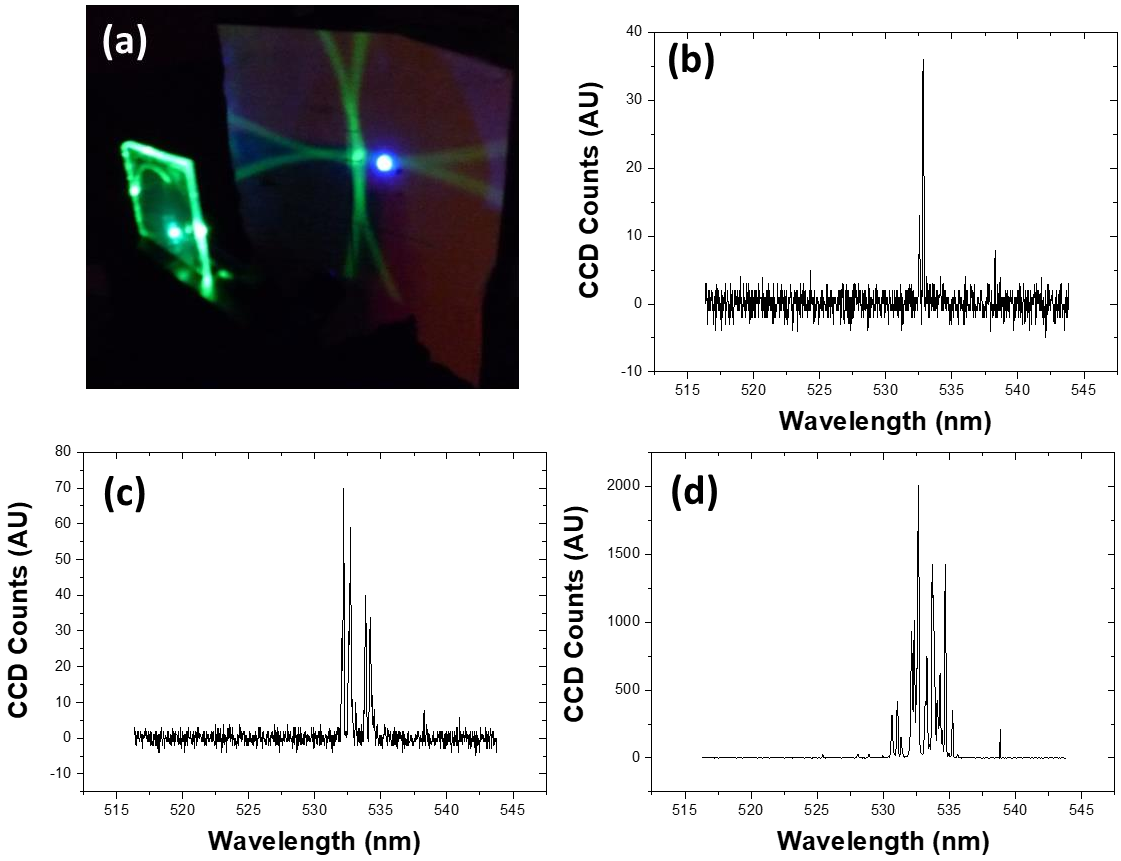

Figure 16 – (a) A picture of the $CsPbBr_3$ nanocrystal laser operating on a 335 nm 2D second order grating under 355 nm excitation. The output beam is projected onto a white screen and takes the shape of a green cross. The remnant of the pump beam can be seen as a blue dot on the screen. (b),(c), and (d) show the emission spectra from the $CsPbBr_3$ laser at 1.0x, 1.3x, and 5x threshold respectively.

We found that when the 335 nm grating was excited with a circular spot from the CryLas, a very bright, cross-shaped beam was emitted from the surface of the sample, as shown on figure 16. Measuring the beam through an Andor fibre coupled CCD camera, we found that the beam turned on above a threshold of ~70 μJcm^{-2} and emitted at a wavelength of ~532.5 nm. At threshold, the spectrum of this beam is a single resolution-limited spike, which would indicate single-mode operation. But as the pump fluence is increased the laser begins to operate in a multimode regime, with more and more spikes appearing in the spectrum as the pump fluence is increased. This is an undesirable feature, but the modes are stable with time and do not move around when pumping with constant power, which shows that they are stable lasing modes and not the results of random lasing or noise in the spectrograph. This lasing behaviour could only be seen on the 335 nm and 340 nm gratings, whilst all other gratings just produced outcoupled ASE. This would indicate that these PNC films have a much narrower resonance condition than the 3D $CH_3NH_3PbBr_3$ films, which could support lasing over a 30 nm range of grating periods.

A major point to note about these lasers is that the surface emitted beam takes the form of a clear cross shape shown in figure 17, rather than the donut shaped beam we saw in the $CH_3NH_3PbBr_3$ lasers. This shows that the PNC laser is operation on the (1,0) and (0,1) modes of the grating, rather than the (1,1) seen with the 3D material. This cross-like beam is much more common in organic polymer lasers, and we hypothesise that it is the refractive index contrast between the grating (n=1.52) and the gain medium(n=1.7 for PNCs, 2.2 for $CH_3NH_3PbBr_3$) that determines which mode is favourable. Hence the high refractive index of the $CH_3NH_3PbBr_3$ gives a (1,1) mode, while the low contrast from PNCs and OSCs favour the (1,0) modes.

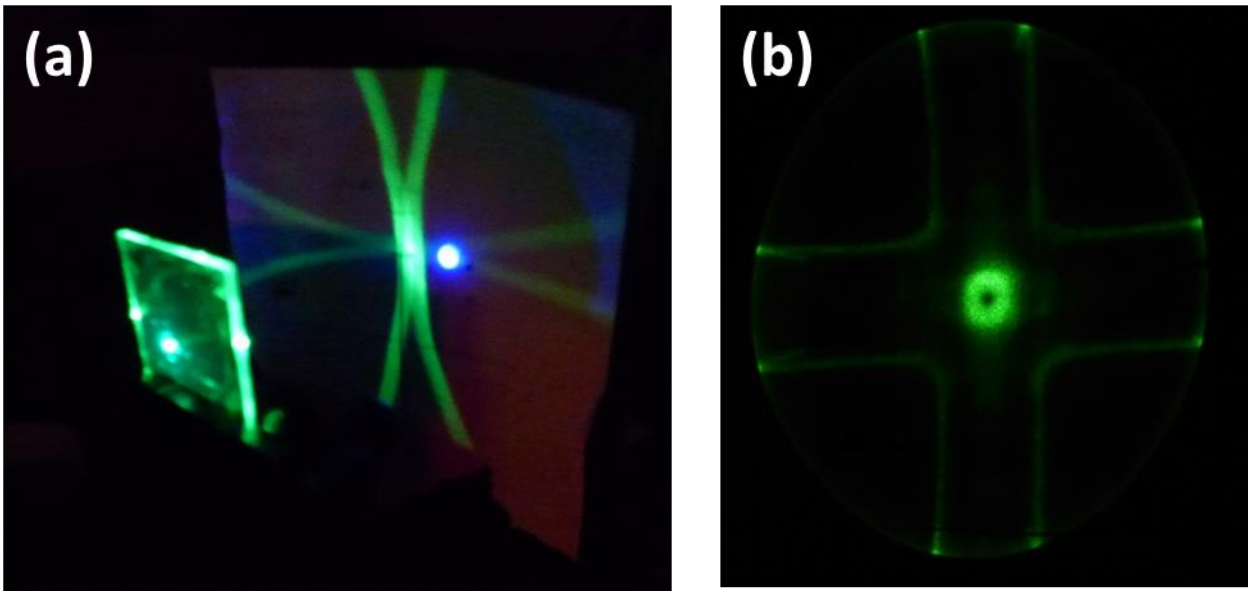

Figure 17 – Surface emitted beam from (a) $CsPbBr_3$ nanocrystal laser on a 335 nm 2D second order grating compared to (b) The output from a bulk $MAPbBr_3$ perovskite laser on a 300 nm 2D second order grating.

With proof of lasing from the 335 nm and 340 nm gratings, we finally had a material which could be supported by our 1D mixed order gratings (MOG) (which had a period of 340 nm). To investigate the effect of these gratings, we fabricated a batch of MOG lasers via nanoimprint lithography, and then deposited the PNCs and CYTOP encapsulant via identical methods to the previous batch. Upon excitation with the CryLas pump laser it immediately becomes clear that the MOG makes a significant difference to the properties of the beam. Firstly, the laser maintains its multimode operation seen in the second order gratings, but the lasing threshold is reduced by a factor of 4 down to ~20 μJ cm^{-2}. Because more and more modes appear as the pump power is increased, the input/output curve does not follow the simple two straight lines which are normally expected of a lasing graph, but the threshold can still be clearly seen in the point where the FWHM abruptly drops to less than 1 nm.

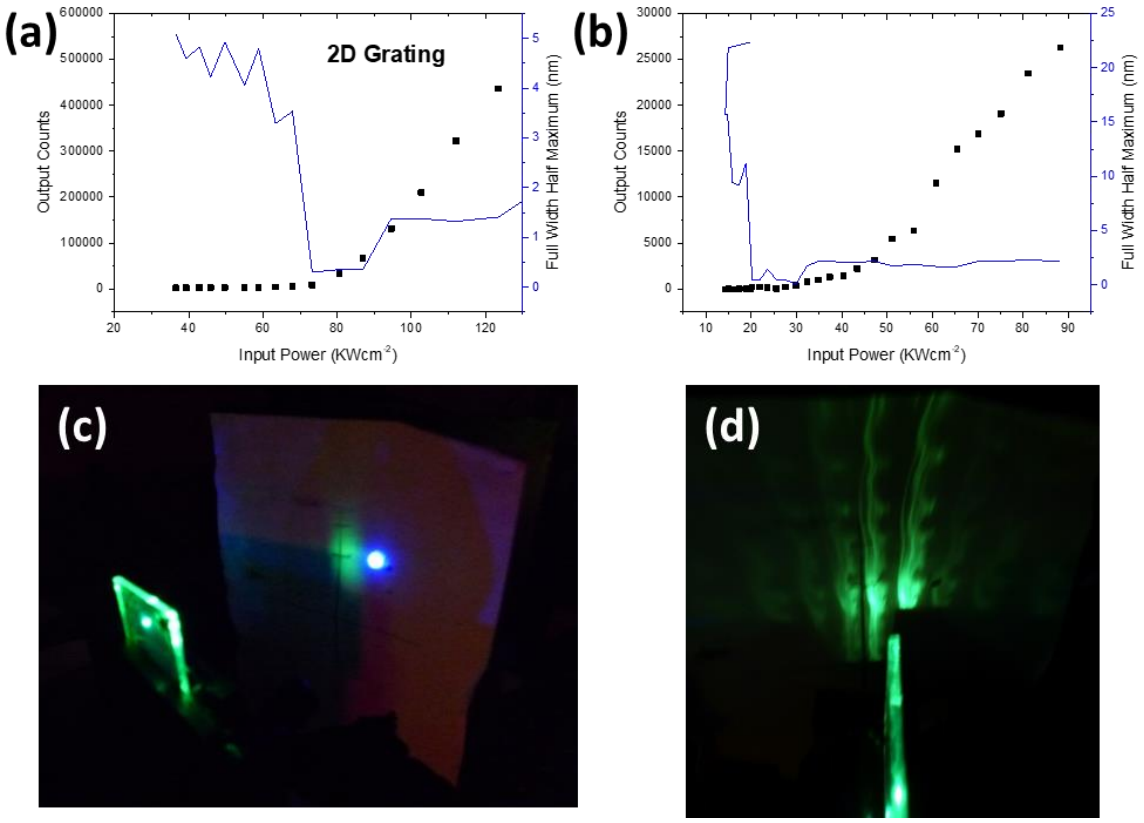

Figure 18 - Lasing threshold for CsPbBr3 on a) a 335 nm 2D grating second order grating and b) a 340 nm 1D mixed order grating. Note that the output counts starts to increase at 20 kWcm^{-2} at the same point that the FWHM drops, but the slope is continuously increasing as more modes are excited. Hence it is not clearly visible in the figure. c) The surface emitted beam from a mixed order grating and d) shows laser light outcoupled from the edge of the film

Secondly, the surface emitted beam is highly divergent, and takes the form of an elliptical spot instead of the cross-like beam seen in the 2D second order gratings. The high divergence is to be expected because the beam is being outcoupled from a much smaller area than in the 2D second order gratings, meaning it will be strongly diffracted as it leaves the grating. The emitted spot is also much dimmer than the beams from the other gratings, which is likely because the MOG has much less outcoupling than the second order gratings, and as such less light escapes the waveguided mode to join the surface emitted beam. This effect can also be clearly seen by the fact that the sample emits coherent laser light out the side of the sample of a similar strength to the light from the surface emitted beam (see figure 18 d). Light emitted in this way has the same spectrum as light from the surface emitted beam, indicating it originates in the laser grating, but this effect is not observed when using second order gratings. This is because most of the MOG does not outcouple light, meaning that a lot of the waveguided light will escape by leaking out the side of the gratings rather than being outcoupled by first order diffraction. Light which escapes the grating in this manner will be waveguided through the film until it escapes from the edge of the sample, leading to

the edge emission we observe. This effect is not clearly visible in second order gratings since they will outcouple most of their light before it leaks out the side of the grating, meaning that the edge emitted light will be too weak to observe.

Degradation and Batch to Batch variability

While green distributed feedback lasing from films of $CsPbBr_3$ is a nice result which to our knowledge has not been reported in the literature, the primary purpose of this work was to demonstrate multicolour lasing across the visible spectrum. We observed strong ASE from the $CsPbBr_{2.25}Cl_{0.75}$ PNC films earlier, so it was expected that they would provide DFB lasing in the same way as the $CsPbBr_3$ films on a grating period of roughly 315 nm. However, the film quality from the $CsPbBr_{2.25}Cl_{0.75}$ proved to be somewhat poorer than the pure $CsPbBr_3$, and all of our attempts at making a laser from this material simply emitted scattered ASE in all directions rather than coherent emission. It is also worth noting that we were not able to investigate ASE from iodide doped PNCs in the above experiments because the $CsPbBr_{1.5}I_{1.5}$ solution we received appeared to degrade over time. The emission from the solution slowly blue shifted over several weeks until it was almost the same colour as the pure $CsPbBr_3$ solution, which would indicate that the iodide component of the nanocrystals had degraded. It is known that bulk 3D films of $CsPbI_3$ are unstable to a phase change to a non-emissive δ phase at room temperature[20]. This effect has not been reported in nanocrystals of $CsPbI_3$, but we judge that the most likely cause for the degradation we observe is the iodide component of the nanocrystals degrading and ceasing to be emissive.

Figure 19 – 2 month old nanocrystal solutions of $CsPbBr_{1.5}Cl_{1.5}$ (left) $CsPbBr_3$ (centre), and $CsPbBr_{1.5}I_{1.5}$ (right). Note that the $CsPbBr_{1.5}I_{1.5}$ solution appears green rather than yellow, indicating that the solution has degraded.

In order to overcome these issues, as well as to provide tuning across the entire visible spectrum, we received several fresh batches of $CsPbX_3$ PNCs at a range of compositions. However on receiving the fresh batches we found that there was significant batch-to-batch variation in the film formation and PLQY of the PNC solutions. We found that it was common for a fresh solution to produce excellent

PLQY, often exceeding 60 %, but they would often form a much more scattering film which could not support ASE. Most batches of $CsPbBr_3$ nanocrystals could be made to support ASE after a significant amount of optimisation, but due to the time spent resolving this effect we were unable to observe lasing or ASE in other mixed halide films before the end of this PhD.

Conclusions

In conclusion, our work with low dimensional perovskites achieved the initial promise of materials with excellent PLQYs at low intensities, but we were not able to convert these initial good results into a reduction in lasing threshold or tuneable lasing. We developed a new form of layered perovskite with an exceptionally high thin film PLQY of 72 %. However, our material did not possess the clear excitonic behaviour seen in some other works. It also had an unusually high ASE threshold of 800 μJcm^{-2} due to a small amount of sub-bandgap absorption in the material, and the reasons for this detrimental behaviour remain unclear. Future work with this material would focus on its use in hybrid polaritonics and exploiting its excellent PLQY to create a high efficiency perovskite LED, or finding alternative structures without this undesirable absorbance peak.

When working with perovskite nanocrystals, our initial idea of encasing them in a PVK matrix produced very low-quality results which we hypothesise is due to quenching interactions between the polymer and the nanocrystals. In spite of this setback, we found that the raw nanocrystals themselves can be spin coated into films with remarkably high quality, which we use to produce bright distributed feedback lasers emitting in the green. However, their lasing threshold of 20 μJcm^{-2} does not improve upon the bulk $CH_3NH_3PbBr_3$ films despite the very high PLQY and low waveguiding loss, and due to time constraints and variability in the precursor solutions we were unable to achieve our main objective of multicolour lasing. This project is still at a fairly early stage, and there is a clear route to improvement on these results through future work, so it is possible that further optimisation will allow us to achieve lasing across the visible spectrum.

References

1. Xin Yu Chin, D.C., Jun Yin, Annalisa Bruno & Cesare Soci, *Lead iodide perovskite light-emitting field-effect transistor.* Nature Communications, 2015. **6**: p. 7383
2. Zhuo Yang, A.S., Krzysztof Galkowski, Nicolas Bruyant, Duncan K. Maude, Amir Abbas Haghighirad, Henry J. Snaith, Paulina Plochocka, Robin J. Nicholas, *Unraveling the exciton binding energy and the dielectric constant in single crystal methylammonium lead tri-iodide perovskite.* J. Phys. Chem. Lett., 2017. **8**(8): p. 1851–1855.

3. Arman Mahboubi Soufiani, F.H., Peter Reece, Rui Sheng, Anita Ho-Baillie, and Martin A. Green, *Polaronic exciton binding energy in iodide and bromide organic-inorganic lead halide perovskites* Applied Physics Letters, 2015. **107**(23): p. 1902
4. Yue Wang, G.T., Alexander L. Kanibolotsky, Peter J. Skabara, Ifor D.W. Samuel and Graham A. Turnbull, *Nanoimprinted polymer lasers with threshold below 100 W/cm2 using mixed-order distributed feedback resonators* Optics Express, 2013. **21**(12): p. 14362-14367.
5. Muhammad T. Sajjad, P.P.M., Hyunchae Chun, Dimali A. Vithanage, Sujan Rajbhandari, Alexander L. Kanibolotsky, Grahame Faulkner, Dominic O'Brien, Peter J. Skabara, Ifor D. W. Samuel, Graham A. Turnbull, *Novel Fast Color-Converter for Visible Light Communication Using a Blend of Conjugated Polymers.* ACS Photonics, 2015. **2**(2): p. 194-199.
6. Rui Su, C.D., Jun Wang, Timothy C.H. Liew, Jiaxin Zhao, Sheng Liu, Weigao Xu, Zhanghai Chen, Qihua Xiong, *Room Temperature Polariton Lasing in All-Inorganic Perovskites.* Nano Letters, 2017. **17**(6): p. 3982–3988.
7. Yani Chen, Y.S., Jiajun Peng, Junhui Tang, Kaibo Zheng, and Ziqi Liang, *2D Ruddlesden–Popper Perovskites for Optoelectronics.* Advanced Materials, 2017. **30**(2): p. 1703487.
8. Letian Dou, A.B.W., Yi Yu, Minliang Lai, Nikolay Kornienko, Samuel W. Eaton, Anthony Fu, Connor G. Bischak, Jie Ma, Tina Ding, Naomi S. Ginsberg, Lin-Wang Wang, A. Paul Alivisatos, Peidong Yang, *Atomically thin two-dimensional organic-inorganic hybrid perovskites.* Science, 2015. **349**(6255): p. 1518-1521.
9. Renzhi Li, C.Y., Rui Ge, Wei Zou, Lu Cheng, Nana Wang, Jianpu Wang, Wei Huang, *Room-temperature electroluminescence from two-dimensional lead halide perovskites.* Applied Physics Letters, 2016. **109**(15): p. 151101.
10. Nana Wang, L.C., Rui Ge, Shuting Zhang, Yanfeng Miao, Wei Zou, Chang Yi, Yan Sun, Yu Cao, Rong Yang, Yingqiang Wei, Qiang Guo, You Ke, Maotao Yu, Yizheng Jin, Yang Liu, Qingqing Ding, Dawei Di, Le Yang, Guichuan Xing, He Tian, Chuanhong Jin, Feng Gao, Richard H. Friend, Jianpu Wang, Wei Huang, *Perovskite light-emitting diodes based on solution-processed self-organized multiple quantum wells.* Nature Photonics, 2016. **10**: p. 699-704.
11. Mingjian Yuan, L.N.Q., Riccardo Comin, Grant Walters, Randy Sabatini, Oleksandr Voznyy, Sjoerd Hoogland, Yongbiao Zhao, Eric M. Beauregard, Pongsakorn Kanjanaboos, Zhenghong Lu, Dong Ha Kim, Edward H. Sargent, *Perovskite energy funnels for efficient light-emitting diodes.* Nature Nanotechnology, 2016. **11**: p. 872-877.
12. Constantinos C.Stoumpos, C.M.M., HsinhanTsai, WanyiNie, Jean-ChristopheBlancon, Duyen H.Cao, FangzeLiu, BoubacarTraoré, ClaudineKatan, JackyEven, Aditya D.Mohite, Mercouri

G.Kanatzidis, *High Members of the 2D Ruddlesden-Popper Halide Perovskites: Synthesis, Optical Properties, and Solar Cells of (CH3(CH2)3NH3)2(CH3NH3)4Pb5I16.* Chem, 2017. **2**(3): p. 326-327.

13. Jun Kang, L.-W.W., *High Defect Tolerance in Lead Halide Perovskite CsPbBr3.* Journal of Physical Chemistry Letters, 2017. **8**: p. 489-493.
14. He Huang , M.I.B., Stephen V. Kershaw, Maksym V. Kovalenko, Andrey L. Rogach, *Lead Halide Perovskite Nanocrystals in the Research Spotlight: Stability and Defect Tolerance.* ACS Energy Letters, 2017. **2**(9): p. 2071–2083.
15. Xie Ziang, L.S., Qin Laixiang, Pang Shuping, Wang Wei, Yan Yu, Yao Li,Chen Zhijian, Wang Shufeng, Du Honglin, Yu Minghui, G. G. Qin, *Refractive index and extinction coefficient of CH3NH3PbI3 studied by spectroscopic ellipsometry* Optical Materials Express, 2014. **5**(1): p. 29-43.
16. Eric T. Hoke, D.J.S., Emma R. Dohner, Andrea R. Bowring, Hemamala I. Karunadasa, Michael D. McGehee, *Reversible photo-induced trap formation in mixed-halide hybrid perovskites for photovoltaics.* Chemical Science, 2015. **6**: p. 613-617.
17. Loredana Protesescu, S.Y., Maryna I. Bodnarchuk, Franziska Krieg, Riccarda Caputo, Christopher H. Hendon, Ruo Xi Yang, Aron Walsh, and Maksym V. Kovalenko, *Nanocrystals of Cesium Lead Halide Perovskites (CsPbX3, X = Cl, Br, and I): Novel Optoelectronic Materials Showing Bright Emission with Wide Color Gamut.* Nano Letters, 2015. **15**(6): p. 3692–3696.
18. Tsutsumi N, I.T., *Organic dye lasers with distributed Bragg reflector grating and distributed feedback resonator.* Optics Express, 2009. **17**(24): p. 21698-703.
19. Michifumi Nagawa, M.I., Toshiki Koyama, Hirofusa Shirai, Yoshio Taniguchi, *Organic solid-state distributed feedback dye laser with a nonmorphological modification grating* Applied Physics Letters, 2000(77): p. 2641.
20. Rachel E. Beal, D., J. Slotcavage, Tomas Leijtens, Andrea R. Bowring, Rebecca, A. Belisle, William H. Nguyen, George F. Burkhard, Eric T. Hoke, Michael D. McGehee, *Cesium Lead Halide Perovskites with Improved Stability for Tandem Solar Cells.* J. Phys. Chem. Lett., 2016. **7**(5): p. 746–751.

Chapter 8 - Resonant Ultrasound Spectroscopy

Introduction

Thus far, this thesis has kept its focus on achieving high performance in perovskite optoelectronic devices, but optimising materials for device applications also requires detailed knowledge of the physical processes occurring within them. Hybrid perovskites have proven to have almost ideal parameters for a wide range of semiconducting applications, but even now the precise reasons for their excellent properties remain poorly understood. Because of this, there is intense interest in studying the fundamental properties of hybrid perovskites in order to find some clues to improving their performance even further, and so a significant portion of the work in this PhD involved collaborations with other groups to study perovskites from a fundamental physics point of view, rather than solely on device applications.

To date, there have been many studies covering the electrical [1], thermal [2], and photophysical [3] properties of $CH_3NH_3PbX_3$ (X = Cl, Br, I). But there have been relatively few studies on how the internal stresses and strains in the crystal impact the material properties. The coupling of the strain with the order parameter is well known to strongly impact the phase transitions and the structure-property relationships of oxide perovskites [4], and it would be of particular interest to see if the same rules hold for halide perovskites. The most sensitive way to measure this coupling is by measuring the elastic and anelastic properties of the material, and to do this we worked with Prof. Irvine's group (dept. of Chemistry, St Andrews) and Prof. Carpenter (dept. Earth Sciences, Cambridge) to study the effect of these parameters using resonant ultrasound spectroscopy (RUS) combined with time resolved photoluminescence and neutron diffraction.

RUS is an advanced spectroscopic technique for measuring the elastic constants and acoustic loss in a material [5]. It works by measuring the acoustic response of pellets or single crystals of a material, and it has been successfully used to study inorganic oxide perovskites for many years [4]. It has played a pivotal role in the study of new materials for ferroelectrics [6], superconductors [7], and piezoelectrics [8], but in this experiment we aimed to use it to study single crystals of $CH_3NH_3PbX_3$ and $CD_3ND_3PbI_3$. The overarching goal was to use this technique to see how the elastic and anelastic properties of the materials changed over a wide range of temperatures in order to gain an insight

into their underlying strains, disorder, and hydrogen bonding. Correlating any trends with changes in photoluminescence or neutron diffraction measurements would also provide an indication to how these parameters affect some of the properties which are of relevance to devices, and possibly provide a route to further optimisation of the material. The effect of the disorder and hydrogen bonding from the methylammonium (MA) cation in $CH_3NH_3PbX_3$ in particular is a subject of intense interest [9, 10], and the inclusion of a deuterated perovskite ($CD_3ND_3PbI_3$) provides us with a measure of control over the strength of this effect due to the difference in mass between the D and H atoms. Performing a direct comparison between $CH_3NH_3PbI_3$ and $CD_3ND_3PbI_3$ would therefore allow us to observe differences which can only be due to the change in hydrogen bonding, thus providing crucial insight into which properties are most strongly impacted by this effect.

Comparison to Oxide Perovskites

Like all perovskites, $CH_3NH_3PbI_3$ and its variants have the general formula ABX_3, where A and B are cations and X is an anion. The simplest perovskite structure is a cubic structure with the $Pm\bar{3}m$ space group, consisting of corner sharing BX_6 octahedra with A cations filling in the gaps between octahedra, but this structure can be distorted via tilting of the octahedra to make crystal structures of different symmetry. These distorted structures are known as polymorphs, and $CH_3NH_3PbI_3$ has been found by many groups to have orthorhombic, tetragonal, and cubic polymorphs in a way similar to common oxide perovskites such as calcium titanate ($CaTiO_3$) [11, 12]. For many years a parameter known as the Goldschmidt factor has been used to predict the stability of oxide perovskites and what polymorph they are likely to adopt. It uses the following equation:

$$Tolerance\ fator\ (t) = \frac{r_A + r_B}{\sqrt{2}\,(r_X + r_B)},$$

where r_a, r_b, and r_x are the ionic radii of the A,B, and X ions respectively. A tolerance factor close to 1 indicates that the ions are in exactly the right size ratio, and hence the crystal will form a cubic structure. Materials which deviate from t=1 will adopt distorted tetragonal, orthorhombic, or rhombohedral structures or may not even form a perovskite at all. This parameter is considered to be quite accurate for oxide perovskites, but work by Palgrave et al. found that applying this equation to lead halide perovskites generally resulted in incorrect predictions [13]. This was due to the ionic bonds from the heavy halogens having a significant covalent component to them, which modified the effective ionic radii and thus resulted in inaccurate predictions. By modifying the effective ionic radii to take this covalency into account, they were able to design new stability fields for halide perovskites which can once again make useful predictions [13] and can greatly assist in the search for new compositions of hybrid perovskites. This behaviour highlights the importance of comparing

the behaviour of lead halide perovskites with oxide perovskites, where the established wisdom is still of use, but in some cases will need to be modified to fit the slightly different physics from the halide anions.

One of the key differences between hybrid perovskites and their oxide counterparts is their organic component. The MA cation is not spherically symmetric, and hence hydrogen bonding or the orientation of the cation add additional variables that can affect the structure-property relationships. Because of this, there have been many theoretical and experimental studies looking into the effect of hydrogen bonding in $CH_3NH_3PbI_3$. Studies using neutron diffraction on deuterated samples have found that the hydrogen/deuterium atoms in the NH_3 part of the MA cation have the strongest hydrogen bonding with the iodine ions in the crystal, as evidenced by short H/D – I distances in $CH_3NH_3PbI_3$ [11]. It is also for this reason that the cubic phase has weaker hydrogen bonding than the tetragonal orthorhombic polymorphs, as the crystal is not able to distort to minimise the distance between the hydrogen and iodide. Several studies have attempted to determine whether the hydrogen bonding drives the octahedral tilting or vice versa in halide perovskites [14-17], but these two effects are strongly dependent on one another and so separating their effects has proven to be quite difficult. Most notably, Cheetham and coworkers [16]. were able to conclude that the hydrogen helps to stabilise the tilting in the PbX_6 octahedra, and also suggested that the directionality of the hydrogen bonding may have an impact on the photophysical properties. This result was of particular interest to us, and in this chapter we aimed to explore this link further by combining an RUS study of hybrid perovskites with an investigation into their photophysics.

The Importance of the Methylammonium Cation

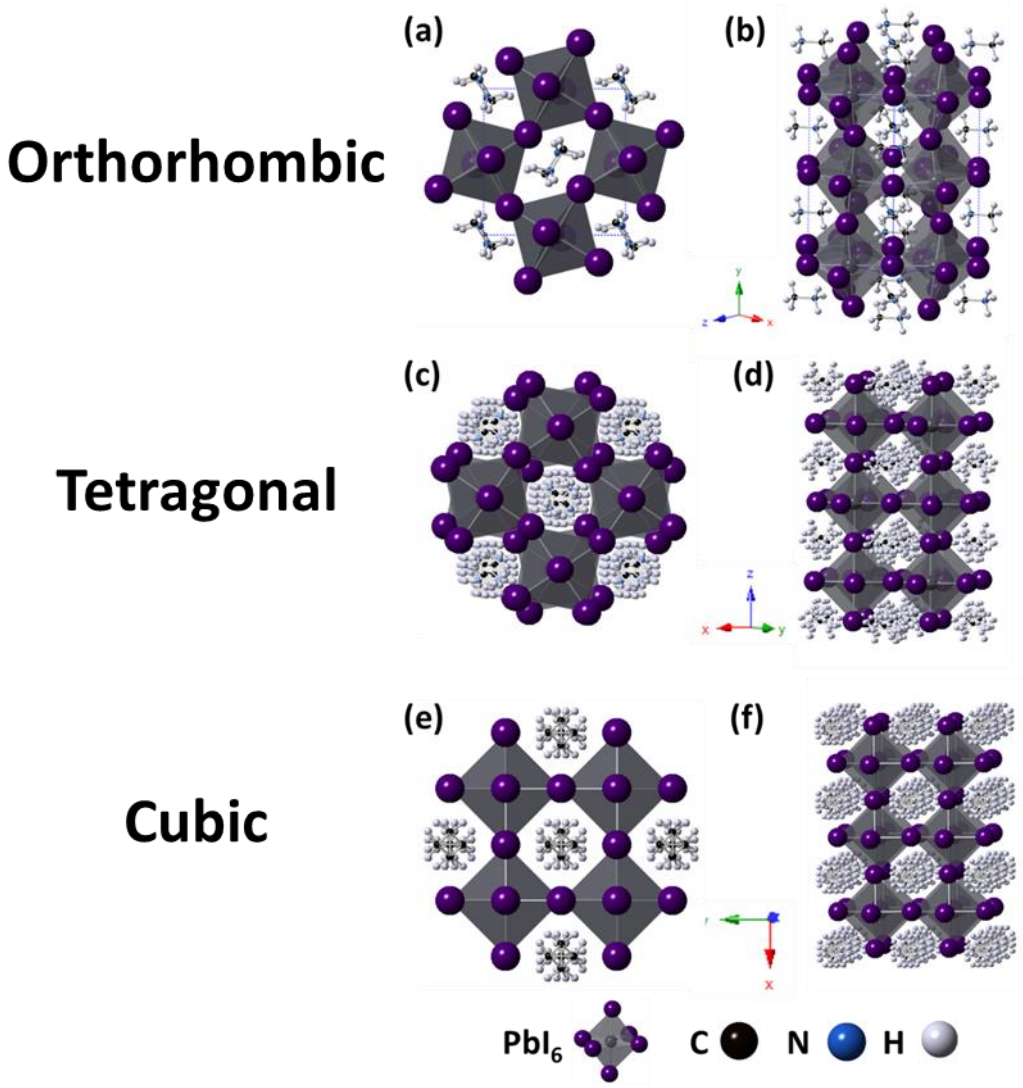

Figure 1 - Structures adopted by $CH_3NH_3PbI_3$ as determined by Whitfield et al..[11] (a and b) Orthorhombic, Pnma, (c and d) tetragonal, I4/mcm and (e and f) cubic, $Pm\bar{3}m$. (a),(c), and (e) show views along the ac plane, while (b),(d), and (f) show the view from the ab plane.

Figure 1 shows the orthorhombic, tetragonal, and cubic polymorphs of $CH_3NH_3PbI_3$, as determined by Whitfield et al. [11, 12]. The MA cation is known to cause significant difficulty in getting accurate structural models of $CH_3NH_3PbI_3$ because the MA cation is able to rotate in the A site, which introduces a large amount of disorder to the system. It is difficult to study this directly with X-rays because the X-ray scattering is dominated by the PbI_6 octahedra rather than the A site, and neutron diffraction is also difficult because the hydrogen in the MA cation has a large cross section for incoherent scattering, which is degrades much of the information from the measurement. It was for these reasons that Dr Julia Payne fabricated deuterated samples in order to achieve high quality neutron diffraction measurements , but a further advantage of this was that the difference in mass

between $CH_3NH_3^+$ and $CD_3ND_3^+$ causes significant differences in the hydrogen bonding between the MA cation and the rest of the structure, the effect of which is currently a subject of intense interest [9, 10]. There are other methods with which we could control the strength of the hydrogen bonding, such as by substituting methylammonium for formamidinium, but in this case the effects of the change in hydrogen bonding would be impossible to separate from other effects such as classical tilting due to the difference in ion sizes. By comparing $CH_3NH_3^+$ and $CD_3ND_3^+$, the only difference is the mass of the H atoms, and so we can directly observe any differences which must be due to this effect.

Principles of Resonant Ultrasound Spectroscopy

RUS is an advanced technique for determining the elastic constants of a material by measuring acoustic resonances in a sample. The setup works by placing a pellet or single crystal of the material between two piezoelectric transducers, where one transducer drives the sample with constant amplitude at ultrasonic frequencies (0.1-1.2 MHz). The other transducer acts as a detector, measuring the amplitude of vibrations in the crystal against the input frequency. Like any simple harmonic oscillator, the sample will have resonances where the amplitude of oscillation spikes at certain frequencies when the excitation matches the frequency of a certain vibrational mode. The resonant frequency of these vibrational modes depends on many factors such as the sample geometry, density and the elastic constants. Absolute values for the elastic constants of each mode can be determined by measuring a sample with a regular and known shape (ideally a parallelepiped) and density. The experimentally measured frequencies of the resonances are then fitted to a simulation and iterated to find a value for the elastic constants that reproduces the observed resonances. In our experiments we are more interested in how the elastic constants of halide perovskites change with temperature, rather than their absolute values, and so we could just use the fact that the elastic constants associated with a the vibrational mode of a small object are directly proportional to the resonant frequency (f_0) squared. In general, the elastic constants (and hence the frequency of the resonances) are expected to slowly decrease with increasing temperature due to thermal elastic softening, but if the material is approaching a phase transition or some other process then the elastic constants can undergo rapid softening or stiffening.

Making the Perovskite Samples

The single crystals of $CH_3NH_3PbX_3$ were synthesised by Dr Julia Payne by the following method: 2 ml of concentrated HX (X = Cl, Br, I) was added to CH_3NH_2 (33%, EtOH) at 0 °C (using an ice bath) under constant stirring. Lead acetate trihydrate was dissolved in HX at 100 °C. The lead-containing solution was added dropwise to the methylammonium halide solution. The samples were left on a hotplate

overnight at 75 °C. White, orange and black crystals formed, depending on the halide (Cl, Br and I respectively). The resulting crystals were filtered, washed with toluene and dried. $CH_3NH_3PbI_3$ was filtered whilst hot to avoid formation of the hydrated phase whilst in contact with the mother liquor.

$CD_3ND_3PbI_3$ was synthesised in a similar manner to the above but with measures taken to completely exclude hydrogen from the synthesis. All glassware was dried prior to use to remove traces of water, and all synthesis was carried out in an argon atmosphere using D_2O and DI instead of their hydrated counterparts. After synthesis, solid state NMR was used to probe the level of deuteration in the $CD_3ND_3PbI_3$ sample using a Bruker Advance III spectrometer, spectra showed a small percentage of H on the ND_3 group of $CD_3ND_3PbI_3$.

Resonant Ultrasound Setup

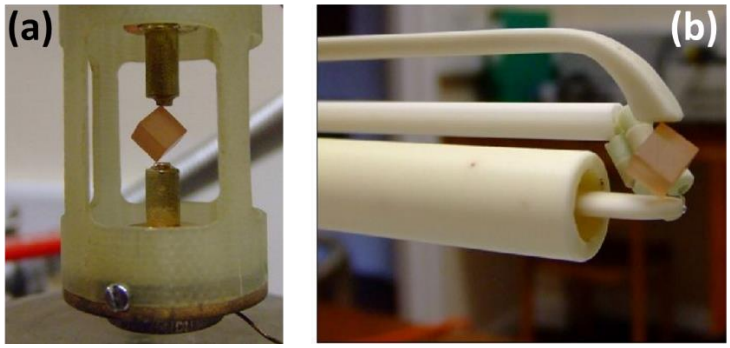

Figure 2 – A parallelepiped sample placed between two transducers in (a) the low temperature RUS setup, and (b) the high temperature RUS setup. Images taken from McKnight et al [19].

To take the RUS measurements we had two separate setups – one designed to measure above room temperature, and one for measuring samples down to 4 Kelvin. The low temperature setup consisted of a home built transducer head controlled by Dynamic Resonance System (DRS) Modulus II electronics, as described by McKnight *et al.* [18]. A single crystal was placed between the two piezoelectric transducers as shown in figure 2(a), with one acting as a resonator and the other as a sensor. This setup was then attached to the end of a stick and lowered into an Orange 50 mm helium flow cryostat, supplied by AS Scientific Products Ltd. The temperature inside the cryostat was measured and regulated using a silicon diode and a LakeShore 340 controller, allowing the setup to control the sample temperature with a precision of ± 0.1 K. Before the measurement, the sample chamber was evacuated to prevent any condensation of air during the measurement, and a few mbars of helium was then added to act as an exchange gas. RUS measurements are taken in 5 K intervals from ~295 K to ~5 K and back to room temperature, with regions of specific interest being covered in 1 K steps. Each spectrum was made of ~65,000 data points between 0.1 and 1.2 MHz, and

the sample was left to reach temperature equilibrium for 20 minutes at each step before the spectrum was collected.

The transducers used for measuring RUS are not rated to work above room temperature, and so measurements above room temperature were taken using the setup on figure 2(b), where the sample is indirectly connected to the transducers by placing it between long alumina rods with the transducers attached to the other end of each rod. These alumina rods protruded horizontally into a Netzsch 1600 °C furnace, which had its temperature recorded via a thermocouple placed several mm from the sample, providing an accuracy of ~± 1 K [20]. The presence of the alumina rods complicates the analysis somewhat since the spectrum will contain many resonance peaks due to the buffer rods in addition to the sample, but so long as the correct sample peaks are identified it is still possible to get good quality data. The high temperature measurements were taken in the same way as the low temperature setup, with the exception that the sample was kept in air rather than low pressure helium. Most measurements in this work were performed using the low temperature setup because the relevant phase transitions are usually below room temperature. But this setup needed to be used in order to observe the behaviour of the cubic phase of $CH_3NH_3PbI_3$, which is stable at temperatures above 327 K.

The samples to be measured in this experiment were single crystals of $CH_3NH_3PbX_3$ or $CD_3ND_3PbI_3$ fabricated by Dr Julia Payne. They were irregular in shape, meaning that they could not be used for measuring the absolute elastic constants, with dimensions of ~1x1x1 mm^3 and masses between 1 and 4 mg. Prior to measurement, the samples were checked optically for the absence of cracks and were measured at room temperature to determine the quality of the spectra. An example spectrum is shown on figure 3(a), and the samples which produced the best spectra were selected for further measurement at a range of temperatures.

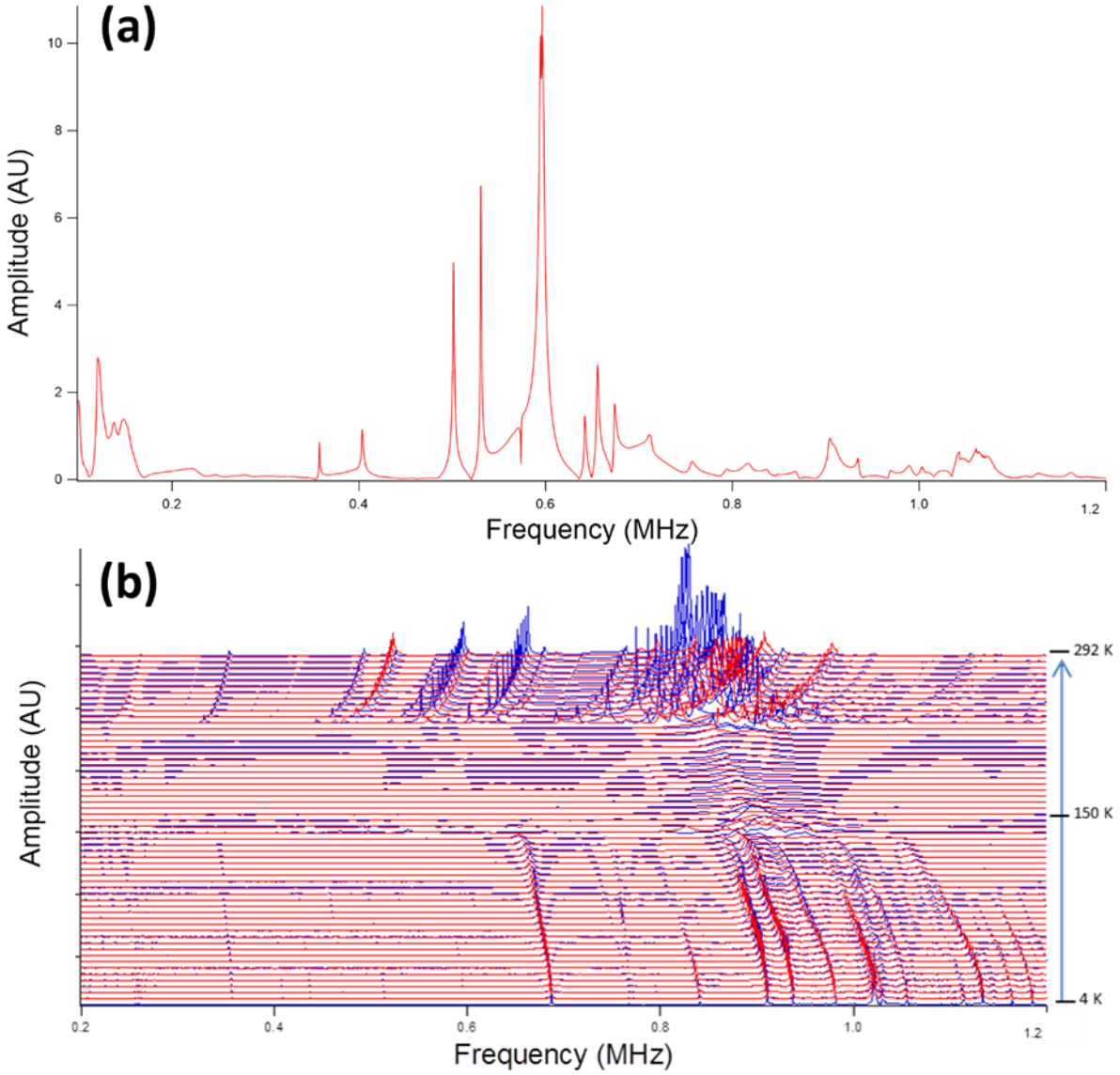

Figure 3 - (a) The RUS spectrum of a single crystal of $CH_3NH_3PbBr_3$ taken at room temperature. The acoustic resonances in the sample can be clearly seen as spikes in the amplitude of oscillation. (b)Full RUS measurement on the same sample from room temperature to 4K and back in 5 K steps. Each spectrum has been offset in the y axis in proportion to its temperature, with the room temperature spectrum at the top and the 4 K spectrum at the bottom. Spectra are plotted with blue lines if they were taken on a cooling cycle and with red lines when taken on a heating cycle.

All spectra were analysed using the Igor Pro 7.0 (Wavemetrics) software package. When measuring variable temperature data, all spectra are plotted on the same graph, with each data set plotted with a y axis offset proportional to its temperature. Spectra taken as the sample was being cooled are coloured blue, while spectra obtained during heating back to room temperature are coloured red. An example data set of $CH_3NH_3PbBr_3$ is shown on figure 3(b). Once the data has been plotted in this way, the clear resonance peaks are selected and then fit to an asymmetric Lorentzian function to determine peak frequency (f), and their full width half maximum Δf. As mentioned earlier, the

single crystal elastic constants associated with each resonance scale with f^2 [21], meaning that an increase or decrease in f^2 corresponds to the elastic constants stiffening or softening respectively. The width of each peak is related to the acoustic loss in the sample, with low loss peaks being narrow and high loss peaks being spread out. This leads us to define a quantity called the inverse mechanical quality factor, taken as $Q^{-1} = \Delta f/f$, which provides a measure of the attenuation in each peak. By fitting curves to each peak, and following the peaks as they evolve with temperature, we can then produce graphs of f^2 and Q^{-1} vs temperature. This allows us to clearly see how the elastic constants and acoustic loss vary with temperature for each resonance.

Octahedral Tilting and Twin Walls

Methylammonium Lead Bromide, $CH_3NH_3PbBr_3$

$CH_3NH_3PbBr_3$ is a material which is of less direct relevance to solar cells, but as we have already shown in this thesis it is still an excellent material for light emitting applications which warrants further study. In the following experiments, $CH_3NH_3PbBr_3$ also was found to have the most easily interpreted results, and so we shall discuss this material before moving on to the iodide and chloride variants. $CH_3NH_3PbBr_3$ is known to be in the cubic ($Pm\bar{3}m$) polymorph at room temperature, and as it is cooled it has been shown to undergo phase transitions at ~235 K, ~154 K and ~148 K [22]. These correspond to a cubic ($Pm\bar{3}m$) to tetragonal ($I4/mcm$) transition at 235 K, and a transition to the orthorhombic ($Pnma$) phase at ~148 K, with an additional phase between the orthorhombic and tetragonal regions that has been suggested to be incommensurate [31].

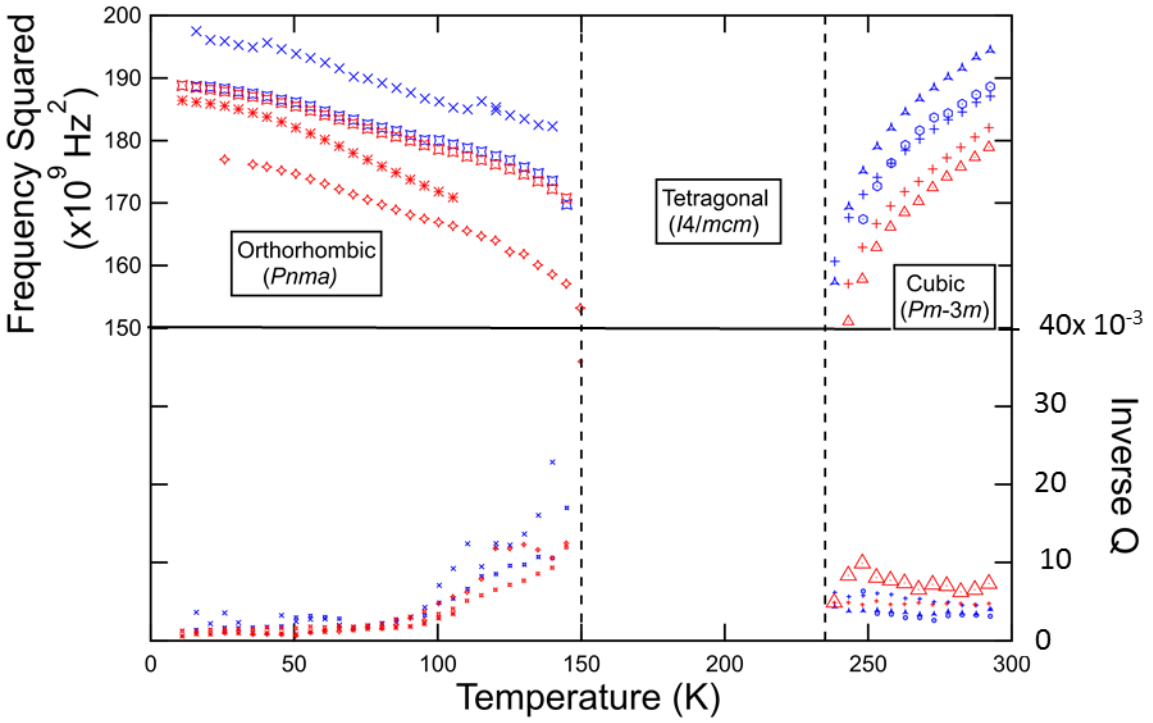

Figure 4 - f^2 and Q^{-1} values for resonance peaks in spectra collected from a single crystal of $CH_3NH_3PbBr_3$ during cooling (blue) and heating (red). Vertical dashed lines represent phase transitions. Due to high attenuation, it was not possible to follow resonance peaks in spectra collected between ~150 and ~235 K, corresponding to the expected limits for the stability field of the tetragonal phase. All f^2 values have been scaled so that they fit on the same plot.

The data on figure 3 (b) shows the raw RUS spectra collected at temperatures between 4 K and 300 K from a single crystal of $CH_3NH_3PbBr_3$. Note that in the region corresponding to the stability field of the tetragonal phase (~235 – 150 K) there are no visible peaks in the spectrum, but clearly defined peaks are visible in the regions corresponding to the cubic and orthorhombic regions. The exact temperatures of the transitions from the RUS data agree closely with the literature results [11], showing a value of 236 ± 3 K for the cubic tetragonal transition and ~147 ± 3 K for the appearance of the orthorhombic phase. In the stability field of the cubic structure, the position of the $CH_3NH_3PbBr_3$ resonance peaks (Figure 3(b)) can be clearly seen to shift to lower frequencies with reducing temperature (~300-235K). Starting from 300 K, the peaks in the cubic region can be clearly seen to shift to lower frequencies as the sample is cooled towards the cubic-tetragonal phase transition, before disappearing completely as the transition is crossed. The resonance peaks reappear when the sample enters the orthorhombic phase (~147 K), but in this phase they shift to higher frequencies as the temperature is reduced towards absolute zero.

To provide a more easily interpreted data set, selected resonance peaks were then fitted with asymmetric Lorentzian functions to give values for f^2 and Q^{-1} against temperature. The resulting

processed data is shown on figure 4, and the values for f^2 of each peak have been arbitrarily scaled so that the values for all peaks can be observed on a single graph. The data is split into three regions corresponding to its three main phases, and the tetragonal region contains no data because almost no resonance peaks are visible in this region. A few very small peaks do exist at ~0.9 MHz, but they show extremely strong attenuation and it was not possible to apply an accurate fit to them. This strong attenuation of the peaks would suggest that the tetragonal region must have extremely high loss coefficient (Q^{-1}), while the cubic and orthorhombic regions generally have fairly low acoustic loss (hence they have very cleanly defined resonances). Close to absolute zero, Q^{-1} remains at a fairly constant low value throughout the orthorhombic region until about 100 K, where it increases dramatically as the phase transition is approached. Q^{-1} in the cubic region follows a similar trend, where it is low for most of the region but is elevated near the phase transition. But the increase in Q^{-1} close to the transition in the cubic region is much less pronounced than in the orthorhombic region. Finally, the f^2 data for $CH_3NH_3PbBr_3$ shows that the peaks undergo a clear softening (decreasing f^2) as the sample is cooled from 300 K towards the cubic-tetragonal phase transition, while the peaks in the orthorhombic region undergo a steady stiffening (increasing f^2) as temperature approaches absolute zero.

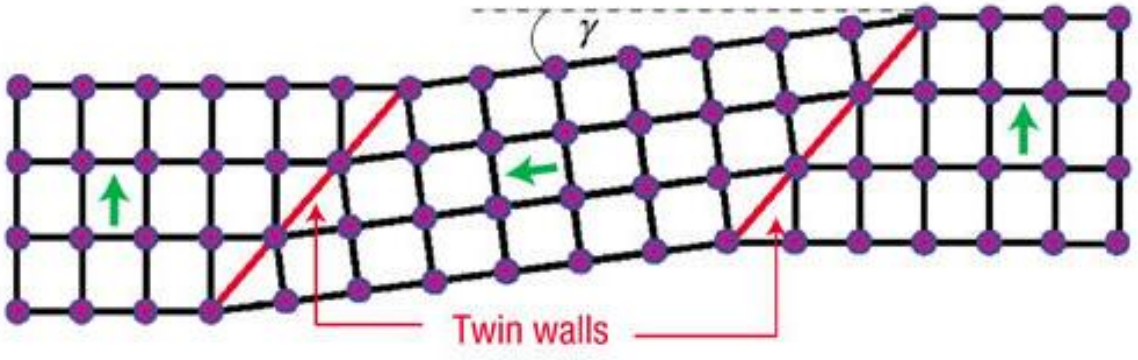

Figure 5 – an illustration of the formation of twin walls taken from Shilo et al. [23]

The behaviour of $CH_3NH_3PbBr_3$ which we observe here closely mirrors the effect of octahedral tilting transitions seen in oxide perovskites such as (Ca,Sr)TiO_3 [24]. It is clear that the tetragonal (*I*4/*mcm*) phase has very high acoustic loss, to the point that the resonances almost completely disappear, while the cubic and orthorhombic phases show very low loss. In the case of oxide perovskites, the high loss seen in the tetragonal phase is due to the motion of ferroelastic twin walls providing a pathway for acoustic attenuation. Twin walls are a phenomenon which occur in tetragonal and orthorhombic perovskites because their unit cell no longer has cubic symmetry. In a cubic

perovskite, all sides of the unit cell are the same length, but in a tetragonal unit cell one of the sides is longer than the other two. This creates a situation where the unit cells within a single crystal can be aligned so their long axes are perpendicular to each other. There is a distortion in the lattice where two regions of different orientation meet, and these distortions are known as twin walls because each anomalous region will be bounded by two of these distortions. These twin walls are free to move through the lattice when the crystal is placed under mechanical stress, dissipating energy in the process. The dissipation of energy by the twin walls is why the tetragonal region sees such high loss, and hence we are unable to observe any clear resonance peaks. These twin wall regions are also present in the orthorhombic phase, but in oxide perovskites they have been shown to become immobile in the orthorhombic phase [24], [4]. This means that the twin walls in the orthorhombic phase cannot cause acoustic loss, and hence the clear resonance peaks with low loss become visible in this region. The precise reasons for the immobile twin walls in the orthorhombic phase remain poorly understood, but our result shows that the same process occurs in halide perovskites as well as oxides.

Turning to the f^2 values, the rapid softening of the elastic constants in the cubic phase as the sample is cooled towards the cubic-tetragonal phase transition is also typical for oxide perovskites [24-26]. Phase transitions are caused by the current phase becoming unstable to the point that it is favourable for the crystal to switch to a different phase, and coupling with strain or with fluctuations associated with the phase transition typically give rise to elastic softening. This can also be seen in the orthorhombic region, where the peaks harden quickly as they are cooled away from the unstable region near the phase transition before entering a roughly linear trend. Unless there are competing effects from incipient phase transitions, it is known that most elastic constants will show a steady stiffening as the sample is cooled towards absolute zero. Hence the linear trend we see in the orthorhombic region of $CH_3NH_3PbBr_3$ is entirely expected, and indicates that there is no evidence of further phase transitions in the material which could be favourable below absolute zero. The overall picture then is that $CH_3NH_3PbBr_3$ undergoes classical octahedral tilting transitions that are almost an exact analogue of oxide perovskites such as $(Ca,Sr)TiO_3$, with all the associated elastic and anelastic properties obeying similar trends.

As a final exploration into the properties of $CH_3NH_3PbBr_3$, we moved to investigate the reports of the intermediate phase in the narrow temperature interval between the orthorhombic and tetragonal phases (148-154 K) [22, 27-29]. To study this, we collected RUS spectra in 1 K steps between 140 and 160 K. The raw spectra are shown on figure 6(a), with the processed data from selected peaks being shown on figure 6(b).

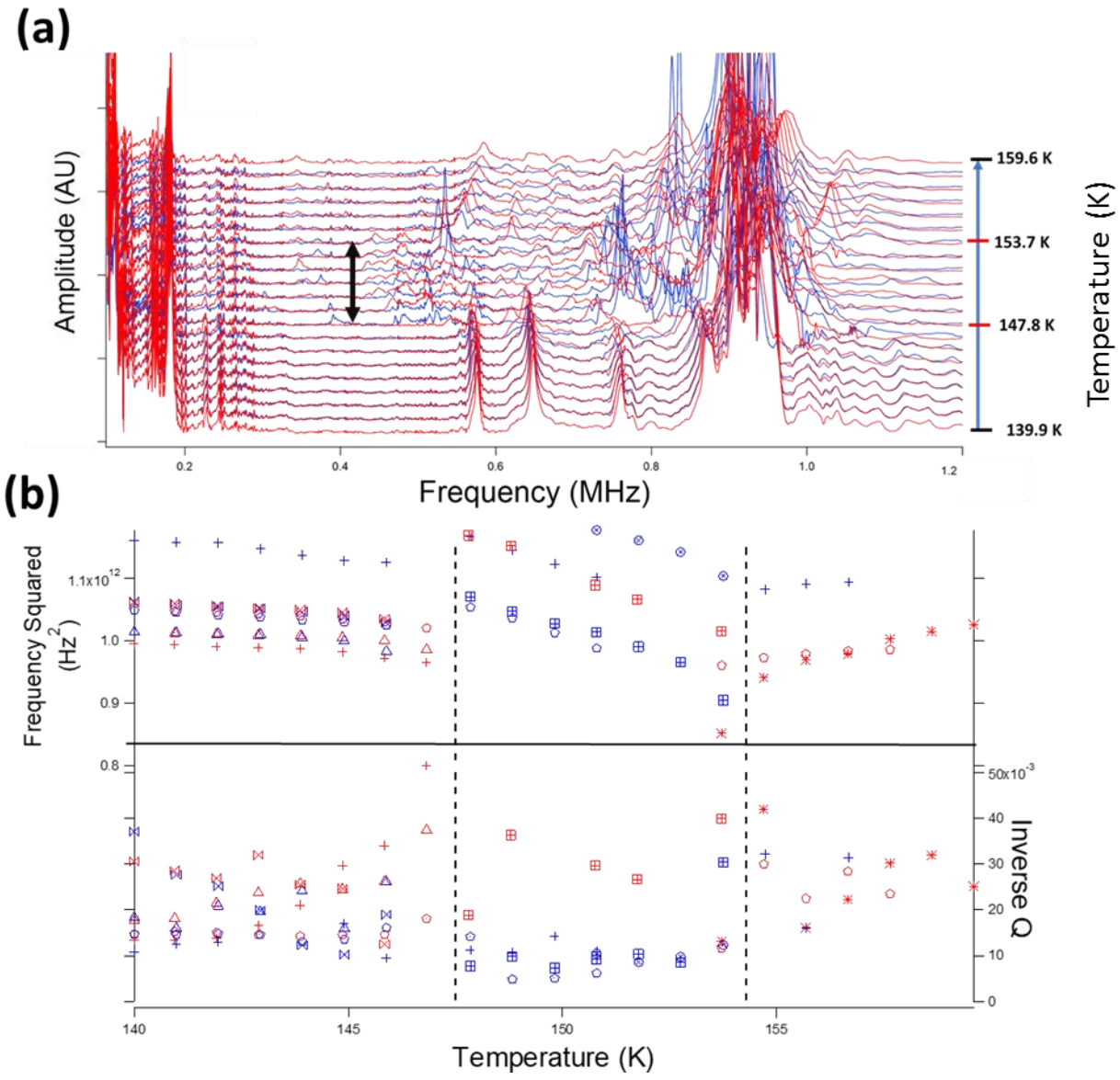

Figure 6 – (a) The raw RUS spectra of $CH_3NH_3PbBr_3$ between 140 and 160 K in 1 K steps. The black arrow shows the region between 147.8 and 153.7 K where peaks from the incommensurate phase are visible. (b) The processed data taken from selected regions peaks. The phase boundaries are shown with dashed lines, and peaks measured in a cooling cycle are shown in blue, while peaks measured in a heating cycle are red. Each individual peak is represented with a different symbol.

As can be seen in figure 6(a), there is a sudden shift in the appearance of the peaks in the 147.6 K spectrum, where the sample leaves the orthorhombic region, but there is a second shift in the peaks at 153.7 K, which would indicate a second phase transition. The temperature of these phase transitions closely matches the literature reports of ~147 and ~154 K [36]. Differential scanning calorimetry (DSC) measurements taken by Dr Julia Payne, which find the phase transitions by measuring spikes in the specific heat capacity as the sample is heated and cooled, also confirmed the presence of two phase transitions at these temperatures. The spectra of the intermediate phase appear to more closely resemble the tetragonal (*I*4/*mcm*) region than the orthorhombic (*Pnma*),

with weakly defined peaks likely caused by attenuation due to twin walls. These results cannot be used to determine the exact nature of this intermediate phase, but they do provide external confirmation of the presence of this phase, and we have shown that it is likely more closely related to the tetragonal phase rather than the orthorhombic.

Methylammonium Lead Iodide, $CH_3NH_3PbI_3$

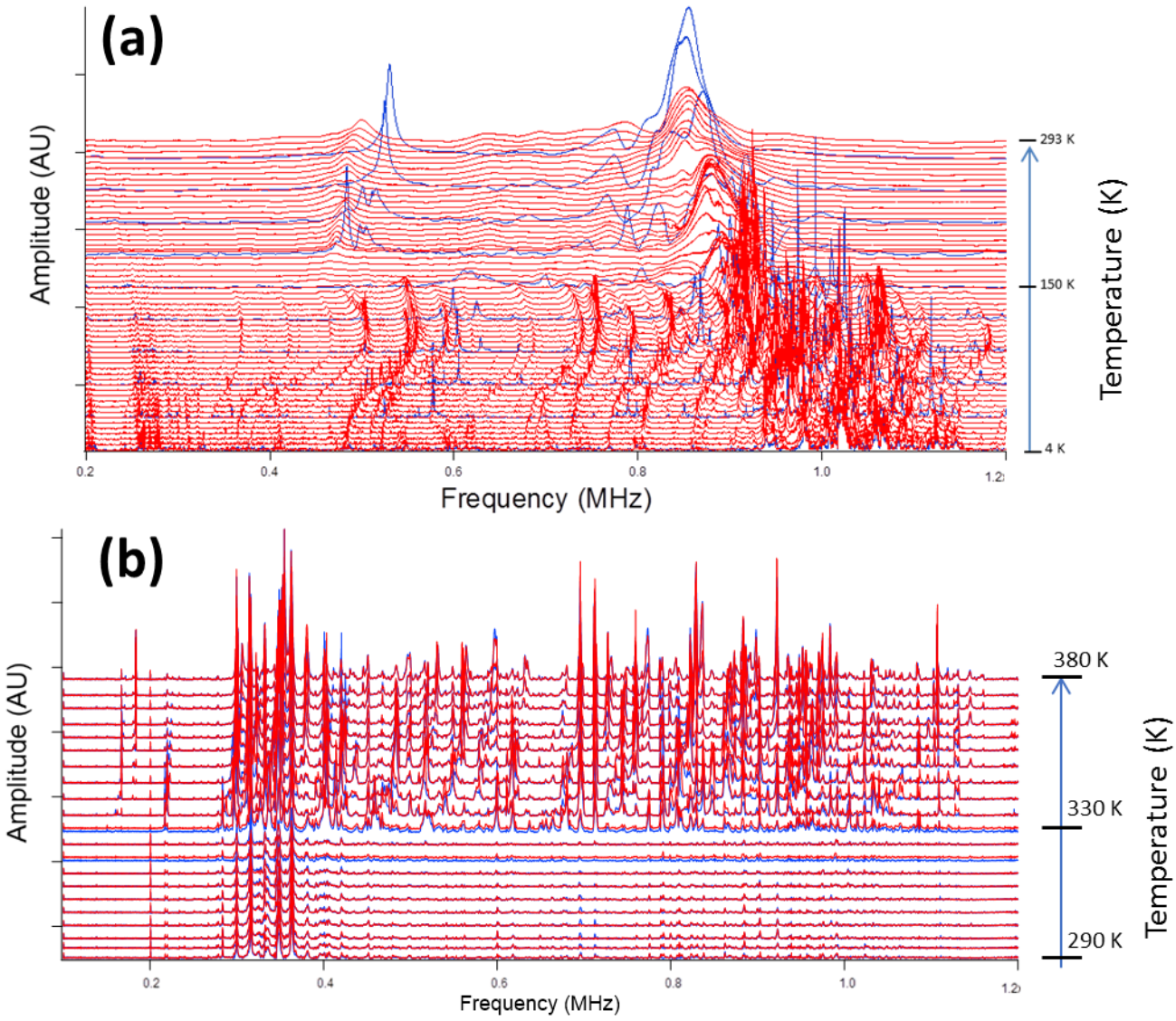

Figure 7 – Raw RUS data sets for $CH_3NH_3PbI_3$ at temperatures between (a) 4 K and 293 K using the low temperature setup, and (b) 290 to 380 K using the high temperature setup. Note that most of the peaks in the high temperature setup are due to the rods rather than the sample, but the phase transition at 330 K can still be clearly seen where the peaks abruptly disappear due to large attenuation in the tetragonal phase.

Figure 7 shows the raw RUS data for a single crystal of $CH_3NH_3PbI_3$ from 4 K to 380 K, with the high temperature setup being used to measure spectra above room temperature. The processed data from selected peaks is shown on figure 8 and, as in the $CH_3NH_3PbBr_3$ case, the values for f^2 of each

peak have been arbitrarily scaled so that the values for all peaks can be observed on a single graph. Looking at the data, it is clear that $CH_3NH_3PbI_3$ has very similar behaviour to $CH_3NH_3PbBr_3$, with three distinct regions corresponding to the cubic (*Pm* $\bar{3}$*m*), tetragonal (*I*4/*mcm*), and orthorhombic (*Pnma*) phases. Many clearly defined peaks are visible in the spectra from 4 K up to the orthorhombic – tetragonal phase transition at ~162 ± 3 K, and the peaks are strongly attenuated in the tetragonal region, with only one peak in this region being clear enough for good fitting. Looking at the high temperature data, the tetragonal-cubic transition is clearly visible at ~328 ± 3 K where many resonance peaks abruptly appear as the sample is heated past the transition. From the literature, the expected sequence of transitions is *Pnma – I4/mcm - Pm* $\bar{3}$*m*, with the *Pnma – I4/mcm* transition at ~165 K and the *I4/mcm - Pm* $\bar{3}$*m* transition at ~327 K [11, 12, 30, 31], which agree almost exactly with our results.

Looking at the Q^{-1} data, it is clear that the acoustic loss in $CH_3NH_3PbI_3$ follows similar rules to those seen in $CH_3NH_3PbBr_3$ earlier. The loss is low in the orthorhombic and cubic regions, with the exception of a small increase in loss near the phase transitions, and there is large loss in the tetragonal region. The high loss in the tetragonal region is once again due to the mobile twin walls in this phase, and this could have some significance because $CH_3NH_3PbI_3$ is in the lossy tetragonal phase at room temperature, meaning that perovskite solar cells will be affected by this behaviour. Twin walls have long been known to have a profound influence on the properties of superconductors and piezoelectrics [32, 33], with the twin walls possessing unusual properties that are not present in the bulk material, and there is now increasing interest in their significance for solar cells. The existence of these twin walls has recently been directly observed in $CH_3NH_3PbI_3$ solar cells by Rothman et al using transmission electron microscopy [34], and while their direct impact on device performance remains unclear, it opens up another possible pathway to optimise the properties of perovskite solar cells.

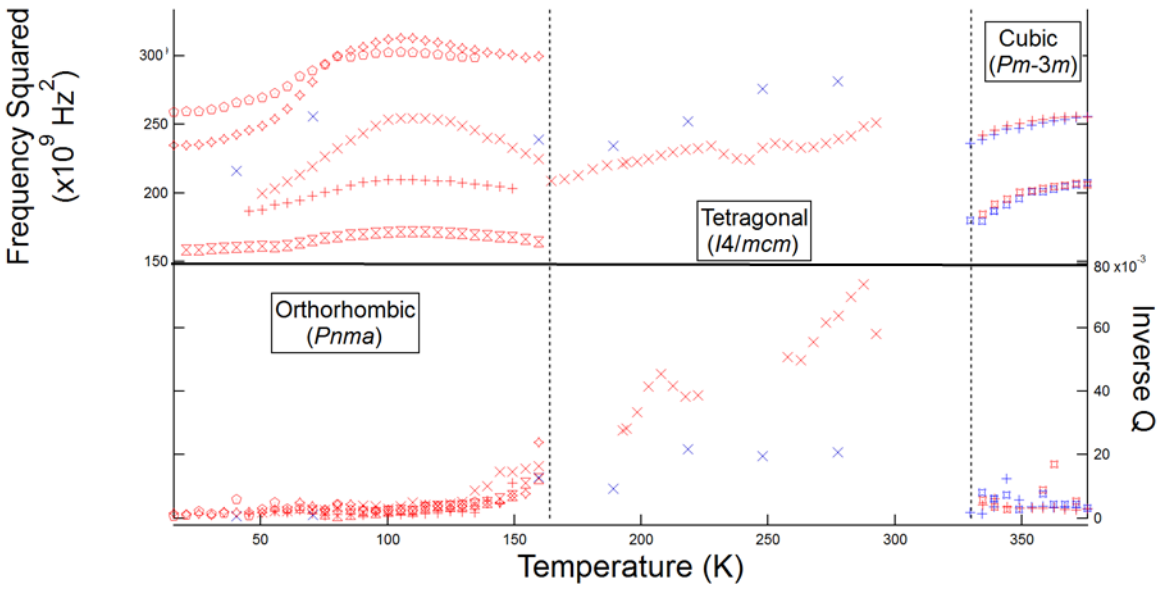

Figure 8 - Variation of f^2 (representing elastic constants) and Q^{-1} (representing acoustic loss) as a function of temperature, for different resonance peaks in a single crystal of $CH_3NH_3PbI_3$ (each represented with a different symbol), scaled to be closer together for clarity. The phase transitions are shown by dotted lines. Blue and red points represent data collected during cooling and heating respectively.

Moving to the f^2 values, the peak frequency of the resonances follows a similar pattern to that seen in $CH_3NH_3PbBr_3$. Starting at 380 K, all the resonance peaks show a clear softening as the temperature is decreased towards the phase transition at 328 K. Below the cubic-tetragonal phase transition, most of the peaks disappear, but the few that remain also show a clear softening with decreasing temperature towards the tetragonal-orthorhombic transition point. This is consistent with the observation that a material generally undergoes softening as it approaches a phase transition. Many clear peaks appear when the sample goes through the tetragonal-orthorhombic transition and, like the observations for $CH_3NH_3PbBr_3$, they all show a clear stiffening (increasing f^2) as the sample is cooled away from the transition point. However, $CH_3NH_3PbI_3$ starts to differ from its bromide counterpart at temperatures below 110 K, where the stiffening trend starts to reverse and the peaks all begin to rapidly soften as they approach absolute zero. This unusual effect cannot be attributed to the appearance of anelastic defects or cracks in the sample because the loss remains unchanged throughout the entire process, meaning it must be due to a real effect in the material. It can be seen in the data that the magnitude of this softening effect varies significantly depending on the peak being studied, with the most affected peaks softening by up to 20 % over the whole process. But despite the differences in magnitude, all the peaks obey the same overarching trend of a hardening followed by a softening.

Since most materials will tend to stiffen rather than soften as they are cooled, the most likely implication of these results is that the material is approaching another phase transition. But there does not appear to be any abrupt changes or discontinuities in the spectra that could indicate another transition. A similar behaviour to this has previously been observed in lanthanum aluminate ($LaAlO_3$) [35], and the interpretation in this case was an incipient instability with a phase transition which is favourable below absolute zero. Hence the material was softening on the approach to this transition but never actually underwent a transition because the transition point cannot be reached. This explanation is equally valid for our observations in $CH_3NH_3PbI_3$, with the key difference that the magnitude of the softening observed in $CH_3NH_3PbI_3$ is nearly 20 times greater than what was seen in $LaAlO_3$. This incipient transition could be caused by tilting due to the mismatch of ion sizes in the $CH_3NH_3PbI_3$. Alternatively, it could be caused by the MA cation due to hydrogen bonding or the alignment of the cations at low temperature. Since this instability is completely absent in the $CH_3NH_3PbBr_3$ sample, it seems likely that the instability is at least partly controlled by the mismatch of ion sizes in the lattice. To see if the MA cation also plays a role in this behaviour, we shall next move on to the $CD_3ND_3PbI_3$ sample to see how the change in mass due to deuteration impacts the instability.

Deuterated Methylammonium Lead Iodide, $CD_3ND_3PbI_3$

We next collected RUS spectra from a single crystal of $CD_3ND_3PbI_3$ at temperatures between 4 and 293 K. The raw spectra are shown on figure 9, and the processed data for f^2 and Q^{-1} of selected peaks are shown on figure 10. The first point to note from this data is that the temperature of the tetragonal to orthorhombic phase transition is almost unchanged by the exchange of deuterium for hydrogen. From the spectra we find a transition temperature of 159 K ± 3 K, and this is backed up by DSC measurements by Dr Julia Payne which found transition temperatures of 161 K/155 K (heating/cooling) for the orthorhombic-tetragonal transition and 327 K/324 K (heating/cooling) for the cubic-tetragonal transition. These transition temperatures are almost identical to the transition temperatures of 162 ± 3 K and 328 ± 3 K we observe in non-deuterated $CH_3NH_3PbI_3$. This means that if the change in cation hydrogen bonding has any effect on the phase transitions, its impact is far weaker than that seen when switching iodine for bromine, which causes the phase transitions to move to 148 ± 3 K and 236 ±3 K. This strongly supports the conclusion that the phase transitions in these materials are primarily driven by octahedral tilting from the size mismatch of the ions, rather than from hydrogen bonds between the MA cations and the rest of the lattice.

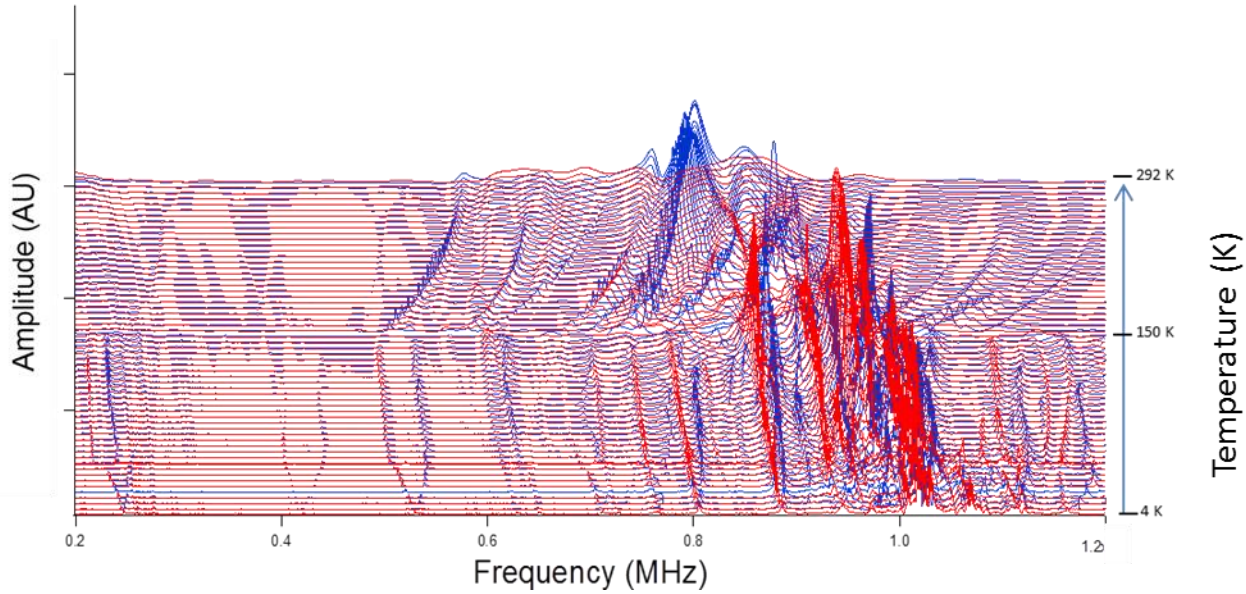

Figure 9 - Primary RUS spectra from a single crystal of $CD_3ND_3PbI_3$. Each spectrum has been offset up the y-axis in proportion to the temperature at which it was collected. Blue spectra collected during cooling, red spectra collected during heating.

On initial inspection, the RUS data for $CD_3ND_3PbI_3$ seems to follow a similar pattern to the previous materials, with low loss in the orthorhombic region and higher loss in the tetragonal region, but on closer inspection there are several key differences. Firstly, the tetragonal phase of $CD_3ND_3PbI_3$ has many clearly defined peaks which, although lossier than in the orthorhombic phase, are significantly clearer than in the tetragonal phase of the non-deuterated materials. This would suggest that the introduction of deuterium has substantially lowered the amount of acoustic attenuation in the tetragonal phase.

The acoustic loss provides a measure of the effective viscosity a twin wall experiences when it is forced to move through the crystal by an external stress. The exact mechanisms for this loss is a matter of great interest in many fields, since controlling the behaviour of twin walls (known as "domain wall engineering") would be a huge breakthrough in many fields of materials science such as memory storage and superconductivity. The main two loss mechanisms that twin walls can experience are extrinsic – caused by the interaction of twin walls with defects in the lattice – and intrinsic – caused by twin wall interactions with phonons [35]. Determining exactly which of these is the dominant mechanism in halide perovskites is a matter for further study, but the more interesting point is that these results show that we can achieve a measure of control over the motion of twin walls in the sample by exchanging hydrogen for deuterium. This could be of great interest in the field of domain wall engineering [32, 33], as it could provide a means for controlling the formation and motion of twin walls without having to make major changes to the perovskite composition.

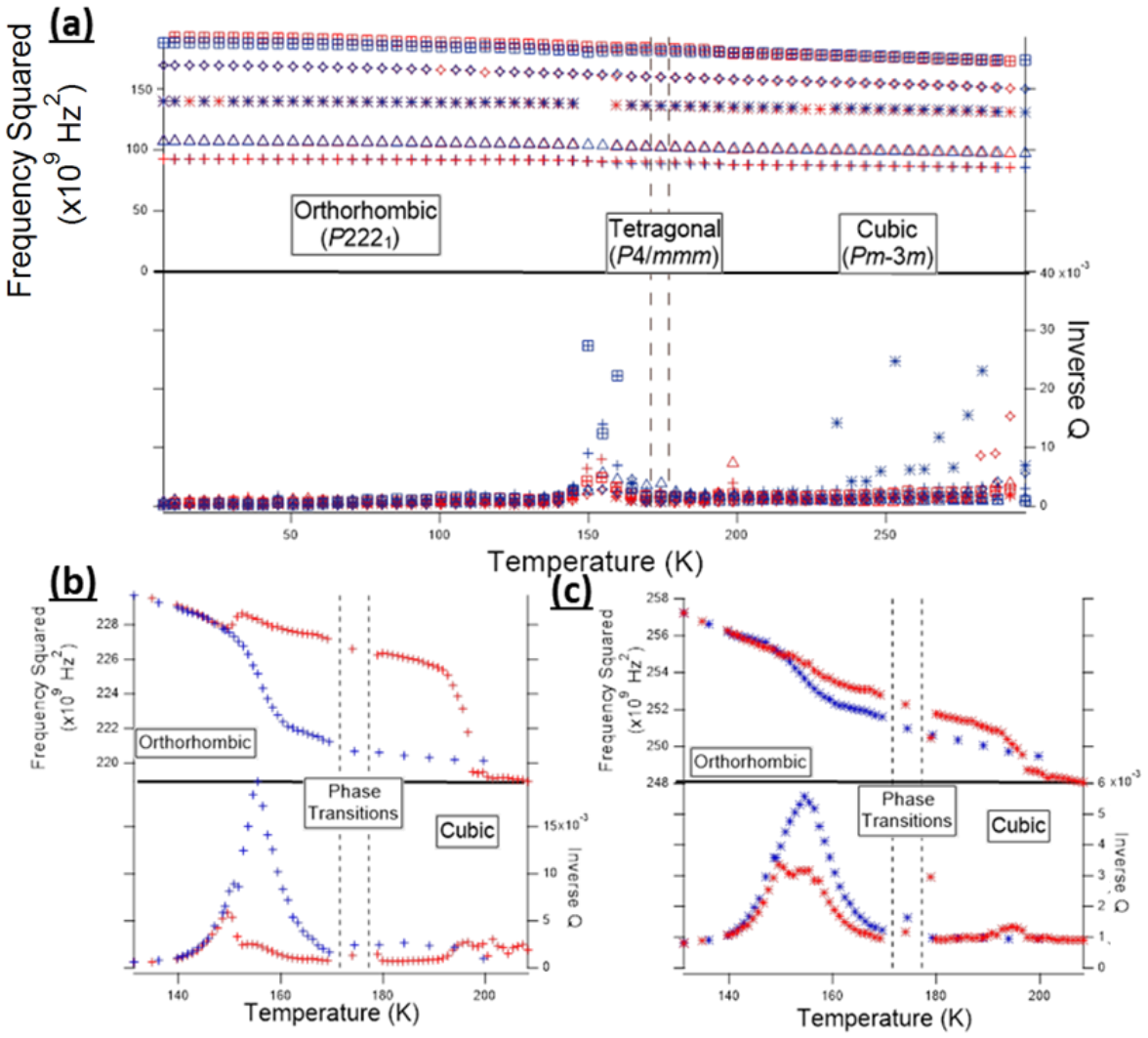

Figure 10 – Compiled data of the f^2 and Q^{-1} of selected resonance peaks from figure 9. (a) shows the data for all peaks at temperatures from 4 K to 293 K. The tetragonal – orthorhombic transition is marked with a vertical broken line. Data collected on cooling and heating are represented by blue and red points respectively. (b) and (c) show zoomed in data for single peaks purely within the orthorhombic region. (b) and (c) show the anomalies in the evolution of f^2 at ~40 K, which may be the result of an additional phase transition.

Secondly, the sudden softening behaviour seen in the $CH_3NH_3PbI_3$ sample at ~110 K (figure 8) is dramatically different in $CD_3ND_3PbI_3$. Instead, the f^2 data follows the standard slow stiffening with decreasing temperature down to ~40 K, at which point there is a sudden change in slope, with some peaks also having a small discontinuity in their positions (figure 10 b and c). This small discontinuity could be indicative of a new phase transition which has been brought on by the change in hydrogen bonding, and this hypothesis is backed up by neutron diffraction data on samples from the same batch (taken by Dr Julia Payne), which showed a very minor hop in lattice parameter at the same temperature as the discontinuity in the RUS data. Since the changes are so minor, we cannot draw concrete conclusions on the exact nature of this transition. But the conclusion that we can draw is

that the incipient instability seen in $CH_3NH_3PbI_3$ is indeed closely related to the effect of hydrogen bonding in the system, since swapping hydrogen for deuterium causes a dramatic shift in its behaviour. This is in addition to our previous observation that the effect is completely removed by swapping I for Br, which would suggest that the instability is related to the hydrogen bonding between MA cation and the PbX_6 octahedra, and this effect is insufficient to cause an instability in the bromide perovskite because the ion sizes are better matched.

Finally, all of the resonances show a significant hysteresis in their f^2 values, with the peaks taken during heating not returning to the values seen on the cooling cycle and remaining different across the entire orthorhombic region. It is also worth noting that the acoustic loss in the tetragonal phase seen during the heating cycle is significantly higher than that seen during cooling, but similar effects to this are also seen in the normal $CH_3NH_3PbI_3$ sample. This hysteresis behaviour can be explained by the dynamics of twin walls in the material. The twin walls can occur on several different axes of the crystal, and if there are equal numbers of twins on each axis then the overall macroscopic symmetry will be cubic. However, if it becomes favourable for twins to be oriented on a preferred axis then the overall symmetry will be broken, and the effective elastic constants for each resonance will depend on the precise orientation of the twins. Hence this hysteresis could be caused by a change in the configuration of the twins as the sample is cooled, and this change is not reversed upon heating.

Hydrogen Bonding and Debye Losses

Methylammonium Lead Chloride, $CH_3NH_3PbCl_3$

As a final part of our investigation with RUS, we studied the properties of $CH_3NH_3PbCl_3$ to see if it could give us any further insight into the effect of hydrogen bonding in hybrid perovskites. Hydrogen bonding is expected to play an even larger role in $CH_3NH_3PbCl_3$ because the radius ratio criteria for tilting transitions are no longer met. It is known to undergo two phase transitions at 171 and 177 K [36], but these appear to be predominantly driven by hydrogen bonding from the ordering of the MA cations in the A site, rather than by octahedral tilting [37]. The expected sequence of phases is similar to the previous materials (cubic to tetragonal to orthorhombic with falling temperature), but the tetragonal phase has a different space group (*P4/mmm* rather than *I4/mcm*) and may even be incommensurate [37]. Additionally, the unit cell of the orthorhombic phase of $CH_3NH_3PbCl_3$ has a different unit cell to the tilted structure in the orthorhombic phase of the other perovskites, despite them both being in the same *Pnma* space group.

Once again, the RUS spectra were collected from single crystals of $CH_3NH_3PbCl_3$ between 4 K and 293 K, and the raw spectra collected for $CH_3NH_3PbCl_3$ in the temperature interval 5-295 K are shown in

figure 11(a), and the compiled data for f^2 and Q^{-1} of selected peaks are shown on figure 11(b). Immediately, it is clear that $CH_3NH_3PbCl_3$ exhibits very different behaviour to its counterparts. As can be seen from the data, the resonance peaks change very little across the entire temperature range, with only a very slight trend of stiffening with decreasing temperature, which is to be expected. The peaks appear to be completely unaffected by the phase transitions, indicating that the phase transitions will at most have only small and subtle impacts on the elastic properties.

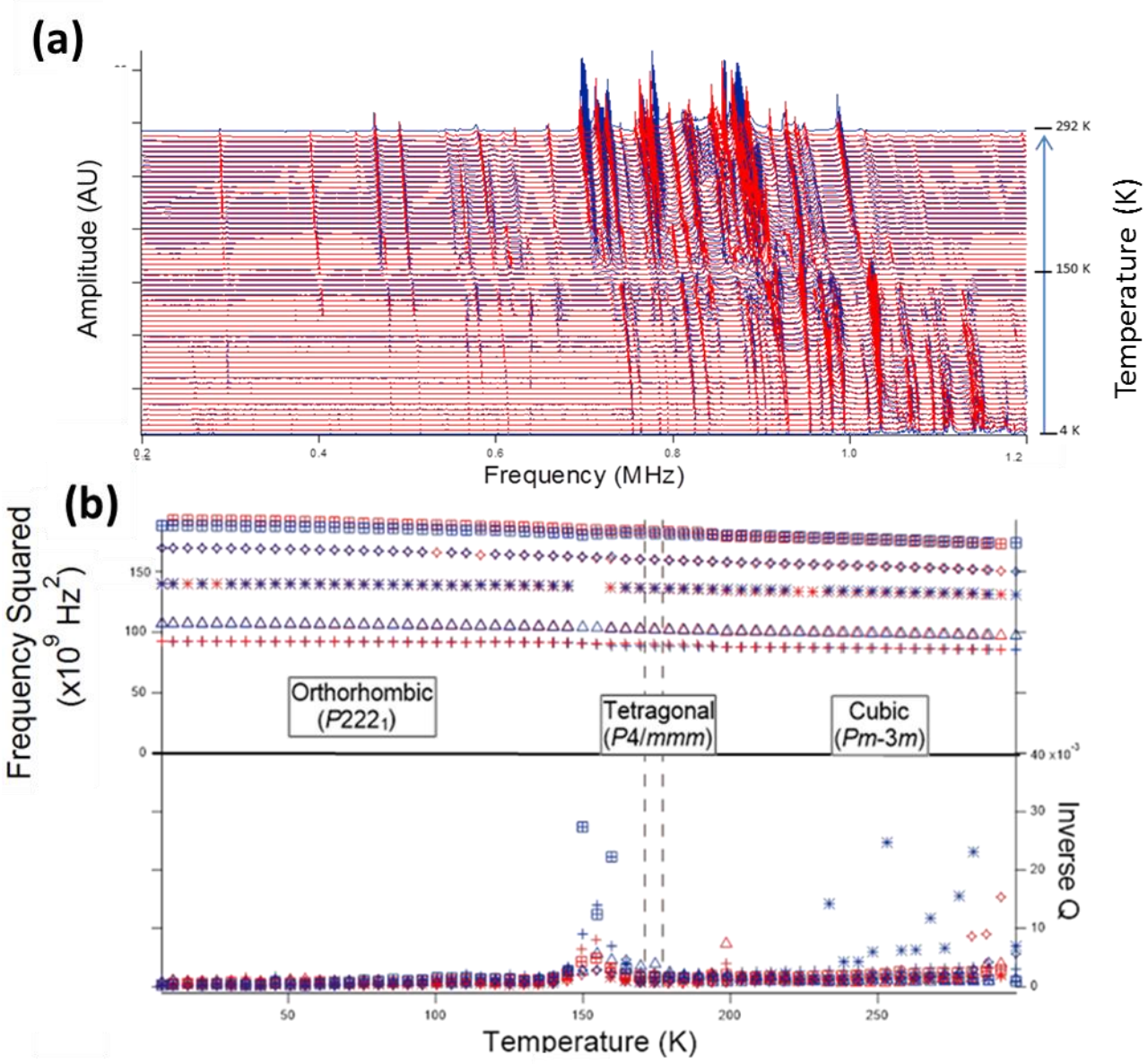

Figure 11 –(a) Raw RUS spectra from a single crystal of $CH_3NH_3PbCl_3$ from 4 K to 293 K. Each spectrum has been offset up the y-axis in proportion to the temperature at which it was collected. Blue spectra collected during cooling, red spectra collected during heating. (b) Variation of f^2 and Q^{-1} with temperature for the resonance peaks in RUS spectra from a single crystal of $CH_3NH_3PbCl_3$. Dotted lines represent the expected phase transition temperatures. Blue points and red points represent values for the cooling sequence and the heating sequence respectively. Each symbol represents a different peak.

The fact that the peaks are unchanged by the phase transitions provides us with information of how the hydrogen bonding impacts the elastic properties. $CH_3NH_3PbI_3$ and $CH_3NH_3PbBr_3$ have acoustic properties which are broadly similar to those seen in most oxide perovskites. When near a phase transition, a stress applied via the RUS setup will induce a strain in the crystal, and this in turn causes the order parameter to relax so that the crystal becomes softer than it would be without coupling. The stronger the coupling, the greater the magnitude of the softening, and the strength of this coupling can be measured from the spontaneous strains in the unit cell of the crystal [38],[39]. Data from the neutron diffraction experiments performed by Dr Julia Payne found that the spontaneous strain in $CD_3ND_3PbI_3$ and $CH_3NH_3PbI_3$ is high, at about 3%. This is close to an order of magnitude higher than normally seen in oxide perovskites [40], and it goes a long way to explain why the magnitude of the softening seen in $CH_3NH_3PbI_3$ is so much greater than in oxides such as $LaAlO_3$ [35]. The phase transitions in $CH_3NH_3PbCl_3$ are caused by ordering of the hydrogen bonds rather than tilting of the octahedra, and so studying this material allows us to see how the strain from the RUS impacts the hydrogen bonds rather than the tilted octahedra. From the literature, the linear strains in the *Pnma* polymorph of $CH_3NH_3PbCl_3$ are roughly 1% [37], and hence by this logic we would expect large softening effects to be visible in the $CH_3NH_3PbCl_3$ spectra, but this is not the case. The implication of this is that the application of a stress in the 1 MHz region does not cause the order parameter to relax i.e. the configuration of hydrogen bonds which are responsible for the phase transitions in this crystal remain fixed on a timescale of ~10^{-6} s and are not disordered by the energy input from the RUS.

Another crystal which has its phase transitions dominated by hydrogen bonding is Lawsonite, ($CaAl_2Si_2O_7(OH)_2.H_2O$), and literature RUS measurements show that the phase transitions of this mineral are also not accompanied by any elastic softening [18, 41, 42]. Instead, the ordering of the hydrogen bonds produces a series of braces through the crystal which causes a substantial stiffening rather than a softening. We do not observe this stiffening effect in $CH_3NH_3PbCl_3$, presumably because the additional hydrogen bonding is relatively weak by comparison to the metal-halide bonds that are already present, and hence the MA cations do not achieve the same bracing effect as water in Lawsonite.

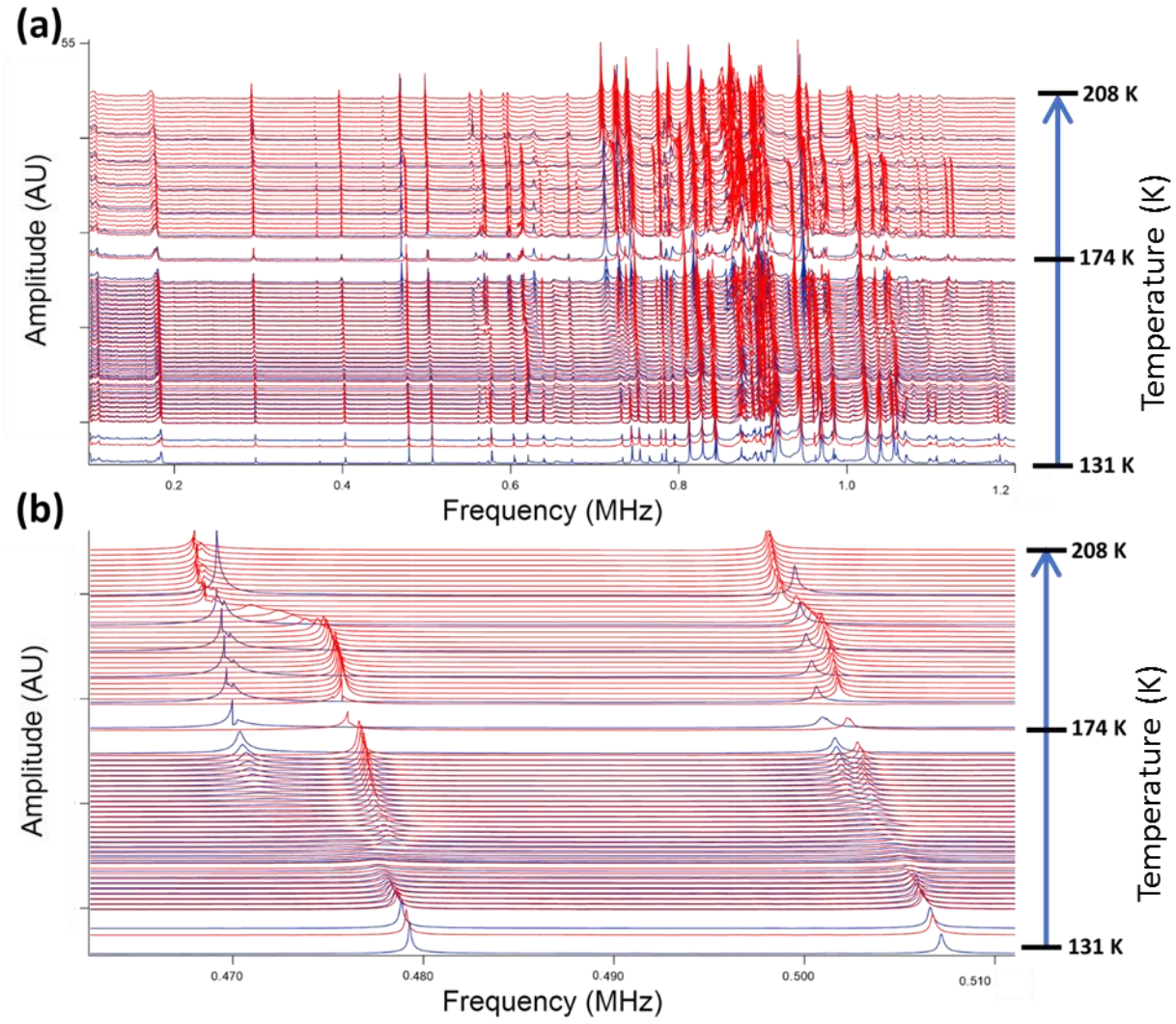

Figure 12 – (a) Raw RUS spectra from a single crystal of $CH_3NH_3PbCl_3$ from 131 K to 208 K in 1 K steps. Each spectrum has been offset up the y-axis in proportion to the temperature at which it was collected. Blue spectra collected during cooling, red spectra collected during heating. (b) A zoomed in image of the same spectra to more clearly show the hysteresis.

Debye Analysis

The only noticeable feature across the entire data set of $CH_3NH_3PbCl_3$ is that there is a narrow spike in Q^{-1} at approximately 160 K, which does not appear to be related to the phase transitions, and so to examine this behaviour more closely we collected a second set of spectra between 130 and 210 K in 1 K steps. This would provide more detail on the spike in Q^{-1} we observed, whilst also allowing us to see any features due to the phase transitions which we may have missed. The raw spectra for this is shown on figure 12 (a), and looking closely at the peaks there appears to be some form of hysteresis in the frequency of the resonance peaks between about 140 K and 200 K. Figure 12(b) shows a zoomed in view of one of the peaks to demonstrate this, and figures 13(a) and (b) show compiled data of the f^2 and Q^{-1} for the peaks at 480 and 510 kHz.

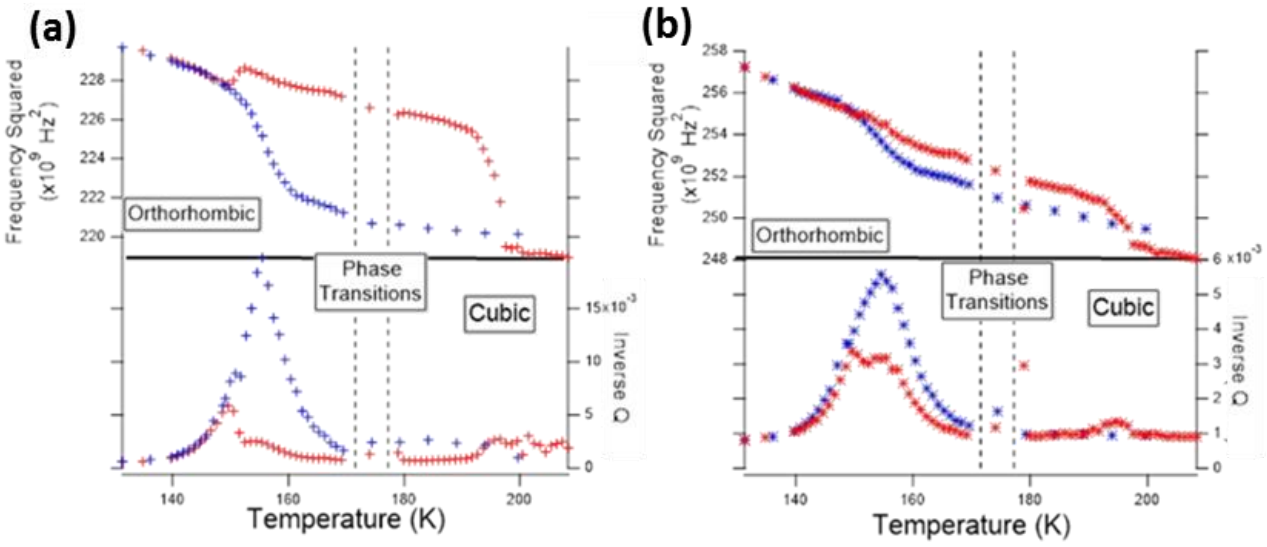

Figure 13 – Compiled data for the f^2 and Q^{-1} values of the resonance peaks at (a) 480 KHz and (b) 510 kHz respectively.

Looking at the data shown on figure 13, there is a clear peak in the Q^{-1} values of the peaks at ~ 155 K, and this is accompanied by a slight stiffening of the resonance with falling temperature. This behaviour is typical of a Debye loss effect associated with a freezing process that is coupled with strain [43]. The peak in loss is caused when the relaxation time (τ) of the process overlaps with one of the normal acoustic resonances in the sample. The acoustic resonance will have an angular frequency (ω), where ω (=$2\pi f$), and the peak in loss will occur when $\omega\tau = 1$. To determine what this freezing process is, we next aimed to calculate the activation energy for this process. This is usually calculated by measuring loss as a function of frequency under constant temperature. However, in RUS we only have access to roughly one logarithmic unit of frequencies, and so we perform the measurement with varying temperature and roughly constant frequency. This has been successfully analysed in a number of cases [4] using the function

$$Q^{-1}(T) = Q_{\mathrm{m}}^{-1}\left[\cosh\left\{\frac{E_{\mathrm{a}}}{\mathrm{R}r_2(\beta)}\left(\frac{1}{T}-\frac{1}{T_{\mathrm{m}}}\right)\right\}\right]^{-1}$$

where the maximum value of Q^{-1}, Q^{-1}_{m}, occurs at temperature T_{m} and the temperature dependence is determined by the activation energy, E_{a}, combined with a spread of relaxation times described by the term $r_2(\beta)$ [44,45]. R is the gas constant and $r_2(\beta)$ = 1 if there is only one relaxation time.

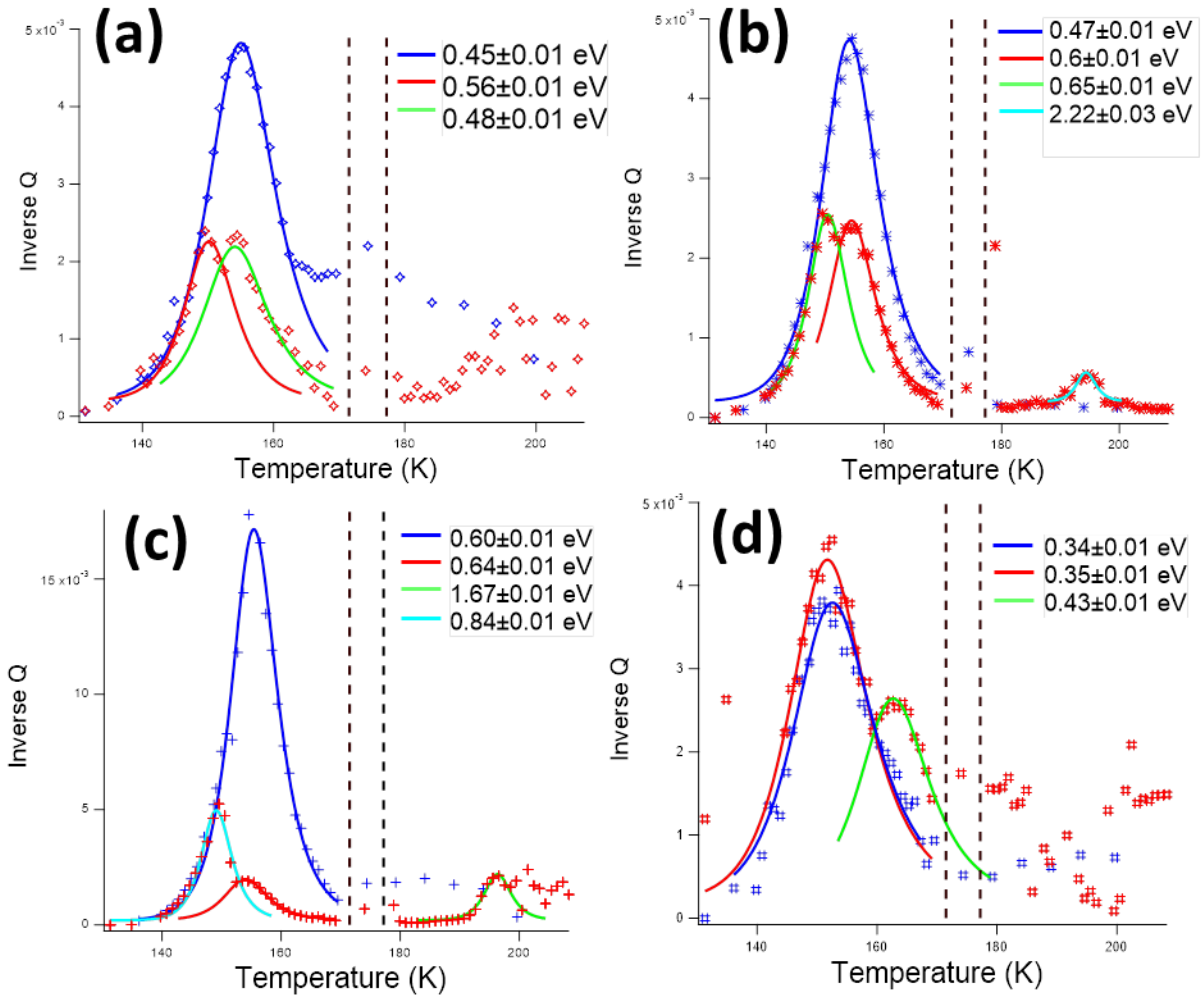

Figure 14 - Fits of Equation 1 to selected loss peaks at (a) 1020 KHz, (b) 510 KHz, (c) 480 KHz and (d) 290 KHz, respectively, for resonances observed during cooling (blue) and heating (red). A constant baseline is removed from each data set prior to fitting. The values of Ea shown for each peak are under the assumption that r_2 (θ) = 1. Activation energies for each fit are shown in the legend.

To extract useful values from this equation, we fit this equation to the Q^{-1} values of the resonance peaks at 1020, 510, 480, and 290 kHz, and the value of E_a that provided the best fit to the data was taken as the activation energy of the loss process. The result of these fits is shown in figure 14. In the cooling data, all the measurements show a single peak in Q^{-1} at ~155 K, and fitting the curves gave estimates of activation energies ranging between 340 and 600 meV. In the heating cycle, there are multiple, smaller peaks around 155 K, and this suggests that several distinct relaxation processes occur through this interval. Fits to these curves gives activation energies in the range of 350-840 meV (see figure 14). We suggest that the lower E_a processes represent a freezing in the rotation of the $CH_3NH_3^+$ cation, while the higher energy processes represent the motion of the Cl^- ions between lattice vacancies. The latter of these processes is closely related to the Hoke effect which we have discussed previously [46], and finding ways to study and overcome this effect is one of the major

focuses of perovskite research today. The motion of halogens in the hybrid perovskite lattice has been previously calculated to have an activation energy of ~0.6 eV by Eames et al [47], which closely matches the activation energy obtained here. The freezing of the MA cation has received less study, but a recent study by Chen et al [48] found that the MA cation in $CH_3NH_3PbI_3$ has a rotational degree of freedom with an activation energy of ~80 meV. This is significantly different from our result of ~ 350 - 600 meV, but this could be due to the slightly different structure of There is less available data on the freezing of the $CH_3NH_3^+$ cation, but Chen et al recently reported that the $CH_3NH_3^+$ cation in $CH_3NH_3PbI_3$ has a rotational degree of freedom with an activation energy of approximately 80 meV, which differs significantly from our result. This could be due to the different structure of $CH_3NH_3PbCl_3$ compared to $CH_3NH_3PbI_3$, as the tilting transitions may significantly affect this result. Future work on this effect would focus how the process changes when the $CH_3NH_3^+$ cation is replaced with $CD_3ND_3^+$, $CH(NH_2)(NH_3)^+$, or Cs^+ ions so as to confirm that the A site cation is the cause of this freezing. Finally, the data shown in Figure 14 (b) and (c) also show a small peak in the heating cycle at ~195 K, and fits to this data estimates these processes to have activation energies of ~ 1.7 – 2.2 eV. We suggest that this corresponds to movement of the Pb^{2+} ion, which was calculated by Eames et al to have an activation energy of 2.3 eV [47].

PL Measurements on Iodide and D-Iodide

As discussed earlier, it is of great interest to determine if different processes we have observed via RUS have a noticeable impact on the photophysical properties. To study this, we worked with Dr Tariq Sajjad from our group at the University of St Andrews to perform a time resolved photoluminescence measurement on $CH_3NH_3PbI_3$ and $CD_3ND_3PbI_3$ to see if any of the photoluminescence parameters could be correlated with the features in the RUS spectra. It would also allow us to see what affects the difference in hydrogen bonding due to the deuteration has on the PL. The same crystals that were used in the RUS study were used for PL measurements, and the crystals were ground into a powder to assist in the measurement. The powder was placed in between two 10 mm quartz disks to hold it in place, and the disks were then transferred to a holder in an Oxford Instruments nitrogen cryostat. The cryostat had transparent windows to allow optical measurements on the sample, and it was pumped down to a pressure of $\sim 10^{-4}$ mbar to prevent condensation of air in the chamber. The sample temperature was controlled using liquid nitrogen and an ohmic heater in a cold finger setup, so that set points between 77 and 300 K could be obtained. To measure photoluminescence, the sample was optically excited with 515 nm light from a Light Conversion™ regeneratively amplified Pharos Laser with 200 fs pulses. The remaining pump light was then filtered out and the photoluminescence was measured with a Hamamatsu streak

camera. Note that we did not have access to liquid helium in this setup so the measurement was limited to a minimum temperature of 77 K.

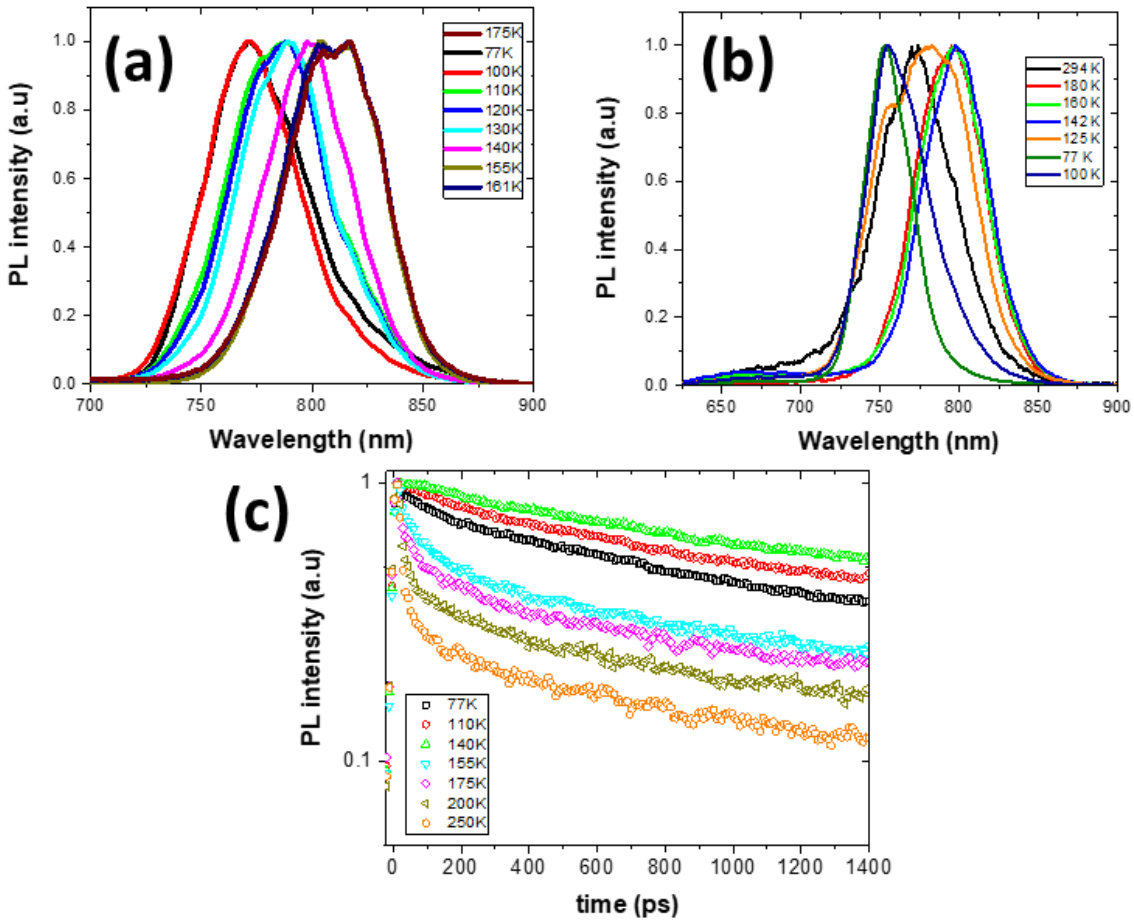

Figure 15 – Normalised photoluminescence spectra for (a) $CH_3NH_3PbI_3$ and (b) $CD_3ND_3PbI_3$ at various temperatures. (c) Time resolved photoluminescence of $CH_3NH_3PbI_3$ – note that the PL lifetime suddenly spikes around 140 K

The raw PL spectra for $CH_3NH_3PbI_3$ and $CD_3ND_3PbI_3$ at a range of temperatures are shown on figure 15 (a) and (b) respectively, and the peak PL counts vs time for $CH_3NH_3PbI_3$ at different temperatures is shown on figure 15 (c). It is important to note that the PL was not measured using an integrating sphere, so it is valid to compare the PL counts on different measurements of the same sample, but the data cannot be used to compare absolute PLQY between samples.

To aid analysis, the peak wavelength and total PL counts for both samples at each temperature were then extracted from the initial data, and the results are shown on figure 16. Looking at the peak PL wavelength, it can immediately be seen that substituting H for D causes the PL to be consistently blue shifted by approximately 20 nm compared to the original $CH_3NH_3PbI_3$. As the temperature is decreased from 300 K, the peak wavelength for both samples shows a slow increase up to approximately 180 K, where it plateaus for both samples. The PL peak for both samples appears to

remain completely constant as the sample crosses the phase transition, and as the samples are cooled further they reach a point where the PL starts to rapidly blue shift with decreasing temperature. The onset point for this sudden blue shift is ~150 K for $CH_3NH_3PbI_3$ and ~130 K for $CD_3ND_3PbI_3$. In both samples, this sudden blue shift is accompanied by a steep increase in the PL counts with decreasing temperature, which up until this point had remained relatively constant. The increase in PL with decreasing temperature continues to the limit of our experimental range of 77 K, but the blue shift of the bandgap appears to plateau for both samples at around 100 K. Note that this sudden rise in PL counts is coupled with a dramatic spike in PL lifetime at 140 K, which would suggest that this rise in PL counts is related to the removal of a major loss pathway.

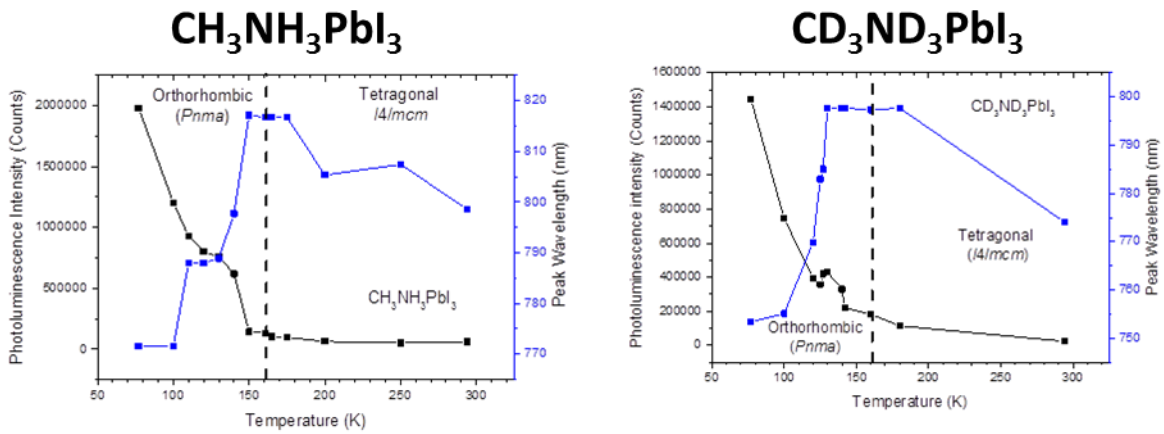

Figure 16- Photoluminescence wavelength (blue data points) and intensity (black data points) versus temperature for (a) $CH_3NH_3PbI_3$ and (b) $CD_3ND_3PbI_3$. Dashed vertical lines represent the phase transition temperatures.

The first point to note about this data is that in both samples the phase tetragonal-orthorhombic transition has little to no impact on the PL properties. This is significant because it shows that, while the tilting transitions have a huge impact on the elastic properties, it would seem that the photophysical properties are relatively unaffected by the tilting. However, the sudden blue shift and rise in PL counts at ~150 K in the $CH_3NH_3PbI_3$ sample seems to indicate that a much more significant process developing below the phase transition. 150 K is the exact temperature at which the peak in Q^{-1} was observed in the $CH_3NH_3PbCl_3$ sample, which leads us to the hypothesis that the shift in photoluminescence behaviour is caused by the freezing of the motion of the MA cations which we discussed in the previous section. The fact that the $CD_3ND_3PbI_3$ sample exhibits similar behaviour at a slightly lower temperature lends further credence to this hypothesis because this change can only be due to the change in mass between D and H, and it would make sense that a change in hydrogen bonding strength would alter the temperature at which this effect would occur. This hypothesis would be significant if confirmed, as it would show that designing an A site cation to freeze at

temperatures closer to room temperature could be a route to significant improvement in PLQY for optoelectronic devices.

Conclusions

In summary, this chapter shows a study of the elastic and photophysical properties of methylammonium lead halides. The overall aims were to see how these hybrid perovskites compare to more standard oxide perovskites, to investigate the effects of hydrogen bonding and tilting on the properties of the samples, and to see if any of the elastic properties had any impact on the photophysical characteristics. We found that $CH_3NH_3PbI_3$ and $CH_3NH_3PbBr_3$ have their phase transitions controlled by octahedral tilting in a similar way to $Ca_xSr_{1-x}TiO_3$, with the exception that the lattice strains and softening processes are close to an order of magnitude greater than seen in most oxides. We observed a sudden softening behaviour in $CH_3NH_3PbI_3$ below ~110 K, which strongly indicates that there is another instability in the crystal leading to a phase transition which would occur below absolute zero.

We were able to exploit the fact that $CH_3NH_3PbCl_3$ does not undergo tilting transitions in order to observe transitions which were controlled by hydrogen bonding rather than tilting. We found that these hydrogen bonding-dominated transitions had very little impact on the elastic properties, but we were also able to observe a separate Debye loss effect at ~150 K which we attribute to the freezing of the motion of the MA cations. This in turn may be responsible for the abrupt change in photoluminescence properties of $CH_3NH_3PbI_3$ at about the same temperature. Finally, we performed a comparison between deuterated and non-deuterated CH_3NHPbI_3 to see how the concomitant change in hydrogen bonding strength affects the material properties. We found that this substitution had a profound impact on the behaviour of the PL with temperature, but during the PL study we were unable to find any indication that the twin walls or the phase transitions had any bearing on the PL characteristics. In the RUS measurements, we additionally found that the deuterium substitution substantially alters the movement of the twin walls in the tetragonal phase, and causes a major change in the incipient instability that is observed at low temperature. The conclusion to draw from this is that all of these processes are to some degree governed by hydrogen bonding in the MA cations. In a different context, it is certainly of interest from the wider perspective of domain wall engineering that the presence of an organic A cation with choice of H or D could be used to control the effective viscosity experienced by a moving twin wall.

References

1. Motta, C., F. El-Mellouhi, and S. Sanvito, *Charge carrier mobility in hybrid halide perovskites.* Scientific Reports, 2015. **5**.
2. Pisoni, A., et al., *Ultra-Low Thermal Conductivity in Organic-Inorganic Hybrid Perovskite CH3NH3PbI3.* Journal of Physical Chemistry Letters, 2014. **5**(14): p. 2488-2492.
3. Grancini, G., et al., *CH3NH3PbI3 perovskite single crystals: surface photophysics and their interaction with the environment.* Chemical Science, 2015. **6**(12): p. 7305-7310.
4. Carpenter, M.A., *Static and dynamic strain coupling behaviour of ferroic and multiferroic perovskites from resonant ultrasound spectroscopy.* Journal of Physics-Condensed Matter, 2015. **27**(26),263201.
5. Zadler, B.J., et al., *Resonant Ultrasound Spectroscopy: theory and application.* Geophysical Journal International, 2004. **156**(1): p. 154-169.
6. Svitelskiy, O., et al., *Resonant ultrasound spectroscopy of KTa(1-x)Nb(x)O(3) ferroelectric relaxor crystals.* Physical Review B, 2008. **78**(6).
7. Shekhter, A., et al., *Bounding the pseudogap with a line of phase transitions in YBa2Cu3O6+delta.* Nature, 2013. **498**(7452): p. 75-77.
8. Tang, L.G. and W.W. Cao, *Characterization of Full Set Material Constants and Their Temperature Dependence for Piezoelectric Materials Using Resonant Ultrasound Spectroscopy.* Jove-Journal of Visualized Experiments, 2016(110).
9. Xu, W.D., et al., *Dissociation of Methylammonium Cations in Hybrid Organic-Inorganic Perovskite Solar Cells.* Nano Letters, 2016. **16**(7): p. 4720-4725.
10. Leguy, A.M.A., et al., *The dynamics of methylammonium ions in hybrid organic-inorganic perovskite solar cells (vol 6, 7124, 2015).* Nature Communications, 2015. **6,** 7124.
11. Whitfield, P.S., et al., *Structures, Phase Transitions and Tricritical Behavior of the Hybrid Perovskite Methyl Ammonium Lead Iodide.* Sci. Rep., 2016. **6**: p. 35685.
12. Weller, M.T., et al., *Complete structure and cation orientation in the perovskite photovoltaic methylammonium lead iodide between 100 and 352 K.* Chem. Commun., 2015. **51**(20): p. 4180-4183.
13. Travis, W., et al., *On the application of the tolerance factor to inorganic and hybrid halide perovskites: a revised system.* Chem. Sci, 2016, 4548-4556 .
14. Lee, J.H., et al., *Resolving the Physical Origin of Octahedral Tilting in Halide Perovskites.* Chem. Mater., 2016. **28**(12): p. 4259-4266.
15. Li, J.R. and P. Rinke, *Atomic structure of metal-halide perovskites from first principles: The chicken-and-egg paradox of the organic-inorganic interaction.* Phys. Rev. B, 2016. **94**(4).

16. Lee, J.H., et al., *Role of hydrogen-bonding and its interplay with octahedral tilting in CH3NH3PbI3.* Chem. Commun., 2015. **51**(29): p. 6434-6437.
17. Lee, J.H., E.H. Kong, and H.M. Jang, *The nature of hydrogen-bonding interaction in the prototypic hybrid halide perovskite, tetragonal CH3NH3PbI3.* Sci. Rep., 2016. **6,** 21687.
18. McKnight, R.E.A., et al., *Acoustic dissipation associated with phase transitions in lawsonite, CaAl2Si2O7(OH)(2)center dot H2O.* American Mineralogist, 2007. **92**(10): p. 1665-1672.
19. McKnight, R.E.A., *Anomalous elastic behaviour associated with phase transitions, observed using resonant ultrasound spectroscopy*. 2009: University of Cambridge.
20. McKnight, R.E.A., et al., *Grain size dependence of elastic anomalies accompanying the alpha-beta phase transition in polycrystalline quartz.* Journal of Physics-Condensed Matter, 2008. **20**(7),075229.
21. A. Migliori, J.S., *Resonant Ultrasound Spectroscopy: Applications to Physics, Material Measurements and Nondestructive Evaluation*. 1997: Wiley VCH
22. Swainson, I.P., et al., *From soft harmonic phonons to fast relaxational dynamics in CH3NH3PbBr3.* Physical Review B, 2015. **92**(10).
23. Doron Shilo, G.R., Kaushik Bhattacharya, *Investigation of twin-wall structure at the nanometre scale using atomic force microscopy.* Nature Materials, 2004. **3**: p. 453-457.
24. Perks, N.J., et al., *Strain relaxation mechanisms of elastic softening and twin wall freezing associated with structural phase transitions in (Ca,Sr)TiO3 perovskites.* Journal of Physics-Condensed Matter, 2014. **26**(50).
25. McKnight, R.E.A., C.J. Howard, and M.A. Carpenter, *Elastic anomalies associated with transformation sequences in perovskites: I. Strontium zirconate, SrZrO3.* Journal of Physics-Condensed Matter, 2009. **21**(1).
26. McKnight, R.E.A., et al., *Elastic anomalies associated with transformation sequences in perovskites: II. The strontium zirconate-titanate Sr(Zr, Ti)O-3 solid solution series.* Journal of Physics-Condensed Matter, 2009. **21**(1),015902.
27. Onodayamamuro, N., et al., *P-T Phase-Relations of Ch3nh3pbx3 (X=Cl, Br, I) Crystals.* Journal of Physics and Chemistry of Solids, 1992. **53**(2): p. 277-281.
28. Knop, O., et al., *Alkylammonium Lead Halides .2. Ch3nh3pbcl3, Ch3nh3pbbr3, Ch3nh3pbi3 Perovskites - Cuboctahedral Halide Cages with Isotropic Cation Reorientation.* Canadian Journal of Chemistry-Revue Canadienne De Chimie, 1990. **68**(3): p. 412-422.
29. Poglitsch, A. and D. Weber, *Dynamic Disorder in Methylammoniumtrihalogenoplumbates(Ii) Observed by Millimeter-Wave Spectroscopy.* Journal of Chemical Physics, 1987. **87**(11): p. 6373-6378.

30. Poglitsch, A. and D. Weber, *Dynamic Disorder in Methylammoniumtrihalogenoplumbates (II) Observed by Millimeter-Wave Spectroscopy.* J. Chem. Phys., 1987. **87**(11): p. 6373-6378.
31. Baikie, T., et al., *Synthesis and crystal chemistry of the hybrid perovskite (CH3NH3) PbI3 for solid-state sensitised solar cell applications.* J. Mater. Chem. A, 2013. **1**(18): p. 5628-5641.
32. Salje, E.K.H., *Multiferroic Domain Boundaries as Active Memory Devices: Trajectories Towards Domain Boundary Engineering.* Chemphyschem, 2010. **11**(5): p. 940-950.
33. Salje, E. and H.L. Zhang, *Domain boundary engineering.* Phase Transitions, 2009. **82**(6): p. 452-469.
34. Rothmann, M.U., et al., *Direct observation of intrinsic twin domains in tetragonal CH3NH3PbI3.* Nature Communications, 2017. **8,** 14547.
35. Carpenter, M.A., et al., *Elastic relaxations associated with the Pm(3)over-barm-R(3)over-barc transition in LaAlO3: IV. An incipient instability below room temperature.* Journal of Physics-Condensed Matter, 2010. **22**(3),035406.
36. Onodayamamuro, N., T. Matsuo, and H. Suga, *Calorimetric and Ir Spectroscopic Studies of Phase-Transitions in Methylammonium Trihalogenoplumbates-(Ii).* Journal of Physics and Chemistry of Solids, 1990. **51**(12): p. 1383-1395.
37. Chi, L.S., et al., *The ordered phase of methylammonium lead chloride CH3ND3PbCl3.* Journal of Solid State Chemistry, 2005. **178**(5): p. 1376-1385.
38. Rehwald, W., *Study of Structural Phase-Transitions by Means of Ultrasonic Experiments.* Advances in Physics, 1973. **22**(6): p. 721-755.
39. Carpenter, M.A. and E.K.H. Salje, *Elastic anomalies in minerals due to structural phase transitions.* European Journal of Mineralogy, 1998. **10**(4): p. 693-812.
40. Carpenter, M.A., et al., *Structural relationships and a phase diagram for (Ca, Sr) TiO3 perovskites.* Journal of Physics-Condensed Matter, 2006. **18**(48): p. 10725-10749.
41. Sondergeld, P., et al., *Ordering and elasticity associated with low-temperature phase transitions in lawsonite.* American Mineralogist, 2005. **90**(2-3): p. 448-456.
42. Carpenter, M.A., *Elastic properties of minerals and the influence of phase transitions.* American Mineralogist, 2006. **91**(2-3): p. 229-246.
43. Norwick, B., *Anelastic relaxation in crystalline solids*. 1972, New York: Academic Press.
44. Weller, M., et al., *ACCURATE DETERMINATION OF ACTIVATION ENTHALPIES ASSOCIATED WITH THE STRESS-INDUCED MIGRATION OF OXYGEN OR NITROGEN IN TANTALUM AND NIOBIUM.* Acta Metall. Mater., 1981. **29**(6): p. 1047-1054.
45. Schaller, R., *Mechanical Spectroscopy Q-1 2001: With Applications to Materials Science*. 2001: Trans Tech Publications.

46. Rehman, W., et al., *Photovoltaic mixed-cation lead mixed-halide perovskites: links between crystallinity, photo-stability and electronic properties.* Energy & Environmental Science, 2017. **10**(1): p. 361-369.

47. Eames, C., et al., *Ionic transport in hybrid lead iodide perovskite solar cells.* Nature Communications, 2015. **6,** 7497.

48. Chen, T., et al., *Rotational dynamics of organic cations in the CH3NH3PbI3 perovskite.* Physical Chemistry Chemical Physics, 2015. **17**(46): p. 31278-31286.

Chapter 9 - Conclusions

In summary, this thesis has focussed on how the excellent semiconducting properties of hybrid perovskites can be optimised for optoelectronic applications, with a particular focus on their use in thin film lasers. We have explored a wide range of variations on the basic hybrid perovskite structure and probed the physics of the material using a wide range of techniques. Hybrid perovskites have proven to be a revolutionary material in the field of thin film solar cells, and as the field has matured there is now increasing interest on their use in light emitting applications such as lasers and light emitting diodes. Hybrid perovskites gain a range of attractive properties by combining the advantages of both organic and inorganic semiconductors. They have strong photoluminescence[1], high charge mobility[2], a large absorption coefficient, and a low exciton binding energy[3, 4] whilst also being cheap and solution processible. However, in spite of their high performance they have been held back from immediate commercialisation by their mediocre stability and the toxicity of their lead component, and the Hoke effect has thus far placed a severe limit on the tuneability of their bandgap[5]. The goals of this thesis were two-fold. First we aimed to collaborate with structural chemists and materials scientists to study the properties of hybrid perovskites on a fundamental level using a variety of advanced spectroscopic techniques such as air photoemission and resonant ultrasound spectroscopy. These would provide insight into the origin of the high performance of perovskites and could lead to the design of a new generation of lead-free materials which maintain the high performance of the current state-of-the-art. Secondly, we aimed to exploit the strong photoluminescence seen in hybrid perovskites to produce high quality thin film lasers of any colour with the potential to achieve continuous wave or even electrical pumping.

In chapter 4, we discussed our work on using Kelvin probe and air photoemission to study the physics of perovskite solar cells. Using the non-inverted structure, we were able to fabricate solar cells with efficiency of up to 10 %. Using air photoemission and Kelvin probe, we measured the energy levels of the constituent parts of this design of solar cell, allowing us to construct a detailed map of how the energy levels evolved throughout the device[6]. This model could then be combined with surface photovoltage measurements to gauge the effectiveness of each layer in the cell design, and to identify possible avenues for improvement. Using these techniques, together with studies on photoluminescence and solar cell performance, allowed us to investigate bismuth doped perovskites as a possible low-lead content alternative to $CH_3NH_3PbI_3$. We found that doping $CH_3NH_3PbI_3$ with even a small amount of bismuth was highly detrimental to the photoluminescence and solar cell performance, and a possible reason for this was the A site vacancies which are introduced by the

extra charge on the Bi^{3+} ion. To test this hypothesis, we used an alternative route to introducing A site vacancies by doping $CH_3NH_3PbI_3$ with $H_3NC_2H_4NH_3^2$. We found that introducing vacancies by this method had far less impact on the performance than when using bismuth. Hence we concluded that it was a property of the Bi^{3+} ion itself, rather than the vacancies it introduced, that was the root of the problem.

While studying perovskites as a solar cell material, we found that $CH_3NH_3PbI_3$ was also remarkably effective as a laser material, and Chapter 5 describes our initial efforts, using the lead acetate deposition route, to achieve an all solution-processed perovskite distributed feedback laser that emitted in the near infrared. We found that producing high quality films with low scattering losses was key to achieving laser operation, as random lasing modes and scattered amplified spontaneous emission would compete with the lasing mode for gain if the film quality was not sufficient. Our best lasers achieved a threshold of ~ 110 μJcm^{-2} under ns pulses or ~4 μJcm^{-2} under fs excitation, and our initial studies showed that the resulting lasers had better than expected stability[7]. This high stability of $CH_3NH_3PbI_3$, combined with the fact that triplet excitons are not present in the material, makes it a highly attractive candidate for achieving continuous wave lasing[8]. We tested this prospect by pumping a $CH_3NH_3PbI_3$ laser with fs pulses at a repetition rate of 80 MHz in order to approach the quasi CW regime, but thermal effects appeared to prevent us from observing lasing in these conditions.

In chapter 6, we aimed to expand upon the achievements of the previous chapter by producing green-emitting perovskite lasers with low thresholds. A key part of achieving the lowest threshold possible was to overcome the intensity dependent PL issues which prevent the material emitting well at low excitation densities. By optimising the deposition process to produce high quality films with small crystals, we were able to maximise the PL at low intensities whilst keeping the scattering losses to a minimum, and by using the optimal technique we were able to produce green lasers with a threshold of ~6 μJcm^{-2} under ns pumping[9]. These $CH_3NH_3PbBr_3$ lasers had single mode outputs with very high quality, and tuning the grating period allowed us to switch the laser between transverse electric and transverse magnetic polarisations. We found that simple encapsulation would allow the lasers to operate for many hours at a time without any sign of degradation, making it easy to perform prolonged experiments at high powers. Finally, we attempted to lower the threshold of these lasers further by exploring the effect of swapping the methylammonium cation in $CH_3NH_3PbI_3$ with formamidinium or caesium. These substitutions were observed to substantially alter the properties of the resulting films, but none of them had properties which were suitable for achieving low threshold lasing.

Our work on achieving strong PL at low intensities using $CH_3NH_3PbBr_3$ had allowed us to achieve high quality lasers with good threshold, but even with these improvements their PLQY was still more than an order of magnitude less than seen in organic polymers, and the Hoke effect was still preventing us achieving good colour tuneability. To combat this, chapter 7 focussed on producing lasing from low dimensional perovskites. Our first step looked at quasi 2D layered perovskites[10], and we developed films based on $(PEA)_2(MA)_{n-1}Pb_nBr_{3n+1}$ to achieve blue-green photoluminescence with a PLQY of up to 72 %. We found that the PLQY of these films would vary strongly with their n value or the choice of antisolvent in their deposition. Their colour could be tuned into the blue to a small degree by substituting some Br for Cl, but any attempts to tune into the red by the addition of I was found to completely kill the PL. Despite the high PLQY and good film quality, they were unable to achieve low threshold stimulated emission because a small amount of sub bandgap absorption dramatically increased their waveguiding loss. Future work with this material would focus on their use in perovskite light emitting diodes, where self-absorption is less of a problem and their excellent PLQY values could allow them to achieve high efficiency.

In our search for colour tuneable perovskites for low threshold lasing we also worked with Dr Credgington's group on $CsPbX_3$ perovskite nanocrystals[11]. These were known to have high PLQY and easily tuneable colour, but our initial attempts at achieving lasing by encasing them in a polymer matrix yielded very poor results. We were able to achieve much better results by making raw films of the pure nanocrystals. These achieved high PLQY, and green-emitting samples demonstrated a good lasing threshold without suffering from the concentration quenching effects one would normally expect in a raw film of nanocrystals. Films of these nanocrystals had a refractive index much closer to those of organic polymers, and this allowed us to experiment with lasing from a much wider range of distributed feedback gratings, with mixed order gratings achieving thresholds as low as 20 μJcm^{-1}. These results are very promising, but we were prevented from achieving our initial goal of colour tuneability because we experienced significant batch-to-batch variation in the performance of our nanocrystals. Future work would focus on overcoming these issues and using perovskite nanocrystals to achieve lasing at all colours in the visible spectrum.

The search for lead-free alternatives to $CH_3NH_3PbI_3$ has been hindered somewhat because the fundamental reasons behind the high performance of hybrid perovskites remain poorly understood, and so it is essential to perform in depth studies on the underlying properties of perovskites to see how they could affect the device performance. One of the key points of interest in this field is how the hydrogen bonding from the organic cation impacts the properties of the crystal as a whole, and it is also of interest to see how these halide perovskites compare to their oxide counterparts. We

aimed to study this by measuring single crystals of $CH_3NH_3PbX_3$ with resonant ultrasound spectroscopy, and found that $CH_3NH_3PbI_3$ and $CH_3NH_3PbBr_3$ both follow tilting transitions which are roughly analogous to some oxide perovskites, with the exception that the magnitude of the strain-induced effects was close to an order of magnitude higher. The phase transitions in $CH_3NH_3PbCl_3$ are controlled by hydrogen bonding rather than tilting, and this allowed us to observe the effects of hydrogen bonding more directly. We found that the phase transitions induced by hydrogen bonding have very little effect on the elastic constants, but we were able to observe several Debye resonances at ~155 K, which we attribute to the freezing of the MA cations and the motion of the halogens. As a final study into the effects of hydrogen bonding we explored the effect of switching hydrogen for deuterium in $CH_3NH_3PbI_3$, and found that the resulting change in hydrogen bonding caused significant differences to the photophysical properties of the material, whilst also having a large effect on the motion of twin walls and its incipient instabilities at low temperature.

Overall, this thesis has studied lead halide perovskites from a wide range of angles, and I hope that this work will encourage further research into perovskites as a lasing medium whilst furthering the understanding of the fundamental properties of hybrid perovskites.

1. Himchan Cho, S.-H.J., Min-Ho Park, Young-Hoon Kim, Christoph Wolf, Chang-Lyoul Lee, Jin Hyuck Heo, Aditya Sadhanala, NoSoung Myoung, Seunghyup Yoo, Sang Hyuk Im, Richard H. Friend, Tae-Woo Lee, *Overcoming the electroluminescence efficiency limitations of perovskite light-emitting diodes.* Science, 2015. **350**(6265): p. 1222-1225.
2. Samuel D. Stranks, G.E.E., Giulia Grancini, Christopher Menelaou, Marcelo J. P. Alcocer, Tomas Leijtens, Laura M. Herz, Annamaria Petrozza, Henry J. Snaith, *Electron-Hole Diffusion Lengths Exceeding 1 Micrometer in an Organometal Trihalide Perovskite Absorber.* Science, 2013. **342**(6156): p. 341-344.
3. Atsuhiko Miyata, A.M., Paulina Plochocka, Oliver Portugall, Jacob Tse-Wei Wang, Samuel D. Stranks, Henry J. Snaith & Robin J. Nicholas, *Direct measurement of the exciton binding energy and effective masses for charge carriers in organic–inorganic tri-halide perovskites.* Nature Physics, 2015. **11**: p. 582-587.
4. Krzysztof Galkowski, A.M., Atsuhiko Miyata, Paulina Plochocka, Oliver Portugall, Giles E. Eperon, Jacob Tse-Wei Wang, Thomas Stergiopoulos, Samuel D. Stranks, Henry J. Snaith, Robin J. Nicholas, *Determination of the exciton binding energy and effective masses for the methylammonium and formamidinium lead tri-halide perovskite family.* Energy & Environmental Science, 2016. **9**: p. 962-970.

5. Eric T. Hoke, D.J.S., Emma R. Dohner, Andrea R. Bowring, Hemamala I. Karunadasa Michael D. McGehee *Reversible photo-induced trap formation in mixed-halide hybrid perovskites for photovoltaics* Chemical Science, 2015. **6**(1): p. 613-617.
6. J. R. Harwell, T.K.B., I. D. Baikie, J. L. Payne, C. Ni, J. T. S. Irvine, G. A. Turnbull, I. D. W. Samuel, *Probing the energy levels of perovskite solar cells via Kelvin probe and UV ambient pressure photoemission spectroscopy* Physical Chemistry Chemical Physics, 2016. **18**: p. 19738-19745
7. Guy L. Whitworth, J.R.H., David N. Miller, Gordon J. Hedley, Wei Zhang, Henry J. Snaith, Graham A. Turnbull, Ifor D. W. Samuel *Nanoimprinted distributed feedback lasers of solution processed hybrid perovskites.* Optics Express, 2016. **24**(21): p. 23677-23684.
8. Michele Cadelano, V.S., Nicola Sestu, Daniela Marongiu, Feipeng Chen, Roberto Piras, Riccardo Corpino, Carlo Maria Carbonaro, Francesco Quochi, Michele Saba, Andrea Mura, Giovanni Bongiovanni, *Can Trihalide Lead Perovskites Support Continuous Wave Lasing?* Advanced Optical Materials, 2015. **3**(11): p. 1557-1564.
9. J.R. Harwell, G.L.W., G.A.Turnbull, I.D.W. Samuel, *Green Perovskite Distributed Feedback Lasers.* Scientific Reports, 2017. **7**: p. 11727
10. Nana Wang, L.C., Rui Ge, Shuting Zhang, Yanfeng Miao, Wei Zou, Chang Yi, Yan Sun, Yu Cao, Rong Yang, Yingqiang Wei, Qiang Guo, You Ke, Maotao Yu, Yizheng Jin, Yang Liu, Qingqing Ding, Dawei Di, Le Yang, Guichuan Xing, He Tian, Chuanhong Jin, Feng Gao, Richard H. Friend, Jianpu Wang, Wei Huang, *Perovskite light-emitting diodes based on solution-processed self-organized multiple quantum wells.* Nature Photonics, 2016. **10**: p. 699-704.
11. Loredana Protesescu, S.Y., Maryna I. Bodnarchuk, Franziska Krieg, Riccarda Caputo, Christopher H. Hendon, Ruo Xi Yang, Aron Walsh, Maksym V. Kovalenko, *Nanocrystals of Cesium Lead Halide Perovskites (CsPbX3, X = Cl, Br, and I): Novel Optoelectronic Materials Showing Bright Emission with Wide Color Gamut.* Nano Letters, 2015. **15**(6): p. 3692-3696.